Spectral Efficient Non-orthogonal Radio Designs For Future Wireless Networks

by

Amirhossein Mohammadian

A thesis submitted in partial fulfillment of the requirements for the degree of

Doctor of Philosophy

in

Communications

Department of Electrical and Computer Engineering
University of Alberta

Abstract

The fifth-generation (5G) and beyond wireless networks aim to increase the current data rates to more than 10 Gbit/s. Thus, the spectrum crunch necessitates increasing spectral efficiency (SE). Key non-orthogonal technologies for this goal are (I) full-duplex wireless, (II) generalized frequency division multiplexing (GFDM), (III) cognitive radio. Non-orthogonal subcarriers instead of orthogonal subcarriers are the basis of GFDM. All these technologies exploit non-orthogonal designs in exchange for a favorable tradeoff between interference and improved SE. However, interference can also increase with radio frequency (RF) impairments. Thus, this research's primary goal is to investigate the interplay among non-orthogonal designs, SE improvement, and RF impairments. To this end, the SE improvement of cellular base stations (BS) with non-orthogonal signaling is investigated. Thus, a GFDM full-duplex BS transceiver with optimal filters is proposed to enhance the SE of both uplink and downlink transmissions. Moreover, the SE enhancement of secondary links in cognitive radios is studied. It is shown that the proposed GFDM-based full-duplex secondary links significantly improve the achievable SE in the presence of RF impairments and adjacent channel interference (ACI) constraints. However, it is also shown that RF impairments may negatively impact potential SE gains. Therefore, standard estimators and deep learning (DL) algorithms are proposed for RF impairment compensation in channel estimation and data detection for GFDM and multiple-input multiple-output (MIMO)-GFDM full-duplex systems. This thesis demonstrates that the non-orthogonal designs enhance the SE. Moreover, the RF impairments limit the SE gain, while the proposed compensation algorithms eliminate their impacts.

Preface

This thesis is an original work conducted by Amirhossein Mohammadian.
RF impairments introduction in Chapter 1 was published in the following paper:

- A. Mohammadian and C. Tellambura, **RF Impairments in Wireless Communication Transceivers: Phase Noise, CFO, and IQ Imbalance-A Survey,** *IEEE Access*, vol. 9, pp. 111718-11179, Aug. 2021.

The results of Chapter 2 were published in the following papers:

- A. Mohammadian, C. Tellambura and M. Valkama, "**Analysis of Self-Interference Cancellation under Phase Noise, CFO and IQ Imbalance in GFDM Full-Duplex Transceivers,** *IEEE Trans. Veh. Technol.*, vol. 69, no. 1, pp. 700-713, Jan. 2020

- A. Mohammadian and C. Tellambura, **Full-Duplex GFDM Radio Transceivers in the Presence of Phase Noise, CFO and IQ Imbalance,** in *Proc. IEEE International Conference on Communications (ICC)*, May 2019, pp. 1-6

The results of Chapter 3 were published in the following papers:

- A. Mohammadian and C. Tellambura, **Cognitive GFDM Full-Duplex Radios with RF Impairments and ACI Constraints,** *IEEE Open J. Commun. Soc.*, vol. 1, pp. 732-749, May. 2020.

- A. Mohammadian and C. Tellambura, **GFDM-Modulated Full-Duplex Cognitive Radio Networks in the Presence of RF Impairments,** in *Proc.*

IEEE International Symposium on Personal, Indoor and Mobile Radio Communications (PIMRC), Sept. 2019, pp. 1-6.

- A. Mohammadian, M. Baghani and C. Tellambura, **Optimal Power Allocation of GFDM Secondary Links with Power Amplifier Nonlinearity and ACI,** *IEEE Wireless Commun. Lett.*, vol. 8, no. 1, pp. 93-96, Feb. 2019.

The results of Chapter 4 were published in the following papers:

- A. Mohammadian and C. Tellambura, **Joint Channel and Phase Noise Estimation and Data Detection for GFDM,** *IEEE Open J. Commun. Soc.*, vol. 2, pp. 915-933, April 2021.

- A. Mohammadian, C. Tellambura and G.Y. Li, **Deep Learning-Based Joint Channel and Phase Noise Estimation and Data Detection In Mult-Carrier Systems,** *IEEE Wireless Commun. Lett.*, June 2021.

The results of Chapter 5 was published in the following paper:

- A. Mohammadian, C. Tellambura and G.Y. Li, **Deep Learning LMMSE Joint Channel, PN, and IQ Imbalance Estimator for Multicarrier MIMO Full-Duplex Systems,** *IEEE Wireless Commun. Lett.*, Oct. 2021.

To My Mom, Dad, and My Beloved Wife

Acknowledgements

First of all, I want to express my sincere gratitude and respect to my supervisor, Prof. Chintha Tellambura who provided encouragement, guidance, and invaluable expertise throughout my PhD program. I extend my sincere gratitude to the PhD supervisory committee member Prof. Hai Jiang and Prof. Masoud Ardakani for evaluating my thesis and providing constructive feedback and comments. I would also like to convey my special thanks to Prof. Ha Nguyen and Dr. Li Cheng for their valuable feedback during my final PhD defense.

My most heartfelt gratitude goes to my beloved wife Mahtab for her immeasurable support, inspiration and encouragement throughout my PhD journey. I would also like to thank my parents and my sister for their support. Furthermore, I would like to thank former and current members of the Wireless Communications lab W5-070 who helped me during my PhD studies.

Table of Contents

List of Tables

List of Figures

Abbreviations

5G	Fifth-generation
ACI	Adjacent channel interference
ACPR	Adjacent channel power ratio
ADAM	Adaptive moment estimation
AGMA	Arithmetic-geometric mean approximation
AWGN	Additive white Gaussian noise
BEM	Basis expansion mode
BER	Bit-error rate
BS	Base station
CFO	Carrier frequency offset
CNN	Convolutional neural network
CP	Cyclic prefix
DL	Deep Learning
DNN	Deep neural network
EVM	Error vector magnitude
FBMC	Filter bank multicarrier
FDD	Frequency Division Duplex

FLOP	Floating point operation
GFDM	Generalized frequency division multiplexing
GP	Geometric programming
i.i.d	Independent and identically distributed
ICI	Inter-carrier interference
IQ imbalance	In-phase and quadrature-phase imbalance
IRR	Image rejection ratio
ISI	Inter-symbol interference
LMMSE	Linear minimum mean square error
LS	Least-squares
MAP	Maximum-a-posteriori
MF	Matched filter
MIMO	Multiple-input multiple-output
MMSE	Minimum mean square error
MSE	Mean squared error
NLS	Non-linear least squares
OFDM	Orthogonal frequency division multiplexing
PA	Power amplifier
PN	Phase noise
PSD	Power spectral density
PU	Primary user
RC	Raised Cosine

RF	Radio frequency
SE	Spectral efficiency
SI	Self-interference
SINR	Signal-to-interference plus-noise ratio
SIR	Signal-to-interference ratio
SISO	Single-input single-output
SNR	Signal-to-noise ratio
SU	Secondary user
TDD	Time Division Duplex
UHF	Ultra high frequency
VHF	Very high frequency
WLAN	Wireless local area networ
WSSUS	Wide-sense stationary uncorrelated scattering
ZF	Zero forcing

Chapter 1

Introduction

One of the main objectives of fifth-generation (5G) mobile communication systems and beyond is to increase the current data rates up to several gigabits per second (Gbit/s) and even exceeding 10 Gbit/s [1]. With the mobile data traffic increasing, more spectrum resources will be necessary for future wireless networks. However, scarce resources and growing user demands result in the spectrum crunch. The spectrum crunch refers to the lack of sufficient wireless spectrum needed to support a growing number of consumer devices and various government and private sector use of radio frequencies within the current spectrum allocation. For an example, currently, almost all countries use spectrum below 6 GHz for International Mobile Telecommunications (IMT) systems [2]. However, existing services and applications use much of this spectrum. Therefore, to alleviate the spectrum crunch, one can try to increase the data rate while keeping the bandwidth usage fixed. In other words, we should increase the spectral efficiency (SE) (measured by bits per second per Hz(bps/Hz)) via technological innovations. For a network with $N_u \geq 1$ number of users, the SE of the network is the total number of information bits that can be transmitted in it over a given total physical bandwidth B allocated. Indeed, the SE measures how efficiently the limited frequency spectrum is utilized by the network, which can be formulated as [3]

$$\eta = \frac{R_c}{B} \text{ [bps/Hz]}, \tag{1.1}$$

where R_c is the summation of data rate of users in the network, $R_c = \sum_{i=1}^{N_u} R_i$, where R_i is the data rate of i-th user. Note that the achievable data rate of each user is $R_i = B_i \log_2(1 + \text{SINR}_i)$[bps] [4], where B_i ($B = \sum_{i=1}^{N_u} B_i$) is allocated bandwidth to the i-th user. Therefore, the data rate of each user is a function of its frequency bandwidth. Hence, how the total bandwidth is allocated to the users is important

All current mobile cellular networks use the principle of orthogonal resource allocation to different users. Two signals $x(\xi)$ and $y(\xi)$ are said to be orthogonal, if

$$\int x(\xi) y^*(\xi) d\xi = 0,$$

where ξ denotes time, frequency, space, or other dimensions. If the above integral is not equal to zero, then the two signals are non-orthogonal. Thus, each user conducts orthogonal signaling within either a specific time slot, frequency band, or code. The fundamental advantage of this approach is that it allows the receiver of one user to entirely separate unwanted signals from its own signal (desired signal) since signals from different users are mutually orthogonal. In time division multiple access (TDMA), frequency division multiple access (FDMA), and orthogonal frequency division multiple access (OFDMA), multiple users are assigned orthogonal time slots, frequency slots, and subcarriers, respectively. Subcarrier separation ensures that they are orthogonal to each other [5, 6].

However, in orthogonal schemes, the bandwidths allocated to the users B_i, $i = 1, ..., N_u$, do not overlap with each other, e.g., for equal bandwidth allocation, $B_i = \frac{B}{N_u}$, $i = 1, ..., N_u$. Thus, the bandwidth per user decreases as the number of users increases. Therefore, each user gets a smaller bandwidth, which results in a decreased data rate per user. However, 5G and beyond networks with massive numbers of users require high data rates. Thus, conventional orthogonal schemes may not answer the demands of future networks.

Thus, one develops non-orthogonal schemes where multiple users can use the same bandwidth concurrently. Therefore, available bandwidth per user increases, which

results in a higher data rate. Hence, the total data rate of the network increases with the fixed bandwidth, which results in higher network SE. However, this SE gain does not come without cost. The cost is the interference between users (which is not there in orthogonal systems, at least in principle). Thus, more sophisticated receiver algorithms are needed, and the error rate of data recovery may increase. Thus, non-orthogonality achieves a higher SE, albeit at the cost of signal processing for interference management. Besides, radio frequency (RF) impairments may also increase the non-orthogonality by amplifying interference signals. Hence, there is a trade-off between achievable SE and the degree of interference. This thesis exploits this trade-off and designs and analyzes high SE non-orthogonal systems based on full-duplex wireless, generalized frequency division multiplexing (GFDM), and cognitive radio.

1.1 Overview

1.1.1 Full-Duplex Wireless

Current wireless nodes allow users to transmit and receive data same time via the so-called half-duplex mode. It allows bidirectional data transfer based on two orthogonal channels typically using time (i.e., Time Division Duplex (TDD)) or frequency (i.e., Frequency Division Duplex (FDD)) dimensions, to provide separation between transmit and receive signals [7]. This orthogonal schemes losses potential SE. As service demands evolve over the wireless networks, more efficient mobile communications typified by higher data rates and SE must be developed to answer ever-growth requirement on the limited cellular radio spectrum. To this end, full-duplex wireless which can simultaneously transmit and receive data on the same frequency band has received a lot of attraction – Figure 1.1.

Full-duplex can potentially double the data rate and increase spectrum utilization efficiency without using any additional bandwidth [7]. However, the fundamental

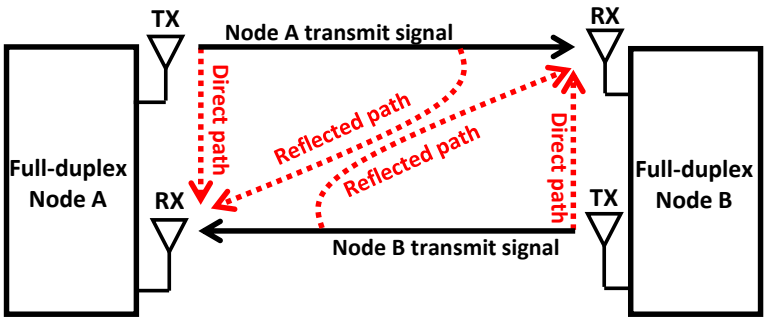

Figure 1.1: Basic block diagram of full-duplex transmission.

challenge in full-duplex wireless is the strong self-interference (SI) signal, caused by the signals leaking from the node's transmission into its own reception. To illustrate this, two full-duplex nodes, Node A and Node B (Figure 1.1) are considered, which transmit and receive signal at the same time and frequency. The SI signal in Node A's receiver (red dotted lines) consists of the leaked transmit signal in the direct path between Node A's transmitter and receiver, and Node A's transmit signal reflected from nearby obstacles/scatterers. The same situation occurs at Node B as well. This SI channel or the residual SI channel between the transmitter and the receiver after applying SI cancellation is assumed to be Rayleigh distributed [8] and in general is modelled as a multipath channel with multiple delays and attenuation components [9]. Because of the short distance between the transmit antenna and the receive antenna at each node, the SI power is too higher than than the receiver noise level [7, 10]. As a practical example, consider a full-duplex small-cell base station (BS) with transmit power of 24 dBm and a receiver noise floor of 100 dBm [7]. As it is shown in Figure 1.2, under assumption of 15 dB isolation between the BS's transmitter and receiver [11, 12], the BS's SI will be 109 dB above the noise floor.

Therefore, to achieve the link SNR equal to that of a half-duplex counterpart, SI needs to be mitigated at least to the noise floor or reasonably close to it. In the literature, SI mitigation of 60 - 113 dB has been reported by using cancellation techniques involve passive methods followed by active analog and active digital SI

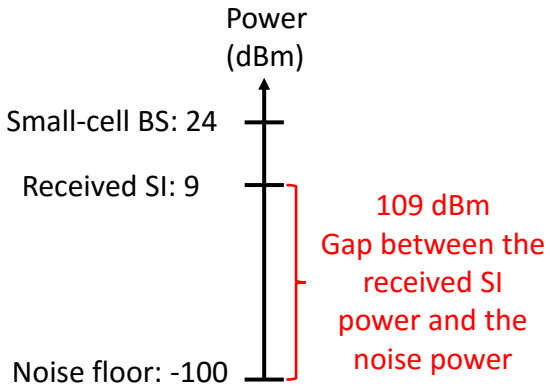

Figure 1.2: Required SI mitigation value considering a full-duplex small-cell BS with 24 dBm transmission power.

cancellation schemes [12–18]. Figure 1.3 shows the he SI cancellation techniques that are applied in each full-duplex node (Node A and Node B in Figure 1.1). Here is the overview of the SI cancellation techniques.

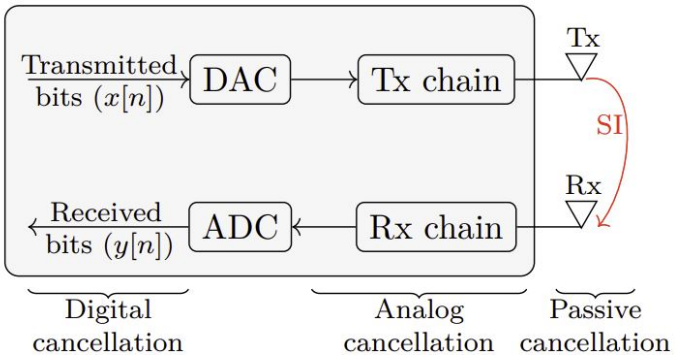

Figure 1.3: SI cancellation techniques in each full-duplex node [7].

- **Passive SI cancellation**: Passive SI cancellation methods rely on isolating the transmit RF chain from the receive RF chain as much as is possible. They aim to suppress SI signal before get into the receiver which prevents dealing with large dynamic range signals. In literature, several techniques for passive suppression are proposed including antenna separation [14, 19–21], phase control [22, 23], and cross-polarization [12, 24–27]. Antenna separation exploits the idea of increasing the pathloss between transmit and receive antennas to suppress

the SI. Moreover, phase control techniques enhances isolation between the antennas by creating near-field nulls in the antenna radiation pattern with phase differences between antenna elements. Furthermore, the cross-polarization techniques aim to electromagnetically isolate the antennas by sending and receiving signals over orthogonal polarization. It has been reported experimentally that between 45 dB and 70 dB SI suppression can be achieved by passive SI cancellation techniques [12, 14, 19–27].

- **Active SI cancellation:** these techniques, analog or digital [9], use active components and exploit the knowledge of a node's own transmit signal in generating a cancellation signal that can be subtracted from the received signal. Note that these cancellation methods require the estimation of the SI channel. If employed before the digitization of the received signal, they are called active analog cancellation methods. The alternative is to cancel the residual SI within the received signal after digitization, and that is called active digital cancellation.

  - **Analog**: The main goal is to suppress SI before it gets into the analog to digital conversion process. These techniques take a copy of the transmitted signal from the transmit antenna, adjust it with appropriate delay, phase and gain, and then subtract it from the received signal at the receiver antenna.
  - **Digital**: These techniques aim to suppress remaining SI after the analog to digital converter by using sophisticated digital signal processing techniques. They generate reconstructed digital samples by taking a copy of transmitted digital samples from transmitter and using SI channel estimations. Then, they subtract the reconstructed samples from the quantized received signal after analog to digital converter.

It has been reported that active analog and digital SI cancellation techniques

achieve 45–60 dB suppression levels [12, 24, 27–29].

Although the aforementioned techniques achieve a high level of SI cancellation, several non-ideal conditions especially RF impairment issues, limit the performance of the SI mitigation. In practice, SI consists of multiple components as the transmit signal is corrupted by the RF impairments, which should be modeled, analyzed, and suppressed.

1.1.2 GFDM Signalling

Multicarrier schemes transmit data over multiple carriers which are normally close spaced. Among various multicarrier designs, orthogonal frequency division multiplexing (OFDM) is the fundamental transmission standard for 4G-wireless, e.g. the LTE standard. OFDM offers robustness against multipath channels and easy implementation based on the Fast Fourier Transform. However, OFDM suffers from disadvantages such as high sensitivity to synchronization errors and strict synchronization process required to keep the orthogonality between subcarriers, low SE due to using one cyclic prefix (CP) per symbol, and high out-of-band emission. These drawbacks challenge the dominance of OFDM for future wireless. Hence, recent research has proposed several non-orthogonal multicarrier waveforms to address the limitations of OFDM, of which GFDM is promising [30].

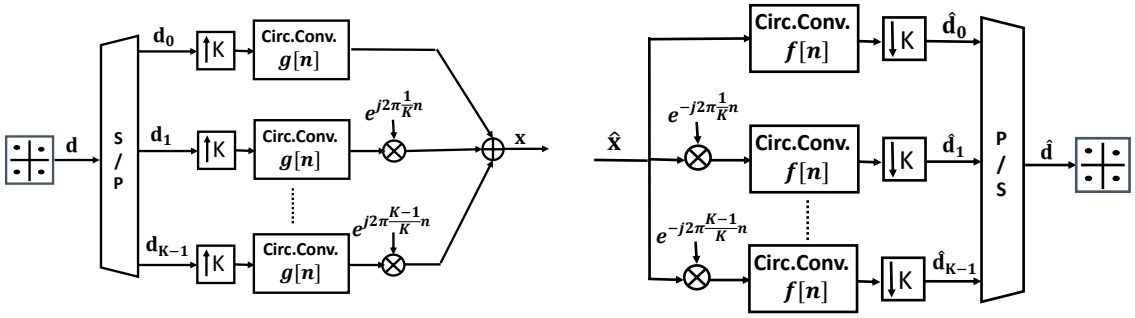

(a) Modulator

(b) Demodulator

Figure 1.4: Block diagram of GFDM modulator and demodulator

GFDM is a flexible block-based multicarrier waveform that includes number of

subcarriers, K, each one carries subsymbols generated in multiple time-slots, M– Figure 1.4. The subcarriers are individually pulse-shaped with a prototype filter that is circularly shifted in time and frequency domain– Figure 1.4a. the discrete GFDM signal per symbol-time interval may be expressed as [30]

$$x[n] = \sqrt{\alpha} \sum_{k=0}^{K-1} \sum_{m=0}^{M-1} d_{k,m} g_m[n] e^{\frac{j2\pi kn}{K}}, \tag{1.2}$$

where α is average transmit power, $0 \leq n \leq N-1$ ($N = MK$), $d_{k,m}$, $k = 0, 2, .., K-1$ and $m = 0, 2, .., M-1$ are independent and identically distributed (i.i.d.) complex data symbols with zero mean and unit variance and $g_m[n] = g[(n - mK) \bmod N]$ is a circularly shifted version of normalized prototype filter $g[n]$ which can be configured as Raised Cosine (RC) or a Root RC filter [31–33].

Moreover, GFDM signal in (1.2) can be written as $\mathbf{x} = \mathbf{dA}$, where $\mathbf{d} \in \mathbb{C}^{1\times N}$ is the data vector and $\mathbf{A} \in \mathbb{C}^{N\times N}$ is a modulation matrix given by $[\mathbf{A}]_{kM+m,n} = g_m[n] e^{\frac{j2\pi kn}{K}}$. The data vector $\mathbf{d}$ can be decomposed into K subvectors $\mathbf{d} = [\mathbf{d}_0^T, ..., \mathbf{d}_{K-1}^T]^T \in \mathbb{C}^{N\times 1}$, where $\mathbf{d}_k = [d_{kM}, ..., d_{kM+M-1}]^T \in \mathbb{C}^{M\times 1}$, for $k = 0, 1, ..., K-1$, denotes the M complex data symbols for the k-th subcarrier.

Note that since GFDM sacrifices orthogonality, its implementation complexity can increase. Thus, several methods have been developed to handle this problem [34]. In the low-complexity implementation of GFDM, discrete GFDM signal may be expressed as [34]

$$\mathbf{x} = \mathbf{F}_N^H \sum_{k=0}^{K-1} \tilde{\mathbf{P}}_k \tilde{\mathbf{\Psi}} \tilde{\mathbf{\Lambda}} \mathbf{F}_M \mathbf{d}_k, \tag{1.3}$$

where $\tilde{\mathbf{\Lambda}} = \overbrace{[\mathbf{I}_M, ..., \mathbf{I}_M]}^{\text{K}} \in \mathbb{C}^{N\times M}$ is the repetition matrix, $\tilde{\mathbf{\Psi}} \in \mathbb{C}^{N\times N}$ is the diagonal frequency-domain filtering matrix that has $\sqrt{M}\mathbf{F}_N(g[n])$ as its diagonal elements, and $\tilde{\mathbf{P}}_k \in \mathbb{C}^{N\times N}$ is a permutation matrix to up-convert the k-th subcarrier to its corresponding frequency[34].

GFDM demodulation

On the other hand, as it is shown in –Figure 1.4b, on the receiver side, the output of the GFDM demodulator at the $k^{'}$-th subcarrier and the $m^{'}$-th time-slot is given by

$$\widehat{d}_{k',m'} = \sum_{n=0}^{N-1} (\hat{x}[n]) f_{m'}[n] e^{\frac{-j2\pi k^{'} n}{K}}, \tag{1.4}$$

where $\hat{x}[n]$ is input of GFDM demodulator and $f_{m'}[n] = f[(n - m'K) \mathrm{mod} N]$ is circularly shifted version of receiver filter impulse response $f[n]$. Note that the receiver filter $f[n]$ is selected such that the effect of transmitter filter is minimized. Moreover, the detected GFDM symbols in (1.4) can be written as $\hat{\mathbf{d}} = \hat{\mathbf{x}}\mathbf{B}$, where $\hat{\mathbf{x}} \in \mathbb{C}^{1\times N}$ is the input signal and $\mathbf{B} \in \mathbb{C}^{N\times N}$ is a demodulation matrix given by $[\mathbf{B}]_{n,k'M+m'} = f_{m'}[n] e^{-j2\pi n \frac{k'}{K}}$. Conventional matched filter (MF) and zero forcing (ZF) are two widely used GFDM receiver structure. The receiver matrix for MF and ZF receivers are written as $\mathbf{B} = \mathbf{A}^H$ and $\mathbf{B} = \mathbf{A}^{-1}$, respectively. For conventional MF and ZF receivers, receiver filters, $\mathbf{f}^{MF} \in \mathbb{C}^{MK\times 1}$ and $\mathbf{f}^{ZF} \in \mathbb{C}^{MK\times 1}$, are equal to first column of the receiver matrix $\mathbf{A}^H$ and $\mathbf{A}^{-1}$, respectively. Furthermore, the receiver filter can be designed for the specific problems, e.g. signal-to-interference ratio (SIR) maximization which has been done in this thesis.

GFDM is flexible because of the degrees of freedom measured by the prototype filter and the number of subcarriers and subsymbols, which can be easily reconfigured to address a multitude of configurations. For example, GFDM turns into OFDM when $M = 1$ and the prototype filter is rectangular. Indeed, OFDM is a special case of GFDM waveform. Furthermore, as a consequence of filtering subcarriers with the prototype filter $g[n]$, out-of-band emissions of GFDM degrades and therefore makes it attractive for noncontiguous frequency bands. Moreover, it has advantage of high SE since one CP is only deployed at the beginning of each packet that contains number of subcarriers and subsymbols. Therefore, GFDM can be a potential alternative for achieving the goals of future wireless systems. This potential has motivated extensive studies of GFDM for cognitive radio networks [35], space-time codes [36], filter designs

[37, 38], multiple-input and multiple-output communications [39] Internet-of-Things [40], and optical networks [41].

1.1.3 Cognitive Radio

Empirically, we know that pre-assigned spectrum slots often go unused at different times and different spatial locations, e.g., over-the-air TV in some locations [42]. The problem is that primary users (PUs) of the spectrum may not be using it temporarily and geographically. Cognitive radio network replaces the inefficient traditional static spectrum management policies by dynamic spectrum access strategies [43]. In other words, it enables secondary users (SUs) to opportunistically access the primary users' spectrum without causing notable degradation to the quality of service of the primary users. Because of this opportunistic access by cognitive (secondary) users, the overall SE clearly improves. Cognitive radios are already included in different wireless standards such as IEEE 802.11 and IEEE 802.11.af, which allow wireless local area network (WLAN) and Wi-Fi operations in TV white space spectrum in the very high frequency (VHF) and ultra high frequency (UHF) bands [44].

There are three types of paradigms for accessing unlicensed SUs to the PUs spectrum, namely, underlay, overlay, and interweave, which are introduced as follow

- **Underlay**: In the underlay paradigm, SUs transmit on licensed bands simultaneously with PUs, but ensure that the resulting interference on PU nodes is less than a specified interference threshold [45]. SUs by adjusting their transmit powers meet the threshold, and if they are unable to do so, they stop their transmission.

- **Overlay** : Overlay paradigm allows concurrent primary and secondary transmissions in which PUs share knowledge of their massages and signal codebooks with SUs. Therefore, SUs can use part of their power for secondary communication and the remainder of the power to assist data transfer between PUs.

- **Interweave**: In the interweave paradigm, SUs are allowed to access a spectrum hole which is an unused frequency band at a specific time or location in which PUs are not transmitting. To be specific, SUs periodically monitor the radio spectrum, intelligently detects occupancy in the different parts of the spectrum, and then opportunistically communicates with minimal adjacent channel interference (ACI) to active neighboring PUs.

Note that underlay and overlay paradigms will constrain the achievable SU rates. Moreover, the burden of implementing such techniques falls on the secondary network.

1.1.4 RF Impairments

The critical issues with the ongoing development of highly flexible radio transceivers for mass-market applications is cost efficiency in terms of power consumption and chip areas, e.g., the cost efficiency of 5G networks should be 10-100X cheaper per Hz than 4G networks. To answer these requirements, one promising solution is using non-ideal low cost RF analog components with long operational lifetime in transceivers. However, these components are generally imperfect due to manufacturing errors, aging and other causes, thus introducing RF impairments.

In terms of contributing to RF impairments, perhaps one of the most critical analog components is the oscillator, which generates a reference signal for frequency and timing synchronization. However, non-ideal imperfections and time-domain instabilities of the oscillator are the sources of significant impairments, including phase noise (PN), carrier frequency offset (CFO), and in-phase (I) and quadrature-phase (Q) imbalance - Figure 1.5. The other crucial analog component in communication systems is the power amplifier (PA), which consumes a significant fraction of the total energy and is primarily nonlinear which introduces distortions. All of these impairments cause in-band and out-of-band distortions. In-band distortions fall inside the operating bandwidth and destroy the performance of the system e.g., they destroy the orthogonality between subcarriers and introduce inter-carrier interference (ICI).

On the other hand, out-of-band distortions fall outside the operating bandwidth. For instance, the spectrum spreading results in interference to adjacent channels. Due to these distortions, the system performance significantly degrades. This degradation can manifest in several ways: (1) a decrease in the signal-to-noise ratio (SNR) and increase the bit-error rate (BER), (2) an increase of the error vector magnitude (EVM) because of phase and amplitude distortions in the signal constellation, (3) a decrease in achievable rates and increase in outages, and (4) a reduction in the quality of channel estimations. Thus, the impacts of RF impairments on wireless transceivers are substantial. Here, the impairments are explained in details.

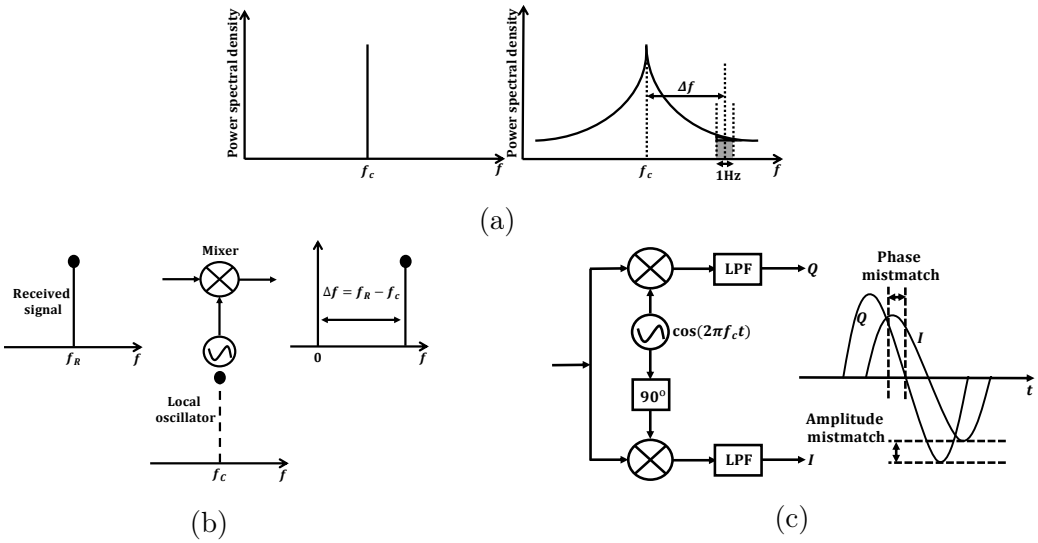

Figure 1.5: RF impairments: PN, CFO and IQ imbalance. (a) Spectral spreading due to PN, (b) CFO between the received signal and the local oscillator and (c) IQ demodulator with amplitude and phase mismatches.

- **PN**: PN occurs when the oscillator cannot generate pure sinusoidal waves with the Dirac spectrum. This happens due to rapid, short-term, random fluctuations in the carrier wave phase generated by oscillators in up-conversion or down-conversion processes of the baseband signal and radio frequency chain. Fig. 1.5a illustrates an ideal oscillator with the Dirac spectrum versus the real oscillator with PN. Engineers typically specify PN in the frequency domain over one Hz

spectrum at an offset of Δf from the carrier. The PN power over this bandwidth is normalized relative to the carrier power – dBc/Hz. For example, in GSM applications, the oscillator's PN should fall below -115 dBc/Hz at 600 kHz offset [46].

PN causes dramatic changes in the frequency spectrum and timing properties of the oscillator output. Specifically, PN widens the power spectral density (PSD) to either side of a signal (Fig. 1.5a), which may result in ACI. Furthermore, due to PN, the effective channel seen by the receiver becomes time-varying, and the transmit signal constellation rotates from symbol to symbol. PN also degrades the performance of channel estimates. In sum, all these effects will degrade the wireless system performance, i.e., reducing the effective SNR, limiting the BER, and reducing data rates.

For an oscillator with phase noise, its output signal can be modeled as $C_{osc} = e^{j(2\pi f_c t + \phi(t))}$, where f_c is carrier frequency and $\phi(t)$ is phase noise. In this thesis, Brownian motion free-running oscillator [31] is considered which generates phase noise $[\phi[n+1] - \phi[n]] \sim \mathcal{N}(0, 4\pi\beta T_s)$, where $\phi[n]$ is Brownian motion with 3-dB bandwidth of β and T_s is the sample interval.

- **CFO**: The CFO occurs when the down-converting local oscillator in the receiver does not perfectly synchronize with the received signal's carrier. Two effects cause this frequency mismatch, namely local oscillator errors and Doppler shifts. First, local oscillator errors occur because of the local oscillators' different physical properties and errors, such that they can never oscillate at an identical frequency. Wireless standards specify the oscillator precision tolerance, e.g., the IEEE 802.11a OFDM-based WLAN requires an error less than $\pm$20 parts per million (PPM), which results that the CFO should be in the range from -40 PPM to +40 PPM [47]. For example, if the transmit and the receive oscillators run at a frequency that is 20 PPM above and 20 PPM below

Table 1.1: Doppler frequency and normalized CFO [48]

System	Carrier frequency (f_c)	Subcarrier spacing (Δf)	Velocity (ν)	Maximum Doppler frequency (f_d)	Normalized CFO (ϵ)
DMB	375 MHz	1 kHz	120 km/h	41.67 Hz	0.042
3GPP	2 GHz	15 kHz	120 km/h	222.22 Hz	0.0148
Mobile WIMAX	2.3 GHz	9.765 kHz	120 km/h	255.55 Hz	0.0263

the identical carrier frequency, receptively, the received baseband signal will have a CFO of 40 PPM. For a carrier frequency of 5.2 GHz, the CFO is thus up to ±208 kHz. Second, the relative motion between the transmitter and the receiver shifts the carrier frequency seen by the receiver, which is the Doppler shift. For example, when a car moves at v =350 km/h, and wireless carrier operates at f_c =2.4 GHz frequency point, the maximum Doppler frequency offset will be over $f_d = \frac{vf_c}{c} = 800$ Hz, where c is speed of light. For several practical cases, Table. 1.1 shows the normalized CFO and Doppler frequency for three different commercial systems.

CFO causes a rotation and an attenuation of transmit symbols and introduces inter-symbol interference (ISI) and ICI. The received signal $r(t)$ after shifting by a frequency offset can be modeled as $s(t) = r(t)e^{j2\pi\Delta ft}$, where Δf indicates the frequency offset between the carrier frequency of the received signal and receiver local oscillator. In literature, the normalized CFO is defined as $\epsilon = \Delta f/f_s$, where f_s indicates subcarrier spacing.

- **IQ imbalance**: The IQ modulator and demodulator are part of the RF front-end of wireless transceivers to transform the complex baseband signals to pass-band centered at the carrier frequency and vice versa. Ideal IQ modulators and demodulators provide two orthogonal channels for the complex signal's real and

imaginary parts. However, mismatches between I and Q branches destroy this orthogonality and lead to IQ imbalance, which degrades the signal quality. We can attribute the mismatches to fabrication process variations, including doping concentration, oxide thickness, mobility, and geometrical sizes over the chip [49]. One can divide the mismatches causing the IQ imbalance into two groups regarding their influences: 1) frequency-flat IQ imbalance causing imperfect 90 phase difference and unequal amplitudes of the I and Q local oscillators, which is constant over the signal bandwidth, 2) frequency-selective IQ imbalance causing the component mismatching in I and Q branches, e.g., imperfect matched low-pass filters, which has different frequency responses over the signal bandwidth. Note that the frequency-selective IQ is severe in wideband systems.

These IQ imbalances result in harmful mirror interference and degrade the system's performance, e.g., BER, Signal-to-interference plus-noise ratio (SINR) and capacity. For example, in single carrier systems, IQ imbalance in transmitter and receiver causes ISI on neighboring signals, and in multicarrier systems, like OFDM, IQ imbalance generates ICI terms on mirror subcarriers (the mirror subcarrier of the k-th OFDM subcarrier is -k). Moreover, IQ imbalance can degrade the performance of channel estimation techniques by introducing the mirror interference terms. Thus, one must compensate IQ imbalance to meet the requirements of standards, e.g., the specifications of 3-rd Generation Partnership Project (3GPP) LTE/LTE-Advanced radio systems limit the minimum attenuation for the in-band image component in the transmitter to 25 dB or 28 dB [50].

The IQ mixer responses in the presence of IQ imbalance is given by $x_{IQ}(t) = g_d * x(t) + g_I * x^*(t)$, where g_d and g_I are the IQ mixer responses for the direct and image signals, respectively. Image rejection ratio (IRR) quantifies the quality of the IQ mixer which is defined as the ratio between the powers of the IQ mixer

response of the image and direct signals IRR = $\frac{|g_I|^2}{|g_d|^2}$ [50].

- **Nonlinear PA**: The most power-hungry block of wireless transceivers is PA which its efficiency is critical. For example, a 1 W PA with 50% draws 2 W from the battery which is higher than the rest of transceiver [46]. The power efficiency of PA is defined as a ratio between average power delivered to the load and average power drawn from DC supply. It is a measure which indicates how effectively the power drawn from the DC supply is converted to useful power at the output. However, there is an inverse relationship between the PA efficiency and its linearity. Because the PA plays a key role in the increased overall power consumption, utilizing the PA in its high efficiency region is necessary which results in high order of non-linearity. The impacts of PA non-linearity can be categorized into two effects: 1) spectral regrowth, which results in high ACI on adjacent channels, and 2) amplitude compression. The common measurement for indicating the level of PA non-linearity is 1 dB compression point. As it is shown in fig. 1.6, in 1 dB compression point, gain of a nonlinear PA deviates 1 dB from the gain of a linear PA. fig. 1.6. .

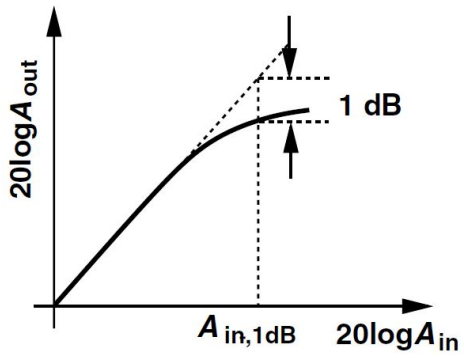

Figure 1.6: PA 1 dB compression point [46]

For characterizing the nonlinear PA behaviour, widely used polynomial model [51, 52] is deployed. The PA response modeled by a third-order polynomial nonlinearity [51] is given by $y(t) = a_1x(t) + a_3x(t)x(t)^2$, where $x(t)$ is the PA

input, a_1 and a_3 are linear and third-order gains.

Note that all the RF impairments mentioned above increase the degree of non-orthogonality and degrade the SE performance of communication systems. The RF impairments introduction in this section was published in [53].

1.2 Motivations and and Literature Review

The aforementioned technologies have significant potential to improve the SE of future wireless networks. However, RF impairments negatively impact the achievable the SE gains. Therefore, the motivations and objectives of this thesis are described in the following subsections.

1.2.1 SE Enhancement of Cellular BSs

In traditional cellular networks, the BS communicates with uplink and downlink users in orthogonal channels. Depending on the type of technology, these orthogonal channels are created by the use of different time-slots, frequency bands, or spreading sequences. Such creations entails a loss of SE (e.g., loss in spectrum usage). To enhance SE, GFDM-based full-duplex BSs are considered that serves uplink and downlink users at the same time and frequency.

In principle, full-duplex BSs can double SE by simultaneously communicating with downlink and uplink users. The users can be full-duplex or half-duplex. However, the BSs experience SI signals (transmit signal appearing as interference on the receive signal path), and the downlink users experience co-channel interference from uplink users. Due to these interference effects, the actual SE gains are diminished, and more research is needed to establish the achievable gains. Fortunately, research on full-duplex radios is already appearing. For example, [54] proposes a protocol to estimate and cancel interference terms to improve the SE. In [55], interference alignment is deployed to address the mutual interference. Moreover, the impact of full-duplex

radios can be incorporated into other emerging technologies such as massive MIMO. For instance, [56] and [57] consider full-duplex massive MIMO BSs and investigate beam-domain representation of channels and energy harvesting, respectively. However, potential SE gains of full-duplex radios will erode due to the presence of RF impairments. They significantly degrade the SI cancellation techniques' performance by introducing in-band and out-of-band distortions and interference.

On the other hand, GFDM achieves higher SE in compared with OFDM. Therefore, the integration of full-duplex and GFDM promises even more gains for cellular BSs. However, unlike OFDM, GFDM uses non-orthogonal sub-carriers and a pulse shaping filter covering several time-slots. Therefore, the latter may be more affected by RF impairments than the former. Thus, is it better to use GFDM than OFDM? In literature, impacts of RF impairments on OFDM full-duplex transceivers has been widely studied. References [27] and [8] clearly show that PN impairs SI cancellation, e.g., 30 dB SI increase due to PNs of two independent oscillators (for up/down conversions). Reference [50] proposes widely-linear digital SI cancellation to compensate for IQ imbalances. Furthermore, the SI and desired channels can be estimated under IQ imbalance [58], and an optimal pilot matrix is proposed. CFO estimation given IQ imbalances is studied in [59]. The collective impact of PN and IQ imbalance is investigated in [60]; it is found that with perfect digital domain cancellation, the average SI power increases linearly with 3-dB PN bandwidth and IQ IRR. Moreover, [51] develops the maximum likelihood estimates of the intended channel, SI channel and RF impairments including the IQ imbalance, PA non-linearity and PN.

On the other hand, the impacts of RF impairments on GFDM half-duplex radios have been somewhat investigated in literature. For example, the collective impact of timing offset, CFO and PN are studied in [31], and an optimal filter in presence of CFO is designed in [61]. Joint channel and IQ imbalance estimation is considered in [33], which develops an IQ imbalance compensation scheme. he CFO estimation problem for GFDM system is studied in [32, 62] and CFO cancellation techniques

are proposed. In addition, for GFDM full-duplex radios, such studies are few and far between. For instance, [63] proposes a digital interference cancellation scheme and derives SI power. But it does not consider analog SI cancellation nor analyze the impacts of the RF impairments.

To be specific, previous studies demonstrate that full-duplex wireless and GFDM each by itself enhance the SE, while RF impairments limit its SE gains. However, none of these works investigate GFDM-based full-duplex BSs in the presence of the RF impairments. Motivated by these observations, the first objective is to design an GFDM full-duplex BS by considering analog and digital SI cancellations, RF impairments, and both uplink and downlink transmissions.

1.2.2 SE Enhancement of Secondary Links

As discussed in Section 1.1.3, in cognitive radios, unlicensed SUs may access the PU spectrum in three different modes. In the underlay and overlay modes, they simultaneously access licensed spectrum with active PUs, but ensure that the resulting interference on PUs is less than a specified interference threshold. However, in these modes, SU must constrain their transmit power levels, limiting the achievable SU rates. On the other hand, in the interweave mode, the SUs access spectrum holes or white spaces, which are free frequency bands in a specific location in which the licensed PUs are not transmitting temporarily. Thus in this case, SUs do not have stringent power constraints. Experiments indicate that conventional static policies lead to spectrum utilization levels varying between 15 % to 85 % [64], thus giving rise to spectrum holes. SUs in the interweave mode periodically monitor the spectrum, detect the occupancy, and then communicate opportunistically over the spectrum holes. The interweave mode effectively uses the underutilized spectrum, e.g., TV white spaces in IEEE 802.11af and IEEE 802.22 standards [65]. Therefore, this thesis considers interweave cognitive radio networks.

One of the main challenge for interweave scenario is the accurate and dynamic sens-

ing of spectrum holes. Two common sensing methods are energy detection and cyclostationary detection [66, 67]. Studies [68, 69] investigate these methods for GFDM amd OFDM systems. [68] illustartes GFDM has a better complementary receiver operating characteristic compared to OFDM based on energy detection method. In addition, reference [69] shows signal detection improves with GFDM due to its cyclostationary autocorrelation properties compared to OFDM. In light of these advantages, GFDM appears as a suitable candidate for interweave cognitive radio networks in terms of spectrum sensing. Furthermore, for both OFDM and GFDM systems, power allocation problem for maximizing the rate of secondary link under constraints of interference thresholds is investigated in [70–74]. The resource allocation for OFDM cognitive radio is first considered in [70], and other heuristic and fast resource allocation methods are proposed in[71, 72]. Furthermore, in [73], GFDM power allocation in cognitive radio is solved via genetic algorithms. In [74], cognitive radio resource allocation is done by particle swarm optimization. However, although the optimization problem is not convex due to the interference on subcarriers, the dual Lagrange multiplier method is used as analytical solution.

On the other hand, in the interweave networks, the secondary link's performance depends on the RF impairments, resulting in in-band distortion, self-interference, noise, and ACI on neighboring PUs. Although GFDM, which uses non-orthogonal sub-carriers to reduce out-of-band emissions, helps to reduce ACI, the drawback is the in-band distortion. Moreover, if the SUs increases their transmit powers, then the ACI constraints could be violated. Therefore, the question is this: Is it better to use GFDM than OFDM for interweave cognitive radio networks? Besides, all of aforementioned works consider half-duplex system for secondary link which results in low SE. Since the SE of the secondary link is limited by ACI constraints on PUs, full-duplex can help to increase the secondary link SE by simulations transmission between secondary nodes in the spectrum hole. In sum, the secondary link SE depends on many tightly coupled, conflicting factors and it seems that deploying full-duplex

GFDM systems can improve it. Motivated by these observations, the second objective is to develops interweave cognitive GFDM full-duplex radios for achieving high SE by considering practical RF impairments, active SI cancellation in analog and digital domains, and the ACI constraints.

1.2.3 RF Impairment Compensation for GFDM Systems

As discussed before, RF impairments degrade the SE of non-orthogonal systems by introducing interference terms. In GFDM systems, they increase the ICI and ISI terms which reduce the SNR, increases the BER, and limit the data rate. Among the considered RF impairments, PN is more critical since it is time varying which destroys coherency between the channel estimate and the actual channel gain. For PN compensation, one solution is to eliminate PN via hardware improvements. But that requires stringent constraints on the fabrication of RF components, increasing the cost [26]. Therefore, to enhance the SE in GFDM systems, the impacts of the PN impairment must be compensated for; which is typically performed in two phases: (1) in this phase, PN impairment is compensated for channel estimation and (2) in this phase, channel estimate from the first stage and further PN impairment compensation are applied for data detection. Therefore, this objective aims to develop efficient algorithms for PN estimation and compensation for the accurate channel estimation and data detection in GFDM systems.

The impacts of PN on OFDM have been widely investigated [75–77], and PN estimation and compensation techniques have been developed. Thus, [78] develops an least-squares (LS) filter for PN compensation. In [79, 80], the PN process is parameterized with a sinusoidal waveform to develop an LS estimator. In contrast, linear-interpolation schemes [81, 82] improves PN estimation accuracy. Moreover, the estimator [83] uses a codebook, which is selected by minimizing the Euclidean distance between the known pilot symbols and the signal constellation. Additionally, the estimators in [84, 85] exploit the PN spectrum's geometrical structure. However,

the aforementioned OFDM works assume perfect channel state information at the receiver, an unrealistic assumption. Thus, channel estimation algorithms are also necessary and have been widely investigated. For instance, [86] investigates joint channel estimation and PN suppression, [87] does so with a power series for PN, or [88] does by using sequential Monte-Carlo and the expectation-maximization approach. Similar estimators that perform time-domain interpolation utilize data and pilot symbols [89, 90]. Finally, [91] uses the expectation conditional maximization method for joint channel, CFO and PN estimation.

Furthermore, the problem of filter bank multicarrier (FBMC) channel estimation has been extensively studied [92–94]. For example, [92] develops an LS estimator that uses pilots but [94] deploys superimposed pilots. Moreover, PN impacts on FBMC systems are studied [95], showing that PN degrades the quality of channel estimation. Therefore, it develops an LS PN compensation algorithm that uses pilots.

Although PN compensation has been widely investigated for OFDM, this is not the case for GFDM. For example, GFDM studies [35, 39, 96] address channel estimation only, without considering PN. Likewise, [97–99] consider joint channel and CFO estimation only. Similarly, [33, 100, 101] compensate for IQ imbalance in GFDM. In addition, [102] compensates for IQ imbalance and PN in multi-carrier systems, which encompasses GFDM as a special case. The focus of [102] differs from this thesis. Moreover, [102] does not derive the Cramér-Rao lower bounds (CRLBs), nor analyze the SINR and sum-rate of GFDM. To the best of our knowledge, joint channel estimation and PN compensation for GFDM systems have not been investigated before the work reported in this thesis.

Moreover, researchers are massively interested in deep learning (DL) networks to improve the performance of classical estimators [103–109]. The advantages of DL-based estimators are two fold. First, they eliminate the iterative process of the classical estimators. Second, they can improve the MSE performance without requiring extra statistical information. References [103, 104] thus develop a DL algorithm for

OFDM channel estimation. This algorithm models the time-frequency response of the channel as a two-dimensional (2D) image and uses a convolutional neural network (CNN). References [106, 107] investigate DL-based channel estimation for massive multiple-input multiple-output (MIMO) systems. Furthermore, [108] proposes an end-to-end fully connected deep neural network (DNN) architecture for channel estimation and data detection in OFDM systems. Moreover, [109] designs a CNN framework for joint OFDM channel estimation and data detection.

However, to the best of our knowledge, no work has investigated DL-based PN compensation for channel estimation and data detection for multicarrier systems, orthogonal (OFDM) or non-orthogonal (GFDM), before. Therefore, the third objective aims to propose algorithms for PN compensation GFDM systems and develop DL algorithms for enhancing the performance.

1.2.4 RF Impairment Compensation for MIMO-GFDM Full-Duplex Systems

The third object (Section 1.2.3) considers PN compensation for GFDM systems. However, the impacts of all RF impairments on the GFDM full-duplex systems are more crucial, and they must be compensated for. To be specific, RF impairments degrade the performance of the SI cancellation techniques in the full-duplex systems and also enhance the ICI and ISI in GFDM systems by increasing degree of non-orthogonality.

To this end, [110, 111] study RF impairment compensation in OFDM-based full-duplex systems. Authors in [110] investigate pilot-aided PN estimation and compensation in OFDM-based full-duplex systems under transmitter and receiver oscillator PN. Two techniques are proposed: 1) frequency-domain technique based on LS estimator, and 2) low-complexity time-domain ICI suppression technique based on the Minimum mean square error (MMSE) estimator. Moreover, at low SNR scenarios, the latter achieves a maximum of 6 dB more SI cancellation than the former. How-

ever, the PN is estimated in [110] by considering the intended signal as an additive noise which considerably reduces the transmission throughput. Thus, authors in [111] incorporate the intended signal in the estimation process and jointly estimate the transmitter non-linearities, PN, and both the SI and intended channels at the baseband. To handle the time-varying PN estimation problem, the basis expansion model (BEM) is adopted to transform the problem to estimate a set of time-invariant coefficients. Then, an estimator is developed to estimate BEM coefficients by using the known SI signal, known pilot symbols, and unknown data symbols received from the other transmitter. The proposed methods achieve a superior SI cancellation performance in OFDM-based full-duplex systems.

On the other hand, reference [112] investigate RF impairments in multiple-input multiple-output (MIMO)-OFDM full-duplex systems. Since full-duplex wireless enables simultaneous transmission, and reception and MIMO transmits multiple streams over the same frequency band [9], integration of full-duplex and MIMO achieves higher SE. However, it is shown that MIMO full-duplex is especially vulnerable to RF impairments due to using a separate RF chain for each antenna. Hence, SI suppression techniques in the presence of RF impairments are critical. Therefore, authors in [112] propose a maximum-a-posteriori (MAP)-based algorithm for joint channel and PN estimation in MIMO-OFDM full-duplex systems.

In sum, RF compensation has been investigated for OFDM-based single-input single-output (SISO) and MIMO full-duplex systems. However, no work addresses RF impairment compensation for the GFDM-based systems. Therefore, the fourth objective aims to develop an efficient algorithm for joint channel and RF impairments estimation in MIMO-GFDM full-duplex systems. PN and IQ imbalance impairments for each transmit and receive antennas will be considered. Moreover, to enhance the performance of the estimator, DL-based network will be developed.

1.3 Thesis Outline

The outline of this thesis is as follows. Chapter 1 provides the introduction, motivation, and contributions. The novel contributions of the thesis are provided in Chapters 2 to 5 and highlighted next. chapter 6 provides the conclusion and the discusses possible future research.

1.3.1 Novel Contributions

- In Chapter 2, SE enhancement of cellular BSs is investigated by considering a GFDM-based full-duplex transceiver for BS that serves uplink and downlink users at the same time and frequency. The GFDM full-duplex transceiver is fully modeled by considering both analog and digital SI cancellation stages and RF impairments including PN, CFO and IQ imbalance. In both uplink and downlink, power analysis is conducted and SIRs are derived. It is shown that GFDM transceiver is more sensitive to the RF impairments than OFDM transceiver. Thus, to mitigate this problem, optimal receiver filters to maximize the SIR of both uplink and downlink are derived. In addition, the rate region is analyzed by maximizing the uplink rate under the constraint of constant downlink rate.

- In Chapter 3, SE enhancement of secondary links in cognitive radios by deploying GFDM-based full-duplex transceivers is investigated. In this system, the secondary link operates in a spectrum hole whose lower and upper adjacent bands are active PUs. Powers of residual SI, desired signal and noise are derived in closed form. Furthermore, the PSD of the transmit signal is derived and is used to quantify the ACI on the PU channels. Finally, The sum rate of the SU link is maximized under the constraints of maximum tolerable interference power on PU bands. Since this problem is non-convex, successive convex approximations is deployed to convert the problem to standard geometric pro-

gramming (GP).

- In Chapter 4, PN compensation in both stages of channel estimation and data detection in GFDM systems is studied. Efficient joint channel and PN estimator and also closed-form algorithm for joint data detection and PN compensation are proposed. To gauge the accuracy of the channel and PN estimators, their CRLBs are derived. Moreover, to enhance the performance of the proposed estimators and also replaces their iterative procedure, DL frameworks are developed, which are trained offline using simulation data and then are exploited for online PN compensation.

- In Chapter 5, joint channel, PN, and IQ imbalance estimation in MIMO-GFDM full-duplex systems is investigated. A BEM is developed for approximating the time varying equivalent channels by using a set of elementary functions and time-invariant coefficients. Moreover, a pilot-aided estimator for joint estimation of the SI channels, intended channels, PN, and IQ imbalance is proposed. Finally, a DL network is developed to enhance the performance of the proposed estimator.

1.3.2 Notations

Gaussian variable $X \sim N(\mu, \sigma^2)$ has mean μ and variance σ^2. The $[n, m]$-th element of matrix $\mathbf{A}$ is $\mathbf{A}[n, m]$. The N-point DFT (discrete fourier transform) matrix is denoted by $\mathbf{F}_N$, while $\mathbf{I}_N$ and $\mathbf{0}_N$ are is the identity and all zero matrix matrices of size $N \times N$. The superscripts $(\cdot)^*$, $(\cdot)^T$, $(\cdot)^H$ and $(\cdot)^{-1}$ indicate the complex conjugation, transpose, Hermitian transpose and matrix inversion. Circular convolution between two vectors $\mathbf{x_1} \in \mathbb{C}^{1\times N}$ and $\mathbf{x_2} \in \mathbb{C}^{1\times N}$ is defined as $x_1[n] \circledast x_2[n] = \sum_{k=0}^{N-1} x_1[n]x_2[n-k]$. Moreover, $\mathbf{A} \circ \mathbf{B}$ indicates the Hadamard product of matrices $\mathbf{A}$ and $\mathbf{B}$. The diagonal matrix formed by vector $\mathbf{x}$ is diag($\mathbf{x}$). $\Re\{z\}$ and $\Im\{z\}$ denote the real and imaginary parts of z. $\mathbb{T}\{\mathbf{A}\}$ is the trace of $\mathbf{A}$, and $\mathbb{E}\{\cdot\}$ indicates the statistical expectation. The rows

of circulant matrix $\mathbf{A}$ are formed by circular right shifts of the elements of vector $\mathbf{a}$.

Chapter 2

SE Enhancement of Cellular BSs

In traditional cellular networks, the BS communicates with uplink and downlink users in orthogonal channels, different time-slots, or frequency bands, which leads to decreased SE (e.g., loss in spectrum usage). To enhance SE, this chapter considers a GFDM-based full-duplex BS that serves uplink and downlink users at the same time and frequency – Figure 2.1. Since the main goal is to provide a comprehensive modeling and analysis of the GFDM full-duplex transceiver with the RF impairments including PN, CFO and IQ imbalance, a cellular network with one BS and two users is considered. Note that this chapter seeks SE improvement by implementing full-duplex transmission in the BS level. However, since a full-duplex transceiver requires a more complex SI cancellation system, the users are assumed simple half-duplex nodes.

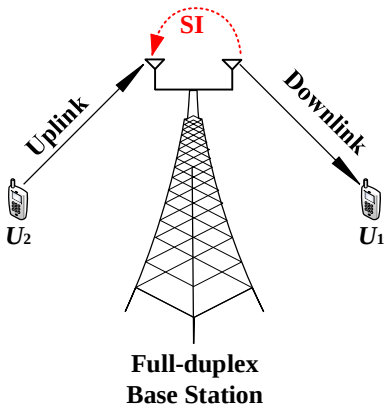

Figure 2.1: GFDM-based full-duplex BS with uplink and downlink users.

The BS transceiver gets the uplink user signal and leaked own SI signal. Moreover, the received downlink signal contains the BS intended signal and the uplink co-channel interference signal. These SI, desired and interference channels are modeled as frequency selective, a natural assumption for high data rate systems, where channels become frequency selective. The BS has two independent local oscillators for up/down conversions and both of them incur IQ imbalances. Moreover, the uplink user has no RF impairments and downlink user suffers from CFO mismatch only.

More specifically, the following contributions are made in this chapter:

- This chapter fully models the GFDM full-duplex transceiver with PN, CFO and IQ imbalance. Both analog and digital SI cancellation stages are included to develop a complementary digital SI cancellation method.

- In the uplink, residual SI power after analog and digital SI cancellations and desired signal power given the RF impairments are derived. Furthermore, in the downlink, desired signal and co-channel interference signal powers are derived.

- This chapter also derives the SIR for both uplink and downlink. When comparing GFDM and OFDM, it is illustrated that the GFDM transceiver is more sensitive to the RF impairments than the OFDM transceiver. To mitigate this problem, optimal receiver filters to maximize the SIR of the GFDM transceiver are designed.

- The rate region is an important concept and refers to the ordered pair of the downlink data rate and uplink data rate. In this problem, these two are mutually dependent because the transmit powers affect both SI and co-channel interference. Furthermore, the rate region by maximizing the uplink rate under the constraint of constant downlink rate is derived. An algorithm for the rate-region computation is also developed.

- All the theoretical derivations are verified with simulation results. Full-duplex

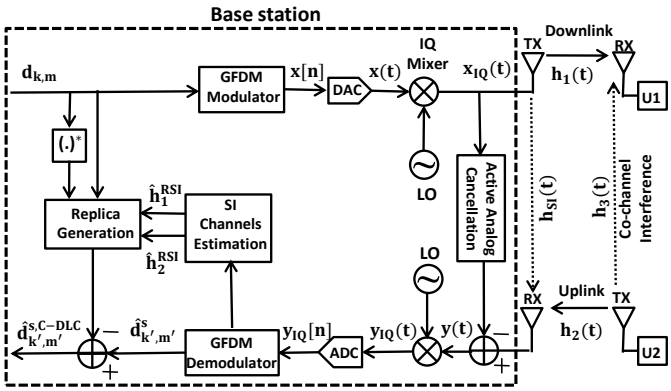

Figure 2.2: Block diagram of BS full-duplex GFDM transceiver and uplink and downlink users.

GFDM and OFDM transceivers are comparatively evaluated. Note that the collective impact of PN, CFO and IQ imbalance has not been investigated previously before the work reported in this thesis.

The results of this chapter were published in [113, 114].

2.1 System Model

The details of the considered system in Figure 2.1 are given in Figure 2.2. The considered system consists of a full-duplex BS equipped with single separate transmit and receive antennas for serving an uplink user U_2 and a downlink user U_1 , simultaneously. The system suffers from PN, CFO and IQ imbalance. The U_2 transmitter has no PN nor IQ imbalance impairments. Moreover, the U_1 receiver has no PN and IQ imbalance but has a CFO mismatch. These simplifying assumptions are made in order to isolate and focus on the effects of RF impairments and SI cancellation on the GFDM transceiver.

2.1.1 Uplink Transmission

The BS GFDM transceiver generates the transmit signal $x[n]$ in (1.2) for M timeslots with K subcarriers. The analog baseband signal, $x(t)$, is passed through the IQ

mixer. I-and Q-branch amplitude and phases mismatches create an undesired signal, which is the mirror image of the original signal. Thus, the IQ mixer output may be written as [50]

$$x_{IQ}(t) = (g_{Tx,d}x(t) + g_{Tx,I}x^*(t))e^{j\phi_{Tx}(t)}, \tag{2.1}$$

where $g_{Tx,d}$ and $g_{Tx,I}$ are the transmitter IQ mixer responses for the direct and image signals, respectively, and $\phi_{Tx}(t)$ is random PN of the local oscillator of the transmitter side. The transmit signal is amplified with a high gain amplifier and sent over the wireless channel. However, part of it appears as SI in the BS local receiver. Consequently, the received signal in BS from U_2 could be expressed as

$$\hat{y}(t) = s(t) * h_2(t) + x_{IQ}(t) * h_{SI}(t) + w_2(t), \tag{2.2}$$

where $s(t)$ is uplink transmit signal from U_2 to BS, $h_2(t)$ is the uplink multipath channel, $h_{SI}(t)$ is the multipath coupling channel between the local transmitter and the receiver of BS, and $w_2(t)$ is additive white Gaussian noise (AWGN) with zero mean and variance N_0. The samples of GFDM signal $s(t)$ may be expressed by (1.2) with α_s being the average transmit power and with i.i.d. input symbols of $d^s_{k,m}$. To suppress the SI signal, active analog cancellation is applied by subtracting the reconstruction signal. Thus, the resulting signal may be expressed as

$$y(t) = s(t) * h_2(t) + x_{IQ}(t) * h_{RSI}(t) + w_2(t), \tag{2.3}$$

where $h_{RSI}(t) = h_{SI}(t) - h_{ALC}(t)$ is residual SI channel where $h_{ALC}(t)$ is estimate of the the multipath coupling channel Empirically, 30 dB SI attenuation is possible with active analog SI cancellation [8]. Next, $y(t)$ goes through the receiver IQ mixer which, similar to transmitter, has IQ imbalances and produces the image signal. Moreover, this model considers CFO between the local oscillators of the transmitter and receiver of BS. Thus, the signal at the output of the IQ mixer is written as

$$y_{IQ}(t) = g_{Rx,d}y(t)e^{-j\phi_{Rx}(t)}e^{j2\pi\Delta_f t} + g_{Rx,I}y^*(t)e^{j\phi_{Rx}(t)}e^{-j2\pi\Delta_f t}, \tag{2.4}$$

where $g_{Rx,d}$ and $g_{Rx,I}$ are the receiver IQ mixer responses for the direct and image signals. Moreover, $\phi_{Rx}(t)$ is random PN of the local oscillator of the receiver side and Δ_f indicates the difference between carrier frequency of the receiver and transmitter local oscillators. According to (2.4) and assuming L-tap propagation channels ($h[n] = \sum_{l=0}^{L-1} h_l \delta[n-l]$), the sampled signal could be expressed as

$$\begin{aligned} y_{IQ}[n] =& \Bigg(\sum_{l=0}^{L-1} h_{RSI}^{I}[n,l]x[n-l] + h_{RSI}^{Q}[n,l]x^*[n-l] + h_2^I[n,l]s[n-l] + \\ & h_2^Q[n,l]s^*[n-l] \Bigg) + w_2^I[n] + w_2^Q[n], \end{aligned} \tag{2.5}$$

where equivalent channel responses for individual signal components can be written as

$$\begin{aligned} h_{RSI}^{I}[n,l] =& g_{Tx,d}g_{Rx,d}h_{RSI,l}e^{j(\phi_{TX}[n-l]-\phi_{RX}[n])}e^{\frac{j2\pi\epsilon n}{K}} + g_{Tx,I}^{*}g_{Rx,I}h_{RSI,l}^{*} \\ & e^{-j(\phi_{TX}[n-l]-\phi_{RX}[n])}e^{\frac{-j2\pi\epsilon n}{K}} \\ h_{RSI}^{Q}[n,l] =& g_{Tx,I}g_{Rx,d}h_{RSI,l}e^{j(\phi_{TX}[n-l]-\phi_{RX}[n])}e^{\frac{j2\pi\epsilon n}{K}} + g_{Tx,d}^{*}g_{Rx,I}h_{RSI,l}^{*} \\ & e^{-j(\phi_{TX}[n-l]-\phi_{RX}[n])}e^{\frac{-j2\pi\epsilon n}{K}} \\ h_2^I[n,l] =& g_{Rx,d}h_{2,l}e^{-j\phi_{RX}[n]}e^{\frac{j2\pi\epsilon n}{K}} \quad h_2^Q[n,l] = g_{Rx,I}h_{2,l}^{*}e^{j\phi_{RX}[n]}e^{\frac{-j2\pi\epsilon n}{K}} \\ w_2^I[n] =& g_{Rx,d}e^{-j\phi_{RX}[n]}e^{\frac{j2\pi\epsilon n}{K}}w_2[n] \quad w_2^Q[n] = g_{Rx,I}e^{j\phi_{RX}[n]}e^{\frac{-j2\pi\epsilon n}{K}}w_2^{*}[n], \end{aligned} \tag{2.6}$$

where ϵ is the normalized CFO by subcarrier spacing. Before deploying active digital cancellation, the samples are sent to GFDM demodulator where the estimated symbol at $k^{'}$-th subcarrier and $m^{'}$-th time-slot is $\widehat{d}^{s}_{k^{'},m^{'}}$ according to (1.4) with receiver filter impulse response $f[n]$. Finally, to further decrease the residual SI signal, classical active digital cancellation techniques [50] can be used. This method utilizes the replica of transmitted symbols, $d_{k',m'}$, and estimation of the equivalent residual SI channel, $\hat{h}_{RSI}^{I}[n,l]$, and then generates and subtracts digital cancellation symbols from the demodulated symbols. Furthermore, [50] shows that after the classical active digital cancellation, conjugate SI signal is the dominant source of distortion. Thus, it proposed widely-linear digital SI cancellation method[50] in which SI image components are also attenuated. This method can be done in similar manner as classical

active digital cancellation by this difference that the replica of conjugate of the transmitted symbols, $d^*_{k',m'}$, and estimation of the equivalent image residual SI channel, $\hat{h}^Q_{RSI}[n,l]$, are utilized to generate digital cancellation symbols. Thus, it is adopted for full-duplex GFDM and refer to the combination of classical active digital cancellation and widely-linear digital SI cancellation as complementary active digital cancellation. The output of complementary active digital cancellation could be expressed as

$$\widehat{d}^{s,C-DLC}_{k',m'} = \left(R^{SI}_{k',m'} - R^{DLC}_{k',m'}\right) + \left(R^{SI,im}_{k',m'} - R^{DLC,i}_{k',m'}\right) + R^{s}_{k',m'} + R^{s,im}_{k',m'} + w^{eq}_{k',m'} + w^{eq,im}_{k',m'}, \tag{2.7}$$

where $R^{SI}_{k',m'}$, $R^{SI,im}_{k',m'}$, $R^{s}_{k',m'}$, $R^{s,im}_{k',m'}$, $w^{eq}_{k',m'}$ and $w^{eq,im}_{k',m'}$ are corresponding terms for SI signal, desired signal and the equivalent noise after GFDM demodulator. Moreover, $R^{DLC}_{k',m'}$ and $R^{DLC,i}_{k',m'}$ are classical digital active cancellation and widely-linear digital SI cancellation terms, respectively, which are written as

$$\begin{aligned} R^{DLC}_{k',m'} &= \sqrt{\alpha} d_{k',m'} \sum_{l=0}^{L-1} \sum_{n=0}^{MK-1} \hat{h}^{I}_{RSI}[n,l] f_{m'}[n] g_{m'}[n-l] e^{\frac{-j2\pi k' l}{K}} \\ R^{DLC,i}_{k',m'} &= \sqrt{\alpha} d^*_{k',m'} \sum_{l=0}^{L-1} \sum_{n=0}^{MK-1} \hat{h}^{Q}_{RSI}[n,l] f_{m'}[n] g^*_{m'}[n-l] e^{\frac{-j2\pi k' (2n-l)}{K}}, \end{aligned} \tag{2.8}$$

where $\hat{h}^{I}_{RSI}[n,l]$ and $\hat{h}^{Q}_{RSI}[n,l]$ indicate equivalent channel estimation of the linear SI signal and the conjugate SI signal, respectively. Note that output of the classical active digital cancellation is derived by, $\widehat{d}^{s,DLC}_{k',m'} = \widehat{d}^{s,C-DLC}_{k',m'} + R^{DLC,i}_{k',m'}$. Clearly, the estimated symbol in (2.7) contains ICI and ISI terms from SI signal and uplink transmitted signal, which are caused by the RF impairments and non-orthogonality of GFDM.

2.1.2 Downlink Transmission

The signal received by U_1 in downlink may be written as

$$r(t) = x_{IQ}(t) * h_1(t) + s(t) * h_3(t) + w_1(t), \tag{2.9}$$

where $h_1(t)$ is downlink multipath channel, $h_3(t)$ is the channel between downlink and uplink users, and $w_1(t)$ is the additive Gaussian noise with zero mean and variance

N_0. This study assumes that the normalized CFO by subcarrier spacing between the oscillators of BS and U_1 transmitters is equal to ϵ. With the L-tap channels, the discrete samples of the received signal become

$$r_{CFO}[n] = \left(\sum_{l=0}^{L-1} h_1^I[n,l]x[n-l] + h_1^Q[n,l]x^*[n-l] + h_{3,l}s[n-l] \right) + w_1[n] \quad (2.10)$$

where the equivalent channel responses are given by

$$h_1^I[n,l] = g_{Tx,d}h_{1,l}e^{j\phi_{TX}[n-l]}e^{\frac{j2\pi\epsilon n}{K}} h_1^Q[n,l] = g_{Tx,I}h_{1,l}e^{j\phi_{TX}[n-l]}e^{\frac{j2\pi\epsilon n}{K}}. \quad (2.11)$$

Thus, signal (2.10) goes through GFDM demodulator and the estimated symbol at $k^{'}$-th subcarrier and $m^{'}$-th time-slot is

$$\widehat{d}_{k',m'} = \sum_{n=0}^{MK-1} (r_{CFO}[n])w_{m'}[n]e^{\frac{-j2\pi k^{'} n}{K}} = U_{k',m'}^d + U_{k',m'}^{d,im} + U_{k',m'}^s + N_{k',m'}^{eq}, \quad (2.12)$$

where $w_{m}[n] = w[n-mK]_{MK}$ is circularly shifted version of receiver filter impulse response $w[n]$. Moreover, $U_{k',m'}^d$ and $U_{k',m'}^{d,im}$ are corresponding terms for downlink signal and $U_{k',m'}^s$ is corresponding term to interference signal from U_2 on U_1 . Finally, $N_{k',m'}^{eq}$ indicates the equivalent noise. All of these terms could be derived by utilizing (2.10), (2.11) and (2.12).

2.2 Signal Power Analysis

This section derives the powers of desired signal, interference signal and noise in both downlink and uplink. It assumes two separate up/down conversion oscillators of the BS. This will result in two separate PN processes. Indeed, if there is a physical separation in the transmitter and receiver of BS, then this model is appropriate. Moreover, single common local oscillator for both up/down conversions has also been considered for compact full-duplex transceivers [8].

2.2.1 Uplink Transmission

In this section, the power of the residual SI signal, the power of desired signal, and the power of the equivalent noise are derived.

Residual SI signal power

This is derived using standard models for the residual SI channel and PN. It is assumed that $h_{RSI}[n] = \sum_{l=0}^{L-1} h_{RSI,l}\delta[n-l]$ is a wide-sense stationary uncorrelated scattering (WSSUS) process. WSSUS processes are commonly used for modeling multipath fading channels, e.g., to describe the short-term variations. The WSSUS model allows the channel correlation function to be time-invariant and the paths with different delays to be uncorrelated. These properties have been observed empirically. For this reason, the system model assumes WSSUS processes for all wireless channels. Accordingly, the taps $h_{RSI,l}$ are mutually independent, $\mathbb{E}_h[h_{RSI,l}] = 0$ and $\mathbb{E}_h\left[|h_{RSI,l}|^2\right] = \sigma^2_{RSI,l}$, $l = 0, 1, ..., L-1$ [8]. Furthermore, Brownian motion free-running oscillators [31] generate PN. The autocorelation function of $\phi[n]$ may be expressed as

$$\mathbb{E}_\phi\left[e^{j\phi[n_1]}e^{-j\phi[n_2]}\right] = e^{-2|n_1-n_2|\pi\beta T_s}. \tag{2.13}$$

Moreover, complex data symbols are uncorrelated ($\mathbb{E}_d[d_{k_1,m_1}d^*_{k_2,m_2}] = \delta[k_1-k_2]\delta[m_1-m_2]$). Moreover, the multipath fading channels, transmitted data and PN are independent random processes. By utilizing them, the variance of the residual SI after active analog cancellation is given by $\sigma^{SI-ALC}_{k',m'} = \mathbb{E}\left[|R^{SI}_{k',m'}|^2\right] = \mathbb{E}_h\left[\mathbb{E}_\phi\left[\mathbb{E}_d\left[|R^{SI}_{k',m'}|^2\right]\right]\right]$, which after straightforward manipulation, is derived as

$$\begin{aligned}\sigma^{SI-ALC}_{k',m'} = \alpha\sum_{l=0}^{L-1}\sum_{n_1=0}^{MK-1}\sum_{n_2=0}^{MK-1} f_{m'}[n_1]f^*_{m'}[n_2]e^{-4|n_1-n_2|\pi\beta T_s} \\ \left(|g_{TX,d}g_{RX,d}|^2 e^{\frac{j2\pi(n_1-n_2)\epsilon}{K}} + |g_{TX,I}g_{RX,I}|^2 e^{\frac{-j2\pi(n_1-n_2)\epsilon}{K}}\right) \\ \times\sum_{k=0}^{K-1}\sum_{m=0}^{M-1}\sigma^2_{RSI,l}g_m[n_1-l]g^*_m[n_2-l]e^{\frac{j2\pi(n_1-n_2)(k-k')}{K}}.\end{aligned} \tag{2.14}$$

The power of the residual SI after complementary active digital cancellation can

be defined as $\sigma^{SI-DLC}_{k',m'} = \mathbb{E}\left[|R^{SI}_{k',m'} - R^{DLC}_{k',m'}|^2\right]$ which is given by

$$\begin{aligned}
\sigma^{SI-DLC}_{k',m'} &= \alpha \sum_{n_1=0}^{MK-1} \sum_{n_2=0}^{MK-1} f_{m'}[n_1] f^*_{m'}[n_2] e^{-4|n_1-n_2|\pi\beta T_s} \\
&\left(|g_{TX,d} g_{RX,d}|^2 e^{\frac{j2\pi(n_1-n_2)\epsilon}{K}} + |g_{TX,I} g_{RX,I}|^2 e^{\frac{-j2\pi(n_1-n_2)\epsilon}{K}} \right) \\
&\times \left\{ \left[\sum_{l=0}^{L-1} \sum_{\substack{k=0 \\ k\neq k' \& m\neq m'}}^{K-1} \sum_{m=0}^{M-1} \sigma^2_{RSI,l} g_m[n_1-l] g^*_m[n_2-l] e^{\frac{j2\pi(n_1-n_2)(k-k')}{K}} \right] \right. \\
&\left. + \left[\sigma^2_{ee} g_{m'}[n_1-l] g^*_{m'}[n_2-l] \right] \right\},
\end{aligned} \tag{2.15}$$

where σ^2_{ee} is the channel estimation error variance, which is modeled as $\sigma^2_{ee} = t \times \kappa$ where t and κ indicate active analog cancellation and active digital cancellation suppression, respectively [8]. Note that (2.14) and (2.15) depend on multipath profile, 3-dB PN bandwidth, normalized CFO, IQ imbalance coefficients, number of subcarriers and time-slots and GFDM receiver and transmitter filters. Thus, all these parameters affect the efficiency of analog and digital SI cancellations. Similarly, the conjugate-residual-SI signal power after active analog cancellation and after complementary active digital cancellation could be formulated as

$$\begin{aligned}
\sigma^{SI-im-ALC}_{k',m'} &= \alpha \sum_{l=0}^{L-1} \sum_{n_1=0}^{MK-1} \sum_{n_2=0}^{MK-1} f_{m'}[n_1] f^*_{m'}[n_2] e^{-4|n_1-n_2|\pi\beta T_s} \\
&\left(|g_{TX,I} g_{RX,d}|^2 e^{\frac{j2\pi(n_1-n_2)\epsilon}{K}} + |g_{TX,d} g_{RX,I}|^2 e^{\frac{-j2\pi(n_1-n_2)\epsilon}{K}} \right) \\
&\times \sum_{k=0}^{K-1} \sum_{m=0}^{M-1} \sigma^2_{RSI,l} g^*_m[n_1-l] g_m[n_2-l] e^{\frac{-j2\pi(n_1-n_2)(k+k')}{K}},
\end{aligned} \tag{2.16}$$

and

$$\sigma_{k',m'}^{SI-im-DLC} = \alpha \sum_{n_1=0}^{MK-1} \sum_{n_2=0}^{MK-1} f_{m'}[n_1] f_{m'}^{*}[n_2] e^{-4|n_1-n_2|\pi\beta T_s}$$
$$\left(|g_{TX,I} g_{RX,d}|^2 e^{\frac{j2\pi(n_1-n_2)\epsilon}{K}} + |g_{TX,d} g_{RX,I}|^2 e^{\frac{-j2\pi(n_1-n_2)\epsilon}{K}} \right)$$
$$\times \left\{ \left[\sum_{l=0}^{L-1} \sum_{\substack{k=0 \\ k\neq k' \& m\neq m'}}^{K-1} \sum_{m=0}^{M-1} \sigma_{RSI,l}^2 g_m^{*}[n_1-l] g_m[n_2-l] e^{\frac{-j2\pi(n_1-n_2)(k+k')}{K}} \right] \right. \tag{2.17}$$
$$\left. + \left[\sigma_{ee}^2 g_{m'}^{*}[n_1-l] g_{m'}[n_2-l] e^{\frac{-j4\pi(n_1-n_2)k'}{K}} \right] \right\},$$

where $\sigma_{k',m'}^{SI-im-ALC} = \mathbb{E}\left[|R_{k',m'}^{SI,im}|^2\right]$ and $\sigma_{k',m'}^{SI-im-DLC} = \mathbb{E}\left[|R_{k',m'}^{SI,im} - R_{k',m'}^{DLC,i}|^2\right]$. Again, the results depend on multiple system parameters, and hence provide the means and flexibility of system performance evaluations for different configurations. Following (2.15) and (2.17), total power of residual SI signal after complementary active digital cancellation may be expressed as

$$\sigma_{k',m'}^{SI} = \sigma_{k',m'}^{SI-DLC} + \sigma_{k',m'}^{SI-im-DLC}. \tag{2.18}$$

Desired uplink signal power

By substituting $k = k'$ and $m = m'$, the desired symbol could be extracted from $R_{k',m'}^{s}$ as

$$d_{k',m'}^{s-up} = \sqrt{\alpha_s} d_{k',m'}^{s} \sum_{l=0}^{L-1} \sum_{n=0}^{MK-1} h_2^{I}[n,l] f_{m'}[n] g_{m'}[n-l] e^{\frac{-j2\pi k' l}{K}}. \tag{2.19}$$

Thus, from (2.19), interference signal could be expressed as $R_{k',m'}^{ss} = R_{k',m'}^{s} - d_{k',m'}^{s-up}$. A WSSUS uplink channel $h_2[n] = \sum_{l=0}^{L-1} h_{2,l}\delta[n-l]$ is assumed. Thus $h_{2,l}$ are mutually independent, $\mathbb{E}[h_{2,l}] = 0$ and $\mathbb{E}\left[|h_{2,l}|^2\right] = \sigma_{2,l}^2$, $l = 0, 1, ..., L-1$. Therefore, the variance of the desired symbol could be expressed as

$$\sigma_{k',m'}^{s} = \mathbb{E}\left[|d_{k',m'}^{s-up}|^2\right] = \alpha_s |g_{RX,d}|^2 \sum_{l=0}^{L-1} \sum_{n_1=0}^{MK-1} \sum_{n_2=0}^{MK-1} \sigma_{2,l}^2$$
$$e^{-2|n_1-n_2|\pi\beta T_s} f_{m'}[n_1] f_{m'}^{*}[n_2] g_{m'}[n_1-l] g_{m'}^{*}[n_2-l] e^{\frac{j2\pi(n_1-n_2)\epsilon}{K}}. \tag{2.20}$$

The interference signals could be considered as $R_{k',m'}^{ss}$ and $R_{k',m'}^{s,im}$. The variance of

the first-term could be calculated as

$$\begin{aligned}\sigma^{R^{ss}}_{k',m'} &= \mathbb{E}\left[|R^{s}_{k',m'} - d^{s-up}_{k',m'}|^2\right] = \mathbb{E}\left[|R^{s}_{k',m'}|^2\right] + \mathbb{E}\left[|d^{s-up}_{k',m'}|^2\right] \\ &- 2\text{real}\left(\mathbb{E}\left[{R^{*s}}_{k',m'} d^{s-up}_{k',m'}\right]\right) = \mathbb{E}\left[|R^{s}_{k',m'}|^2\right] + \mathbb{E}\left[|d^{s-up}_{k',m'}|^2\right] \\ &- 2\mathbb{E}\left[|d^{s-up}_{k',m'}|^2\right] = \sigma^{R^s}_{k',m'} - \sigma^{s}_{k',m'}\end{aligned} \tag{2.21}$$

where $\sigma^{R^s}_{k',m'} = \mathbb{E}\left[|R^{s}_{k',m'}|^2\right]$ is equal to

$$\begin{aligned}\sigma^{R^s}_{k',m'} = \alpha_s |g_{RX,d}|^2 \sum_{l=0}^{L-1} \sum_{n_1=0}^{MK-1} \sum_{n_2=0}^{MK-1} \sum_{k=0}^{K-1} \sum_{m=0}^{M-1} \sigma^2_{2,l} e^{-2|n_1-n_2|\pi\beta T_s} \\ f_{m'}[n_1] f^*_{m'}[n_2] g_m[n_1 - l] g^*_m[n_2 - l] e^{\frac{j2\pi(n_1-n_2)(\epsilon+k-k^{'})}{K}}.\end{aligned} \tag{2.22}$$

Moreover, the variance of the second term could be expressed as

$$\begin{aligned}\sigma^{R^{s,im}}_{k',m'} = \alpha_s |g_{RX,I}|^2 \sum_{l=0}^{L-1} \sum_{n_1=0}^{MK-1} \sum_{n_2=0}^{MK-1} \sum_{k=0}^{K-1} \sum_{m=0}^{M-1} \sigma^2_{2,l} e^{-2|n_1-n_2|\pi\beta T_s} \\ f_{m'}[n_1] f^*_{m'}[n_2] g^*_m[n_1 - l] g_m[n_2 - l] e^{\frac{-j2\pi(n_1-n_2)(\epsilon+k+k^{'})}{K}}.\end{aligned} \tag{2.23}$$

Obviously, derived results are function of system parameters including amount of PN, CFO, IQ imbalance, channel propagation and GFDM parameters. The total power of the interference signal is given by

$$\sigma^{s,i}_{k',m'} = \sigma^{R^s}_{k',m'} + \sigma^{R^{s,im}}_{k',m'} - \sigma^{s}_{k',m'}. \tag{2.24}$$

Equivalent noise power

Since additive Gaussian noise is $\mathcal{CN}(0, N_0)$, the variance of direct equivalent noise $w^{eq}_{k',m'}$ in (2.7) is given by

$$\sigma^{w^{eq}}_{k',m'} = \mathbb{E}\left[|w^{eq}_{k',m'}|^2\right] = |g_{RX,d}|^2 N_0 \sum_{n=0}^{MK-1} |f_{m'}[n]|^2. \tag{2.25}$$

Similarly, the power of image equivalent noise $w^{eq,im}_{k',m'}$ in (2.7) is written as

$$\sigma^{w^{eq,im}}_{k',m'} = \mathbb{E}\left[|w^{eq,im}_{k',m'}|^2\right] = |g_{RX,I}|^2 N_0 \sum_{n=0}^{MK-1} |f_{m'}[n]|^2. \tag{2.26}$$

According to (2.25) and (2.26), noise power depends on IQ coefficient, noise variance and the receiver filter. Moreover, they are independent of subcarrier index. Finally, the total noise power can be written as

$$\sigma^{w}_{k',m'} = \sigma^{w^{eq}}_{k',m'} + \sigma^{w^{eq,im}}_{k',m'}. \tag{2.27}$$

2.2.2 Downlink Transmission

Here, the power of the downlink signal and interference signal between the two users and noise are derived in closed-form. According to the WSSUS model for downlink channel $h_1[n] = \sum_{l=0}^{L-1} h_1[l]\delta[n-l]$, $h_{1,l}$ are mutually independent, $\mathbb{E}[h_{1,l}] = 0$ and $\mathbb{E}\left[|h_{1,l}|^2\right] = \sigma_{1,l}^2$, $l = 0, 1, ..., L-1$.

Desired downlink signal power

According to (2.12), desired downlink symbol can be extracted from $U_{m',k'}^d$ by substituting $k = k'$ and $m = m'$ as

$$d_{k',m'}^{s-down} = \sqrt{\alpha} d_{k',m'} \sum_{l=0}^{L-1} \sum_{n=0}^{MK-1} h_1^I[n,l] w_{m'}[n] g_{m'}[n-l] e^{\frac{-j2\pi k' l}{K}}. \tag{2.28}$$

The variance of the desired downlink symbol is thus written as

$$\begin{aligned} \sigma_{k',m'}^d = \mathbb{E}\left[|d_{k',m'}^{s-down}|^2\right] = \alpha |g_{TX,d}|^2 \sum_{l=0}^{L-1} \sum_{n_1=0}^{MK-1} \sum_{n_2=0}^{MK-1} \sigma_{1,l}^2 \\ e^{-2|n_1-n_2|\pi\beta T_s} w_{m'}[n_1] w_{m'}^*[n_2] g_{m'}[n_1-l] g_{m'}^*[n_2-l] e^{\frac{j2\pi(n_1-n_2)\epsilon}{K}}. \end{aligned} \tag{2.29}$$

Now by subtracting the desired downlink symbol in (2.28), interference signals may be considered as $U_{k',m'}^d - d_{k',m'}^{s-down}$ and $U_{k',m'}^{d,im}$. Similar to (2.21) and according to (2.10), (2.11) and (2.12), the variance of the first term could be calculated as $\sigma_{k',m'}^{U^d} - \sigma_{k',m'}^d$ where $\sigma_{k',m'}^{U^d} = \mathbb{E}\left[|U_{k',m'}^d|^2\right]$ is given by

$$\begin{aligned} \sigma_{k',m'}^{U^d} = \alpha |g_{TX,d}|^2 \sum_{l=0}^{L-1} \sum_{n_1=0}^{MK-1} \sum_{n_2=0}^{MK-1} \sum_{k=0}^{K-1} \sum_{m=0}^{M-1} \sigma_{1,l}^2 e^{-2|n_1-n_2|\pi\beta T_s} \\ w_{m'}[n_1] w_{m'}^*[n_2] g_m[n_1-l] g_m^*[n_2-l] e^{\frac{j2\pi(n_1-n_2)(\epsilon+k-k')}{K}}. \end{aligned} \tag{2.30}$$

Furthermore, the variance of the second term is given by

$$\begin{aligned} \sigma_{k',m'}^{U^{d,im}} = \alpha |g_{TX,I}|^2 \sum_{l=0}^{L-1} \sum_{n_1=0}^{MK-1} \sum_{n_2=0}^{MK-1} \sum_{k=0}^{K-1} \sum_{m=0}^{M-1} \sigma_{1,l}^2 e^{-2|n_1-n_2|\pi\beta T_s} \\ w_{m'}[n_1] w_{m'}^*[n_2] g_m^*[n_1-l] g_m[n_2-l] e^{\frac{j2\pi(n_1-n_2)(\epsilon-k-k')}{K}}. \end{aligned} \tag{2.31}$$

Thus, the total power of the interference signal is given by

$$\sigma_{k',m'}^{d-i} = \sigma_{k',m'}^{U^d} + \sigma_{k',m'}^{U^{d,im}} - \sigma_{k',m'}^d. \tag{2.32}$$

The results clearly show that power of different components of desired downlink signal are dependent of phase 3-dB PN bandwidth, CFO parameter, IQ imbalance coefficients, multipath profile of channels and GFDM parameters.

Co-channel interference signal power

Again the WSSUS model is assumed for co-channel interference channel between the uplink user and the downlink user, which is expressed as $h_3[n] = \sum_{l=0}^{L-1} h_{3,l}\delta[n-l]$. Thus, the taps $h_{3,l}$ are mutually independent, $\mathbb{E}[h_{3,l}] = 0$ and $\mathbb{E}\left[|h_{3,l}|^2\right] = \sigma_{3,l}^2$, $l = 0, 1, ..., L-1$. Following (2.10), (2.11) and (2.12), the variance of the interference signal from U_2 onto U_1 can be expressed as

$$\sigma_{k',m'}^{U^s} = \alpha_s \sum_{l=0}^{L-1} \sum_{n_1=0}^{MK-1} \sum_{n_2=0}^{MK-1} \sum_{k=0}^{K-1} \sum_{m=0}^{M-1} \sigma_{3,l}^2 w_{m'}[n_1] w_{m'}^*[n_2] \\ g_m[n_1-l] g_m^*[n_2-l] e^{\frac{j2\pi(n_1-n_2)(\epsilon+k-k^{'})}{K}}. \tag{2.33}$$

This co-channel interference (2.33) is a function of multipath profile of channel between the two users, the normalized CFO and the transmit and receive filters of GFDM.

Equivalent noise power

Since additive noise is distributed as $\mathcal{N}(0, N_0)$, the variance of equivalent noise in (2.12) may be expressed as

$$\sigma_{k',m'}^{N^{eq}} = \mathbb{E}\left[|N_{k',m'}^{eq}|^2\right] = N_0 \sum_{n=0}^{MK-1} |w_{m'}[n]|^2. \tag{2.34}$$

Similar to the case of uplink transmission, the power of equivalent noise depends on the variance of noise and summation of the receiver filter coefficients and is independent of the index of the subcarrier.

2.3 SIR Formulation and Filter Optimization

Here, SIRs for both downlink and uplink are derived, and SIR-maximizing optimal receiver filters for BS and U_1 are proposed.

2.3.1 Uplink Transmission

From (2.18), (2.20) and (2.24), the SIR of the estimated symbol in the k'-th subcarrier and the m'-th subsymbol is written as

$$\Gamma^{up}_{k',m'} = \frac{\sigma^{s}_{k',m'}}{\sigma^{SI}_{k',m'} + \sigma^{s,i}_{k',m'}}. \tag{2.35}$$

Since it uses non-orthogonal waveforms, one can expect GFDM to perform worse than OFDM in the presence of RF impairments. This suggests that it should achieve lower SIR than OFDM. Fortunately, the performance of GFDM can be improved by exploiting the degrees of freedom inherent in receiver prototype filter $f[n]$. However, the SIR depends on both transmit and receive filter prototypes ($g[n]$ and $f[n]$). To retain the benefits of GFDM, such as lower out-of-band emissions, $g[n]$ is fixed to be a conventional filter of raised cosine type.

Following that, receiver filter $\{f[n]\}$ to maximize the SIR given RF impairments can be optimized. Denote $\mathbf{f}_{\mathbf{k}',\mathbf{m}'} = \mathbf{S}_{k'}\mathbf{M}_{m'M}\mathbf{f}_{0,0} \in \mathbb{C}^{MK\times 1}$ contains samples of $f_{k',m'}[n] = f_{m'}[n]e^{\frac{-j2\pi k' n}{K}}$ in (1.4), where $\mathbf{f}_{0,0} \in \mathbb{C}^{MK\times 1}$ is the column vector including receiver filter $f[n]$ samples, $\mathbf{M}_{m'M} \in \mathbb{C}^{MK\times MK}$ circularly shifts $\mathbf{f}_{0,0}$ and $\mathbf{S}_{k'} = \text{diag}\left(\left[1, e^{\frac{-j2\pi k'}{K}}, ..., e^{\frac{-j2\pi k'(MK-1)}{K}}\right]\right) \in \mathbb{C}^{MK\times MK}$ is the subcarrier mapping matrix. It is worth mentioning that (1.4) could be expressed as $\hat{d}^{s}_{k',m'} = \mathbf{y}_{IQ}\mathbf{f}_{k',m'}$ where $\mathbf{y}_{IQ} \in \mathbb{C}^{1\times MK}$ contains $y_{IQ}[n]$. Moreover, the derived variances in matrix form can be written as $\sigma^{s}_{k',m'} = \alpha_s \mathbf{f}^{H}_{k',m'}\mathbf{V}^{s}_{k',m'}\mathbf{f}_{k',m'}$, $\sigma^{SI}_{k',m'} = \alpha \mathbf{f}^{H}_{k',m'}\mathbf{V}^{SI}\mathbf{f}_{k',m'}$ and $\sigma^{s,i}_{k',m'} = \alpha_s\left(\mathbf{f}^{H}_{k',m'}\mathbf{V}^{R}\mathbf{f}_{k',m'} - \mathbf{f}^{H}_{k',m'}\mathbf{V}^{s}_{k',m'}\mathbf{f}_{k',m'}\right)$ where

$$V^{s}_{k',m'}[n_2, n_1] = \sum_{l=0}^{L-1} |g_{RX,d}|^2 \sigma^2_{2,l} e^{-2|n_1-n_2|\pi\beta T_s} g_{m'}[n_1 - l] g^{*}_{m'}[n_2 - l] e^{\frac{j2\pi(n_1-n_2)(\epsilon+k')}{K}}. \tag{2.36}$$

$$V^{SI}[n_2,n_1] = e^{-4|n_1-n_2|\pi\beta T_s}\Bigg\{\Bigg[\sum_{l=0}^{L-1}\sum_{\substack{k=0\\k\neq k'\&m\neq m'}}^{K-1}\sum_{m=0}^{M-1}\sigma^2_{RSI,l}g_m[n_1-l]g^*_m[n_2-l]$$
$$\Big(|g_{TX,d}g_{RX,d}|^2 e^{\frac{j2\pi(n_1-n_2)(\epsilon+k)}{K}} + |g_{TX,I}g_{RX,I}|^2 e^{\frac{-j2\pi(n_1-n_2)(\epsilon-k)}{K}} + |g_{TX,I}g_{RX,d}|^2$$
$$e^{\frac{j2\pi(n_1-n_2)(\epsilon-k)}{K}} + |g_{TX,d}g_{RX,I}|^2 e^{\frac{-j2\pi(n_1-n_2)(\epsilon+k)}{K}}\Big)\Bigg] + \Bigg[\sigma^2_{ee}g_{m'}[n_1-l]g^*_{m'}[n_2-l] \quad (2.37)$$
$$\Big(|g_{TX,d}g_{RX,d}|^2$$
$$e^{\frac{j2\pi(n_1-n_2)(\epsilon+k^{'})}{K}} + |g_{TX,I}g_{RX,I}|^2 e^{\frac{-j2\pi(n_1-n_2)(\epsilon-k^{'})}{K}} + |g_{TX,I}g_{RX,d}|^2 e^{\frac{j2\pi(n_1-n_2)(\epsilon-k^{'})}{K}}$$
$$+ |g_{TX,d}g_{RX,I}|^2 e^{\frac{-j2\pi(n_1-n_2)(\epsilon+k^{'})}{K}}\Big)\Bigg]\Bigg\}$$

$$V^{R}[n_2,n_1] = \sum_{l=0}^{L-1}\sum_{k=0}^{K-1}\sum_{m=0}^{M-1}\sigma^2_{2,l}g_m[n_1-l]g^*_m[n_2-l]e^{-2|n_1-n_2|\pi\beta T_s} \quad (2.38)$$
$$\Big(|g_{RX,d}|^2 e^{\frac{j2\pi(n_1-n_2)(\epsilon+k)}{K}} + |g_{RX,I}|^2 e^{\frac{-j2\pi(n_1-n_2)(\epsilon+k)}{K}}\Big).$$

Now, in order to find $\mathbf{f}_{0,0}$ that maximizes SIR, the SIR is rewriten in matrix form as

$$\Gamma^{up} = \frac{\alpha_s\sum_{k'=0}^{K-1}\sum_{m'=0}^{M-1}\mathbf{f}^H_{k',m'}\mathbf{V}^s_{k',m'}\mathbf{f}_{k',m'}}{\sum_{k'=0}^{K-1}\sum_{m'=0}^{M-1}\mathbf{f}^H_{k',m'}\mathbf{V}\mathbf{f}_{k',m'} - \alpha_s\mathbf{f}^H_{k',m'}\mathbf{V}^s_{k',m'}\mathbf{f}_{k',m'}} = \frac{\mathbf{f}^H_{0,0}\mathbf{T}_1\mathbf{f}_{0,0}}{\mathbf{f}^H_{0,0}(\mathbf{T}_2-\mathbf{T}_1)\mathbf{f}_{0,0}} \quad (2.39)$$

where $\mathbf{V} = \alpha\mathbf{V}^{SI} + \alpha_s\mathbf{V}^R$, $\mathbf{T}_1 = \alpha_s\sum_{k'=0}^{K-1}\sum_{m'=0}^{M-1}\mathbf{M}^H_{m'M}\mathbf{S}^H_{k'}\mathbf{V}^s_{k',m'}\mathbf{S}_{k'}\mathbf{M}_{m'M}$ and $\mathbf{T}_2 = \sum_{k'=0}^{K-1}\sum_{m'=0}^{M-1}\mathbf{M}^H_{m'M}\mathbf{S}^H_{k'}\mathbf{V}\mathbf{S}_{k'}\mathbf{M}_{m'M}$. Therefore, the filter design problem for maximizing the SIR could be formulated as

$$\mathbf{f}^{opt}_{0,0} = \arg\ \max_{\mathbf{x}}\ \frac{\mathbf{x}^H\mathbf{T}_1\mathbf{x}}{\mathbf{x}^H(\mathbf{T}_2-\mathbf{T}_1)\mathbf{x}} \quad (2.40)$$
$$s.t.\ \ ||\mathbf{x}||^2 = 1$$

where $\mathbf{x}\in\mathbb{C}^{MK\times 1}$ and $||\mathbf{x}||$ indicates norm of $\mathbf{x}$. To solve this, first consider the Cholesky factorization as $\mathbf{T}_2-\mathbf{T}_1 = \mathbf{L}\mathbf{L}^H$. This can be substituted in (2.40) to yield

$$\frac{\mathbf{x}^H\mathbf{T}_1\mathbf{x}}{\mathbf{x}^H(\mathbf{T}_2-\mathbf{T}_1)\mathbf{x}} = \frac{\mathbf{x}^H\mathbf{T}_1\mathbf{x}}{\mathbf{x}^H(\mathbf{L}\mathbf{L}^H)\mathbf{x}} = \frac{\mathbf{y}^H\mathbf{L}^{-1}\mathbf{T}_1\mathbf{L}^{H-1}\mathbf{y}}{\mathbf{y}^H\mathbf{y}}$$

where $\mathbf{y} = \mathbf{L}^H\mathbf{x}$. The above ratio is known as the Rayleigh quotient [115]. It can be readily shown that the Rayleigh quotient reaches its maximum value when $\mathbf{y}$ is

the corresponding eigenvector of the maximum eigenvalue of $\mathbf{L}^{-1}\mathbf{T}_1\mathbf{L}^{H-1}$. But, this eigenvalue remains the same if $\mathbf{L}^{H-1}\mathbf{L}^{-1}\mathbf{T}_1 = (\mathbf{T}_2 - \mathbf{T}_1)^{-1}\mathbf{T}_1$. Therefore, the optimal receiver filter is given by [116]

$$\mathbf{f}_{0,0}^{opt} \propto \max\left[\text{eigenvector}\left((\mathbf{T}_2 - \mathbf{T}_1)^{-1}\mathbf{T}_1\right)\right]. \tag{2.41}$$

Thus, this optimal receiver filter maximizes the SIR of the GFDM full-duplex under the RF impairments after active analog cancellation and complementary digital linear cancellation.

2.3.2 Downlink Transmission

Due to the full duplex operation of the BS, uplink and downlink transmissions occupy same frequency and time slots. Thus, interference from U_2 in uplink on U_1 in downlink decreases the performance of the downlink. The uplink section has proposed the SIR-maximizing receiver filter. However, with two stage SI cancellations, residual SI as a main source of interference on the desired uplink signal is eliminated. But since there is no interference cancellation in the downlink, receiver filter design alleviates the effects of interference signal from other user. By utilizing (2.30), (2.31) and (2.33), SIR for the k'-th subcarrier and m'-th subsymbol can be expressed as

$$\Gamma_{k',m'}^{down} = \frac{\sigma_{k',m'}^{d}}{\sigma_{k',m'}^{d-i} + \sigma_{k',m'}^{U^s}}. \tag{2.42}$$

Similar to the uplink case, the variance terms in (2.42) can be written as a function of the receiver filter. Let us denote $\mathbf{w}_{\mathbf{k',m'}} = \mathbf{S}_{k'}\mathbf{M}_{m'M}\mathbf{w}_{0,0} \in \mathbb{C}^{MK\times 1}$ where $\mathbf{w}_{0,0} \in \mathbb{C}^{MK\times 1}$ is the column vector including receiver filter $w[n]$ samples. The variances could be expressed in matrix form as $\sigma_{k',m'}^{d} = \alpha\mathbf{w}_{k',m'}^{H}\eta_{k',m'}^{d}\mathbf{w}_{k',m'}$, $\sigma_{k',m'}^{U^s} = \alpha_s\mathbf{w}_{k',m'}^{H}\eta^{s}\mathbf{w}_{k',m'}$ and $\sigma_{k',m'}^{d-i} = \alpha\left(\mathbf{w}_{k',m'}^{H}\eta^{d,i}\mathbf{f}_{k',m'} - \mathbf{w}_{k',m'}^{H}\eta_{k',m'}^{d}\mathbf{w}_{k',m'}\right)$ where

$$\eta_{k',m'}^{d}[n_2,n_1] = \sum_{l=0}^{L-1}|g_{TX,d}|^2\sigma_{1,l}^2 e^{-2|n_1-n_2|\pi\beta T_s} g_{m'}[n_1-l]g_{m'}^{*}[n_2-l]e^{\frac{j2\pi(n_1-n_2)(\epsilon+k')}{K}}, \tag{2.43}$$

$$\eta^{s}[n_2, n_1] = \sum_{l=0}^{L-1} \sum_{k=0}^{K-1} \sum_{m=0}^{M-1} \sigma_{3,l}^{2} g_m[n_1 - l] g_m^{*}[n_2 - l] e^{\frac{j2\pi(n_1-n_2)(\epsilon+k)}{K}}, \tag{2.44}$$

and

$$\begin{aligned} \eta_{m'}^{d-i}[n_2, n_1] = & \sum_{l=0}^{L-1} \sum_{k=0}^{K-1} \sum_{m=0}^{M-1} \sigma_{1,l}^{2} g_m[n_1 - l] g_m^{*}[n_2 - l] \\ & e^{-2|n_1-n_2|\pi\beta T_s} \Big(|g_{TX,d}|^2 e^{\frac{j2\pi(n_1-n_2)(\epsilon+k)}{K}} + |g_{TX,I}|^2 e^{\frac{j2\pi(n_1-n_2)(\epsilon-k)}{K}} \Big). \end{aligned} \tag{2.45}$$

By utilizing (2.43), (2.45) and (2.44), the SIR of the downlink can be written as

$$\Gamma^{down} = \frac{\alpha \sum_{k'=0}^{K-1} \sum_{m'=0}^{M-1} \mathbf{w}_{k',m'}^{H} \eta_{k',m'}^{d} \mathbf{w}_{k',m'}}{\sum_{k'=0}^{K-1} \sum_{m'=0}^{M-1} \mathbf{w}_{k',m'}^{H} \eta^{T} \mathbf{w}_{k',m'} - \alpha \mathbf{w}_{k',m'}^{H} \eta_{k',m'}^{d} \mathbf{w}_{k',m'}} = \frac{\mathbf{w}_{0,0}^{H} \mathbf{T}_3 \mathbf{w}_{0,0}}{\mathbf{w}_{0,0}^{H} (\mathbf{T}_4 - \mathbf{T}_3) \mathbf{w}_{0,0}} \tag{2.46}$$

where $\eta^{T} = \alpha_s \eta^{s} + \alpha \eta^{d-i}$, $\mathbf{T}_3 = \alpha \sum_{k'=0}^{K-1} \sum_{m'=0}^{M-1} \mathbf{M}_{m'M}^{H} \mathbf{S}_{k'}^{H} \eta_{k',m'}^{d} \mathbf{S}_{k'} \mathbf{M}_{m'M}$ and $\mathbf{T}_4 = \sum_{k'=0}^{K-1} \sum_{m'=0}^{M-1} \mathbf{M}_{m'M}^{H} \mathbf{S}_{k'}^{H} \eta^{T} \mathbf{S}_{k'} \mathbf{M}_{m'M}$. Following (2.40) and (2.46), optimal uplink receiver filter is given by

$$\mathbf{w}_{0,0}^{opt} \propto \max \left[\text{eigenvector} \left((\mathbf{T}_4 - \mathbf{T}_3)^{-1} \mathbf{T}_3 \right) \right]. \tag{2.47}$$

2.4 Achievable Rate Region

The achievable rate region is the pair (R_d, R_u) where R_u is the uplink data rate, and R_d is the downlink data rate. In cellular systems, data rates are typically asymmetric ($R_d \gg R_u$). Thus, it is necessary to consider the rate region of the two directions, and the individual transmission rate of each direction must be evaluated. However, R_d and R_u are mutually dependent because the transmit powers affect both SI and co-channel interference. Therefore, the rate region can be obtained by maximizing the uplink rate under the constraint of constant downlink rate.

Here, both downlink and uplink rates are expressed and their rates are formulated. By using residual SI power after complementary digital linear cancellation (2.18), desired signal (2.20) and equivalent thermal noise (2.27) for uplink in Section 2.2.1, and Similarly, according to derived expressions (2.29)-(2.34) for downlink in Section 2.2.2, SINR of uplink and downlink can be formulated as

Algorithm 1 Maximum uplink rate for a downlink target rate.

1: Set maximum allowable power P_{max}.
2: Compute $R_{th} = R_d(P_{max}, P_{max})$ using (2.49).
3: If $R_c \leq R_{th}$, set $\alpha^{opt} = P_{max}$ and find $\alpha_s^{opt} = P_{max}$ via bisection method until $R_d(\alpha, \alpha_s) = R_c$ and stop.
4: If $R_c > R_{th}$, set $\alpha_s^{opt} = P_{max}$ and find $\alpha^{opt} = P_{max}$ via bisection method until $R_d(\alpha, \alpha_s) = R_c$ and stop.

$$\begin{aligned}\Upsilon_{k',m'}^{up} &= \frac{\sigma_{k',m'}^{s}}{\sigma_{k',m'}^{SI} + \sigma_{k',m'}^{s,i} + \sigma_{k',m'}^{w}} = \frac{\alpha_s A_{k',m'}^{up}}{\alpha_s B_{k',m'}^{up} + \alpha C_{k',m'}^{up} + D_{k',m'}^{up}} \\ \Upsilon_{k',m'}^{down} &= \frac{\sigma_{k',m'}^{d}}{\sigma_{k',m'}^{d-i} + \sigma_{k',m'}^{U^s} + \sigma_{k',m'}^{N^{eq}}} = \frac{\alpha A_{k',m'}^{down}}{\alpha B_{k',m'}^{down} + \alpha_s C_{k',m'}^{down} + D_{k',m'}^{down}}\end{aligned} \tag{2.48}$$

where $A_{k',m'}^{up} = \mathbf{f}_{k',m'}^H \mathbf{V}_{k',m'}^s \mathbf{f}_{k',m'}$, $B_{k',m'}^{up} = \mathbf{f}_{k',m'}^H (\mathbf{V}^R - \mathbf{V}_{k',m'}^s) \mathbf{f}_{k',m'}$, $C_{k',m'}^{up} = \mathbf{f}_{k',m'}^H \mathbf{V}^{SI} \mathbf{f}_{k',m'}$, $D^{up} = \sigma_{k',m'}^w$, $A_{k',m'}^{down} = \mathbf{w}_{k',m'}^H \eta_{k',m'}^d \mathbf{w}_{k',m'}$, $B_{k',m'}^{down} = \mathbf{w}_{k',m'}^H (\eta^{d-i} - \eta_{k',m'}^d) \mathbf{w}_{k',m'}$, $C_{k',m'}^{down} = \mathbf{w}_{k',m'}^H \eta^s \mathbf{w}_{k',m'}$ and $D^{down} = \sigma_{k',m'}^{N^{eq}}$. According to (2.48), the uplink and downlink achievable rates may be expressed as

$$\begin{aligned}R_u(\alpha, \alpha_s) &= \sum_{k'=0}^{K-1} \sum_{m'=0}^{M-1} \log_2 \left(1 + \Upsilon_{k',m'}^{up}\right) \\ R_d(\alpha, \alpha_s) &= \sum_{k'=0}^{K-1} \sum_{m'=0}^{M-1} \log_2 \left(1 + \Upsilon_{k',m'}^{down}\right).\end{aligned} \tag{2.49}$$

Note that both uplink and downlink rates are dependent of system parameters, and different configurations could be considered for evaluating their performance.

Following (2.49), the optimized rate region is formulated as

$$\max_{\alpha, \alpha_s} R_u(\alpha, \alpha_s) \tag{2.50a}$$

$$\mathbf{s.t.}\ R_d(\alpha, \alpha_s) = R_c \tag{2.50b}$$

$$\alpha \leq P_{\max}, \alpha_s \leq P_{\max} \tag{2.50c}$$

where R_c is a constant and P_{max} indicates maximum allowable power that can be consumed in uplink and downlink transmissions. The problem (2.50) is not convex in general because the objective function $R_u(\alpha, \alpha_s)$ is the logarithm of a rational function. However, it can be solved optimally by utilizing the following property.

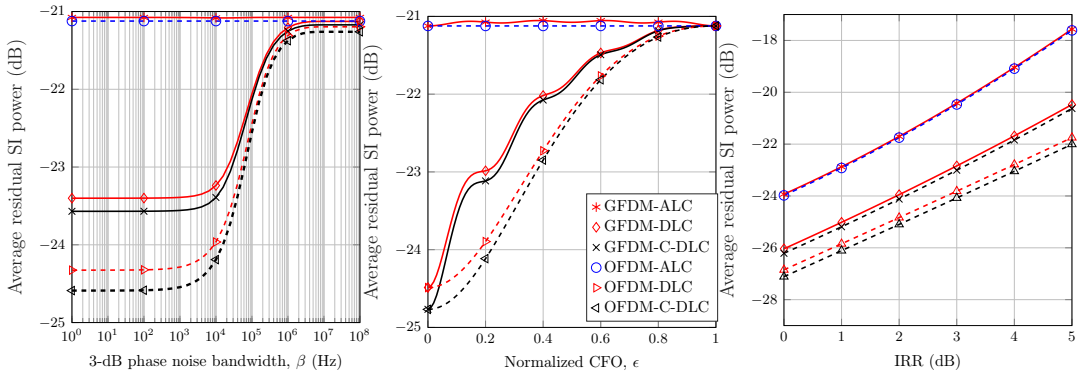

(a) (b) (c)

Figure 2.3: Average residual SI power versus 3-dB PN bandwidth, normalized CFO and IRR.

Proposition 1 *: Given the target rate constraint $R_d(\alpha, \alpha_s) = R_c$, $R_u(\alpha, \alpha_s)$ is monotonically increasing over α_s. Thus, the optimization problem (2.50) is equivalent to maximizing α_s under the same constraints. Define $R_{th} = R_d(P_{max}, P_{max})$ as the threshold rate. The solution of equivalent problem is equal to $\alpha_s^{opt} = P_{max}$ when $R_c \leq R_{th}$ and otherwise is $\alpha^{opt} = P_{max}$.*

Proof: See Appendix A.1.

Proposition 1 is exploited to develop Algorithm 1, which deploys the bisection method to optimally solve (2.50).

2.5 Simulation Results

Here, the derived uplink and downlink expressions are verified with simulation results. Moreover, GFDM full-duplex and OFDM are both evaluated and compared in the presence of PN, CFO and IQ imbalance. It should be emphasized that the derivations make no restrictive assumptions on 3-dB PN bandwidth, normalized CFO, IRR, GFDM parameters and the channel delay profile. In other words, the derived results are valid for arbitrary scenarios. However, the following specific parameter values are considered. For both GFDM and OFDM, the CP is equal to the length of the channel, and the number of subcarriers is 32. Additionally, GFDM uses $M = 5$ time

slots and a root raised-cosine filter with the roll-off factor 0.1. Sampling frequency is equal to 15.36 MHz [8]. Each wireless channel has five ($L = 5$) independent Rayleigh fading taps. The power delay profile of SI channel in [8] is utilized which is -30 dB, -65 dB, -70 dB and -75 dB for delays of 0, 1, 2 and 4 samples. Note that 30 dB antenna separation results in -30 dB attenuation of the main tap. Without loss of generality, SI channel $h_{SI}[n]$ is 10 dB stronger than interference channel between two users $h_3[n]$. The multipath downlink channel between BS transmitter and U_1 has power profile of $[-30, -55, -60, -65, -70]$ dBs. Moreover, downlink channel $h_1[n]$ is 20 dB stronger than uplink $h_2[n]$ channel. The same IQ imbalance level, $\text{IRR}_{Tx} = \text{IRR}_{Rx}$, is considered for both transmitter and receiver. Consider 30 dB and 50 dB analog and digital SI cancellations, respectively. Therefore, effective channel estimation error variance is equal to 80 dB. Furthermore, the noise variance is -60 dB, and the maximum allowable power is -10 dB. The theoretical results are shown with dash lines.

2.5.1 Full-duplex OFDM results

GFDM is a general form of OFDM. Thus, in the signal model (1.2), by setting number of time-slots is equal to one, $M = 1$, and prototype filter $g[n]$ is equal to rectangular pulse shape, GFDM reduces to OFDM. Therefore, all the derived expressions can also be used for full-duplex OFDM

2.5.2 SI Signal Power

Next, the residual SI power analysis (2.18) is verified by simulation results. Moreover, the comparative OFDM results are also shown. GFDM with zero-forcing receiver (legend GFDM-ZF) with $\alpha = 0$ dB is assumed.

In Figure 2.3, average residual SI is plotted versus the 3-dB PN bandwidth, normalized CFO and IQ imbalance for GFDM-ZF. Solid and dashed lines represent GFDM and OFDM, respectively. There are five markers per each line. These represent the

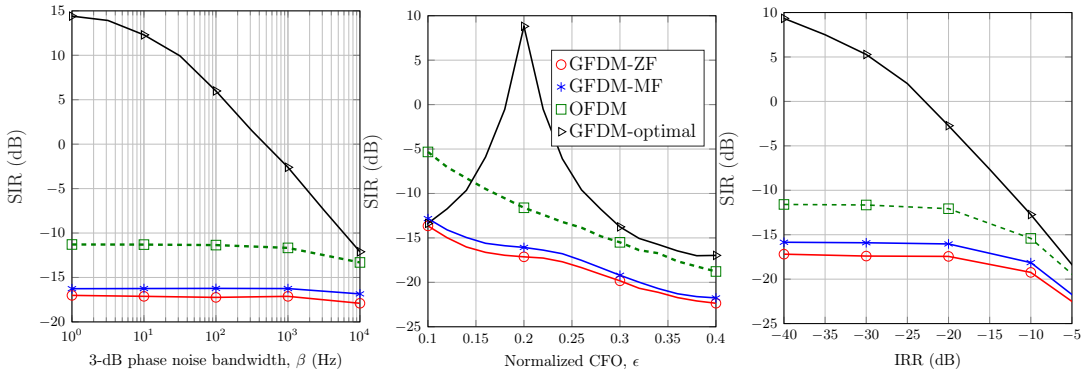

(a) (b) (c)

Figure 2.4: Uplink SIR versus 3-dB PN bandwidth, normalized CFO and IRR.

simulated points. For clarity, more simulation points are not shown. GFDM with active analog cancellation (legend GFDM-ALC) is considered in (2.14) and (2.16). Also considered is GFDM with both active digital cancellation and complementary digital linear cancellation (legends GFDM-DLC and GFDM-C-DLC) in (2.15) and (2.17).

First of all, the simulation results fully match the derived residual SI power. This match points to an independent verification of the validity of the derivations.

This figure also alludes to how the three cancellation techniques will be affected the RF impairments. Observe that C-DLC is slightly more effective than DLC. The former employs conjugate residual SI cancellation, which improves the performance significantly. Also note that ALC achieves the worst performance among the three techniques.

In Figure 2.3a, for fixed values of CFO $\epsilon = 0.1$ and 2.5 dB IQ imbalance, residual SI is plotted as a function of PN β. This figure depicts the effects of PN on the performance of the three SI cancellation techniques. For instance, the performance of ALC is not sensitive to a PN increase. However, the situation is different for both DLC and C-DLC. For the range $1 \leq \beta \leq 10^4$, both remain roughly constant regardless of β, but their performance degrades beyond that. However, this limit is less than that of ALC.

In Figure 2.3b, PN is set at 10 Hz and IQ imbalance at 2.5 dB and change CFO ϵ. This figure depicts the effects of CFO on the performance of the SI cancellation techniques. With increasing ϵ, the residual SI power after either DLC or C-DLC increases and approaches that after ALC. According to (2.14)-(2.17), 3-dB PN bandwidth, β, and normalized CFO, ϵ, appear in the exponential terms, and the trends in Figure 2.3a and Figure 2.3b for higher values of β and ϵ can be due to these exponential terms.

Figure 2.3c shows that residual SI increases with increasing IQ imbalance. In this figure, $\beta = 10$ Hz and $\epsilon = 0.1$ are fixed and IRR is changed. This figure depicts the effects of IQ imbalance on the performance of the SI cancellation techniques. Clearly, all of them rapidly degrade with the increasing IQ imbalance. Finally, OFDM achieves lower residual SI than GFDM does. The reason may be that non-orthogonal subcarriers of GFDM leads to more interference.

2.5.3 Uplink and Downlink SIR

This verifies the uplink and downlink SIR expressions (2.35) and (2.42) via simulations. Moreover, GFDM with the optimal SIR-maximizing receiver filter (legend GFDM-optimal) is compared against GFDM with matched filter receiver (legend GFDM-MF) and GFDM-ZF. The optimal filter is derived for the parameter values $\beta = 50$ Hz, $\epsilon = 0.2$, and IRR=-37.5 dB, and this derived filter is used for all other parameter values. The average transmit powers in uplink and downlink are assumed equal, i.e., $\alpha = \alpha_s$.

Figure 2.4 plots the uplink SIR as a function of 3-dB PN bandwidth, normalized CFO and IRR. GFDM-MF, GFDM-ZF, GFDM with optimal receiver filters and OFDM are compared. Solid and dashed lines represent GFDM and OFDM, respectively. There are four or five marker points per each line. These represent the simulated points. For clarity, more simulation points are not shown.

In all of the three sub figures, theoretical uplink SIR (2.35) and numerical simula-

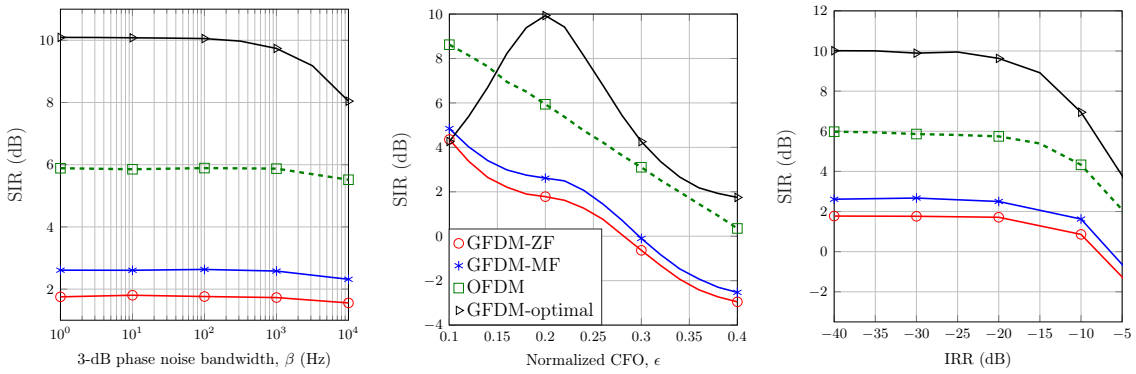

(a) (b) (c)

Figure 2.5: Downlink SIR versus 3-dB PN bandwidth, normalized CFO and IQ imbalance.

tion result match perfectly. This fact points to the validity of the derivations.

Figure 2.4a illustrates SIR versus PN (β) for a 20% CFO and -37.5 dB IQ imbalance. Obviously, the GFDM-optimal degrades the most with increasing PN β. It is seen that GFDM-optimal always achieve higher SIR than the others, e.g., for a 10 Hz PN, 25 dB higher SIR than full-duplex OFDM. A surprising observation is that OFDM achieves higher SIR GFDM-MF and GFDM-ZF. The reason is that GFDM uses non-orthogonal subcarriers, which generate some mutual interference, which will penalize the SIR measure. Clearly, ZF and MF strategies are not sufficient to mitigate this effect. This however can be reversed by the use of optimal receiver filters.

In Figure 2.4b, the SIR is plotted as a function of CFO for a 50 Hz PN and -37.5 dB IQ imbalance. GFDM-ZF, GFDM-MF and OFDM reduce SIR for large CFOs. However, these methods are outperformed by the optimal-filter based GFDM, e.g., for CFO $\epsilon = 0.2$, it achieves 20 dB more SIR than OFDM. Although the optimal filter and GFDM achieves lower SIR than OFDM for small CFO , e.g. $\epsilon = 0.1$, since this fitter was optimized for $\epsilon = 0.2$. However, the receiver filter can be optimized for lower CFO to improve the SIR.

Figure 2.4c represents the SIR versus IQ imbalance (measured by IRR) for fixed PN ($\beta = 50$ Hz) and CFO ($\epsilon = 0.2$). In all cases, increasing IQ imbalance degrades the

SIR. Furthermore, GFDM-optimal outperforms OFDM, e.g., 17 dB gain is possible at -30 dB IQ imbalance.

Figure 2.5 plots the downlink SIR as a function of 3-dB PN bandwidth, normalized CFO and IRR. GFDM-MF, GFDM-ZF, GFDM with optimal receiver filters and OFDM are compared. Solid and dashed lines represent GFDM and OFDM, respectively. There are four or five marker points per each line. These represent the simulated points. For clarity, more simulation points are not shown.

This figure shows a perfect match between theoretical (2.42) and simulations results. In all cases, OFDM achieves higher SIR than GFDM-MF and GFDM-ZF. Figure 2.5a shows SIR versus PN β for CFO ($\epsilon = 0.2$) and IQ imbalance (IRR $= -37.5$ dB). Increasing PN (β) decreases SIR in all cases. However, the solution is to use optimal filter based GFDM, which outperforms the others and significantly increase the SIR, e.g., for $\beta = 10$ Hz, it achieves an SIR 4 dB higher than OFDM.

Figure 2.5b illustrates the SIR as a function of normalized CFO for PN ($\beta = 50$ Hz) and IQ imbalance (IRR $= -37.5$ dB). For GFDM-MF and GFDM-ZF and OFDM, increasing CFO (ϵ) directly amounts to the decrease of SIR. However, similar to Figure 2.5a, GFDM-optimal alleviates this problem and achieves higher SIR than others, e.g. for $\epsilon = 0.2$, it achieves 4 dB more than OFDM. Similar to Figure 2.4, by adjusting optimized point over the range of small CFO, the SIR can be improved.

In Figure 2.5c, the SIR is plotted versus IQ imbalance measured by IRR for PN ($\beta = 50$ Hz) and CFO ($\epsilon = 0.2$). In all cases, more IQ imbalance (higher values of the IRR) degrades the SIR. However, this problem can be mitigated by the use of the optimal filters, which achieves higher SIR than OFDM. For example, for a -30 dB IQ imbalance, GFDM-optimal achieves 4 dB more in SIR than OFDM.

The main lesson of Figure 2.4 and Figure 2.5 is that RF impairments degrade the performance of GFDM-MF and GFDM-ZF much more than that of OFDM. This makes sense since GFDM relies on non-orthogonal waveforms. Fortunately, this

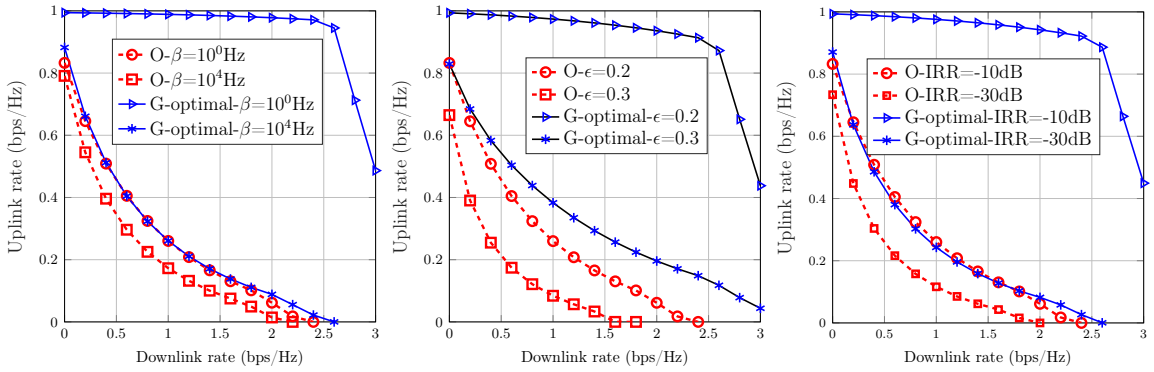

(a) (b) (c)

Figure 2.6: Rate regions parameterized by 3-dB PN bandwidth, normalized CFO and IRR.

problem can be rectified with use of the proposed GFDM optimal receiver filters in both uplink and downlink. Indeed, in uplink, the optimal filter reduces the influence of residual SI power and self-interference caused by RF impairments. Moreover, in downlink, since no SI cancellation is employed, receiver filter design can be used to suppress the uplink-user interference and achieve higher SIR.

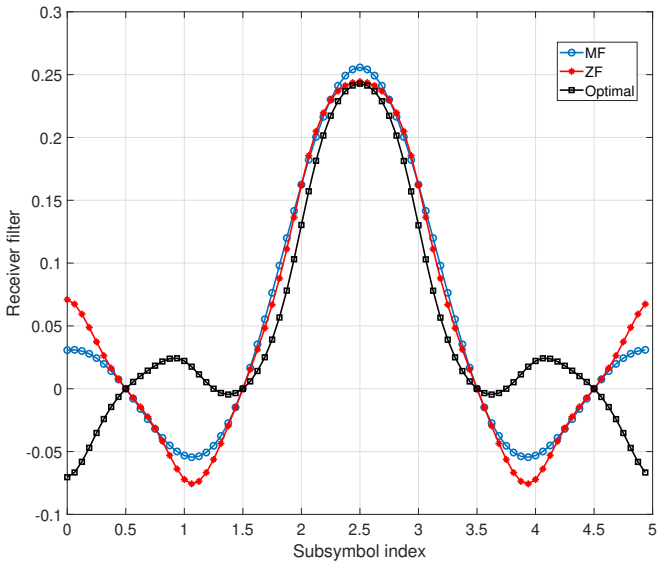

Figure 2.7: Receiver filters

Moreover, Figure 2.7 illustrates the receiver filters for MF, ZF and proposed optimal filter (2.41) in the BS receiver. The number of subcarriers is 32, the number of

subsymbols is 5, and the transmitter filter is a root raised-cosine filter with the roll-off factor 0.1. In addition, $\beta = 50$ Hz, $\epsilon = 0.2$, and IRR=-37.5 dB. Note that the optimized filter is designed to maximize the SIR.

2.5.4 Achievable Rate Region

Figure 2.6 shows the rate regions parameterized by PN bandwidth, normalized CFO and IQ imbalance. The solid lines and dashed lines represent GFDM and OFDM. This figure includes analytical results only, no simulations. "G" and "O" stands for GFDM and OFDM. Since it was found earlier that OFDM outperforms GFDM with ZF and MF filters, only GFDM with optimal uplink and downlink filters (2.41) and (2.47) is compared with OFDM.

In Figure 2.6a, the rate region is evaluated for CFO ($\epsilon = 0.2$) and IQ imbalance (-37.5 dB) and for PN values $\beta = 10^0, 10^4$ Hz. Obviously, higher PN results in lower maximum uplink rate. Moreover, GFDM-Optimal achieves higher uplink rate than OFDM, e.g., for downlink rate of 1.5 bps/Hz and 1 Hz PN, the uplink rate increases 500% over OFDM.

In Figure 2.6b, the rate region is evaluated for fixed PN (50 Hz) and IQ imbalance (-37.5 dB) and two values of CFO $\epsilon = 0.2, 0.3$. Clearly, increasing CFO ϵ decreases the uplink rate, but this trend can be countered by the optimal filter. For example, with $R_c = 1.5$ bps/Hz and $\epsilon = 0.2$, the optimal filter based GFDM achieves an uplink rate 300% more than OFDM. Finally, Figure 2.6c considers PN ($\beta = 50$ Hz) and CFO ($\epsilon = 0.2$) and IRR=-30,-10 dB. Similar to the two other cases, the maximum uplink rate decreases with more IQ imbalance, and the optimal filters provide higher rates, e.g., $R_c = 1.5$ bps/Hz and IRR=-30 dB, achievable uplink rate for the optimal filter is five times greater than OFDM. All of these results indicate the benefits of the optimal receiver filter.

2.6 Conclusion

This chapter investigated a GFDM full-duplex BS in the presence of three common RF impairments – PN, CFO and IQ imbalance. The purpose of the investigation is to provide a comprehensive and comparative evaluation of GFDM, a potential alternative to OFDM in future communication standards. To this end, this study considered a simple network of a full-duplex BS and half-duplex uplink and downlink users. This network helps to delineate the interplay among the various forms of interference signals and to determine their overall impact. In the uplink, this chapter investigated both analog and digital SI cancellations and derived residual SI and desired signal powers in closed-form. For the downlink, this chapter derived both desired signal and co-channel interference powers. For both uplink and downlink, the SIR, receiver filters for maximizing the SIR, the rates, and the closed-form optimized rate region were derived. A computational algorithm for the rate region was developed. This chapter presented simulation results to verify the analytical derivations.

The results cast light on the impact of the RF impairments on the performance of the SI cancellation methods. Active analog cancellation is less sensitive to these impairments, but active digital cancellation and complimentary digital linear cancellation can be highly sensitive. GFDM then performs worse than OFDM. The reason is that GFDM uses non-orthogonal sub-carriers, and their interaction with RF impairments ends up generating more interference. However, the good news is that GFDM has built-in degrees-of-freedom due to the transmit and receive side filters. They can be optimized to mitigate the effects of RF impairments. For example, GFDM with optimal filters readily outperforms GFDM-MF or OFDM-ZF in terms of SIR and rates. Furthermore, while OFDM outperforms GFDM in terms of rate and SIR in some scenarios, the optimal filter based GFDM sometimes provides 500% more rate than OFDM.

This work has several limitations. While this work investigated the three most

common RF impairments, several other impairments were not considered. For example, timing offset strongly affects the SI cancellation methods and increases residual SI power, which could thus be investigated. Moreover, this work was limited to a single cell system. However, practical cellular networks consist of multiple cells and are subject to both inter-cell and intra-cell interference signals. It is imperative to investigate how the multi-cell interference will affect the performance of GFDM full-duplex BSs.

Chapter 3

SE Enhancement of Secondary Links

Chapter 2 demonstrates that a well-designed GFDM full-duplex transceiver with optimal receiver filter will outperform OFDM one in the presence of RF impairments. This chapter, to even more efficiently utilize the spectrum, aims to integrate full-duplex GFDM and cognitive radio networks. As discussed in Section 1.1.3, in cognitive networks, unlicensed SUs may access the PU spectrum in three different modes, including underlay, overlay and interweave. In the two first modes, SU will have to constrain their transmit power levels, limiting the achievable SU rates. However, in the interweave mode, the SUs access spectrum holes or white spaces, which are free frequency bands in a specific location in which the licensed PUs are not transmitting temporarily [117]. Thus in this case, SUs do not have stringent power constraints. SUs in the interweave mode periodically monitor the spectrum, detect the occupancy in the different parts of the system, and then communicate opportunistically over the spectrum holes with minimal interference.

Nevertheless, in the interweave mode, SUs do not have complete freedom to choose their power levels. In Figure 3.1, the number of active PUs are high, and so spectrum holes are placed in a highly congested spectral region [52]. Without loss of generality, consider a secondary link operating over spectrum hole sh_1 in Figure 3.1. This spectrum hole is surrounded by two active PUs in upper and lower adjacent channels, PU_r and PU_l, respectively. Thus, SUs transmitting in sh_1 must ensure that the

leakage from their transmissions on to PU_r and PU_l is below a threshold level (the ACI threshold). Note that it is sufficient consider only the two neighboring channels. Since the PSD of the SU signals is rapidly decreasing with the increasing frequency separation [52].

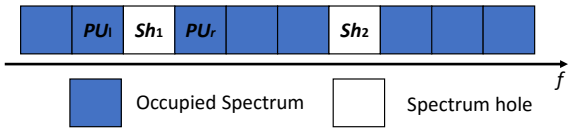

Figure 3.1: Occupied spectrum by PUs and spectrum holes.

Despite the restriction of the ACI thresholds, implementing GFDM full-duplex SUs over sh_1 can increase the data rate. However, the impacts of RF impairments must be considered since they degrade the SI cancellation performance and introduce in-band and out-of-band interference. For this reason, this chapter investigates the performance of full-duplex GFDM transceivers operating over sh_1 in the presence of PN, IQ imbalance, CFO, and a nonlinear PA. Moreover, to maximize the secondary link's SE, this chapter studies the power allocation problem for maximizing the secondary sum-rate given the ACI thresholds. For the GFDM full-duplex SU nodes, analog domain and digital domain SI cancellations are considered and two oscillator setups are studied: 1) two independent oscillators for local transmitter and receiver and 2) one common shared oscillator. In the former one, the transmitter and receiver experience different PN processes, while in the former one, the PN process for both is the same. It is shown that the commonly shared oscillator cancels more PN than two independent oscillators.

More specifically, the following contributions are made:

- A system model is established in which GFDM-based full-duplex secondary link operates in a spectrum hole whose lower and upper adjacent bands are active PUs. This chapter theoretically models GFDM full-duplex transceivers in detail based on well-known GFDM modulator/demodulator structures, existing

SI cancellation methods and practical RF impairments models. Active analog and digital cancellation techniques and RF impairments including PN, IQ imbalance, CFO, and nonlinear PA are addressed.

- Powers of residual SI, desired signal and noise are derived in closed form. Moreover, SINR is derived. Furthermore, this chapter derives the PSD of the transmit signal and uses it to quantify the ACI on the PU channels.

- The sum rate of the SU link is maximized under the constraints of maximum tolerable interference power on PU bands. Since this problem is non-convex, successive convex approximations is deployed to convert the problem to standard geometric programming (GP). Note that deriving the sum rate and solving the power allocation problem have not done before the work reported in this thesis.

- The resulting problem is solved via common CVX tool [118]. All the theoretical derivations are verified with simulation results. To determine the performance gains of full-duplex GFDM, full-duplex OFDM results are presented. Note that even for full-duplex OFDM, the interweave cognitive network has not been investigated previously.

The results of this chapter were published in [119–121].

3.1 System Model

The full-duplex cognitive radio link in Figure 3.2 uses GFDM and has two full-duplex nodes (as SU_1 and SU_2) in the presence of PN, IQ imbalance, CFO and nonlinear PA. As mentioned before, the effects of the transmissions of SU_1 and SU_2 must not exceed the ACI thresholds.

The channel coefficient SU_i to SU_j is h_{ij}, $i, j \in \{1, 2\}$ and $i \neq j$. The channel coefficient h_{ii}, $i \in \{1, 2\}$ represents the SI channel at SU_i. Furthermore, $h_{l,i}$ and

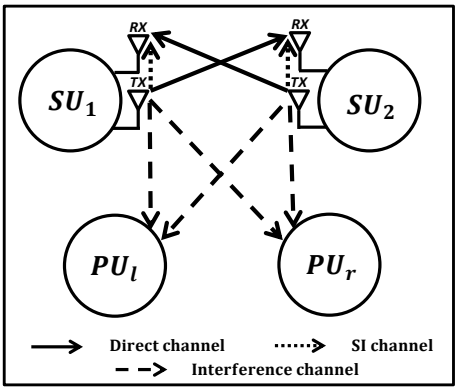

Figure 3.2: The full-duplex cognitive radio link over the spectrum hole.

$h_{r,i}$, $i \in \{1, 2\}$, represent the channels between SU_i and lower and upper active PUs, respectively.

Without loss of generality, this chapter takes SU_1 to analyze the signal model and SI cancellation process in detail.SU_1 transmits GFDM signal $x_1[n]$, which is expressed by (1.2) with the average transmit power p_1 and with i.i.d. input symbols of $d^1_{k,m}$. After digital to analog converter, the analog GFDM baseband signal $x_1(t)$ goes through the IQ mixer, which has certain non-zero IQ imbalance. Thus, the IQ and PN impaired signal may be written as [50]

$$y_1^{IQ}(t) = (g_{Tx,d}x_1(t) + g_{Tx,I}x_1^*(t))e^{j\phi_{Tx,1}(t)}, \tag{3.1}$$

where $g_{Tx,d}$ and $g_{Tx,I}$ are the transmitter IQ mixer responses for the direct and image signals, respectively, and $\phi_{Tx,1}(t)$ is random PN of the local oscillator of the SU_1 local transmitter. Moreover, the PA response is modeled by a third-order Hammerstein nonlinearity [51] as

$$y_1(t) = a_1 y_1^{IQ}(t) + a_3 y_1^{IQ}(t)|y_1^{IQ}(t)|^2, \tag{3.2}$$

where a_1 and a_3 are linear and third-order gains. Moreover, $y_1^{IQ}(t)|y_1^{IQ}(t)|^2$ can be approximated by $(g_{Tx,d}x_{PA,1}(t) + g_{Tx,I}x^*_{PA,1}(t))e^{j\phi_{Tx,1}(t)}$ [51], where $x_{PA,1}(t) = x_1(t)|x_1(t)|^2$. Note that Hammerstein model is widely used in literature for characterizing a nonlinear PA [50–52, 122]. Moreover, a third order polynomial is considered since it is the strongest nonlinearity and model the behaviour of nonlinear PA pre-

cisely [52]. The central limit theorem tells us that, when $MK \to \infty$, the GFDM signal sample Gaussian distributed [120]. Thus, following the Bussgang theorem [52, 120], the output of the Hammerstein nonlinear PA can be written as summation of a linear scaling of the input signal and nonlinear distortion noise.

The output signal $y_1(t)$ is transmitted to SU_2 through wireless channel $h_{12}(t)$ and a part of it leaks to the SU_1 local receiver through the SI channel $h_{11}(t)$. Thus, the received signal at the local receiver of SU_1, including the SI signal and the signal-of-interest from SU_2, is given by

$$r_1(t) = y_2(t) * h_{21}(t) + y_1(t) * h_{11}(t) + n_1(t), \tag{3.3}$$

where $y_2(t)$ is the desired transmitted signal from SU_2, and $n_1(t)$ is a circular symmetric complex Gaussian noise with zero mean and variance σ_n^2. By assuming IQ mixer responses of SU_2 same as SU_1, $y_2(t)$ may be written as

$$y_2(t) = a_1 y_2^{IQ}(t) + a_3 y_2^{IQ}(t)|y_2^{IQ}(t)|^2, \tag{3.4}$$

where $y_2^{IQ}(t)$ is equal to

$$y_2^{IQ}(t) = (g_{Tx,d} x_2(t) + g_{Tx,I} x_2^*(t)) e^{j\phi_{Tx,2}(t)}, \tag{3.5}$$

where $\phi_{Tx,2}(t)$ is random PN of the local oscillator of the SU_2 local transmitter and $x_2(t)$ is the analog GFDM baseband signal similar to (1.2) with the average transmit power p_2 and i.i.d input symbols of $d_{k,m}^2$.

At the first stage of SU_1 local receiver, active analog cancellation is employed to suppress the strong SI signal by subtracting the analog reconstruction signal. Thus, the resulting signal may be written in general form as

$$\hat{r}_1(t) = y_2(t) * h_{21}(t) + y_1(t) * h_1(t) + n_1(t), \tag{3.6}$$

where $h_1(t) = h_{11}(t) - h_{ALC}(t)$ is the residual SI channel and $h_{ALC}(t)$ is estimate of the SI channel [51]. Note that analog SI cancellation typically achieves 30 dB

attenuation [8]. Following the active analog cancellation, attenuated received signal $\hat{r}_1(t)$ goes through the receiver IQ mixer. By taking into account the IQ imbalance and CFO between the local oscillators of the transmitter and receiver of SU_1, the output signal may be expressed as

$$r_{IQ,1}(t) = g_{Rx,d}\hat{r}_1(t)e^{-j\phi_{Rx,1}(t)}e^{j2\pi\Delta_f t} + g_{Rx,I}\hat{r}_1^*(t)e^{j\phi_{Rx,1}(t)}e^{-j2\pi\Delta_f t}, \tag{3.7}$$

where $g_{Rx,d}$ and $g_{Rx,I}$ are the receiver IQ mixer responses for the direct and image signals. $\phi_{Rx,1}(t)$ is random PN of the local oscillator of SU_1 local receiver and Δ_f indicates the difference between carrier frequency of the receiver and transmitter local oscillators. Notice that oscillator of SU_1 receiver and SU_2 transmitter are independent of each other. However, in this chapter, two different scenarios are considered for oscillators of SU_1 transmitter and receiver: 1) two separate oscillators where $\phi_{Tx,1}(t)$ and $\phi_{Rx,1}(t)$ are statistically independent random processes and 2) single shared oscillator where $\phi_{Tx,1}(t) = \phi_{Rx,1}(t)$.

Following the IQ mixer, the baseband analog signal $r_{IQ,1}(t)$ is then converted to discrete samples. $h_{21}[n]$ and $h_1[n]$ are modeled by multipath fading channels with L_1 and L_2 paths ($h_{21}[n] = \sum_{l_1=0}^{L_1-1} h_{21,l_1}\delta[n-l_1]$ and $h_1[n] = \sum_{l_2=0}^{L_2-1} h_{1,l_2}\delta[n-l_2]$), respectively. The sampled is expressed as

$$\begin{aligned} r_{IQ}[n] = &\sum_{l_1=0}^{L_1-1} a_1\left(h_{21}^I[n,l_1]x_2[n-l_1] + h_{21}^Q[n,l_1]x_2^*[n-l_1]\right) + a_3\big(h_{21}^I[n,l_1]x_{PA,2}[n-l_1] + \\ &h_{21}^Q[n,l_1]x_{PA,2}^*[n-l_1]\big) + \sum_{l_2=0}^{L_2-1} a_1\left(h_1^I[n,l_2]x_1[n-l_2] + h_1^Q[n,l_2]x_1^*[n-l_2]\right) + a_3\big(h_1^I[n,l_2]' \\ &x_{PA,1}[n-l_2] + h_1^Q[n,l_2]x_{PA,1}^*[n-l_2]\big) + n_1^I[n] + n_1^Q[n] \end{aligned} \tag{3.8}$$

where equivalent desired and residual SI channels responses and equivalent noise

components for the individual signal components can be written as

$$\begin{aligned}
h_{21}^{I}[n,l_1] =& g_{Tx,d}g_{Rx,d}h_{21,l_1}e^{j(\phi_{TX,2}[n-l_1]-\phi_{RX,1}[n])}e^{\frac{j2\pi\epsilon n}{K}}+ \\
& g_{Tx,I}^{*}g_{Rx,I}h_{21,l_1}^{*}e^{-j(\phi_{TX,2}[n-l_1]-\phi_{RX,1}[n])}e^{\frac{-j2\pi\epsilon n}{K}} \\
h_{21}^{Q}[n,l_1] =& g_{Tx,I}g_{Rx,d}h_{21,l_1}e^{j(\phi_{TX,2}[n-l_1]-\phi_{RX,1}[n])}e^{\frac{j2\pi\epsilon n}{K}}+ \\
& g_{Tx,d}^{*}g_{Rx,I}h_{21,l_1}^{*}e^{-j(\phi_{TX,2}[n-l_1]-\phi_{RX,1}[n])}e^{\frac{-j2\pi\epsilon n}{K}} \\
h_{1}^{I}[n,l_2] =& g_{Tx,d}g_{Rx,d}h_{1,l_2}e^{j(\phi_{TX,1}[n-l_2]-\phi_{RX,1}[n])}e^{\frac{j2\pi\epsilon n}{K}}+ \\
& g_{Tx,I}^{*}g_{Rx,I}h_{1,l_2}^{*}e^{-j(\phi_{TX,1}[n-l_2]-\phi_{RX,1}[n])}e^{\frac{-j2\pi\epsilon n}{K}} \\
h_{1}^{Q}[n,l_2] =& g_{Tx,I}g_{Rx,d}h_{1,l_2}e^{j(\phi_{TX,1}[n-l_2]-\phi_{RX,1}[n])}e^{\frac{j2\pi\epsilon n}{K}}+ \\
& g_{Tx,d}^{*}g_{Rx,I}h_{1,l_2}^{*}e^{-j(\phi_{TX,1}[n-l_2]-\phi_{RX,1}[n])}e^{\frac{-j2\pi\epsilon n}{K}} \\
n_1^{I}[n] =& g_{Rx,d}e^{-j\phi_{RX,1}[n]}e^{\frac{j2\pi\epsilon n}{K}}n_1[n] \\
n_1^{Q}[n] =& g_{Rx,I}e^{j\phi_{RX,1}[n]}e^{\frac{-j2\pi\epsilon n}{K}}n_1^{*}[n],
\end{aligned} \tag{3.9}$$

where ϵ represents the CFO which is normalized by subcarrier spacing (labeled as normalized CFO). Obviously, the digital baseband signal (3.8) contains not only linear components but also its complex conjugate. Then, the resulted samples are sent to GFDM demodulator which the transmitted symbol from SU_2 at $k^{'}$-th subcarrier and $m^{'}$-th time-slot is detected by

$$\widehat{d}_{k^{'},m^{'}}^{2} = \sum_{n=0}^{MK-1}(r_{IQ}[n])f_{m^{'}}[n]e^{-j2\pi\frac{k^{'}}{K}n} = R_{k^{'},m^{'}}^{21} + R_{k^{'},m^{'}}^{1} + w_{k^{'},m^{'}}^{eq,I} + w_{k^{'},m^{'}}^{eq,Q}, \tag{3.10}$$

where $f_{m^{'}}[n] = f[n - m^{'}K]_{MK}$ is circularly shifted version of receiver filter impulse response $f[n]$. Moreover, $R_{k^{'},m^{'}}^{21} = R_{k^{'},m^{'}}^{21,I} + R_{k^{'},m^{'}}^{21,Q} + R_{k^{'},m^{'}}^{21,PA,I} + R_{k^{'},m^{'}}^{21,PA,Q}$ is a corresponding term of the received signal from SU_2 transmitter after GFDM demodulation, where $R_{k^{'},m^{'}}^{21,I}, R_{k^{'},m^{'}}^{21,Q}, R_{k^{'},m^{'}}^{21,PA,I}, R_{k^{'},m^{'}}^{21,PA,Q}$ are intended signal components in (3.8) applied to GFDM demodulator. Furthermore, $R_{k^{'},m^{'}}^{1} = R_{k^{'},m^{'}}^{1,I} + R_{k^{'},m^{'}}^{1,Q} + R_{k^{'},m^{'}}^{1,PA,I} + R_{k^{'},m^{'}}^{1,PA,Q}$ is a corresponding term of the residual SI signal from SU_1 receiver after GFDM demodulation, where $R_{k^{'},m^{'}}^{1,I}, R_{k^{'},m^{'}}^{1,Q}, R_{k^{'},m^{'}}^{1,PA,I}, R_{k^{'},m^{'}}^{1,PA,Q}$ residual SI signal components in (3.8) applied to GFDM demodulator. Finally, $w_{k^{'},m^{'}}^{eq,I}$ and $w_{k^{'},m^{'}}^{eq,Q}$ are corresponding linear

and conjugate equivalent noise terms. The samples (3.8) go into the GFDM demodulator.

At the output the GFDM demodulator, active digital cancellation is applied by deploying the replica of transmitted symbols and their conjugate, $d^{1}_{k',m'}$ and $d^{*1}_{k',m'}$, and estimation of the linear equivalent residual SI channel and conjugate equivalent residual SI channel, $\hat{h}^{I}_{1}[n,l_2]$ and $\hat{h}^{Q}_{1}[n,l_2]$. The output of active digital cancellation may thus be expressed as

$$\widehat{d}^{2,DLC}_{k',m'} = d^{2,s}_{k',m'} + d^{21}_{k',m'} + d^{RSI,1}_{k',m'} + w^{eq,I}_{k',m'} + w^{eq,Q}_{k',m'}, \tag{3.11}$$

where $d^{21}_{k',m'} = R^{21}_{k',m'} - d^{2,s}_{k',m'}$ is interference of SU_2, $d^{RSI,1}_{k',m'} = R^{1}_{k',m'} - R^{DLC,I}_{k',m'} - R^{DLC,Q}_{k',m'}$ is residual SI of SU_1, and $d^{2,s}_{k',m'}$ is the desired symbol which is extracted from $R^{21}_{k',m'}$ as

$$d^{2,s}_{k',m'} = \sqrt{p_2} d^{2}_{k',m'} \sum_{l_1=0}^{L_1-1} \sum_{n=0}^{MK-1} (a_1 + 2Ka_3p_2\gamma[n-l_1]) h^{I}_{21}[n,l_1] f_{m'}[n] g_{m'}[n-l_1] e^{\frac{-j2\pi k' l_1}{K}}, \tag{3.12}$$

where $\gamma[n] = \sum_{m=0}^{M-1} |g_m[n]|^2$.

Proof: See Appendix B.1.

Moreover, $R^{DLC,I}_{k',m'}$ and $R^{DLC,Q}_{k',m'}$ are linear and conjugate active digital cancellation symbols, which are generated by

$$\begin{aligned} R^{DLC,I}_{k',m'} =& \sqrt{p_1} d^{1}_{k',m'} \sum_{l_2=0}^{L_2-1} \sum_{n=0}^{MK-1} \hat{h}^{I}_{1}[n,l_2](a_1 + 2Ka_3p_1 \\ & \gamma[n-l_2]) f_{m'}[n] g_{m'}[n-l_2] e^{-j2\pi \frac{k'}{K} l_2} \\ R^{DLC,Q}_{k',m'} =& \sqrt{p_1} d^{*1}_{k',m'} \sum_{l_2=0}^{L_2-1} \sum_{n=0}^{MK-1} \hat{h}^{Q}_{1}[n,l_2](a_1 + 2Ka_3p_1 \\ & \gamma[n-l_2]) f_{m'}[n] g^{*}_{m'}[n-l_2] e^{-j2\pi \frac{k'}{K}(2n-l_2)}. \end{aligned} \tag{3.13}$$

Proof: See Appendix B.2.

In (3.11), non-orthogonal subcarriers of GFDM and and residual SI signal due to RF impairments cause inter carrier interference and inter symbol interference.

3.2 Power Analysis and SINR Derivation

Here, the SINR of the desired signal transmitted from SU_2 to SU_1 given the RF impairments is analyzed. For this goal, the power levels of different components in (3.11) are extracted including the desired signal, interference signal, residual SI signal and AWGN. Note that two distinct oscillator configurations for local transmitter and receiver of SU_1 are studied in detail, namely 1) two separate oscillators and 2) single shared oscillator. The free-running oscillator model with Brownian motion [31] is used to generate PN $[\phi[n+1]-\phi[n]] \sim \mathcal{N}(0, 4\pi\beta T_s)$, where $\phi[n]$ is Brownian motion with 3-dB bandwidth of β and the autocorrelation of $\phi[n]$ is

$$\mathbb{E}\left[e^{j\phi[n_1]}e^{-j\phi[n_2]}\right] = e^{-2|n_1-n_2|\pi\beta T_s}, \tag{3.14}$$

Furthermore, all the channels (h_{ij}, h_{ii}, $h_{l,i}$ and $h_{r,i}$) are WSSUS processes. Each is a mutually independent set of multipath components.

3.2.1 Power of the desired symbol

Let $\mathbb{E}[h_{21,l_1}] = 0$ and $\mathbb{E}\left[|h_{21,l_1}|^2\right] = \sigma^2_{21,l_1}$, $l_1 = 0, ..., L_1$. The power of the desired symbol $d^{2,s}_{k',m'}$, derived in (3.12), is given by $p^{2,s}_{k',m'} = \mathbb{E}\left[|d^{2,s}_{k',m'}|^2\right] = p_2 T^{2,s,1}_{k',m'} + p_2^2 T^{2,s,2}_{k',m'} + p_2^3 T^{2,s,3}_{k',m'}$, $T^{2,s,1}_{k',m'}$, $T^{2,s,2}_{k',m'}$ and $T^{2,s,3}_{k',m'}$ are derived as

$$\begin{aligned} T^{2,s,1}_{k',m'} &= |a_1|^2 \sum_{l_1=0}^{L_1-1} \sum_{n_1=0}^{MK-1} \sum_{n_2=0}^{MK-1} \sigma^2_{21,l_1} f_{m'}[n_1] f^*_{m'}[n_2] \\ &e^{-4|n_1-n_2|\pi\beta T_s} \Big(|g_{TX,d} g_{RX,d}|^2 e^{\frac{j2\pi(n_1-n_2)\epsilon}{K}} + |g_{TX,I} g_{RX,I}|^2 \\ &e^{\frac{-j2\pi(n_1-n_2)\epsilon}{K}} \Big) g_{m'}[n_1-l_1] g^*_{m'}[n_2-l_1], \end{aligned} \tag{3.15}$$

$$\begin{aligned} T^{2,s,2}_{k',m'} &= 4K\Re[a_1 a_3^*] \sum_{l_1=0}^{L_1-1} \sum_{n_1=0}^{MK-1} \sum_{n_2=0}^{MK-1} \sigma^2_{21,l_1} f_{m'}[n_1] f^*_{m'}[n_2] \\ &e^{-4|n_1-n_2|\pi\beta T_s} \Big(|g_{TX,d} g_{RX,d}|^2 e^{\frac{j2\pi(n_1-n_2)\epsilon}{K}} + |g_{TX,I} g_{RX,I}|^2 \\ &e^{\frac{-j2\pi(n_1-n_2)\epsilon}{K}} \Big) g_{m'}[n_1-l_1] g^*_{m'}[n_2-l_1] \gamma[n_1-l_1], \end{aligned} \tag{3.16}$$

and

$$T^{2,s,3}_{k',m'} = 4K^2|a_3|^2 \sum_{l_1=0}^{L_1-1} \sum_{n_1=0}^{MK-1} \sum_{n_2=0}^{MK-1} \sigma^2_{21,l_1} f_{m'}[n_1] f^*_{m'}[n_2]$$
$$e^{-4|n_1-n_2|\pi\beta T_s} \Bigg(|g_{TX,d} g_{RX,d}|^2 e^{\frac{j2\pi(n_1-n_2)\epsilon}{K}} + |g_{TX,I} g_{RX,I}|^2 \qquad (3.17)$$
$$e^{\frac{-j2\pi(n_1-n_2)\epsilon}{K}} \Bigg) g_{m'}[n_1 - l_1] g^*_{m'}[n_2 - l_1] \gamma[n_1 - l_1] \gamma[n_2 - l_1].$$

Proof: See Appendix B.3.

Note that oscillators in SU_2 transmitter, $\phi_{Tx,2}(t)$, and SU_1 receiver, $\phi_{Rx,1}(t)$, are independent. Clearly, the power of the desired symbol depends on the impairments including PN, IQ imbalance, CFO and nonlinear PA.

3.2.2 Interference Powers

The power of interference terms in output of active digital cancellation (3.11) caused by the desired signal, $d^{21}_{k',m'} = R^{21}_{k',m'} - d^{2,s}_{k',m'}$, should be derived. It can be readily shown in Appendix A that, $d^{21}_{k',m'}$ and $d^{2,s}_{k',m'}$ are independent. Thus, total interference power can be derived by $p^{21}_{k',m'} = p^{21,t}_{k',m'} - p^{2,s}_{k',m'}$, where $p^{21,t}_{k',m'} = \mathbb{E}\left[|R^{21}_{k',m'}|^2\right]$. Due to the independence among complex data, channel coefficients and PN terms, after vanishing several cross terms that are equal to zero, $p^{21,t}_{k',m'} = p_2 T^{21,t,1}_{k',m'} + p_2^2 T^{21,t,2}_{k',m'} + p_2^3 T^{21,t,3}_{k',m'}$, where $T^{21,t,1}_{k',m'}$, $T^{21,t,2}_{k',m'}$ and $T^{21,t,3}_{k',m'}$ are derived as

$$T^{21,t,1}_{k',m'} = K|a_1|^2 \sum_{l_1=0}^{L_1-1} \sum_{n=0}^{MK-1} \sum_{m_1,m_2=0}^{MK-1} \sigma^2_{21,l_1} f_{m'}[n] f_{(m'+m_1)_M}[n]$$
$$e^{-4\pi\beta T_s m_1 K} (|g_{TX,d}|^2 + |g_{TX,I}|^2) \Bigg(|g_{RX,d}|^2 e^{\frac{j2\pi\epsilon(n-\zeta[n,m_1])}{K}} + \qquad (3.18)$$
$$|g_{RX,I}|^2 e^{-\frac{j2\pi\epsilon(n-\zeta[n,m_1])}{K}} \Bigg) g_{m_2}[n - l_1] g_{(m_2+m_1)_M}[n - l_1],$$

$$T^{21,t,2}_{k',m'} = 4K^2 \Re[a_1 a_3^*] \sum_{l_1=0}^{L_1-1} \sum_{n=0}^{MK-1} \sum_{m_1,m_2,m_3=0}^{MK-1} \sigma^2_{21,l_1} f_{m'}[n]$$
$$f_{(m'+m_1)_M}[n] e^{-4\pi\beta T_s m_1 K} (|g_{TX,d}|^2 + |g_{TX,I}|^2) \Bigg(|g_{RX,d}|^2 \qquad (3.19)$$
$$e^{\frac{j2\pi\epsilon(n-\zeta[n,m_1])}{K}} + |g_{RX,I}|^2 e^{-\frac{j2\pi\epsilon(n-\zeta[n,m_1])}{K}} \Bigg) g_{m_2}[n - l_1]$$
$$g_{(m_1+m_2)_M}[n - l_1] |g_{(m_1+m_3)_M}[n - l_1]|^2,$$

and

$$T_{k',m'}^{21,t,3} = K^3|a_3|^2 \sum_{l_1=0}^{L_1-1} \sum_{n=0}^{MK-1} \sum_{m_1,m_2,m_3,m_4=0}^{MK-1} \sigma_{21,l_1}^2 f_{m'}[n]$$
$$f_{(m'+m_1)_M}[n] e^{-4\pi\beta T_s m_1 K} (|g_{TX,d}|^2 + |g_{TX,I}|^2) \Big(|g_{RX,d}|^2$$
$$e^{\frac{j2\pi\epsilon(n-\zeta[n,m_1])}{K}} + |g_{RX,I}|^2 e^{-\frac{j2\pi\epsilon(n-\zeta[n,m_1])}{K}} \Big) g_{m_3}[n-l_1] \tag{3.20}$$
$$g_{(m_3+m_1)_M}[n-l_1] g_{m_4}[n-l_1] g_{(m_1+m_2)_M}[n-l_1] \Big(4 g_{m_4}[n-l_1]$$
$$g_{(m_1+m_2)_M}[n-l_1] + 2 g_{m_2}[n-l_1] g_{(m_1+m_4)_M}[n-l_1]] \Big).$$

Proof: See Appendix B.4.

Throughout the chapter, $(x)_M$ denotes the operation x modulo M and $\zeta[n, m_1] = (n - m_1 K)_{MK}$. To reduce complexity, we deploy $\sum_{k=0}^{K-1} e^{-j2\pi \frac{k(n_1-n_2)}{K}} = K \sum_{t=0}^{M-1} \delta(n_1 - n_2 - tK)$. Obviously, the interference power terms depend on the desired channel multipath profile, 3-dB PN bandwidth, IQ imbalance coefficients, normalized CFO, nonlinear PA coefficients and GFDM parameters.

3.2.3 Power of the Residual SI Signal

Next, the power of residual SI after active digital cancellation is derived. In Chapter 2, the same is done for separate oscillator for transmitter and receiver of SU_1 without considering nonlinear PA. First, the power of active digital cancellation symbols in (3.13) is derived. Note that $\mathbb{E}[h_{1,l_2}] = 0$ and $\mathbb{E}\left[|h_{1,l_2}|^2\right] = \sigma_{1,l_2}^2$. The sum power of two active digital cancellation symbols in (3.11) can be written as $p_{k',m'}^{11,s} = \mathbb{E}\left[|R_{k',m'}^{DLC,I} + R_{k',m'}^{DLC,Q}|^2\right]$. Since $R_{k',m'}^{DLC,I}$ and $R_{k',m'}^{DLC,Q}$ are independent, $p_{k',m'}^{11,s} = \mathbb{E}\left[|R_{k',m'}^{DLC,I}|^2\right] + \mathbb{E}\left[|R_{k',m'}^{DLC,Q}|^2\right] = p_1 T_{k',m'}^{11,t,1} + p_1^2 T_{k',m'}^{11,t,2} + p_1^3 T_{k',m'}^{11,t,3}$, where $T_{k',m'}^{11,t,1}$, $T_{k',m'}^{11,t,2}$ and $T_{k',m'}^{11,t,3}$, after a straightforward manipulation, are expressed by

$$T^{11,t,1}_{k',m'} = |a_1|^2 \sum_{l_2=0}^{L_2-1} \sum_{n_1=0}^{MK-1} \sum_{n_2=0}^{MK-1} \sigma^2_{1,l_2} f_{m'}[n_1] f^*_{m'}[n_2] \Lambda^{l_2}_{n1,n2}$$
$$\Big(|g_{TX,d} g_{RX,d}|^2 e^{\frac{j2\pi(n_1-n_2)\epsilon}{K}} + |g_{TX,I} g_{RX,I}|^2 e^{\frac{-j2\pi(n_1-n_2)\epsilon}{K}} + \quad (3.21)$$
$$|g_{TX,I} g_{RX,d}|^2 e^{\frac{j2\pi(n_1-n_2)(\epsilon-2k')}{K}} + |g_{TX,d} g_{RX,I}|^2 e^{\frac{-j2\pi(n_1-n_2)(\epsilon+2k')}{K}} \Big)$$
$$g_{m'}[n_1 - l_2] g^*_{m'}[n_2 - l_2],$$

$$T^{11,t,2}_{k',m'} = 4K\Re[a_1 a_3^*] \sum_{l_2=0}^{L_2-1} \sum_{n_1=0}^{MK-1} \sum_{n_2=0}^{MK-1} \sigma^2_{1,l_2} f_{m'}[n_1] f^*_{m'}[n_2]$$
$$\Lambda^{l_2}_{n1,n2} \Big(|g_{TX,d} g_{RX,d}|^2 e^{\frac{j2\pi(n_1-n_2)\epsilon}{K}} + |g_{TX,I} g_{RX,I}|^2 e^{\frac{-j2\pi(n_1-n_2)\epsilon}{K}} + \quad (3.22)$$
$$|g_{TX,I} g_{RX,d}|^2 e^{\frac{j2\pi(n_1-n_2)(\epsilon-2k')}{K}} + |g_{TX,d} g_{RX,I}|^2 e^{\frac{-j2\pi(n_1-n_2)(\epsilon+2k')}{K}} \Big)$$
$$g_{m'}[n_1 - l_2] g^*_{m'}[n_2 - l_2] \gamma[n_1 - l_2],$$

and

$$T^{11,t,3}_{k',m'} = 4K^2 |a_3|^2 \sum_{l_2=0}^{L_2-1} \sum_{n_1=0}^{MK-1} \sum_{n_2=0}^{MK-1} \sigma^2_{1,l_2} f_{m'}[n_1] f^*_{m'}[n_2] \Lambda^{l_2}_{n1,n2}$$
$$\Big(|g_{TX,d} g_{RX,d}|^2 e^{\frac{j2\pi(n_1-n_2)\epsilon}{K}} + |g_{TX,I} g_{RX,I}|^2 e^{\frac{-j2\pi(n_1-n_2)\epsilon}{K}} + \quad (3.23)$$
$$|g_{TX,I} g_{RX,d}|^2 e^{\frac{j2\pi(n_1-n_2)(\epsilon-2k')}{K}} + |g_{TX,d} g_{RX,I}|^2 e^{\frac{-j2\pi(n_1-n_2)(\epsilon+2k')}{K}} \Big)$$
$$g_{m'}[n_1 - l_2] g^*_{m'}[n_2 - l_2] \gamma[n_1 - l_2] \gamma[n_2 - l_2],$$

where $\Lambda^{l_2}_{n1,n2}$ is a single function for representing PN term given by

$$\Lambda^{l_2}_{n1,n2} = \mathbb{E}[e^{j(\phi_{TX,1}[n_1-l_2] - \phi_{RX,1}[n_1] - \phi_{TX,1}[n_2-l_2] + \phi_{RX,1}[n_2])}] = e^{-\frac{1}{2}\mathbb{E}[|\phi_{TX,1}[n_1-l_2] - \phi_{RX,1}[n_1] - \phi_{TX,1}[n_2-l_2] + \phi_{RX,1}[n_2]|^2]}. \quad (3.24)$$

After finding the power of active digital cancellation symbols in (3.21)-(3.23), the power of residual SI is derived. According to independency between $d^{RSI,1}_{k',m'}$ and $R^{DLC,I}_{k',m'} + R^{DLC,Q}_{k',m'}$ in (3.11) , the power of residual SI, $d^{RSI,1}_{k',m'} = R^1_{k',m'} - R^{DLC,I}_{k',m'} - R^{DLC,Q}_{k',m'}$, is equal to $p^1_{k',m'} = p^{1,t}_{k',m'} - p^{11,s}_{k',m'}$, where $p^{1,t}_{k',m'} = \left[|R^1_{k',m'}|^2\right]$. Due to several cross terms that are equal to zero, it is found that $p^{1,t}_{k',m'} = p_1 T^{1,t,1}_{k',m'} + p_1^2 T^{1,t,2}_{k',m'} + p_1^3 T^{1,t,3}_{k',m'}$, where by using output of active digital cancellation (3.11), $T^{1,t,1}_{k',m'}$, $T^{1,t,2}_{k',m'}$ and $T^{1,t,3}_{k',m'}$ are derived by

$$T^{1,t,1}_{k',m'} = K|a_1|^2 \sum_{l_2=0}^{L_2-1} \sum_{n=0}^{MK-1} \sum_{m_1,m_2=0}^{MK-1} \sigma^2_{1,l_2} f_{m'}[n] f_{(m'+m_1)_M}[n]$$
$$\Lambda^{l_2}_{n,Kn+m_1}(|g_{TX,d}|^2 + |g_{TX,I}|^2)\Big(|g_{RX,d}|^2 e^{\frac{j2\pi\epsilon(n-\zeta[n,m_1])}{K}} + \tag{3.25}$$
$$|g_{RX,I}|^2 e^{-\frac{j2\pi\epsilon(n-\zeta[n,m_1])}{K}}\Big) g_{m_2}[n-l_2] g_{(m_2+m_1)_M}[n-l_2],$$

$$T^{1,t,2}_{k',m'} = 4K^2 \Re[a_1 a_3^*] \sum_{l_2=0}^{L_2-1} \sum_{n=0}^{MK-1} \sum_{m_1,m_2,m_3=0}^{MK-1} \sigma^2_{1,l_2} f_{m'}[n]$$
$$f_{(m'+m_1)_M}[n] \Lambda^{l_2}_{n,Kn+m_1}(|g_{TX,d}|^2 + |g_{TX,I}|^2)\Big(|g_{RX,d}|^2 \tag{3.26}$$
$$e^{\frac{j2\pi\epsilon(n-\zeta[n,m_1])}{K}} + |g_{RX,I}|^2 e^{-\frac{j2\pi\epsilon(n-\zeta[n,m_1])}{K}}\Big) g_{m_2}[n-l_2]$$
$$g_{(m_1+m_2)_M}[n-l_2] |g_{(m_1+m_3)_M}[n-l_2]|^2,$$

and

$$T^{1,t,3}_{k',m'} = K^3|a_3|^2 \sum_{l_2=0}^{L_2-1} \sum_{n=0}^{MK-1} \sum_{m_1,m_2,m_3,m_4=0}^{MK-1} \sigma^2_{1,l_2} f_{m'}[n]$$
$$f_{(m'+m_1)_M}[n] \Lambda^{l_2}_{n,Kn+m_1}(|g_{TX,d}|^2 + |g_{TX,I}|^2)\Big(|g_{RX,d}|^2$$
$$e^{\frac{j2\pi\epsilon(n-\zeta[n,m_1])}{K}} + |g_{RX,I}|^2 e^{-\frac{j2\pi\epsilon(n-\zeta[n,m_1])}{K}}\Big) g_{m_3}[n-l_2] \tag{3.27}$$
$$g_{(m_3+m_1)_M}[n-l_2] g_{m_4}[n-l_2] g_{(m_1+m_2)_M}[n-l_2]\Big(4 g_{m_4}[n-l_2]$$
$$g_{(m_1+m_2)_M}[n-l_2] + 2 g_{m_2}[n-l_2] g_{(m_1+m_4)_M}[n-l_2]]\Big).$$

Now, (3.24) is derived for the two oscillator configurations.

Two separate oscillators

Thus, the transmitter and receiver of SU_1 will have independent Brownian motion processes $\phi_{Tx,1}(t)$ and $\phi_{Rx,1}(t)$. Therefore, two PN difference terms $\phi_{TX,1}[n_1 - l_2] - \phi_{TX,1}[n_2 - l_2]$ and $\phi_{TX,1}[n_2] - \phi_{TX,1}[n_1]$ in (3.24) are mutually independent normal random variables. Then, by using the presented PN function in (3.14), (3.24) can be written as

$$\Lambda^{l_2,ind}_{n1,n2} = e^{-4|n_1-n_2|\pi\beta T_s}. \tag{3.28}$$

One common shared oscillator

We now have $\phi_{Tx,1}(t) = \phi_{Rx,1}(t) = \phi_1(t)$. In this configuration, for every pair of n_1 and n_2 for every value of l_2, we should find two non-overlapped groups of the PN differences in time. According to the properties of Wiener processes, they will be independent, and we can use (3.14) to find (3.24). After several manipulations, (3.24) for the common oscillator case is derived as

$$\Lambda_{n1,n2}^{l_2,comm} = \begin{cases} e^{-4|n_1-n_2|\pi\beta T_s} & |n_1 - n_2| < l_2 \\ e^{-4l_2\pi\beta T_s} & |n_1 - n_2| \geq l_2 \end{cases}. \tag{3.29}$$

By inserting (3.28) and (3.29) in (3.21)-(3.23) and (3.25)-(3.27), power of residual SI for the case of independent oscillator and common shared oscillator are derived, respectively. Obviously, derived expression in (3.21)-(3.23) and (3.25)-(3.27) is function of system parameters and can be derived for any arbitrary configurations.

3.2.4 Power of AWGN

Next, the power of equivalent noise components in (3.11) is derived. With AWGN $n_1[n] \sim \mathcal{N}(0, \sigma_n^2)$, the variance of linear equivalent noise $w_{k',m'}^{eq,I}$ in (3.11) is given by

$$\sigma_{k',m'}^{n,I} = \mathbb{E}\left[|w_{k',m'}^{eq,I}|^2\right] = |g_{RX,d}|^2\sigma_n^2 \sum_{n=0}^{MK-1} |f_{m'}[n]|^2. \tag{3.30}$$

Similarly, the power of conjugate equivalent noise $w_{k',m'}^{eq,Q}$ in (3.11) is written as

$$\sigma_{k',m'}^{n,Q} = \mathbb{E}\left[|w_{k',m'}^{eq,Q}|^2\right] = |g_{RX,I}|^2\sigma_n^2 \sum_{n=0}^{MK-1} |f_{m'}[n]|^2. \tag{3.31}$$

Variances in (3.30) and (3.31) show that noise power depends on IQ imbalance coefficients, noise variance and the receiver filter. Thus, the total noise power can be written as $\sigma_{k',m'}^{n} = \sigma_{k',m'}^{n,I} + \sigma_{k',m'}^{n,Q}$.

3.2.5 SINR Formulation

Finally, following the (3.15)-(3.17),(3.21)-(3.23) and (3.25)-(3.27), (3.30) and (3.31), the SINR associated with the desired signal transmitted from SU_2 to SU_1 may be formulated as

$$\Gamma^{21}_{k',m'} = \frac{p^{2,s}_{k',m'}}{p^{21}_{k',m'} + p^{1}_{k',m'} + \sigma^{n}_{k',m'}} = \frac{\sum_{a=1}^{3} p_2^a T^{2,s,a}_{k',m'}}{\left(\sum_{a=1}^{3} p_2^a T^{21,s,a}_{k',m'} + p_1^a T^{11,s,a}_{k',m'}\right) + \sigma^{n}_{k',m'}}, \tag{3.32}$$

where $T^{2,s,a}_{k',m'} = T^{21,t,a}_{k',m'} - T^{2,s,a}_{k',m'}$ and $T^{11,s,a}_{k',m'} = T^{1,t,a}_{k',m'} - T^{11,t,a}_{k',m'}$, $a = 1, 2, 3$. Clearly, (3.32) is a function of system parameters and specially average transmit power of SU_1, p_1 and that of SU_2, p_2.

3.3 ACI Derivation

Here, the ACI, caused by out-of-band emission of the two full-duplex nodes SU_1 and SU_2, on the lower and upper neighboring PUs is investigated. To do that, recall that the channels between SU_i and lower and upper active PUs, $h_{l,i}$ and $h_{r,i}$, $i \in \{1, 2\}$, are frequency selective channels. It is assumed that they are constant over each frequency bin in frequency domain. To derive ACI caused by SU_1, we first need to derive the PSD of the SU_1 transmitted output $y_1(t)$ in (3.5). By using the nonlinear PA output (3.2), the autocorrelation function of $y_1(t)$, $R_{y_1y_1}(t, \tau) = \mathbb{E}[y_1(t)y_1^*(t - \tau)]$, can be written as

$$R_{y_1y_1}(t, \tau) = e^{-2|\tau|\pi\beta T_s} \left(|g_{Tx,d}|^2 + |g_{Tx,I}|^2\right) R_{Z1,Z1}(t, \tau), \tag{3.33}$$

where $Z_1(t) = a_1x_1(t) + a_3x_{PA,1}(t)$ and $R_{Z_1Z_1}(t, \tau) = \mathbb{E}\left[Z_1(t)Z_1^*(t - \tau)\right]$. Reference [120] proved that $R_{Z_1Z_1}(t, \tau)$ is a cyclostationary process with the property of $R_{Z_1Z_1}(t, \tau) = R_{Z_1Z_1}(t + MT_s, \tau)$. By taking the expectation over one period, the average autocorrelation function can be derived $\bar{R}_{Z_1Z_1}(t, \tau)$. By taking its Fourier transform, the PSD of $Z_1(t)$ has been given as [120]

$$S_{Z_1Z_1}(f) = p_1\eta_1(f) + {p_1}^2\eta_2(f) + {p_1}^3\eta_3(f), \tag{3.34}$$

where $\eta_1(f)$, $\eta_2(f)$ and $\eta_3(f)$ are derived in [120]. By taking Fourier transform of autocorrelation in (3.33) the PSD of $y_1(t)$ may be expressed by $S_{y_1y_1}(f) = p_1S_{1,1}(f) + p_1^2S_{1,2}(f) + p_1^3S_{1,3}(f)$, where $S_{1,1}(f)$, $S_{1,2}(f)$ and $S_{1,3}(f)$ may be written as

$$S_{1,i}(f) = \frac{4\pi\beta T_s\left(|g_{Tx,d}|^2 + |g_{Tx,I}|^2\right)}{(2\pi\beta T_s)^2 + 4\pi^2 f^2} \otimes \eta_i(f), \quad i = 1, 2, 3. \tag{3.35}$$

By using the PSD of SU_1 transmit output $y_1(t)$ (3.35), the ACI generated by SU_1 on lower and upper channels can be derived as $P_{l,1} = p_1\psi_{l1,1} + p_1^2\psi_{l1,2} + p_1^3\psi_{l1,3}$ and $P_{r,1} = p_1\psi_{r1,1} + p_1^2\psi_{r1,2} + p_1^3\psi_{r1,3}$, respectively, where $\psi_{l,i}$ and $\psi_{r,i}$, $i = 1, 2, 3$, may be expressed as

$$\begin{aligned}
\psi_{l1,i} &= \sum_{d=K+1}^{2K} H_{l,1}(d-K) \int_{f_d - 1/(2T_s)}^{f_d + 1/(2T_s)} S_{1,i}(f)df \\
\psi_{r1,i} &= \sum_{d=K+1}^{2K} H_{r,1}(d-K) \int_{-f_d - 1/(2T_s)}^{-f_d + 1/(2T_s)} S_{1,i}(f)df,
\end{aligned} \tag{3.36}$$

where $f_d = \frac{K+2d+1}{2T_s}$, and $H_{l,1}(d)$ and $H_{r,1}(d)$ are channel gain of $h_{l,1}(t)$ and $h_{r,1}(t)$, respectively, in $d-$th frequency bin. Similarly, the ACI of SU_2 on the lower and upper channels could be derived.

3.4 Sum Rate Maximization

Now, the maximization of the sum rate of the full-duplex link given the ACI constraints on lower and upper neighboring channels of the spectrum hole is formulated. By utilizing the derived SINR expression (3.32), the achievable rates of SU_1 and SU_2 are formulated as follows:

$$\begin{aligned}
R^{21}(p_1, p_2) &= \sum_{k'=0}^{K-1}\sum_{m'=0}^{M-1} \log_2(1 + \Gamma^{21}_{k',m'}) \\
R^{12}(p_1, p_2) &= \sum_{k'=0}^{K-1}\sum_{m'=0}^{M-1} \log_2(1 + \Gamma^{12}_{k',m'}),
\end{aligned} \tag{3.37}$$

where these rates are specified in the the units of bits/second per Hertz or bps/Hz. Note that rates of SU_1 and SU_2 depend on all the system parameters. Thus, these expressions allow for comparative performance evaluations of different parameter configurations. Moreover, impacts of RF impairments on the system performance can be qualified and measured, and thus design guidelines can be developed. By utilizing the ACI expressions (3.36) and the above rates (3.37), the sum-rate maximization problem may be formulated as

$$\max_{p_1,p_2} R^{21}(p_1,p_2) + R^{12}(p_1,p_2) \tag{3.38}$$

$$\begin{aligned} s.t. \quad & p_1 \leq P_{\max}, p_2 \leq P_{\max}, \\ \textstyle\sum_{a=1}^{3} p_1^a \psi_{l1,a} < I_{l,max}, \quad & \textstyle\sum_{a=1}^{3} p_1^a \psi_{r1,a} < I_{r,max}, \\ \textstyle\sum_{a=1}^{3} p_2^a \psi_{l2,a} < I_{l,max}, \quad & \textstyle\sum_{a=1}^{3} p_2^a \psi_{r2,a} < I_{r,max} \end{aligned} \tag{3.39}$$

where P_{max} is the maximum allowable transmit power, $I_{l,max}$ and $I_{r,max}$ are the maximum tolerable interference power on the lower and upper PUs from each full-duplex node, respectively. The constraints force that the average transmit power of SU_1 and SU_2 should be lower than

$$\begin{aligned} p_1 < P'_{1,max} &= \min\left\{P_{\max}, root^{+}(\sum_{a=1}^{3} p_1^a \psi_{l1,a} - I_{l,max}), root^{+}(\sum_{a=1}^{3} p_1^a \psi_{r1,a} - I_{r,max})\right\} \\ p_2 < P'_{2,max} &= \min\left\{P_{\max}, root^{+}(\sum_{a=1}^{3} p_2^a \psi_{l12,a} - I_{l,max}), root^{+}(\sum_{a=1}^{3} p_2^a \psi_{r2,a} - I_{r,max})\right\} \end{aligned} \tag{3.40}$$

where $root^{+}(f(x))$ stands for the set of the real positive roots of $f(x) = 0$. Because of the interference constraints, the problem (3.38) is not convex. Non-convex problems are in general very tough to handle. Thus, a series of successive convex approximations is deployed until convergence. To do that, the denominator and nominator of SINR are approximated with affine functions based on first-order Taylor series expansion as $f(x(t)) = f(x(t-1)) + f^{'}(x(t-1))(x(t) - x(t-1))$, where t is the iteration index and $x(t-1)$ is the optimal solution of $t-1$ iteration [123]. Therefore, SINRs of SU_2

and SU_1 are approximated by

$$\begin{aligned}\tilde{\Gamma}^{21}_{k',m'}(t) &= \frac{A^2_{k',m'}(t-1)p_2(t) + E^2_{k',m'}(t-1)}{B^2_{k',m'}(t-1)p_2(t) + C^1_{k',m'}(t-1)p_1(t) + F^2_{k',m'}(t-1)} \\ \tilde{\Gamma}^{12}_{k',m'}(t) &= \frac{A^1_{k',m'}(t-1)p_1(t) + E^1_{k',m'}(t-1)}{B^1_{k',m'}(t-1)p_1(t) + C^2_{k',m'}(t-1)p_2(t) + F^1_{k',m'}(t-1)}.\end{aligned} \tag{3.41}$$

Proof: See Appendix B.5.

Now the sum rate optimization problem is given as

$$\max_{p_1,p_2} \sum_{k'=0}^{K-1}\sum_{m'=0}^{M-1} \log_2(1+\tilde{\Gamma}^{21}_{k',m'}) + \sum_{k'=0}^{K-1}\sum_{m'=0}^{M-1} \log_2(1+\tilde{\Gamma}^{12}_{k',m'}) \tag{3.42}$$

$$s.t. \quad p_1 \leq P'_{1,\max}, p_2 \leq P'_{2,\max}. \tag{3.43}$$

Then, (3.42) is converted into a minimization problem, and after that transform it to a logarithm of a multiplication terms as

$$\min_{p_1,p_2} \log \prod_{k'=0}^{M-1}\prod_{m'=0}^{K-1} (1+\tilde{\Gamma}^{21}_{k',m'})^{-1} + \log \prod_{k'=0}^{M-1}\prod_{m'=0}^{K-1} (1+\tilde{\Gamma}^{12}_{k',m'})^{-1}. \tag{3.44}$$

To write fractional terms of (3.44) in the form of posynomial functions, the arithmetic-geometric mean approximation (AGMA) can be used [118]. In this method, a fraction of two posynomial functions, $F(x) = \frac{\sum_{k=1}^{N_f} f_k(x)}{\sum_{i=1}^{N_g} g_i(x)}$, is converted to the posynomial function as

$$\tilde{F}(x(t)) = \sum_{k=1}^{N_f} f_k(x) \left(\prod_{i=1}^{N_g} \left(\frac{g_i(x(t))}{\eta_i(t)} \right)^{\eta_i(t)} \right), \tag{3.45}$$

where $\eta_i(t) = \frac{g_i(t-1)}{\sum_{i'=1}^{N_g} g_{i'}(t-1)}$. Therefore, by using the AGMA, two sum rate components in (3.44) are converted to (3.46).

The optimal powers are given by

$$\min_{p_1(t),p_2(t)} \prod_{k'=0}^{M-1}\prod_{m'=0}^{K-1}\Bigg(B^2_{k',m'}(t-1)p_2(t)+C^1_{k',m'}(t-1)p_1(t)+F^2_{k',m'}(t-1)\Bigg)\Bigg(B^1_{k',m'}(t-1)$$
$$p_1(t)+C^2_{k',m'}(t-1)p_2(t)+F^1_{k',m'}(t-1)\Bigg)(\Delta_1(t-1))^{-\frac{E^2_{k',m'}(t-1)+F^2_{k',m'}(t-1)}{\Delta_1(t-1)}}$$
$$(\Delta_2(t-1))^{-\frac{E^1_{k',m'}(t-1)+F^1_{k',m'}(t-1)}{\Delta_2(t-1)}}(\frac{p_2(t)\Delta_1(t-1)}{p_2(t-1)})^{-\frac{p_2(t-1)(A^2_{k',m'}+B^2_{k',m'})}{\Delta_1(i-1)}}$$
$$(\frac{p_1(t)\Delta_2(t-1)}{p_1(t-1)})^{-\frac{p_1(t-1)(A^1_{k',m'}+B^1_{k',m'})}{\Delta_2(i-1)}}(\frac{p_1(t)\Delta_1(t-1)}{p_1(t-1)})^{-\frac{p_1(t-1)C^1_{k',m'}}{\Delta_1(t-1)}}$$
$$(\frac{p_2(t)\Delta_2(t-1)}{p_2(t-1)})^{-\frac{p_2(t-1)C^2_{k',m'}}{\Delta_2(t-1)}}, \tag{3.46}$$

where the two delta terms in (3.46) are given by

$$\begin{aligned}\Delta_1(t) &= (A^2_{k',m'}(t)+B^2_{k',m'}(t))p_2(t)+C^1_{k',m'}(t)p_1(t)+E^2_{k',m'}(t)\\ &\quad +F^2_{k',m'}(t)\\ \Delta_2(t) &= (A^1_{k',m'}(t)+B^1_{k',m'}(t))p_1(t)+C^2_{k',m'}(t)p_2(t)+E^1_{k',m'}(t)\\ &\quad +F^1_{k',m'}(t).\end{aligned} \tag{3.47}$$

Since problem (3.46) is a GP, Algorithm 2 can solve with the constraints of (3.43) by utilizing the CVX tool [118], which uses an interior point method. The number of iterations is $\frac{\log(c/t_0\beta)}{\log(\eta)}$, where c, t_0, $0<\beta<1$ and η are the number of constraints, the initial point to approximate the accuracy, the stopping criterion and the updating parameter, respectively. The computation required for the AGMA in each iteration in the problem is KM, and the total computational complexity is $KM\frac{\log(2/t_0\beta)}{\log(\eta)}$. The full algorithm is given above.

3.5 Simulation Results

Here, first, the residual SI powers for both cases of Case 1- two independent oscillators and Case 2- single shared oscillator in (3.24)-(3.29) are verified via simulation results.

Algorithm 2 Sum Rate Maximization Algorithm

2: Set $t \leftarrow 1$ and initialize $p_1(0) = p_2(0) = P_{max}$ and Calculate $\Delta_1(0)$ and $\Delta_2(0)$ by (3.47) .
3: **do while** $|p_1(t) - p_1(t-1)| \leq \varrho$ and $|p_2(t) - p_2(t-1)| \leq \varrho$ and $t < I_{\max}$
4: Derive $p_1(t)$ and $p_2(t)$ by solving (3.46) given constraints (3.43).
5: Update $\Delta_1(t)$ and $\Delta_2(t)$ by $p_1(t)$ and $p_2(t)$ by using (3.47).
6: $t \leftarrow t + 1$ 7: **end do** 8: **return**

The following results are given for both GFDM and OFDM. First, the SINR expression (3.32) is computed. Second, the PSD of transmitted signal (3.35) is verified with simulation results and adjacent channel power ratio (ACPR). Third, the sum rate maximization of the full-duplex link (3.46) given PU interference constraints (3.43) is solved for several different scenarios.

3.5.1 System Parameters

GFDM and OFDM

Note that GFDM includes OFDM as a special case. Thus, by setting $M = 1$, and prototype filter $g[n]$ equal to rectangular pulse shape, we get OFDM. Therefore, all the derived expressions can also be used for OFDM.

The considered parameters for simulating GFDM have $K = 32$ subcarriers, $M = 5$ time-slots, root raised-cosine filter with the roll-off factor 0.1 and zero forcing receiver [31] for GFDM. OFDM also uses 32 subcarriers. Sampling time is equal to 100 ns [8] and the CP for both GFDM and OFDM is equal to the length of the channel.

PA Non-linearity

linear and non-linear PAs are considered: (1) linear, denoted by PA_1, with the polynomial coefficients $a_1 = 15.0008 + j0.0908$ and $a_3 = 0$ and, (2) nonlinear, denoted by PA_2 with $\{a_1, a_3 = -23.0826 + j3.3133\}$. Variance of the noise is 0 dB and maximum allowable power is equal to PA 1- dB compression point, $P_{max} = P_{1dB} = 23$ dBm, that is derived from [120].

Channel Models

ITU outdoor channel model A is considered for generating multi-path components of $h_{21}(t) = h_{12}(t)$ with power delay profile of 0 dB, -1 dB, -9 dB, -10 dB, -15 dB and -20 dB for delays of 0, 3, 7, 11, 17 and 25 samples. Furthermore, The power delay profile of SI channel in [8] is utilized for $h_{11}(t) = h_{22}(t)$ which is 0 dB, -35 dB, -40 dB and -45 dB for delays of 0, 1, 2 and 4 samples. Moreover, interference channels between two nodes and PUs in lower and upper channels are generated from a 6-tap multipath model with exponential power profile $\sigma_i^2 = \sum_{k=0}^{6} \exp(i-k)/2$, $i = 0, ..., 6$.

Moreover, in Figure 3.3-Figure 3.7, simulation results are shown with markers. Moreover, theoretical results for linear PA_1 and nonlinear PA_2 are indicated with solid and dotted lines, respectively.

Note that GFDM with a linear PA has lower out-of-band emissions compared with OFDM. Moreover, this advantage is retained in the presence of nonlinear PA [120]. Moreover, GFDM offers flexible design of its prototype filter to further reduce out-of-band emissions [99]. However, digital predistortion [124] and crest factor reduction[125] techniques can be deployed for both GFDM and OFDM to reduce nonlinear interference. Since these techniques increase the complexity of the system, this work compares conventional GFDM and OFDM only. However, digital pre-distorion and crest-factor reduction are potential future works.

To verify the accuracy of the derived expressions, simulations of residual SI power analysis (3.24)-(3.29) and SINR (3.32) are plotted. Furthermore, the SINRs of GFDM and OFDM are compared.

3.5.2 Power Analysis

Figure 3.3 shows the SU_1 residual SI power in (3.24)-(3.29) versus 3-dB PN bandwidth for two cases; Case 1- two independent oscillators in (3.28) or Case 2 single shared oscillator (3.29). Node SU_1 uses $p_1 = 17$ dBm transmit power and GFDM. The set of IQ imbalance and CFO parameters are indicated by the legend (IRR dB, ϵ).

To evaluate the system performance given the RF impairments, three scenarios for Case 1 are investigated; 1) linear PA with no IQ imbalance and CFO (legend C1-PA_1 ($-\infty$,0)), 2) linear PA with IQ imbalance and CFO (legend C1- PA_1 (-37.5,0.05)), and 3) nonlinear PA with IQ imbalance and CFO (legend C1- PA_2 (-37.5,0.05)). Similarly, aforementioned scenarios are considered for Case 2 with this exception that CFO is equal zero for all cases. The observations have been summarized as follows:

- The simulation results for residual SI power fully match with the derived residual SI power in (3.24)-(3.29) for both Case 1 (3.28) and Case 2 (3.29).

- Promisingly, residual SI power for Case 2 is significantly lower than that for Case 1 in all cases, e.g. when PA_1 ($-\infty$,0) and $\beta = 10$ kHz, Case 2 achieves 40 dB lower residual SI power. This due to the fact that Case 2 cancels more PN by receiver oscillator than Case 1. Furthermore, CFO disappears for Case 2, which decreases residual SI power, e.g. when PA_1 (-37.5,0.02) and $\beta = 10$ kHz, 30 dB is difference between two oscillator setups. Note that [8] demonstrated that Case2 is more beneficial for OFDM full-duplex transceivers given PN impairment. However, the results clearly confirm that Case 2 preserve its beneficial in the presence of other RF impairments and is a realistic scenario for compact GFDM and OFDM full-duplex transceivers.

- Moreover, since SU_1 average transmit power $p_1 = 17$ dBm is lower than $P_{1dB} = 23$ dBm, PA_2 works in linear region. Therefore, interference terms due to the nonlinearity are negligible and residual SI power for both PAs are equal. But, in Case 2, a gap exists between the nonlinear PA and the linear PA results, e.g., for Case 2 with (-37.5,0) and $\beta = 10$ kHz, 14 dB gap exists between PA_1 and PA_2. The reason is that receiver oscillator cannot perfectly eliminate the nonlinear PA terms. On the other hand, in Case 1, PA_1 achieves lower residual SI power than PA_2 but the gap between them is not as high as Case 2.

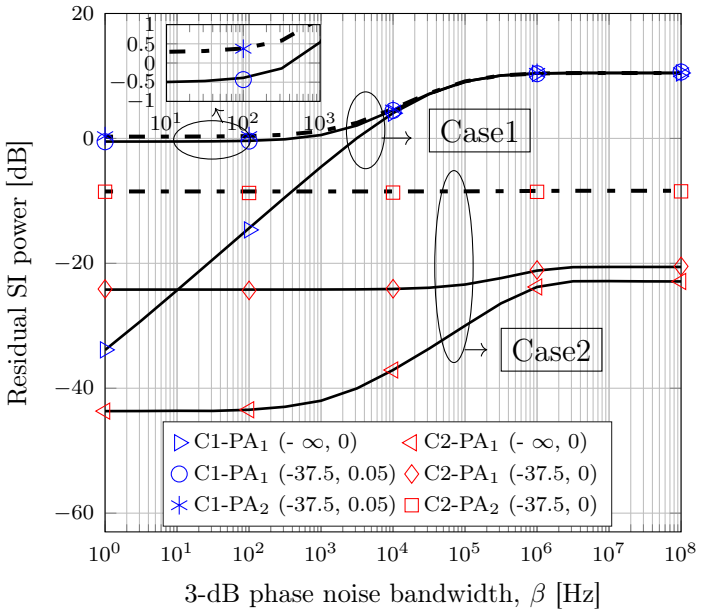

Figure 3.3: SU_1 residual SI power versus 3 dB PN bandwidth. Legends C1 and C2 denote Case 1 and Case 2, respectively.

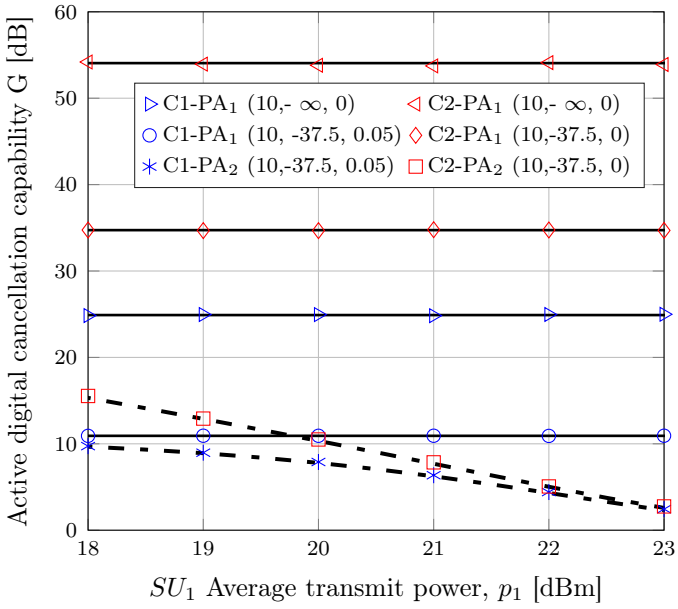

Figure 3.4: SU_1 active digital cancellation capability (50) versus SU_1 average transmit power, p_1.

By using the derived residual SI power expressions (3.21)-(3.27), for illustrating impacts of RF impairments especially nonlinear PA on SI digital cancellation, active digital cancellation capability (G) is defined as the ratio between residual SI power before and after active digital cancellation

$$G = \frac{1}{MK} \frac{\sum_{k'=0}^{K-1} \sum_{m'=0}^{M-1} p_{k',m'}^{1,t}}{\sum_{k'=0}^{K-1} \sum_{m'=0}^{M-1} p_{k',m'}^{1}}. \tag{3.48}$$

Figure 3.4 represents SU_1 active digital cancellation capability (G) in (3.48) versus average transmit power p_1 for the two oscillator setups. SU_1 uses GFDM. In this figure, the set of phase noise, IQ imbalance and CFO parameters are indicated by the legend (β [kHz],IRR dB, ϵ). Three scenarios have been investigated for Case 1; 1) linear PA with PN (legend PA_1 (10,-∞,0)), 2) linear PA with PN, IQ imbalance and CFO (legend PA_1 (10, -37.5,0.05)), and 3) nonlinear PA with PN, IQ imbalance and CFO (legend PA_2 (10, -37.5,0)). Same scenarios are considered for Case 2 which CFO is equal to zero. The observations have been summarized as

- With linear PA_1, G does not depend on the average transmit power. Thus, G remains constant for different transmit power levels. But this property does not hold for nonlinear PA_2. With increasing average transmit power approaching 23 dBm, active digital cancellation capability (G) decreases. Thus, with a non-linear PA, nonlinear interference terms are not negligible and reduce the capability of active digital cancellation.

- Similar to Figure 3.3, a single oscillator (Case 2) outperforms the use of two (Case 1) in terms of digital cancellation capability (G), e.g. when PA_1 (10, -37.5,0.05) with $p_1 = 21$ dBm, 20 dB is difference between the two oscillator setups. Furthermore, RF impairments reduce digital cancellation capability (G). Furthermore, since nonlinear interference terms are dominant in higher average transmit power, e.g. $p_1 = p_{1dB} = 23$ dBm, digital cancellation capabilities of these two oscillator setups converge to the same value. Thus, nonlinear PA plays a main role in decreasing the digital cancellation capability.

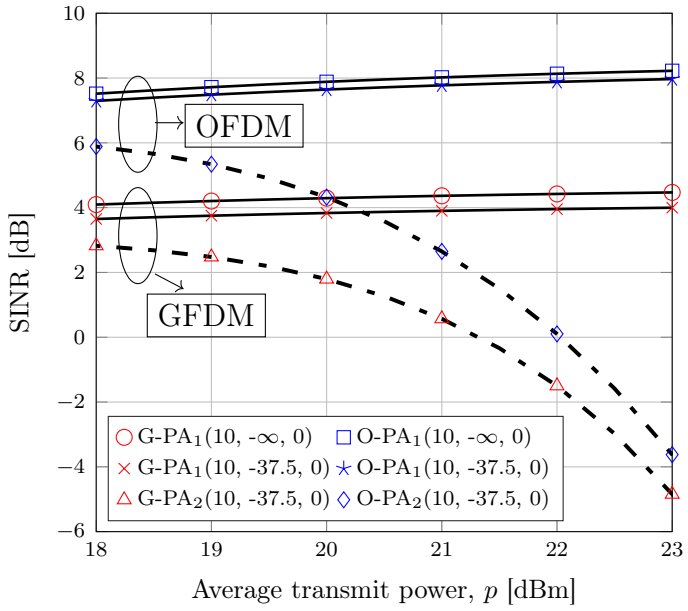

Figure 3.5: SINR vs average transmit power. SU_1 and SU_2 transmit at equal power levels, $p_1 = p_2 = p$. Legends "G" and "O" represent GFDM and OFDM.

It is notable that Figure 3.3 and Figure 3.4 illustrate that the single oscillator (Case 2) outperforms the use of two (Case 1) in the presence of RF impairments. Thus, the single oscillator option is promising for full-duplex transceivers, and it is exclusively deployed for the remaining figures.

3.5.3 SINR Analysis

Figure 3.5 shows the SINR of SU_1 in (3.32) versus average transmit power. The average transmit power of SU_1 and SU_2 are equal ($p_1 = p_2 = p$). Moreover, the parameters of RF impairments are the same for both nodes. Furthermore, SINR results for OFDM are presented. Three scenarios have been investigated for OFDM and GFDM; 1) linear PA with PN (legend PA$_1$ (10,-∞,0)), 2) linear PA with PN and IQ imbalance (legend PA$_1$ (10, -37.5,0)), and 3) nonlinear PA with PN and IQ imbalance (legend PA$_2$ (10, -37.5,0)). Note that since Case 2 is utilized, CFO does not exist. Furthermore, the PSD is estimated via the averaged periodogram algorithm with 50% overlap and the Hanning window [52]. The observations of Figure 3.5 have

been summarized as follows:

- The theoretical (3.32) and simulated results match perfectly. This match verifies the accuracy of the derived expressions of desired symbol in (3.15)-(3.17), interference terms in (3.18)-(3.20) and thermal noise in (3.30) and (3.31).

- It is well known that GFDM confers the advantages of filter bank implementation and low peak-to-average power ratio [30]. Thus, one may expect that GFDM outperforms OFDM in terms of SINR. Unfortunately, this is not true, and there is about a 4 dB gap between OFDM and GFDM results. This is because non-orthogonality of GFDM causes more ICI and ISI terms and increases residual SI power. Furthermore, interference terms from SU_2 with GFDM is higher than OFDM. Therefore, SINR of of the SU link using GFDM is lower than that using OFDM. However, for both OFDM and GFDM, the RF impairments reduce the SINR.

- Observe that, in all cases, when linear PA_1 is deployed, by increasing the average transmit power, SINR increases. The reason is that by increasing power, the effect of thermal noise in SINR (3.32) decreases. On the other hand, when nonlinear PA_2 is utilized, by increasing average transmit power and approaching to $p_{1dB} = 23$ dBm, SINR power monotonically decreases. It is due to the fact that nonlinear interference terms in nominator and denominator of SINR (3.32) are function of square and cube of power. Thus, in higher average transmit power, PA_2 works in nonlinear region and the interference terms are not negligible. In result, they reduce the power of desired terms and increase the power of interference and residual SI terms.

Next the derived PSD of transmitted signal from SU_1 in (3.35) is verified by simulation results. Moreover, we compare the ACPR of GFDM and OFDM.

3.5.4 PSD Analysis and ACPR

In Figure 3.6, PSD of transmitted signal from SU_1 in (3.35) is plotted versus the frequency in the presence of PN, IQ imbalance, and nonlinear PA. To show the effect of PA nonlinearity, the average transmit power is equal to $p_1 = p_{sat} = 27$ dB (that is derived from [120]) and PAs operate in the nonlinear region. GFDM is deployed in the transmitter of SU_1. Three scenarios similar to the ones in Figure 3.5 are considered. The observations are summarized as follows:

- The simulation results verify the derived PSD of the transmit signal of SU_1 (3.35) in the presence of RF impairments.
- PSD is typically utilized to characterize broadband random signals and estimates the frequency content of the signal. PSD enables the evaluates in-band and out-of-band emissions (e.g., interference). Figure 3.6 shows that RF impairments increase the out-of-band emission, increasing the interference on neighboring PUs. Especially, nonlinear PA causes spectrum regrowth due to out-of-band interference terms. These terms are function of square and cube of average transmit power and when the PA operates in the nonlinear region, their effects are much more severe, e.g. when (10,-37.5,0), out-of-band emission of PA_2 is -6 dB higher than PA_1.

By using PSD of SU_1 output signal (3.35), to show the impacts of RF impairments on the out-of-band emission, the ACPR is defined as

$$\zeta = \frac{\int_{B_1}^{B_2} S_{y_1 y_1}(f) df}{\int_{-B_1}^{B_1} S_{y_1 y_1}(f) df} \tag{3.49}$$

where $[B_1, B_2]$ is a frequency interval of upper adjacent channel and $[-B_1, B_1]$ is a frequency interval of the main channel. In Figure 3.6, $B_1 = 5$ MHz and $B_2 = 15$ MHz.

It is interesting to find how out-of-band emissions depend on the multicarrier modulation format used by the transceivers. Thus, Figure 3.7 plots the ACPR for GFDM

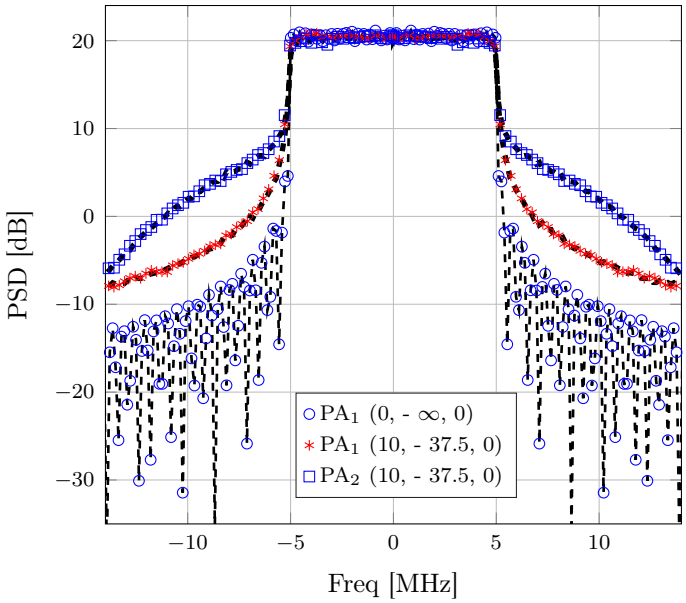

Figure 3.6: PSD of SU_1 output signal versus frequency

and OFDM versus transmit power of SU_1. Three scenarios as per Figure 3.5 are considered. The observations are summarized as follows.

- Because GFDM uses non-orthogonal subcarriers, it has higher out-of-band emissions than OFDM. But GFDM achieves lower ACPR in all cases, e.g., when PA_1 (10,-∞,0) and the transmit power of SU_1 is 21 dBm, ACPR of OFDM is approximately 7 dB higher than GFDM. The reason is that GFDM has a filter bank structure, which reduces the out-of-band emission. Although [30] confirmed this, the present work illustrates that GFDM preserves this advantage even in the presence of the RF impairments and thus has lower interference on neighboring PUs.

- As seen in Figure 3.6, RF impairments including PN and IQ imbalance increase ACPR and out-of-band emission, e.g., when $p_1 = 21$ dBm, there is 8 dB gap between PA_1 (10,-37.5,0) and PA_1 (10,-∞,0). Furthermore, the RF impairments decrease the gap between ACPR of OFDM and GFDM, e.g. at PA_1 (10,-∞,0), the gap is 7 dB, whereas when PA_1 (10,-37.5,0), the gap is 2.3 dB.

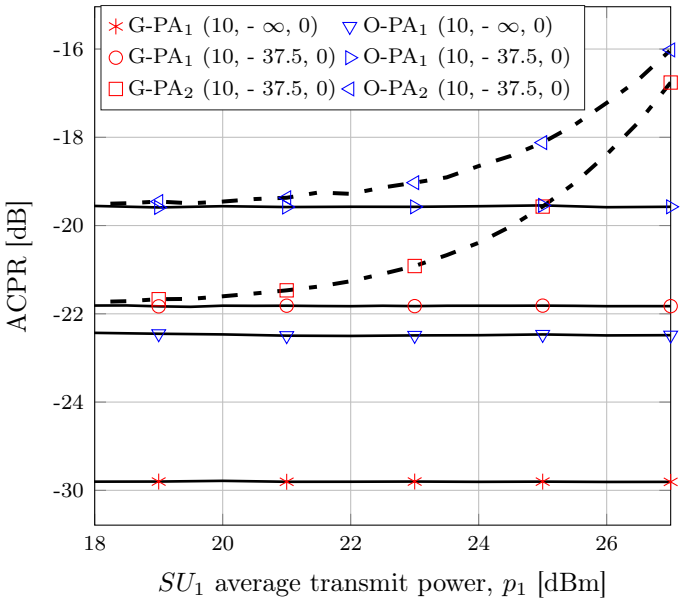

Figure 3.7: ACPR of SU_1 versus average transmit power of SU_1, p_1.

- On the other hand, when linear PA is deployed, the ACPR is independent of average transmit power and the gaps between GFDM and OFDM results is constant. However, when nonlinear PA_2 is deployed, by approaching to PA 1-dB compression point, ACPR monotonically increases and out-of-band emission on neighboring channel boosts since the power of nonlinear terms increases. Moreover, by approaching to PA 1- dB compression point, the gap between GFDM and OFDM decreases.

While OFDM outperforms GFDM in terms higher SINR (Figure 3.5), the converse holds from the perspective of out-of-band emissions (Figure 3.7). The SINR impacts the secondary link rate while out-of-band emission translates into interference on neighboring PU channels, a critical problem in cognitive radio networks. In the next section, the trade-off between these two effects is investigated.

3.5.5 Sum Rate Maximization

Figure 3.8 represents the optimized sum rate of SU link in (3.46) under ACI constraints in (3.43). For comparative purposes, the optimized sum rate results of full-

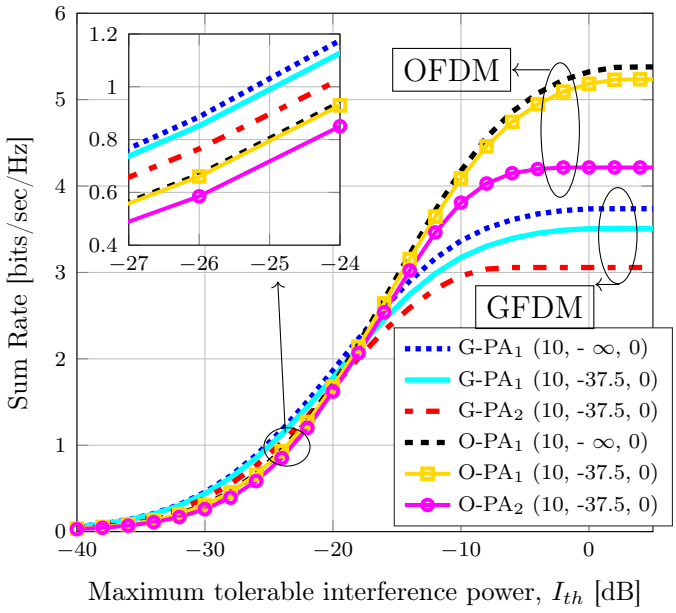

Figure 3.8: The optimized sum rate of SU link versus ACI constraint. Maximum tolerable interference power on the lower and upper PUs are same, $I_{l,max} = I_{r,max} = I_{th}$.

duplex OFDM is presented. Moreover, SU_1 and SU_2 are identical in the sense that they both have the same RF impairments. Furthermore, maximum tolerable interference on the lower and upper PUs is the same, $I_{l,max} = I_{r,max} = I_{th}$. Three scenarios as in Figure 3.5 are considered for GFDM and OFDM. The observations are explained as follows:

- On one hand, when the maximum tolerable interference power is high, e.g., $I_{th} = 0$ dB, the ACI constraint is not dominant and since full-duplex OFDM has higher SINR, it achieves higher sum rate. On the other hand, when the maximum tolerable interference power is tight, full-duplex GFDM can achieve higher sum rate since it has lower out-of-band emissions than OFDM, e.g., when PA$_1$ (10, -∞,0), at $I_{th} = -36$ dB, the optimized sum rate of full-duplex GFDM is more than double that of full-duplex OFDM. It is notable that the critical requirement for realizing SU link in the spectrum hole is low ACI on neighboring PUs. Thus, full-duplex GFDM, which has lower ACI, offers more data rates when exploiting the spectrum hole.

- However, RF impairments decrease the sum rate for GFDM and OFDM. For example, the when 3-dB PN bandwidth, IQ imbalance and CFO increase, the optimized sum rate in all cases decrease, due to increasing residual SI, ICI and ISI. Moreover, nonlinear PA_2 achieves lower sum rate in compared with linear PA_1, due to in-band and out-of-band nonlinear interference terms.

Next the performance of the proposed algorithm in (3.46) is compared with two benchmarks : (1) Non-optimized algorithm; the transmit powers of SU_1 and SU_2 are set to maximum powers $P'_{1,max}$ and $P'_{2,max}$ in (3.40), respectively, and the sum rate in (3.38) is derived without any optimization and (2) Exhaustive search; the sum rate in (3.38) under ACI constraints in (3.43) is calculated for all possible SU_1 and SU_2 average transmit powers. For exhaustive search, we examine 10000 $\times$ 10000 (p_1,p_2) sets that are generated between zero and maximum powers $P'_{1,max}$ and $P'_{2,max}$ in (3.40). Moreover, different RF impairments are considered for SU_1 and SU_2 to understand how the proposed algorithm deals with different parameter configurations. The nonlinear PA_2 with PN 10 [kHz] are considered for both SU_1 and SU_2. The IQ imbalance of SU_2 and the receiver of SU_1 is equal to -37.5 dB and the only difference is the IQ imbalance of SU_1 transmitter which is equal to -17.5 dB. As can be seen, the proposed algorithm outperforms the non-optimized algorithm. On the other hand, the optimality gap (i.e., between the proposed algorithm and the exhaustive search), which is caused by approximation in (3.41), is almost negligible. Note that when the ACI threshold decreases, the optimality gap almost vanishes. This is because, smaller thresholds result in smaller transmit power allocations, and consequently, the impacts of nonlinear terms decrease. Thus, the error of the approximation in (3.41) is negligible.

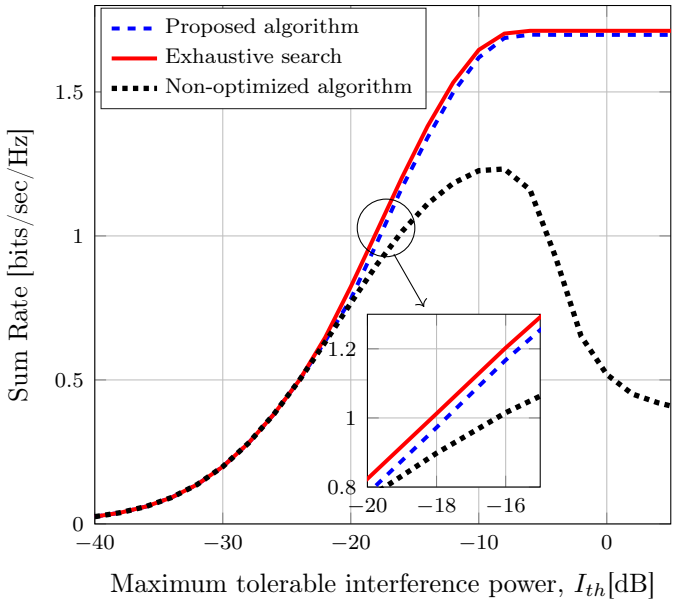

Figure 3.9: The optimized SU-link sum rate of versus ACI threshold for the different algorithms. Identical thresholds for lower and upper PU channels: $I_{l,max} = I_{r,max} = I_{th}$.

3.6 Conclusion

This chapter has investigated the performance of full-duplex GFDM transceivers operating over a spectrum hole (whose lower and upper adjacent bands are PU active) in the presence of PN, IQ imbalance, CFO, and nonlinear PA. Both analog and digital SI cancellation techniques were considered and the residual SI power was derived for two cases - (1) two independent oscillators per transceiver and (2) single shared oscillator per transceiver. In addition, the powers of desired signal, interference signal and equivalent noise, SINR and the PSD are derived. The power allocation was determined to maximize the sum rate of the secondary link. For this, a series of successive convex approximations is deployed to reach a standard geometric programming problem. Moreover, it is shown that the gap between the proposed algorithm and an exhaustive search is negligible.

Some insights and implications of the findings are as follows.

1. Since simulation results fully match the derived analytical expressions, they have

been validated. Thus, they may help us to quantify the tolerance of the system toward RF impairments and may also lead to RF circuit design guidelines and more.

2. In the presence of RF impairments, the single-shared oscillator setup significantly decreases the residual SI compared with that of two independent oscillators. Thus, the single setup may be beneficial for for up and down conversions in full-duplex transceivers.

3. Moreover, this chapter extensively evaluated the impacts of RF impairments on a GFDM full-duplex link operating over a spectrum hole. The results show that RF impairments increase the residual SI power and out-of-band emissions. These results provide practical guidance for designing full-duplex GFDM links in secondary networks subject to interference constraints.

4. Finally, this study finds that the full-duplex GFDM link achieves significantly higher rates than the full-duplex OFDM link. For instance, the sum rate gains as high as 100% are sometimes achieved. Therefore, given RF impairments, GFDM is a potential candidate for realizing full-duplex links in secondary networks.

This chapter focused on the ability of full-duplex GFDM transceivers to handle RF impairments and non-linear PA effects for a link over a spectrum hole. Cognitive and full-duplex radios offer a clear path for addressing the spectrum crunch. Hence, they offer invaluable developments for the emerging 5G and beyond wireless standards.

This work has several limitations. First, the assumption of perfect spectrum sensing may not hold in practical settings, and spectrum sensing errors will affect both the sum rate and interference levels on the primary users and also introduce primary interference on secondary receivers. These factors will then impact the throughput maximization of the secondary link. Spectrum sensing techniques include energy detection and others (see [67, 126, 127] and references therein). The impacts of dynamic

spectrum sensing and sensing errors for the considered system should thus be investigated. Second, this study considered only a few constraints, such as the maximum allowable transmit power and ACI constraints on the neighboring PUs. Therefore, additional constraints that involve spectrum sensing errors and also quality of service parameters of primary users can be considered for system level optimization.

Chapter 4

RF Impairment Compensation for GFDM Systems

As shown before, RF impairments can induce interference and thus degrade the performance of non-orthogonal systems. In GFDM systems, they can increase the ICI and ISI terms. Among the considered RF impairments, PN is more critical since time variations destroy the coherency between the channel estimate and the actual channel gain. Therefore, this chapter addresses the following problem: how can we efficiently execute joint channel estimation, PN compensation, and data detection for GFDM? This problem is essential and challenging. In particular, because of its non-orthogonal subcarriers, GFDM is limited by inherent ICI and ISI terms, which PN boosts. That is why PN compensation for GFDM is essential. This fact motivates the development of PN estimation and compensation algorithms.

The estimation process has two stages focusing on 1) channel estimation, and 2) data detection. Both stages compensate for PN. The first stage performs channel estimation. The second stage uses these estimates to detect each subsequent symbols' data. Moreover, to reduce the complexity of PN estimation, the interpolation techniques from [89] are deployed, which were initially designed for OFDM receivers, for GFDM systems.

Specifically, this chapter makes the following contributions:

- An efficient channel and PN estimator based on the non-linear least squares

(NLS) approach for the first stage is proposed. Moreover, for the second stage, this chapter proposes two algorithms for joint data detection and PN compensation: 1) iterative linear LS algorithm, and 2) closed-form LS algorithm. All algorithms utilize pilot symbols and deploy time interpolation to reduce computational complexity.

- To enhance the performance of the proposed estimators and also replaces their iterative procedure, DL frameworks are developed, which are trained offline using simulation data and then are exploited for online PN compensation.

- To quantify the impacts of PN, the effective SINR for three cases is derived: 1) ideal compensation of PN, 2) no compensation for PN, and 3) compensation of PN with the proposed algorithm.

- To gauge the accuracy of the channel and PN estimators, this chapter derives their Cramér-Rao lower bounds (CRLBs). The CRLB is a lower bound on the mean-squared error (MSE) of an unbiased estimator [128]. A trade-off exists between the accuracy and complexity of the estimators. Thus, their complexity analysis is provided.

- Finally, extensive numerical and theoretical results are presented. These consider MF and ZF GFDM receivers and compare their performances. Importantly, it is shown that the proposed estimators significantly reduce GFDM receivers' sensitivity to PN impairments.

The results of this chapter were published in [129, 130].

4.1 System Model

Figure 4.1 shows the GFDM block diagram with PN.

A quasi-static frequency selective channel constant during a GFDM packet is considered which changes from packet to packet [91]. Each packet has $N_b + 1$ GFDM

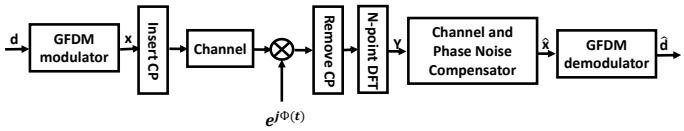

Figure 4.1: GFDM block diagram with PN.

symbols, where N_b may be selected depending on the wireless channel's coherence time. In contrast, PN varies from one symbol to another, and thus symbol-wise estimation of PN is needed, a necessity for accurate data detection. In contrast, a single channel estimate can be used for all symbols in a packet. In the GFDM packet (Figure 4.2), blue circles and red squares indicate pilot and data symbols, respectively. The first symbol is a GFDM pilot block, which is known at the receiver. The remaining symbols are comb-type symbols in the payload portion of the packet (data and pilot subcarriers).

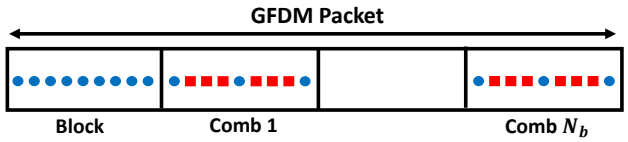

Figure 4.2: Timing of symbols within a GFDM packet.

In each GFDM symbol, the received baseband signal after the removal of CP may be expressed as [8]

$$y[n] = e^{j\phi[n]}(h[n] \circledast x[n]) + w[n], \;\; n = 0, 1, ..., N-1, \tag{4.1}$$

where $\phi[n]$ is the random PN of the local oscillator, $h[n]$ is the equivalent discrete-time baseband channel impulse response with length L_{ch}, $x[n]$ is the GFDM signal in (1.2), and $w[n]$ is AWGN with variance σ_w^2. The channel is modeled as a quasi-static, frequency-selective fading channel [33]. The channel length is shorter than the CP ($L_{ch} - 1 \leq L_{cp}$).

In addition, to model PN, the standard free-running oscillator with a Brownian motion process is deployed. Following the above details, the output samples in frequency domain can be derived by taking the DFT of the received baseband signal

$y[n]$ (4.1) as

$$Y[l] = J[l] \circledast (H[l]X[l]) + W_n[l],\ l = 0, 1, ..., N-1, \tag{4.2}$$

where

- $J[l] = \frac{1}{N}\sum_{n=0}^{N-1} e^{j\phi[n]} e^{-j\frac{2\pi ln}{N}}$ is the frequency response of PN,
- $H[l] = \sum_{n=0}^{L_{ch}-1} h[n] e^{-j\frac{2\pi ln}{N}}$ is the channel frequency response,
- $X[l] = \sum_{n=0}^{N-1} x[n] e^{-j\frac{2\pi ln}{N}}$ is the transmitted GFDM symbols in the frequency domain,
- $W_n[l] = \sum_{n=0}^{N-1} w[n] e^{-j\frac{2\pi ln}{N}}$ is the frequency response of AWGN.

The channel coefficients $H[l]$ are circularly symmetric Gaussian variables with mean zero and variance $\sigma_h^2 = \mathbb{E}\{|H[l]|^2\}$ [33, 89]. To reveal the impact of PN, circular convolution (4.2) must be expanded. This expansion yields the received signal (4.2) as

$$Y[l] = J[0]H[l]X[l] + \sum_{r=1}^{N-1} J[(l-r)_N]H[r]X[r] + W_n[l], \tag{4.3}$$

where $(l-r)_N$ stands for $((l-r) \mathrm{mod} N)$. Equation (4.3) indicates that PN causes two types of distortions: 1) common phase error, $J[0]$, and 2) ICI, which is the second term of (4.3). By using matrix notation, (4.3) can be compactly represented as

$$\mathbf{y} = \mathbf{JHx} + \mathbf{W_n}, \tag{4.4}$$

where

- $\mathbf{y} = [Y[0], ..., Y[N-1]]^T \in \mathbb{C}^{N\times 1}$ is received signal vector,
- $\mathbf{J} = \begin{bmatrix} J[0] & J[N-1] & \cdots & J[1] \\ J[1] & J[0] & \cdots & J[2] \\ \vdots & \vdots & \ddots & \vdots \\ J[N-1] & J[N-2] & \cdots & J[0] \end{bmatrix} \in \mathbb{C}^{N\times N}$ is circulant PN matrix,

- $\mathbf{H} = \text{diag}([H[0], ..., H[N-1]]) \in \mathbb{C}^{N \times N}$ is the channel frequency response matrix,
- $\mathbf{x} = \mathbf{F}_N \mathbf{A} \mathbf{d} = [X[0], ..., X[N-1]]^T \in \mathbb{C}^{N \times 1}$ is the GFDM data vector and $\mathbf{A}$ is the GFDM modulator,
- $\mathbf{W_n} = [W_n[0], ..., W_n[N-1]]^T \in \mathbb{C}^{N \times 1}$ is the additive white Gaussian noise vector.

If there is no PN, $\mathbf{J}$ becomes the identity matrix.

4.2 Joint Channel Estimation and PN Compensation

To detect the data vector $\mathbf{x}$ in (4.4), channel matrix $\mathbf{H}$ and PN matrix $\mathbf{J}$ are required. However, in practice, the receiver does not know them and must estimate them. This scenario is widely investigated (e.g., for OFDM systems see [131–133] and references therein). Thus, this chapter proposes three algorithms. Algorithm 3 uses one block-type pilot GFDM symbol for joint channel and PN estimation in the first stage of the estimation process. In the second stage, Algorithm 4 or Algorithm 5 can be used for data detection. They both utilize comb-type GFDM symbols to for PN compensation and data detection. Note that the channel estimate from Stage 1 is used in Stage 2; and thus last two algorithms use the output from Algorithm 3. This usage is possible because wireless channels are usually slowly varying compared to PN, which may change significantly from one GFDM symbol to another. Thus, previous PN estimates cannot detect the data symbols in the payload portion of the packet and must be estimated per symbol for accurate data detection. However, the first stage's channel estimate can be used during the whole packet.

4.2.1 Joint Channel and PN Estimation

Herein, this chapter proposes Algorithm 3 for joint estimation of channel coefficients and PN. It deploys one block-type pilot symbol, i.e., all $N = MK$ subsymbols are known at the receiver. The output (4.4) motivates the following optimization problem for this estimation:

$$\min_{\mathbf{H},\mathbf{J}} ||\mathbf{y} - \mathbf{JHx}||^2. \tag{4.5}$$

This problem (4.5) can be solved via the LS approach [134]. That is, $\mathbf{H}$ and $\mathbf{J}$ are estimated by minimizing the squared Euclidean distance between the observation vector $\mathbf{y}$ and the reconstructed noiseless observation $\mathbf{JHx}$ [134]. LS problems can be linear (standard) or non-linear, depending on whether the cost function is a linear function of the unknown parameters or not [135]. While the linear case has a closed-from solution, the non-linear case is solved through successive iterative algorithms and by linearizing the non-linear cost function [135]. Clearly, the problem at hand (4.5) is non-linear function of the entries of $\mathbf{H}$ and $\mathbf{J}$ because of the matrix product. This fact motivates an NLS estimator. To this end, the proposed algorithm exploits two ideas:

1. To save computational complexity, this chapter first reduces the number of unknown channel and PN parameters, $2N-1$, by relating the frequency response of channel to its time response and by interploating PN.

2. The resulting NLS problem is approximated by the linear one. With this idea, this chapter develops an iterative channel and PN estimator.

Step 1: To this end, the received signal in frequency domain (4.4) is written as

$$\mathbf{y} = \mathbf{J}'\mathbf{H}'\mathbf{x} + \mathbf{W_n}, \tag{4.6}$$

where

$$\mathbf{H}' = J[0]\mathbf{H} = \text{diag}([H'[0], ..., H'[N-1]]) \in \mathbb{C}^{N\times N}$$

$$\mathbf{J}' = \frac{1}{J[0]}\mathbf{J} = \begin{bmatrix} J'[0] & J'[N-1] & \cdots & J'[1] \\ J'[1] & J'[0] & \cdots & J'[2] \\ \vdots & \vdots & \ddots & \vdots \\ J'[N-1] & J'[N-2] & \cdots & J'[0] \end{bmatrix} \in \mathbb{C}^{N\times N}, \tag{4.7}$$

where $H'[l] = J[0]H[l]\ \ l = 0, 1, ..., N-1$, $J'[0] = 1$ and $J'[l] = J[l]/J[0],\ \ l = 1, ..., N-1$. Moreover, $\mathbf{J}'$ is circulant matrix which is formed by elements of $\tilde{\mathbf{J}} = [J'[0], J'[1], ..., J'[N-1]]^T \in \mathbb{C}^{N\times 1}$.

Note that there are N channel coefficients $H'[l],\ \ l = 0, ..., N-1$, and $N-1$ PN parameters $J'[l],\ \ l = 1, ..., N-1$. Since the number of known pilots, N, is less than the number of unknown parameters, $2N-1$, this problem is underdetermined and the solution is not unique. To avoid this conundrum, the channel and PN are modeled with fewer parameters to reduce the number of unknowns.

Channel Model

Since the channel length, L_{ch}, is much smaller than the GFDM symbol size N, similar to [33], we can relate channel frequency response $H'[l],\ \ l = 0, ..., N-1$, to its time response $h'[n],\ \ n = 0, ..., L_{ch}-1$, through

$$\tilde{\mathbf{h}} = \mathbf{F}_h \bar{\mathbf{h}}, \tag{4.8}$$

where

$$\begin{aligned} &\tilde{\mathbf{h}} = [H'[0], ..., H'[N-1]]^T \in \mathbb{C}^{N\times 1} \\ &\bar{\mathbf{h}} = [h'[0], ..., h'[L_{ch}-1]]^T \in \mathbb{C}^{L_{ch}\times 1} \\ &\mathbf{F}_h = \begin{bmatrix} 1 & 1 & \cdots & 1 \\ 1 & e^{-j\frac{2\pi}{N}} & \cdots & e^{-j\frac{2\pi(L-1)}{N}} \\ \vdots & \vdots & \ddots & \vdots \\ 1 & e^{-j\frac{2\pi(N-1)}{N}} & \cdots & e^{-j\frac{2\pi(N-1)(L-1)}{N}} \end{bmatrix} \in \mathbb{C}^{N\times L_{ch}}, \end{aligned} \tag{4.9}$$

where $h'[l] = J[0]h[l],\ \ l = 0, 1, ..., L_{ch}-1$. Moreover, $\mathbf{F}_h$ contains the first L_{ch} columns of the DFT matrix $\mathbf{F}_N$. In this way, $\bar{\mathbf{h}}$ is estimated instead of $\tilde{\mathbf{h}}$, which reduces the

number of unknown parameters into L_{ch}.

PN Model

To reduce the number of unknowns, PN is interpolated. Thus, time domain PN components $e^{j\phi[n]},\ n = 0, ..., N-1$ can be interpolated from $e^{j\phi[q(N-1)/(Q-1)]},\ q = 0, ..., Q-1 (Q < N)$ as [89]

$$\tilde{\mathbf{p}} \approx \boldsymbol{\Upsilon} \bar{\mathbf{p}}, \tag{4.10}$$

where

$$\begin{aligned} \tilde{\mathbf{p}} &= \left[e^{j\phi[0]}, e^{j\phi[1]}, ..., e^{j\phi[N-1]}\right]^T \in \mathbb{C}^{N\times 1} \\ \bar{\mathbf{p}} &= \left[e^{j\phi[0]}, e^{j\phi[(N-1)/(Q-1)]} ..., e^{j\phi[N-1]}\right]^T \in \mathbb{C}^{Q\times 1}, \end{aligned} \tag{4.11}$$

and $\boldsymbol{\Upsilon} \in \mathbb{C}^{N\times Q}$ is called interpolation matrix. It helps to approximate PN with fewer time samples. Thus, instead of estimating $J'[l],\ l = 0, ..., N-1$, approximate PN samples are computed. With PN component $J[l]$ and interpolation scheme (4.10),

$$\tilde{\mathbf{J}} = \frac{1}{N}\mathbf{F}_N \tilde{\mathbf{c}} \approx \mathbf{F}_c \bar{\mathbf{c}}, \tag{4.12}$$

where $\mathbf{F}_c = \frac{1}{N}\mathbf{F}_N \boldsymbol{\Upsilon} \in \mathbb{C}^{N\times Q}$, $\tilde{\mathbf{c}} = \frac{1}{J[0]}\tilde{\mathbf{p}}$, and

$$\begin{aligned} \tilde{\mathbf{J}} &= [J'[0], J'[1], ..., J'[N-1]]^T \in \mathbb{C}^{N\times 1} \\ \bar{\mathbf{c}} &= \frac{1}{J[0]}\bar{\mathbf{p}} = [c[0], ..., c[Q-1]]^T \in \mathbb{C}^{Q\times 1}. \end{aligned} \tag{4.13}$$

Therefore, $\bar{\mathbf{c}}$ can be estimated instead of $\tilde{\mathbf{J}}$, which appears the number of unknown parameters to be Q. However, since $J'[0] = 1$, the number of parameters is in fact $Q-1$.

Remark 2 (Interpolation matrix $\boldsymbol{\Upsilon}$)

This matrix can be determined in two ways. First, if PSD of PN is unknown, a non-optimal, interpolation matrix $\boldsymbol{\Upsilon}$ can be constructed from linear interpolation as [89]

$$\boldsymbol{\Upsilon}_L[n_1, m_1] = \begin{cases} m_1 - \frac{(n_1-1)(Q-1)}{N-1} & \frac{(m_1-1)(N-1)}{Q-1} \le n_1 - 1 \le \frac{m_1(N-1)}{Q-1} \\ \frac{(n_1-1)(Q-1)}{N-1} - (m_1-2) & \frac{(m_1-2)(N-1)}{Q-1} \le n_1 - 1 \le \frac{(m_1-1)(N-1)}{Q-1} \\ 0, & otherwise \end{cases} \tag{4.14}$$

where $n_1 = 1, 2, ..., N$ and $m_1 = 1, 2, ..., Q$. Second, if the PSD of PN is known, the optimal interpolation matrix can be derived by minimizing the MSE of interpolating $\tilde{\mathbf{p}}$ from $\bar{\mathbf{p}}$ as

$$\boldsymbol{\Upsilon}_O = arg\min_{\boldsymbol{\Upsilon}} \mathbb{E}||\tilde{\mathbf{p}} - \boldsymbol{\Upsilon}\bar{\mathbf{p}}||^2. \tag{4.15}$$

Thus, the solution of (4.15) is the optimal interpolation matrix, which is given by

$$\boldsymbol{\Upsilon}_O = \mathbf{R}_{\tilde{\mathbf{p}},\bar{\mathbf{p}}}\mathbf{R}_{\bar{\mathbf{p}}}^{-\mathbf{1}}, \tag{4.16}$$

where $\mathbf{R}_{\tilde{\mathbf{p}},\bar{\mathbf{p}}} = \mathbb{E}\{\tilde{\mathbf{p}}\bar{\mathbf{p}}^{\mathbf{H}}\}$ and $\mathbf{R}_{\bar{\mathbf{p}}} = \mathbb{E}\{\bar{\mathbf{p}}\bar{\mathbf{p}}^{\mathbf{H}}\}$, which based on the autocorelation of $\phi[n]$ in (3.14) and PN expressions in (4.11) can be derived as

$$\begin{aligned} \mathbf{R}_{\tilde{\mathbf{p}},\bar{\mathbf{p}}}[\mathbf{n_1}, \mathbf{m_1}] &= \mathbf{e}^{-\mathbf{2}|(\mathbf{n_1}-\mathbf{1})-\frac{(\mathbf{m_1}-\mathbf{1})(\mathbf{N}-\mathbf{1})}{\mathbf{Q}-\mathbf{1}}|\pi\beta\mathbf{T_s}} \\ \mathbf{R}_{\bar{\mathbf{p}}}[\mathbf{m_1}, \mathbf{m_2}] &= \mathbf{e}^{-\mathbf{2}|(\mathbf{m_1}-\mathbf{m_2})|\frac{\mathbf{N}-\mathbf{1}}{\mathbf{Q}-\mathbf{1}}\pi\beta\mathbf{T_s}}, \end{aligned} \tag{4.17}$$

where $n_1 = 1, 2, ..., N$ and $m_1, m_2 = 1, 2, ..., Q$. Thus, by substituting (4.17) in (4.16), the optimal interpolation matrix is given. Note that, it depends on the bandwidth, β, of PN. To determine the bandwidth, the receiver requires the PSD of PN. The PSD of the free-running oscillator typically is the Lorenzian spectrum [136], which can be estimated from two single point PSD measurements [137]. Therefore, it is not unrealistic to assume that the receiver knows β through prior measurements.

Consequently, the optimization problem in (4.5) is converted to joint $\bar{\mathbf{h}}$ (4.8) and $\bar{\mathbf{c}}$ (4.12) estimation problem as

$$\min_{\bar{\mathbf{h}},\bar{\mathbf{c}}} ||\mathbf{y} - \mathbf{J}'\mathbf{H}'\mathbf{x}||^2 \tag{4.18}$$

$$s.t. \quad J'[0] = 1, \tag{4.19}$$

where $\mathbf{H}'$ is related to $\bar{\mathbf{h}}$ by (4.8) and $\mathbf{J}'$ is related to $\bar{\mathbf{c}}$ by (4.12). Thus, by relating frequency response of channel to its time response in (4.8) and also deploying interpolation technique for approximating PN components in (4.10), the number of unknowns parameters in (4.5) from $2N - 1$ into $L_{ch} + Q - 1$ in (4.18). However, the resulting optimization problem (4.18) is non-linear with a non-convex cost function [33, 89].

Step 2: To solve the estimation problem (4.18), a NLS iterative estimator of $\bar{\mathbf{h}}$ and $\bar{\mathbf{c}}$ is proposed. This algorithm employs local linearization with a first-order approximation. First, initialize $\bar{\mathbf{c}}$ by setting $\hat{\mathbf{c}}_0 = [1, 1, ..., 1]^T \in \mathbb{C}^{Q\times 1}$. Second, by substituting it in (4.12) and (4.7), and deriving the $\mathbf{J}'_0$, the optimal $\bar{\mathbf{h}}$ of (4.18) is given by

$$\hat{\mathbf{h}}_0 = \left(\mathbf{F}_h^H \mathbf{X}^H {\mathbf{J}'_0}^H \mathbf{J}'_0 \mathbf{X} \mathbf{F}_h\right)^{-1} \mathbf{F}_h^H \mathbf{X}^H {\mathbf{J}'_0}^H \mathbf{y}, \tag{4.20}$$

where $\mathbf{X} = \text{diag}(\mathbf{x})$. Let $\hat{\mathbf{h}}_{i-1}$ and $\hat{\mathbf{c}}_{i-1}$ be the parameter estimates at the $(i-1)$-th iteration. If $\Delta\bar{\mathbf{h}}$ and $\Delta\bar{\mathbf{c}}$ are the estimation errors, the parameter estimates in the i-th iteration are given by

$$\hat{\mathbf{h}}_i = \hat{\mathbf{h}}_{i-1} + \Delta\bar{\mathbf{h}} \ , \ \hat{\mathbf{c}}_i = \hat{\mathbf{c}}_{i-1} + \Delta\bar{\mathbf{c}}. \tag{4.21}$$

Furthermore,

$$\hat{\mathbf{H}}'_i = \hat{\mathbf{H}}'_{i-1} + \Delta\mathbf{H}' \ , \ \hat{\mathbf{J}}'_i = \hat{\mathbf{J}}'_{i-1} + \Delta\mathbf{J}', \tag{4.22}$$

where estimation errors $\Delta\mathbf{H}'$ and $\Delta\mathbf{J}'$ are related to $\Delta\bar{\mathbf{h}}$ and $\Delta\bar{\mathbf{c}}$ via (4.8) and (4.12), respectively. By substituting (4.21) and (4.22) in (4.18) and using (4.8) and (4.12), the optimization problem (4.18) to estimate $\Delta\bar{\mathbf{h}}$ and $\Delta\bar{\mathbf{c}}$ is given as

$$\begin{aligned} &\min_{\Delta\bar{\mathbf{h}},\Delta\bar{\mathbf{c}}} ||\mathbf{y} - \ (\mathbf{J}'_{i-1} + \Delta\mathbf{J}')(\mathbf{H}'_{i-1} + \Delta\mathbf{H}')\mathbf{x}||^2 \\ &\approx \min_{\Delta\bar{\mathbf{h}},\Delta\bar{\mathbf{c}}} ||\mathbf{z} - \mathbf{T}'_{i-1}\mathbf{F}_c\Delta\bar{\mathbf{c}} - \hat{\mathbf{J}}'_{i-1}\mathbf{X}\mathbf{F}_h\Delta\bar{\mathbf{h}}||^2 \end{aligned} \tag{4.23}$$

$$s.t. \quad \mathbf{G}\Delta\bar{\mathbf{c}} = 0, \tag{4.24}$$

where $\mathbf{z} = \mathbf{y} - \ \hat{\mathbf{J}}'_{i-1}\hat{\mathbf{H}}'_{i-1}\mathbf{x} \in \mathbb{C}^{N\times 1}$, $\mathbf{T}'_{i-1} \in \mathbb{C}^{N\times N}$ is the circulant matrix formed by elements of $\hat{\mathbf{H}}'_{i-1}\mathbf{x}$, and $\mathbf{G} = [G[0], G[1], ..., G[Q-1]] \in \mathbb{C}^{1\times Q}$ is the first row of $\mathbf{F}_c = \frac{1}{N}\mathbf{F}_N\boldsymbol{\Upsilon}$ matrix. Note that, this approximation ignores the cross term between $\Delta\bar{\mathbf{h}}$ and $\Delta\bar{\mathbf{c}}$. Moreover, based on the constraint in (4.24), $\Delta\bar{c}[0]$ from parameter estimates can be removed by substituting $\mathbf{F}'_c\Delta\bar{\mathbf{c}}'$ instead $\mathbf{F}_c\Delta\bar{\mathbf{c}}$ in (4.23). We have

$$\mathbf{F}_c\Delta\bar{\mathbf{c}} = \mathbf{F}'_c\Delta\bar{\mathbf{c}}', \tag{4.25}$$

where

$$\Delta\bar{\mathbf{c}}' = [\Delta c'[1], ..., \Delta c'[Q-1]]^T \in \mathbb{C}^{Q-1\times 1}$$
$$\mathbf{F}'_c = \mathbf{S}_2 - \frac{1}{G[0]}\mathbf{S}_1\left([G[1], G[2], ..., G[Q-1]]\right) \tag{4.26}$$
$$\mathbf{F}_c = [\mathbf{S}_1|\mathbf{S}_2]\ ,\ \mathbf{S}_1 \in \mathbb{C}^{N\times 1}\ ,\ \mathbf{S}_2 \in \mathbb{C}^{N\times Q-1}.$$

In this way, by applying (4.25), constraint (4.24) is satisfied and optimization problem in (4.23) can be written as

$$\min_{\Delta\bar{\mathbf{h}},\Delta\bar{\mathbf{c}}'} ||\mathbf{z} - \mathbf{T}'_{i-1}\mathbf{F}'_c\Delta\bar{\mathbf{c}}' - \hat{\mathbf{J}}'_{i-1}\mathbf{X}\mathbf{F}_h\Delta\bar{\mathbf{h}}||^2. \tag{4.27}$$

For solving (4.27), all the parameters that should be estimated are decomposed into their real and imaginary parts and put them together in a vector $\mathbf{\Theta} \in \mathbb{C}^{2(L_{ch}+Q-1)\times 1}$ as

$$\mathbf{\Theta} = \left[\Re\{\bar{\mathbf{h}}\}^T, \Im\{\bar{\mathbf{h}}\}^T, \Re\{\bar{\mathbf{c}}'\}^T, \Im\{\bar{\mathbf{c}}'\}^T\right]^T. \tag{4.28}$$

Thus, by deploying (4.28), the non-linear optimization problem in (4.27) is reformatted as a linear LS problem, given by

$$\min_{\mathbf{\Theta}} ||\bar{\mathbf{z}} - \mathbf{\Gamma}\Delta\mathbf{\Theta}||^2, \tag{4.29}$$

where $\bar{\mathbf{z}} = \left[\Re\{\mathbf{z}\}^T, \Im\{\mathbf{z}\}^T\right]^T \in \mathbb{C}^{2N\times 1}$ and matrix $\mathbf{\Gamma} \in \mathbb{C}^{2N\times 2(L_{ch}+Q-1)}$ is derived in (C.4) (Appendix C.1). The LS solution of (4.29) yields the optimal estimate of unknown matrix $\Delta\mathbf{\Theta}$ in the i-th iteration as

$$\Delta\mathbf{\Theta} = (\mathbf{\Gamma}^T\mathbf{\Gamma})^{-1}\mathbf{\Gamma}^T\bar{\mathbf{z}}. \tag{4.30}$$

Accordingly, from (4.30) and (4.28), $\Delta\bar{\mathbf{h}}$ and $\Delta\bar{\mathbf{c}}'$ are derived. Then, by using (4.25), $\Delta\bar{\mathbf{c}}$ is derived from $\Delta\bar{\mathbf{c}}'$. Finally, estimates of $\bar{\mathbf{h}}$ and $\bar{\mathbf{c}}$ will be updated by (4.21).

The proposed joint channel and PN estimation method is summarized in Algorithm 3. It recursively works until the objective function stops improving or until it reaches the maximum number of iterations.

Note that in Step 4 of Algorithm 3, near optimal incremental terms $\Delta\bar{\mathbf{h}}$ and $\Delta\bar{\mathbf{c}}$ are derived by (4.30) through setting $\mathbf{\Theta}$ in (4.28) as predetermined $\hat{\mathbf{\Theta}}_{i-1}$, which results

in $||\bar{\mathbf{z}} - \mathbf{\Gamma}\Delta\mathbf{\Theta}||^2_{\mathbf{\Theta}=\hat{\mathbf{\Theta}}_{i-1}} \leq ||\bar{\mathbf{z}} - \mathbf{\Gamma}\Delta\mathbf{\Theta}||^2_{\mathbf{\Theta}=\hat{\mathbf{\Theta}}_i}$ [33, 89]. Thus, the objective function decreases with the number of iterations and converges to a local minimum. The convergence and accuracy of this algorithm is experimentally investigated in Section 3.5. Moreover, the output of the algorithm, which is the channel estimate, is utilized in Algorithm 2 for data detection and and PN estimation.

Algorithm 3 Joint Channel and PN Estimation

1: Set $\hat{\mathbf{c}}_0 = [1, 1, ..., 1]^T$ and find the initial $\hat{\mathbf{h}}_0$ by using (4.20)
2: Set the maximum number of iteration $I_{\max}$ and $i = 1$.
3: **do while** $|\mho_i - \mho_{i-1}| \leq \epsilon$, and $i < I_{\max}$,
4: Derive $\Delta\bar{\mathbf{h}}$ and $\Delta\bar{\mathbf{c}}$ by finding $\Delta\mathbf{\Theta}_o$ in (4.30) .
5: Update the estimates on $\bar{\mathbf{h}}$ and $\bar{\mathbf{c}}$ by (4.21) .
6: $i \leftarrow i + 1$
7: **end do**
where $\mho_i = ||\mathbf{y} - \mathbf{J}'_i\mathbf{H}'_i\mathbf{x}||^2$

4.2.2 Joint Data Symbol and PN Estimation

This algorithm uses comb-type GFDM symbols and uses the first-stage channel estimate. It performs PN compensation and data detection. Consider the vector $\mathbf{d} = \mathbf{d}_d + \mathbf{d}_p$, where $\mathbf{d}_d \in \mathbb{C}^{N\times 1}$ and $\mathbf{d}_p \in \mathbb{C}^{N\times 1}$ indicate data vector and pilots sequence, respectively. Furthermore, one pilot subsymbol every Δk subcarriers is assumed for pilot sequence $\mathbf{d}_p$ and the rest of subsymbols are zeros, which are the position of data vector $\mathbf{d}_d$. Thus, the number of pilot subcarriers is $K_p = \lfloor \frac{K}{\Delta k} \rfloor$.

Let $\mathbf{v} = [v_1, v_2, ..., v_P]^T \in \mathbb{C}^{P\times 1}$ shows the position of pilot symbols in data vector $\mathbf{d}$, where $P = MK_p$ indicates the total number of pilot symbols. Then, we have $\mathbf{d}_p = [d^{v_1}, 0, 0, ..., 0, d^{v_2}, ..., d^{v_{P-1}}, 0, 0, ..., 0, d^{v_P}]$, and $\mathbf{d}_d = \mathbf{d} - \mathbf{d}_p$. Furthermore, similar to the first stage, interpolation is employed to reduce the complexity of PN estimation.

Two algorithms are next developed for joint data and PN estimation (stage 2). First, similar approach as in [89] is considered and an iterative algorithm to solve the joint NLS estimation problem is proposed. This algorithm first detects GFDM symbols, passes the output through the GFDM demodulator, and finally outputs the

transmitted complex data symbols. Second, a closed-form LS algorithm is proposed as well, which includes the GFDM demodulator and directly detects transmitted complex data symbols.

Algorithm 4

The data detection and PN estimation problem can be formulated as

$$\min_{\mathbf{x}_d, \bar{\mathbf{c}}} ||\mathbf{y} - \mathbf{J}\mathbf{H}' (\mathbf{x}_p + \mathbf{x}_d)||^2, \tag{4.31}$$

where $\mathbf{y}$ is the observed signal, $\mathbf{J}$ is the circulant matrix formed by the elements of $\mathbf{F}_c\bar{\mathbf{c}}$ in (4.12), $\mathbf{x}_d = \mathbf{F}_N\mathbf{A}\mathbf{d}_d \in \mathbb{C}^{N\times 1}$ and $\mathbf{x}_p = \mathbf{F}_N\mathbf{A}\mathbf{d}_p \in \mathbb{C}^{N\times 1}$.

As with the original channel and PN estimation problem (4.5), (4.31) is solved via the LS approach [134]. Thus, $\mathbf{x}_d$ and $\bar{\mathbf{c}}$ by minimizing the squared distance between the observation vector $\mathbf{y}$ and the reconstructed noiseless observation $\mathbf{J}\mathbf{H}' (\mathbf{x}_p + \mathbf{x}_d)$. Note that (4.31) is a non-linear function of unknown parameters of $\mathbf{x}_d$ and $\bar{\mathbf{c}}$ with a non-convex cost function. Therefore, it has no closed-form solution [135]. Therefore, similar to the first stage, an iterative algorithm is proposed. It has two steps:1) detecting the data symbol by assuming that PN is known, 2) estimating the PN with the detected data symbol. The algorithm runs until the predefined maximum number of iterations is reached, or the cost function reaches a plateau.

step 1: Suppose that vector $\hat{\mathbf{c}}_{i-1}$ (estimation of $\bar{\mathbf{c}}$) and PN matrix $\hat{\mathbf{J}}_{i-1}$ are known in the $(i-1)$-th iteration. By solving the linear LS problem, the optimal data symbol is given by

$$\hat{\mathbf{x}}_{d,i-1} = (\mathbf{H}')^{-1} \left(\hat{\mathbf{J}}_{i-1}^H \hat{\mathbf{J}}_{i-1}\right)^{-1} \hat{\mathbf{J}}_{i-1}^H \left(\mathbf{Y} - \hat{\mathbf{J}}_{i-1}\mathbf{H}'\mathbf{x}_p\right). \tag{4.32}$$

step 2: By deploying estimated symbol in (4.32), the optimal $\hat{\mathbf{c}}_i$ is derived by solving a linear LS problem as

$$\hat{\mathbf{c}}_i = \left(\mathbf{F}_c^H \mathbf{T}''^H_{i-1} \mathbf{T}''_{i-1} \mathbf{F}_c\right)^{-1} \mathbf{F}_c^H \mathbf{T}''^H_{i-1} \mathbf{Y}, \tag{4.33}$$

where $\mathbf{T}''_{i-1} \in \mathbb{C}^{N\times N}$ is the circulant matrix formed by elements of $\mathbf{H}' (\hat{\mathbf{x}}_{d,i-1} + \mathbf{x}_p)$.

The iterative joint data and PN estimation is summarized in Algorithm 4. Note that in order to correct the scaling ambiguity in $\mathbf{H}'$, the common phase error $J[0]$ is estimated by using LS method to minimize the cost function, given by

$$\min_{J[0]} \sum_{l=0}^{N-1} |Y[l] - J[0]H'[l]X_p[l]|^2, \tag{4.34}$$

where $X[l]$ is l-th element of vector $\mathbf{x}_p$. By solving the minimization problem, the estimate of common phase error is derived as

$$\hat{J}[0] = \frac{\sum_{l=0}^{N-1} H'^*[l]X_p^*[l]Y[l]}{\sum_{l=0}^{N-1}|H'[l]|^2|X_p[l]|^2}. \tag{4.35}$$

The proposed algorithm outputs the GFDM symbol $\hat{\mathbf{x}}$, and complex data symbols are demodulated as $\hat{\mathbf{d}} = \mathbf{B}\hat{\mathbf{x}}$, where $\mathbf{B} \in \mathbb{C}^{N\times N}$ is the demodulation matrix. The matrix depends on the type of the receiver. This chapter considers two common GFDM receivers; namely, MF and ZF [33].

Algorithm 4 Joint Data and PN Estimation

1: Set $\hat{\mathbf{c}}_0 = [\hat{J}[0], \hat{J}[0], ..., \hat{J}[0]]^T \in \mathbb{C}^{Q\times 1}$
2: Set $I_{\max}$ and $i = 1$.
3: **do while** $|\varrho_i - \varrho_{i-1}| \leq \epsilon$, and $i < I_{\max}$
4: Compute optimal data $\hat{\mathbf{x}}_{i-1}$ by (4.32) .
5: Compute PN $\hat{\mathbf{c}}_i$ by (4.33) .
6: $i \leftarrow i + 1$
7: **end do**
where $\varrho_i = ||\mathbf{y} - \mathbf{J}_i\mathbf{H}'\left(\mathbf{x}_p + \hat{\mathbf{x}}_{d,i-1}\right)||^2$.

Algorithm 5

With the transmit GFDM signal (1.2) and (4.4), the observed signal with comb-type GFDM symbols may be expressed as

$$\mathbf{y} = \mathbf{F}_N\mathbf{E}\mathbf{F}_N^H\mathbf{H}'\mathbf{F}_N\mathbf{A}\mathbf{d} + \mathbf{W}_\mathbf{n}, \tag{4.36}$$

where $\mathbf{d} = \mathbf{d}_d + \mathbf{d}_p$, and $\mathbf{E} = \text{diag}(\tilde{\mathbf{p}})$ indicates the PN matrix in time domain. In (4.36), the multiplication of channel and GFDM signal is converted into time domain,

and then multiply the output with the PN matrix in time domain, and finally convert the result to the frequency domain. After passing the observed signal (4.36) through the PN compensator and GFDM demodulator, transmitted complex data symbols can be detected as

$$\hat{\mathbf{d}} = \mathbf{C}\dot{\mathbf{p}}, \tag{4.37}$$

where $\mathbf{C} = \mathbf{B}\mathbf{F}_N^H (\mathbf{H}')^{-1} \mathbf{F}_N \hat{\mathbf{y}} \boldsymbol{\Upsilon} \in \mathbb{C}^{N \times Q}$, where $\mathbf{B} \in \mathbb{C}^{N \times N}$ is the GFDM demodulation matrix and $\hat{\mathbf{y}} = \text{diag}(\mathbf{F}_N^H \mathbf{y}) \in \mathbb{C}^{N \times N}$ is the observed signal in time domain. Moreover, in (4.37), the conjugate of PN $\tilde{\mathbf{p}}^*$ ias approximated by using interpolation matrix $\boldsymbol{\Upsilon}$ as $\tilde{\mathbf{p}}^* = \boldsymbol{\Upsilon}\dot{\mathbf{p}}$, where $\dot{\mathbf{p}} \in \mathbb{C}^{Q \times 1}$ is the unknown vector. Let $\mathbf{d}_p^v = [d_p^{v_1}, d_p^{v_2}, ..., d_p^{v_P}]^T \in \mathbb{C}^{P \times 1}$ be pilot vector corresponding to pilot index set $\mathbf{v}$. Therefore, we can have

$$\mathbf{d}_p^v = \mathbf{C}_P \dot{\mathbf{p}}, \tag{4.38}$$

where $\mathbf{C}_P \in \mathbb{C}^{P \times Q}$ matrix corresponds to pilot index set $\mathbf{v}$, which is derived from matrix $\mathbf{C}$ in (4.37). Since $\mathbf{d}_p^v$ and $\mathbf{C}_P$ are known, the unknown vector $\dot{\mathbf{p}}$ can be estimated by using linear LS estimator as

$$\dot{\mathbf{p}} = \left(\mathbf{C}_P^H \mathbf{C}_P\right)^{-1} \mathbf{C}_P^H \mathbf{d}_p^v. \tag{4.39}$$

By substituting the estimated $\dot{\mathbf{p}}$ in (4.37), the transmitted complex data symbols can be obtained. This closed-form joint data and PN estimation is summarized in Algorithm 5.

Algorithm 5 Joint Data and PN Estimation

1: Compute PN unknowns $\dot{\mathbf{p}}$ by (4.39).
2: Compute data symbols $\hat{\mathbf{d}}$ via $\dot{\mathbf{p}}$ in (4.37).

4.3 DL-Based PN Compensation

This subsection proposes DL schemes to improve PN compensation performance for both stages: 1) channel estimation and 2) data detection, as it is shown in fig. 4.3.

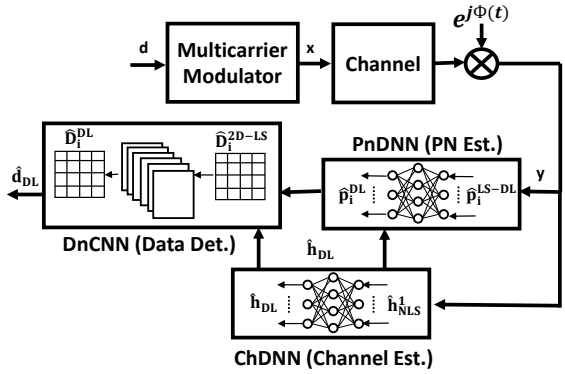

Figure 4.3: DL-based PN compensation block diagram.

4.3.1 DL-based channel estimation

The conventional NLS Algorithm 3 in section 4.2.1 for estimating channel requires many iterations to converge, resulting in high computational complexity. Moreover, although it offers the advantage of requiring minimum statistical information, its channel estimates have the MSE higher than that of other biased estimators, e.g., LMMSE, which deploys more statistical information (PN correlation matrix, channel correlation matrix, and noise variance). Thus, a DL network, named ChDNN, is developed to replace the iterative NLS estimator and improve its MSE performance without requiring more statistical information.

The proposed ChDNN network is a fully connected DNN with L layers, including one input layer, $L-2$ hidden layers, and one output layer. The NLS estimated channel, Algorithm 3, is considered in the first iteration, $\hat{\mathbf{h}}_{NLS}^{1}$, as the input to the ChDNN network. Moreover, each hidden layer of the network includes multiple neurons. The output of each hidden layer is a nonlinear function of the weighted sum of its preceding layer's output values. The output of the ChDNN network is the estimate

of the channel, which can be expressed as

$$\hat{\mathbf{h}}_{DL} = f_c(\hat{\mathbf{h}}^1_{NLS}; \Theta^c) = f_c^{(L-1)}\left(...f_c^{(1)}\left(\hat{\mathbf{h}}^1_{NLS}; \Theta^c_1\right); \Theta^c_L\right), \tag{4.40}$$

where $\Theta^c \triangleq \{\Theta^c_l\}_{l=1}^{L-1}$ is the set of parameter values for the ChDNN network. Moreover, $f_c^{(l)}$ and Θ^c_l, $l = 1, ..., L-1$, indicate the nonlinear function, and parameters of the l-th layer including weight matrix $\mathbf{W}^c_l$ and bias vector $\mathbf{b}^c_l$, respectively. Note that $f_c^{(l)}\left(\hat{\mathbf{h}}^1_{NLS}; \Theta^c_l\right) = f_c^{(l)}\left(\mathbf{W}^c_l\left(f^{(l-1)}\left(\hat{\mathbf{h}}^1_{NLS}; \Theta^c_{l-1}\right)\right) + \mathbf{b}^c_l\right)$, is the output of the l-th layer.

Before online deployment, the ChDNN network parameters, Θ^c, should be optimized through off-line training by deploying a training set and known desired outputs. Optimal Θ^c can be obtained by minimizing a loss function, defined as the MSE between the estimated channel and the actual channel. And it is expressed as

$$L(\Theta^c) = \frac{1}{|\mathcal{H}|}\sum_{\mathbf{h}\in\mathcal{H}} ||\hat{\mathbf{h}}_{DL} - \mathbf{h}||^2, \tag{4.41}$$

where $\mathcal{H}$ indicates set of training channel samples, $|\mathcal{H}|$ is the size of the training set, and $\mathbf{h}$ is the actual channel.

4.3.2 DL-based PN estimation and data detection

This subsection develops DL networks to enhance the PN estimation and data detection performance of Algorithm 5 in Section section 4.2.2.

PN estimation

To improve this, a fully connected DNN, named PnDNN, is developed which has L' layers including one input, $L'-2$ hidden layers, and an output layer in addition to an input layer. The input of PnDNN is the LS estimated PN, Algorithm 5, by using the first stage ChDNN channel estimated $\hat{\mathbf{h}}_{DL}$ in (4.40), which is given by (4.39) as

$$\hat{\mathbf{p}}^{LS-DL} = \left(\mathbf{C}^H_{P,DL}\mathbf{C}_{P,DL}\right)^{-1}\mathbf{C}^H_{P,DL}\mathbf{d}^v_p, \tag{4.42}$$

where $\mathbf{C}_{P,DL} \in \mathbb{C}^{P\times Q}$ matrix corresponds to pilot index set $\mathbf{v}$, which is derived from matrix $\mathbf{C}_{DL} = \mathbf{B}\mathbf{F}_N^H \left(\mathbf{F}_N \hat{\mathbf{h}}_{DL}\right)^{-1} \mathbf{F}_N \text{diag}(\mathbf{F}_N^H \mathbf{y})\boldsymbol{\Upsilon}$. The output of the PnDNN network is the PN estimation, which can be formulated as

$$\hat{\mathbf{p}}^{DL} = f_p(\hat{\mathbf{p}}^{LS-DL}; \Theta^p) = f_p^{(L'-1)}\left(...f_p^{(1)}\left(\hat{\mathbf{p}}^{LS-DL}; \Theta_1^p\right); \Theta_{L'}^p\right), \tag{4.43}$$

where $\Theta^p \triangleq \{\Theta_l^p\}_{l=1}^{L'-1}$ is the set of parameter values for the PnDNN , $f_p^{(l)}$ and Θ_l^p, $l = 1, ..., L'-1$, indicate the nonlinear function and the parameters of the l-th layer including weight matrix $\mathbf{W}_l^p$ and bias vector $\mathbf{b}_l^p$, respectively. Through offline training, known desired outputs and training set are deployed to optimize the parameters of PnDNN Θ^p by minimizing the MSE loss function as

$$L(\Theta^p) = \frac{1}{|\mathcal{P}|}\sum_{\mathbf{p}\in\mathcal{P}} ||\hat{\mathbf{p}}^{DL} - \mathbf{p}||^2, \tag{4.44}$$

where $\mathcal{P}$ indicates set of training PN samples, $|\mathcal{P}|$ is the size of the training set, and $\mathbf{p}$ is the actual PN.

Data detection

By using the ChDNN estimated channel $\hat{\mathbf{h}}_{DL}$ in (4.40), PnDNN estimated PN $\hat{\mathbf{p}}^{DL}$ in (4.43) and Algorithm 5, the complex data symbols can be derived as

$$\hat{\mathbf{d}}^{LS,DL} = \mathbf{C}_{DL}\hat{\mathbf{p}}^{DL}. \tag{4.45}$$

To improve the data detection performance, a CNN-based deep learning image denoising algorithm, named DnCNN [138] is deployed. The adopted DnCNN is a feed-forward residual-learning-based CNN, which has L'' layers, including one input layer, $L''-2$ convolutional layers, and one output layer. The input to the DnCNN network is real and imaginary values of noisy data matrix $\hat{\mathbf{D}}^{2D-LS} \in \mathbb{C}^{B_1\times B_2}$, which is derived by reshaping the LS estimated data symbols $\hat{\mathbf{d}}^{LS,DL} \in \mathbb{C}^{N\times 1}$ into size of $B_1 \times B_2$, where $B_1 B_2 = N$. The output of the DnCNN is the estimated transmitted

complex data symbols, which can be expressed as

$$\hat{\mathbf{D}}^{DL} = f_d\left(\hat{\mathbf{D}}^{2D-LS}; \Theta^d\right), \tag{4.46}$$

where Θ^d is the set of parameter values, including filter matrices and bias vectors for the DnCNN network, and f_d is the DnCNN function. The parameter set of DnCNN is optimized by minimizing the MSE loss function over the training set, which is defined as

$$L(\Theta^d) = \frac{1}{|\mathcal{D}|}\sum_{\mathbf{D}\in\mathcal{D}} ||\hat{\mathbf{D}}^{DL} - \mathbf{D}||^2, \tag{4.47}$$

where $\mathcal{D}$ indicates set of training data symbol samples, $|\mathcal{D}|$ is the size of the training set, and $\mathbf{D}$ is the actual data symbols. Finally, the detected data matrix $\hat{\mathbf{D}}^{DL} \in \mathbb{C}^{B_1\times B_2}$ in (4.46) is reshaped to vector $\hat{\mathbf{d}}^{DL} \in \mathbb{C}^{N\times 1}$.

Note that the trained PnDNN and DnCNN are deployed for all the comb-type symbols in the packet. the proposed DL-based PN compensation algorithm is summarized in Algorithm 6.

Algorithm 6 DL-Based PN Compensation

Offline: Train the DL networks ChDNN, PnDNN and DnCNN by using training sets and actual outputs.
Online: Consider packet of multicarrier symbols
1) Estimate channel $\hat{\mathbf{h}}_{DL}$ in (4.40) using the pilot symbol,
2) stage 2: For remaining comb-type symbols in the packet, first estimate PN $\hat{\mathbf{p}}^{DL}$, by (4.43), and then detect data symbols $\hat{\mathbf{d}}^{DL}$ by (4.46)

4.4 Performance Analysis

This section investigates the impacts of PN on the effective SINR and the sum-rate of GFDM. Moreover, the CRLB is derived to evaluate the MSE performance of Algorithm 1. Finally, the complexity of the proposed algorithms is analyzed.

4.4.1 Effective SINR Derivation

The effective SINR can quantify the impacts of PN on GFDM performance. Thus, this measure is derived for three different cases. These are 1) Ideal compensation for

PN, 2) No compensation of PN, and 3) PN compensation with Algorithm 1. As is customary, data symbols, PN, the channel coefficients, and the additive white Gaussian noise terms are assumed to be independent random variables [8, 33].

Case 1: Ideal Compensation of PN

If both **J** and **H** matrices in (4.4) are perfectly known, the receiver can perform ideal compensation. Although this case is unrealizable, it yields an upper bound of the achievable effective SINR, which serves as a performance benchmark for any PN compensation algorithm. To derive this bound, note that the term **JHx** in (4.4) is the desired component. Thus, based on $\mathbb{E}\{\mathbf{W_n}^H\mathbf{W_n}\} = \sigma_w^2$, the effective SINR can be derived as

$$\text{SINR}_{\text{ideal}} = \frac{\mathbb{E}\{\mathbf{x}^H\mathbf{H}^H\mathbf{J}^H\mathbf{JHx}\}}{\sigma_w^2} = \frac{\sigma_h^2\sigma_d^2}{N\sigma_w^2}\sum_{l_1=0}^{N-1}\left(|\gamma_{l_1'}|^2 + |\gamma_{M+l_1'}|^2\right), \tag{4.48}$$

where $\{\gamma_0, \gamma_1, ..., \gamma_{2M-1}\}$ indicates the frequency response of the prototype filter and $l_1' = (l_1)_M$.

Proof: See Appendix C.2.

As can be observed in the expression (4.48), the derived effective SINR is independent of the 3-dB PN bandwidth β, which makes sense since PN is ideally compensated.

Case 2: No Compensation of PN

This case yields a lower bound of achievable effective SINR, which gauges the PN compensation algorithm's performance improvement. To this end, the effective SINR is derived. To do that, the received signal in (4.4) is written as

$$\mathbf{y} = \mathbf{Hx} + (J[0] - 1)\mathbf{Hx} + (\mathbf{J} - J[0]\mathbf{I}_N)\mathbf{Hx} + \mathbf{W_n}. \tag{4.49}$$

Similar to the derivation in (4.48), by using the signal model (4.49) and after

straightforward mathematical manipulation, the effective SINR is given by

$$\mathrm{SINR}_{\mathrm{No}} = \frac{\mathbb{E}\{\mathbf{x}^H\mathbf{H}^H\mathbf{H}\mathbf{x}\}}{\left(\mathbb{E}\{|J[0]-1|^2\} + \sum_{l=1}^{N-1}\sigma_{J,l}^2\right)\mathbb{E}\{\mathbf{x}^H\mathbf{H}^H\mathbf{H}\mathbf{x}\} + \sigma_w^2} = \frac{\mathrm{SINR}_{\mathrm{ideal}}}{2(1-\mu)\mathrm{SINR}_{\mathrm{ideal}}+1}, \tag{4.50}$$

where $\sigma_{J,l}^2 = \mathbb{E}\{|J[l]|^2\}$ and $\mu = \Re\{\mathbb{E}\{J[0]\}$ (derived in (C.10), Appendix C.3). Note that the constant μ depends on PN bandwidth β. For example, if the bandwidth is zero ($\beta = 0$), μ will also be zero, and the SINR of Case 2 will be equal to that of the ideal case ($\mathrm{SINR}_{\mathrm{No}} = \mathrm{SINR}_{\mathrm{ideal}}$). Thus, depending on the noise bandwidth, the SINR of Case 2 is bounded as

$$\frac{\mathrm{SINR}_{\mathrm{ideal}}}{2\mathrm{SINR}_{\mathrm{ideal}}+1} < \mathrm{SINR}_{\mathrm{No}} \leq \mathrm{SINR}_{\mathrm{ideal}}. \tag{4.51}$$

Case 3: Proposed algorithms

The effective SINR achieved with the proposed PN compensation algorithm is derived. That SINR can be compared with the upper and lower bounds from case 1 and case 2, respectively. Thus, the effectiveness of the proposed algorithm is evaluated. To derive the effective SINR, let $\hat{\mathbf{J}}$ be the estimate of PN matrix $\mathbf{J}$ by the proposed estimation algorithm. Thus, we can rewrite the system model (4.4) as

$$\mathbf{y} = \hat{\mathbf{J}}\mathbf{H}\mathbf{x} + \left(\mathbf{J}-\hat{\mathbf{J}}\right)\mathbf{H}\mathbf{x} + \mathbf{W}_{\mathbf{n}}, \tag{4.52}$$

where $\mathbf{J}$ and $\hat{\mathbf{J}}$ are circulant matrices formed by the elements of $\tilde{\mathbf{j}} = \frac{1}{N}\mathbf{F}_N\tilde{\mathbf{p}}$ and $\tilde{\mathbf{j}}_{\mathbf{app}} = \mathbf{F}_c\bar{\mathbf{p}}$ in (4.12), respectively. Thus, the effective SINR is formulated as

$$\mathrm{SINR}_{\mathrm{prop}} = \frac{\mathbb{E}\{\mathbf{x}^H\mathbf{H}^H\hat{\mathbf{J}}^H\hat{\mathbf{J}}\mathbf{H}\mathbf{x}\}}{\mathbb{E}\{\mathbf{x}^H\mathbf{H}^H\left(\mathbf{J}-\hat{\mathbf{J}}\right)^H\left(\mathbf{J}-\hat{\mathbf{J}}\right)\mathbf{H}\mathbf{x}\} + \sigma_w^2} = \frac{\xi_1\mathrm{SINR}_{\mathrm{ideal}}}{(1+\xi_1-2\Re\{\xi_2\})\,\mathrm{SINR}_{\mathrm{ideal}}+1}, \tag{4.53}$$

where $\xi_1 = \frac{1}{N}\mathbb{T}\{\boldsymbol{\Upsilon}\mathbf{R}_{\bar{\mathbf{p}}}\boldsymbol{\Upsilon}^H\}$ and $\xi_2 = \frac{1}{N}\mathbb{T}\{\mathbf{R}_{\tilde{\mathbf{p}},\bar{\mathbf{p}}}\boldsymbol{\Upsilon}^{\mathbf{H}}\}$.

Proof: See Appendix C.4.

Note that $\mathbf{R}_{\bar{\mathbf{p}}}$ and $\mathbf{R}_{\tilde{\mathbf{p}},\bar{\mathbf{p}}}$ are derived in (4.17) and $\boldsymbol{\Upsilon}_L$ is expressed in (4.14) for linear interpolation. Moreover, the effective SINR (4.53) derived for optimal interpolation

matrix $\boldsymbol{\Upsilon}_O = \mathbf{R}_{\tilde{\mathbf{p}},\bar{\mathbf{p}}}\mathbf{R}_{\bar{\mathbf{p}}}^{-1}$ in (4.16) can be simplified as

$$\mathrm{SINR}_{\mathrm{prop},O} = \frac{\xi \mathrm{SINR}_{\mathrm{ideal}}}{(1-\xi))\,\mathrm{SINR}_{\mathrm{ideal}} + 1}, \tag{4.54}$$

where $\xi = \frac{1}{N}\mathbb{T}\{\mathbf{R}_{\tilde{\mathbf{p}},\bar{\mathbf{p}}}\mathbf{R}_{\bar{\mathbf{p}}}^{-1}\mathbf{R}_{\tilde{\mathbf{p}},\bar{\mathbf{p}}}^{H}\}$. If the length, Q, of interpolation vector equals the number of data symbols N, $\tilde{\mathbf{p}} = \bar{\mathbf{p}}$ and thus $\mathbf{R}_{\tilde{\mathbf{p}},\bar{\mathbf{p}}} = \mathbf{R}_{\bar{\mathbf{p}}}$. In this case, $\xi = 1$. Moreover, $\bar{\mathbf{p}}$ is a subvector of $\tilde{\mathbf{p}}$ and so $\mathbf{R}_{\bar{\mathbf{p}}}$ is a submatrix of $\mathbf{R}_{\tilde{\mathbf{p}},\bar{\mathbf{p}}}$. Therefore, it is true that $\mathbb{T}\{\mathbf{R}_{\tilde{\mathbf{p}},\bar{\mathbf{p}}}\mathbf{R}_{\bar{\mathbf{p}}}^{-1}\mathbf{R}_{\tilde{\mathbf{p}},\bar{\mathbf{p}}}^{H}\} > \mathbb{T}\{\mathbf{R}_{\bar{\mathbf{p}}}\mathbf{R}_{\bar{\mathbf{p}}}^{-1}\mathbf{R}_{\bar{\mathbf{p}}}^{H}\} = Q$. In this case, $\xi > \frac{Q}{N}$. Depending on the range of ξ, $\mathrm{SINR}_{\mathrm{prop},O}$ may be bounded as

$$\frac{\frac{Q}{N}\mathrm{SINR}_{\mathrm{ideal}}}{(1-\frac{Q}{N})\mathrm{SINR}_{\mathrm{ideal}} + 1} < \mathrm{SINR}_{\mathrm{prop},O} \leq \mathrm{SINR}_{\mathrm{ideal}}. \tag{4.55}$$

4.4.2 Cramér-Rao Lower Bound (CRLB)

CRLB is a lower bound on the covariance matrix of any unbiased estimator of unknown parameters [128]. If an unbiased estimator achieves this lower bound, the estimator is said to be efficient. It thus achieves the smallest possible MSE among all unbiased methods. Thus, the CRLB is widely used to evaluate the quality of estimators. In the following, CRLBs are derived for the channel and PN estimates computed during the first block-type pilot of the GFDM packet (Figure 4.2). Moreover, the N pilot symbols are i.i.d. complex random variables with mean zero and the identical variance. They are also independent of data symbols, channel coefficients, PN, and additive noise.

To derive the CRLBs, the received signal (4.6) is expressed as

$$\mathbf{Y} = \mathbf{S}_{\boldsymbol{\Theta}} + \bar{\mathbf{W}}, \tag{4.56}$$

where

$$\mathbf{S}_{\boldsymbol{\Theta}} = \mathbf{J}'_{\mathbf{app}}\mathbf{H}'\mathbf{x}\ ,\ \bar{\mathbf{W}} = \mathbf{W}_{\mathbf{n}} + (\mathbf{J}' - \mathbf{J}'_{\mathbf{app}})\mathbf{H}'\mathbf{x}, \tag{4.57}$$

where $\mathbf{J}'$ and $\mathbf{J}'_{\mathbf{app}}$ are circulant matrices formed by the elements of $\tilde{\mathbf{J}} = \frac{1}{N}\mathbf{F}_N\tilde{\mathbf{c}}$ and $\tilde{\mathbf{J}}_{\mathbf{app}} = \mathbf{F}_c\bar{\mathbf{c}}$ in (4.12). Note that $\mathbf{J}' - \mathbf{J}'_{\mathbf{app}}$ indicates the the approximation error

in (4.10). Similar to Appendix C.4, after straightforward derivations, the covariance matrix of $\bar{\mathbf{W}}$ is equal to $\mathbb{E}\{\bar{\mathbf{W}}\bar{\mathbf{W}}^{\mathbf{H}}\} = \sigma_{\bar{w}}^2\mathbf{I}_N$, where $\sigma_{\bar{w}}^2$ can be derived as

$$\begin{aligned}
\sigma_{\bar{w}}^2 &= \mathbb{E}\{\mathbf{x}^H\mathbf{H}^H\left(\mathbf{J}' - \mathbf{J}'_{\mathbf{app}}\right)^H\left(\mathbf{J}' - \mathbf{J}'_{\mathbf{app}}\right)\mathbf{H}\mathbf{x}\} + \sigma_w^2 \\
&= \mathbb{E}\{||\tilde{\mathbf{J}} - \tilde{\mathbf{J}}_{\mathbf{app}}||^2\}\sigma_h^2\sigma_d^2\sum_{l_1=0}^{N-1}\left(|\gamma_{l'_1}|^2 + |\gamma_{M+l'_1}|^2\right) + \sigma_w^2 \\
&= \frac{\sigma_h^2\sigma_d^2}{N}\sum_{l_1=0}^{N-1}\left(|\gamma_{l'_1}|^2 + |\gamma_{M+l'_1}|^2\right)\Bigg(1 + \frac{1}{N}\mathbb{T}\{\boldsymbol{\Upsilon}\mathbf{R}_{\bar{\mathbf{p}}}\boldsymbol{\Upsilon}^H\} \\
&- 2\Re\Big\{\frac{1}{N}\mathbb{T}\{\mathbf{R}_{\tilde{\mathbf{p}},\bar{\mathbf{p}}}\boldsymbol{\Upsilon}^{\mathbf{H}}\}\Big\}\Bigg) + \sigma_w^2,
\end{aligned} \tag{4.58}$$

Since $\mathbf{R}_{\bar{\mathbf{p}}}$ and $\mathbf{R}_{\tilde{\mathbf{p}},\bar{\mathbf{p}}}$ in (4.17) depend on PN bandwidth β, $\sigma_{\bar{w}}^2$ is a function of β. According to the CRLB, for any unbiased estimator $\hat{\boldsymbol{\Theta}}$ of $\boldsymbol{\Theta}$, the covariance matrix, $\mathbf{R}_{\hat{\boldsymbol{\Theta}}} = \mathbb{E}\{(\hat{\boldsymbol{\Theta}} - \boldsymbol{\Theta})(\hat{\boldsymbol{\Theta}} - \boldsymbol{\Theta})^H\}$, should satisfy

$$\mathbf{R}_{\hat{\boldsymbol{\Theta}}} \geq \boldsymbol{\Omega}_{\hat{\boldsymbol{\Theta}}}^{-1}, \tag{4.59}$$

where $\boldsymbol{\Omega}_{\hat{\boldsymbol{\Theta}}} \in \mathbb{C}^{2(L_{ch}+Q-1)\times 2(L_{ch}+Q-1)}$ is the Fisher information matrix, which is given by

$$\boldsymbol{\Omega}_{\hat{\boldsymbol{\Theta}}} = \frac{2}{\sigma_{\bar{w}}^2}\Re\Bigg\{\left(\frac{\partial\mathbf{S}_{\boldsymbol{\Theta}}}{\partial\boldsymbol{\Theta}}\right)^T\left(\frac{\partial\mathbf{S}_{\boldsymbol{\Theta}}}{\partial\boldsymbol{\Theta}}\right)^*\Bigg\}. \tag{4.60}$$

Note that (4.59) implies that $\mathbf{R}_{\hat{\boldsymbol{\Theta}}} - \boldsymbol{\Omega}_{\hat{\boldsymbol{\Theta}}}^{-1}$ is positive semidefinite. However, $\partial\mathbf{S}_{\boldsymbol{\Theta}}/\partial\boldsymbol{\Theta}$ is derived in (C.14) element by element (see Appendix C.5). Therefore, by substituting (C.14) in Fisher information matrix (4.60),

$$\begin{aligned}
&\mathbb{E}\{|h'[n_1] - \hat{h}'[n_1]|^2\} \geq \boldsymbol{\Omega}_{\hat{\boldsymbol{\Theta}}}^{-1}[n_1+1, n_1+1] \\
&+ \boldsymbol{\Omega}_{\hat{\boldsymbol{\Theta}}}^{-1}[n_1+L_{ch}+1, n_1+L_{ch}+1] \quad n_1 = 0, 1, ..., L_{ch}.
\end{aligned} \tag{4.61}$$

$$\begin{aligned}
\mathbb{E}\{|c'[n_2] - \hat{c}'[n_2]|^2\} &\geq \boldsymbol{\Omega}_{\hat{\boldsymbol{\Theta}}}^{-1}[n_2+2L_{ch}, n_2+2L_{ch}] \\
&+ \boldsymbol{\Omega}_{\hat{\boldsymbol{\Theta}}}^{-1}[n_2+2L_{ch}+Q-1, n_2+2L_{ch}+Q-1] \\
&n_2 = 1, ..., Q-1.
\end{aligned} \tag{4.62}$$

4.4.3 Computational Complexity Analysis

This chapter analyzes the number of real-valued multiplications required for joint channel and PN estimation in Algorithm 3 and joint data symbol and PN compensation in Algorithm 4.

Table 4.1: Complexity growth of Algorithm 1

Step number	Multiplications
Step 4	$\mathcal{O}(N^3 + 16N^2(L_{ch} + Q) + 8N(L_{ch} + Q)^2)$
Step 5	0

In Algorithm 3, the iteration process contains Step 4 and Step 5. In Step 4, unknown matrix $\boldsymbol{\Delta\Theta}$ is optimally estimated via (4.30). This operation requires three matrix multiplications and one matrix inverse. Moreover, this step also constructs Γ matrix based on the expressions derived in Appendix A. Note that Step 5 avoids multiplications. Due to these reasons, the complexity growth is summarized in Table 4.1. Since the maximum value of Q is equal to N and also the channel length, L_{ch}, and the number of time-slots M is relatively small, the computational complexity of the proposed NLS joint channel and PN estimator is roughly in the order of K^3.

Table 4.2: Complexity growth of Algorithm 2

Step number	Multiplications
Step 4	$\mathcal{O}(3N^3 + N^2Q + NQ)$
Step 5	$\mathcal{O}\big(N^3 + 2N^2Q\big)$

On the other hand, the iteration process of Algorithm 4 contains steps four and five. In the former one, the optimal data symbol is derived by (4.32). This operation requires six matrix multiplications and two matrix inverses. Moreover, in the latter one, PN estimation is obtained by (4.33), which requires six matrix multiplications and one matrix inverse. The complexity growth of the steps in each iteration is

Table 4.3: Simulation parameters

Parameter	Value
Number of subcarriers (K)	32
Number of time slots (M)	5
Modulation	$16-$QAM
Prototype Filter	Root Raised-Cosine
Roll-off factor (r_f)	0.1
Sampling time (T_s) [8]	100 ns
Channel length (L_{ch})	26
Channel model [139]	ITU outdoor channel A
Power delay profile [139]	0 dB, -1 dB, -9 dB, -10 dB, -15 dB and -20 dB for delays of 0, 3, 7, 11, 17 and 25 samples
CP length (L_{cp})	26
Length of interpolation vector	$Q_1 = 10$; $Q_2 = 32$
3-dB PN bandwidth	$\beta_1 = 100$ Hz; $\beta_2 = 1$ kHz
SNR values (dB)	SNR_1=20; SNR_2=30; SNR_3=40
GFDM packet length ($N_b + 1$)	6
Pilot subcarrier spacing Δ_k	4
Maximum iterations, $I_{\max}$	3

summarized in Table 4.2. Similar to Algorithm 3, since the maximum value of Q is equal to N and the number of time-slots M is relatively small, the computational complexity of the estimator is roughly in the order of K^3.

Finally, the proposed closed-form algorithm in Section 4.2.2, Algorithm 5, requires nine matrix multiplications and two matrix inversions, according to (4.37) and (4.39). The complexity of Algorithm 5 is $\mathcal{O}(N^3 + 5N^2Q + NQ^2)$. Similar to Algorithm 4, since the complexity is in order of N^3, $N = MK$, and the number of time-slots M is relatively small, the computational complexity of this estimator is roughly in the order of K^3. Note that this complexity of Algorithm 5 is less than that of Algorithm 4 because complexity per iteration is higher in the latter.

4.5 Simulation Results

This section measures the impacts of PN. First, the derived sum-rate and effective SINR expressions are verified via simulation results. Next, the MSE of the joint

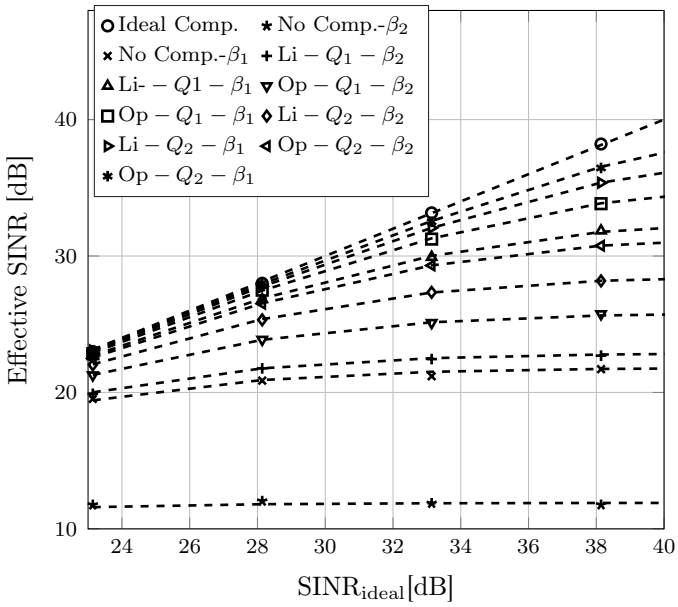

Figure 4.4: Effective SINRs versus SNR for Case 1 (legend "Ideal comp."), Case 2 (legend "No comp."), and Case 3, legends "Li" and "Op" represent linear and optimal interpolation.

channel and PN estimator (Algorithm 3) and the CRLB are evaluated and compared. Finally, the BER of the joint data and PN estimator (Algorithm 4) is examined.

The simulation parameters are listed in Table 4.3. Each simulation result is averaged over 1000 independent trials. Pilot symbols are randomly generated complex 16-QAM (quadrature amplitude modulation) symbols. Optimal pilot design for for the considered system is an important and interesting topic and is left as future work.

All the DL networks are implemented with Keras and Tensorflow using a GPU. The ChDNN network contains three hidden layers with 128, 64, and 32 neurons per layer. Moreover, The PnDNN network contains two hidden layers with 128 and 64 neurons per layer. In both ChDNN and PnDNN, each hidden layer is followed by the ReLU activation function. In addition, DnCNN is composed of 20 convolutional layers(The first one deploys 64 filters of size $3 \times 3 \times 1$ followed by a ReLU; Each of the succeeding 18 layers deploys 64 filters of size $3 \times 3 \times 64$ followed by batch-normalization and ReLU; the last layer deploys one $3 \times 3 \times 64$ filter) [138]. Moreover, in DnCNN, the considering reformatting size for the noisy data is 32×5 ($B_1 \times B_2$).

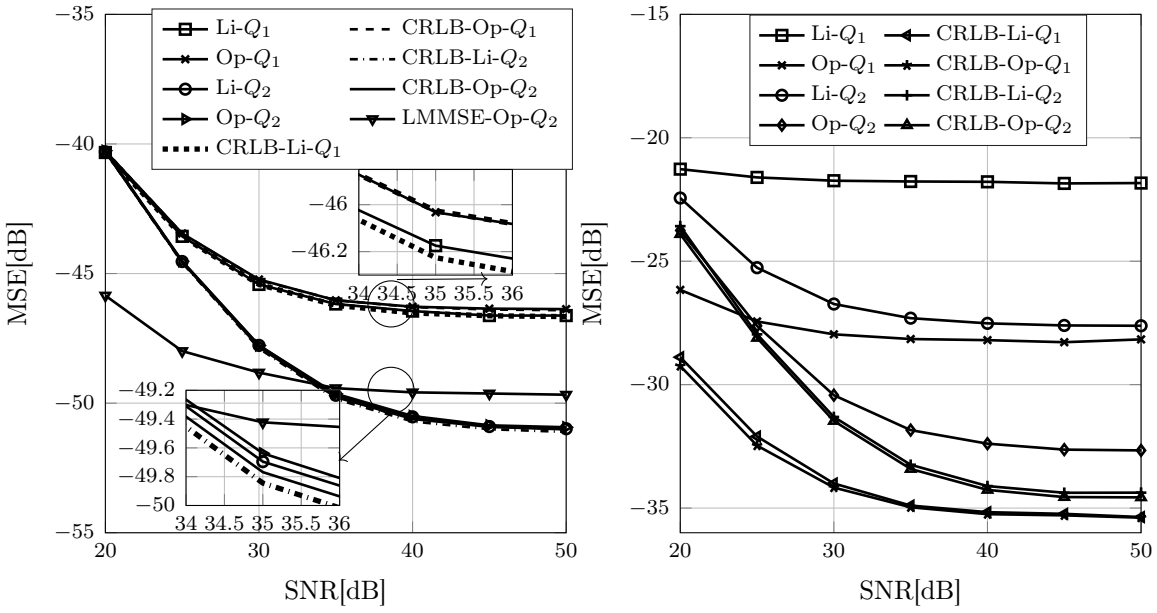

(a) Estimated Channel

(b) Estimated PN

Figure 4.5: MSE performance of Algorithm 3 with linear ("Li") and optimal ("Op") interpolations.

For all networks, an adaptive moment estimation (ADAM) optimizer is exploited for minimizing the loss functions and finding the optimal parameters. Moreover, the training rate is set to 0.001, the batch size is 128, and the number of iterations is at most 500. Similar to the training approach in [109], the networks are trained with a group of SNR values ({10 dB, 20 dB, 30 dB}), 90000 data samples (30000 for each training SNR). Moreover, the validation set consists of 9000 data samples, and the testing set consists of 24000 data samples (4000 for each testing SNR).

4.5.1 Effective SINR Performance

In Figure 4.4, the derived SINRs for Case 1 (4.48), Case 2 (4.50), and Case 3 (4.53) versus $\text{SINR}_{\text{ideal}}$ in (4.48) are plotted. For these three cases, both linear and optimal interpolation are considered. Moreover, the PN bandwidth is set as 100 Hz or 1 kHz. Dashed lines show the theoretical results. The observations can be summarized as follows:

- The simulation results fully match with the derived effective SINRs in (4.48),

(4.50), (4.53).

- When the PN bandwidth increases, the effective SINRs of the last two cases decrease, e.g., without PN compensation, and when the PN increases from 100 Hz to 1 kHz at an SNR of 30 dB, the SINR decreases by about 10 dB. In other words, when PN increases, the power of interference terms increases, reducing the SINR.

- Promisingly, the proposed algorithm significantly improves effective SINR. Moreover, optimal interpolation achieves higher effective SINR than linear interpolation. Furthermore, a larger interpolation vector Q increases the effective SINR in both cases, e.g., optimal interpolation with Q_2 achieves an SINR more or less that of ideal case for 100-Hz PN.

4.5.2 Channel Estimation

To examine the performance of Algorithm 3, the MSE of channel and PN estimates in Figure 4.5a and Figure 4.5b are plotted, respectively. Both linear and optimal interpolation are considered. Moreover, CRLB's of these estimations confirms the accuracy of Algorithm 3. Note that the number of iterations $I_{\max}$ is set at three, and PN bandwidth is 1 kHz.

The estimators developed thus far do not use statistics of the signals and channel gains. However, to compare the performance of Algorithm 1 with other estimators, an iterative linear minimum mean square error (LMMSE) estimator is developed. Unlike Algorithm 1, this estimator requires the channel correlation matrix, PN correlation matrix and the noise variance. In (4.18), at the i-th iteration, PN $\hat{\mathbf{c}}_{i-1}$ is assumed given. Therefore, the LMMSE channel estimate is computed by

$$\hat{\mathbf{h}}_i = \sigma_h^2 \mathbf{F}_h^H \mathbf{X}^H \mathbf{J}_i'^H \left(\sigma_w^2 \mathbf{I}_N + \sigma_h^2 \mathbf{J}'_{i-1} \mathbf{X} \mathbf{F}_h \mathbf{F}_h^H \mathbf{X}^H \mathbf{J}'^H_{i-1} \right)^{-1} \mathbf{y}, \tag{4.63}$$

where $\mathbf{J}'_{i-1}$ is PN circulant matrix formed by elements of $\mathbf{F}_c \hat{\mathbf{c}}_{i-1}$. By using estimate

$\hat{\mathbf{h}}_i$, LMMSE PN estimate is computed as

$$\hat{\mathbf{c}}_i = \mathbf{R}_{\bar{\mathbf{p}}}\mathbf{F}_c^H \mathbf{T'}_i^H \left(\sigma_w^2 \mathbf{I}_N + \mathbf{T'}_i \mathbf{F}_c \mathbf{R}_{\bar{\mathbf{p}}} \mathbf{F}_c^H \mathbf{T'}_i^H\right)^{-1} \mathbf{y}, \tag{4.64}$$

where $\mathbf{T}'_i$ is the circulant matrix formed by elements of $\hat{\mathbf{H}}'_i\mathbf{x}$, $\hat{\mathbf{H}}'_i = \text{diag}(\mathbf{F}_h\hat{\mathbf{h}}_i)$, and $\mathbf{R}_{\bar{\mathbf{p}}}$ is PN correlation matrix in (4.17). Similar to Algorithm 1, the LMMSE estimator recursively works until the objective function stops improving or until it reaches the maximum number of iterations. In Figure 4.5a, for LMMSE, optimal interpolation with $Q = 32$ is considered and PN bandwidth is 1 kHz.

The observations of Figure 4.5 can be summarized as follows:

- The MSE of the channel estimates closely match the CRLB (Figure 4.5a). This match confirms that Algorithm 1 is an efficient unbiased estimator and its channel estimates can be reliably deployed for data detection.

- In addition, in low SNRs, the biased LMMSE estimator obtains lower MSE than the Algorithm 1. However, Algorithm 1 outperforms the LMMSE estimator in high SNRs.

- In Figure 4.5b, a gap exists between the MSE of PN estimates and the CRLB in all cases, which is due to the use of interpolation. However, this gap decreases when the interpolation size increases. Furthermore, the gap can be reduced by choosing optimal interpolation rather than linear interpolation.

- Promisingly, the MSE of both channel and PN estimates decreases for larger interpolation vectors, Q. For example, when the optimal interpolation is used, the difference between the MSE of channel estimates for Q_1 and Q_2 at an SNR of 30 dB is 3 dB. However, larger Q increases the computational complexity. Therefore, complexity and MSE performance exhibit a trade-off.

Moreover, to verify the impacts of PN on the performance of the proposed NLS estimator in Algorithm 3, MSE's of estimated channel and PN versus PN bandwidth

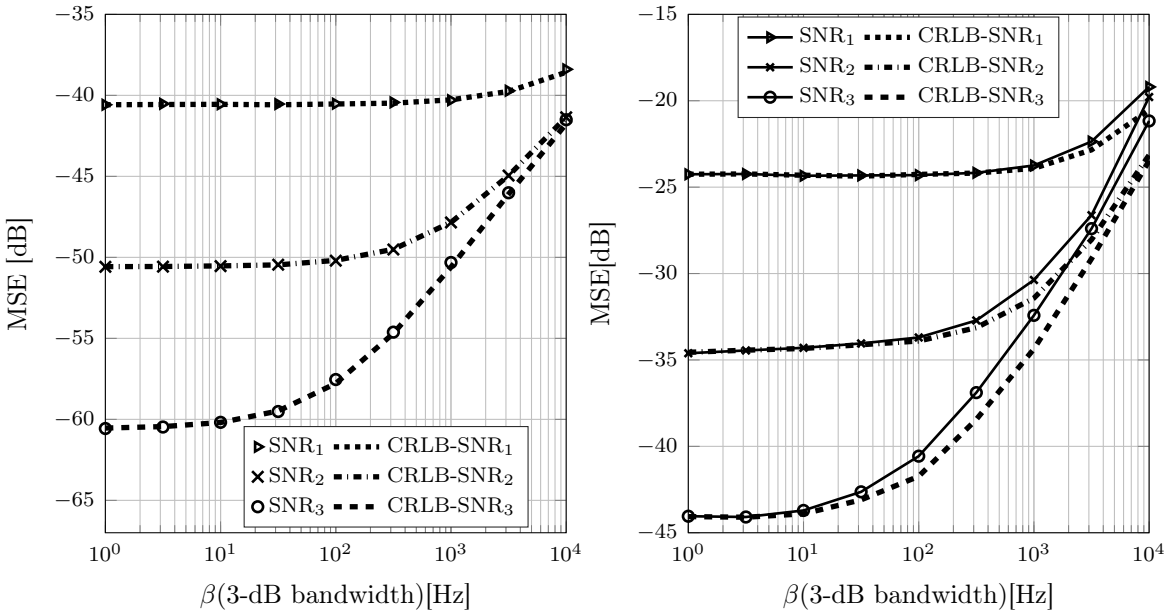

(a) Estimated Channel

(b) Estimated PN

Figure 4.6: MSE of channel and PN estimates as a function of the PN bandwidth.

β are illustrated in Figure 4.6a and Figure 4.6b, respectively. Optimal interpolation ($Q = 32$) and also SNR values 20, 30 and 40 dB are considered. Furthermore, the number of iterations $I_{\max}$ is set at three. The observations from Figure 4.6 are summarized as follows:

- From Figure 4.6a, close match between the MSE of channel estimates and CRLB is observed. This match shows that the proposed algorithm is able to compensates for the effect of different PN bandwidths.

- From Figure 4.6b, the MSE of the PN estimate and CRLB are fairly close. However, a gap exists, which is due to the interpolation errors of PN. This points to the trade off between the MSE performance and computational complexity.

- Unsurprisingly, when PN bandwidth increases, the MSE's of both channel and PN estimation increase. Moreover, for the large PN regime, the MSE becomes more or less independent of the SNR, and the power of interference terms (due to PN) increases and dominates the additive white noise terms.

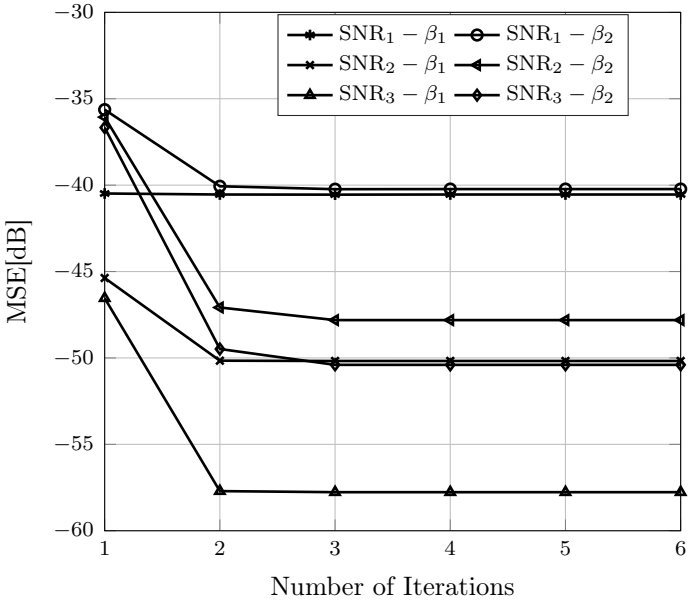

Figure 4.7: MSE of Algorithm 3 as a function of the number of iterations.

To gauge the convergence rate of Algorithm 3, in Figure 4.7, the MSE of channel estimates (Algorithm 1) is plotted versus the number of iterations. The same SNR values as per Figure 4.6 and 100 Hz and 1 kHz PN bandwidths, and optimal interpolation ($Q = 32$) are considered. For the 100-Hz PN, the algorithm converges after two iterations for all SNRs, while just three iterations are needed for the 1 kHz PN in high SNRs. These observations suggest that the proposed estimator is fast and requires just three iterations to ensure convergence.

4.5.3 Data Detection

Thus far, it is shown that the proposed joint NLS channel and PN estimator obtains satisfactory channel estimates, which can then be deployed for data detection. This is done in Algorithm 4. It uses comb-type GFDM symbols with pilot subcarrier spacing $\Delta_k = 4$. This section considers Case 1, with perfect channel and PN knowledge, (legend Perfect Ch. & PN), Case 2, with perfect knowledge of channel but no information about the PN, (legend No comp.), Case 3 – Algorithm 4 in Section 4.2.2 (legend Algorithm 4), and Case 3 – closed-form data detection algorithm in Section

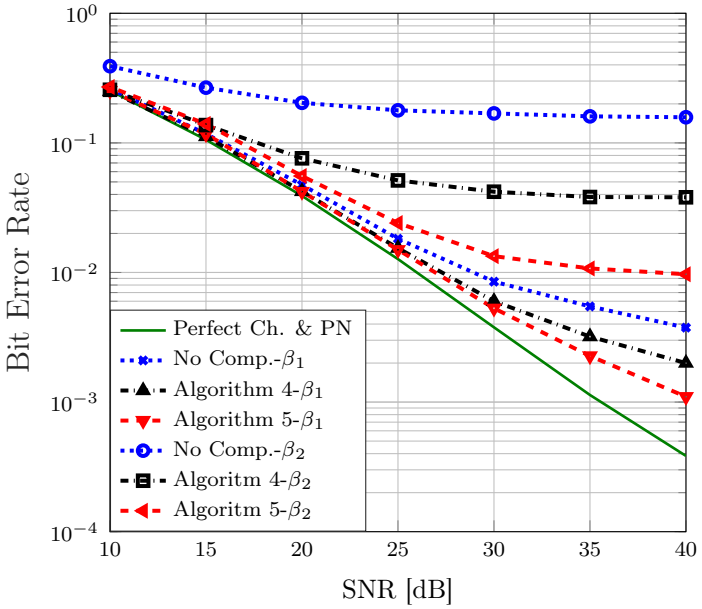

Figure 4.8: BER versus SNR for Case 1, Case 2 and Case 3 – Algorithm 4 and Case 3 – Algorithm 5 .

4.2.2 (legend Algorithm 5). Note that Case 1 yields the BER lower bound of BER and thus serves as a performance benchmark for the proposed algorithms. On the other hand, Case 2 yields the BER upper bound and is utilized to evaluate the improvement of the proposed algorithms.

Moreover, $I_{\max}$ in Algorithm 4 is set at three and also PN bandwidths values 100 Hz and 1 kHz and optimal interpolation are considered. Furthermore, since the ZF receiver outperforms MF one in the presence of PN, it is examined exclusively in this figure. Note that the ZF receiver can cancel more interference terms than the MF, which boosts the desired signal and hence improves the BER. The observations of Figure 4.8 can be summarized as follows:

- When the PN bandwidth increases, the BER increases in all cases. Undoubtedly, the increased PN degrades the MSE's of channel and PN estimates (Figure 4.6). Fortunately, this degradation is more or less completely eliminated by both Algorithm 4 and Algorithm 5. For example, for 100 Hz PN, Algorithm 5 achieves a BER close to that of the perfect channel and PN estimation scenario.

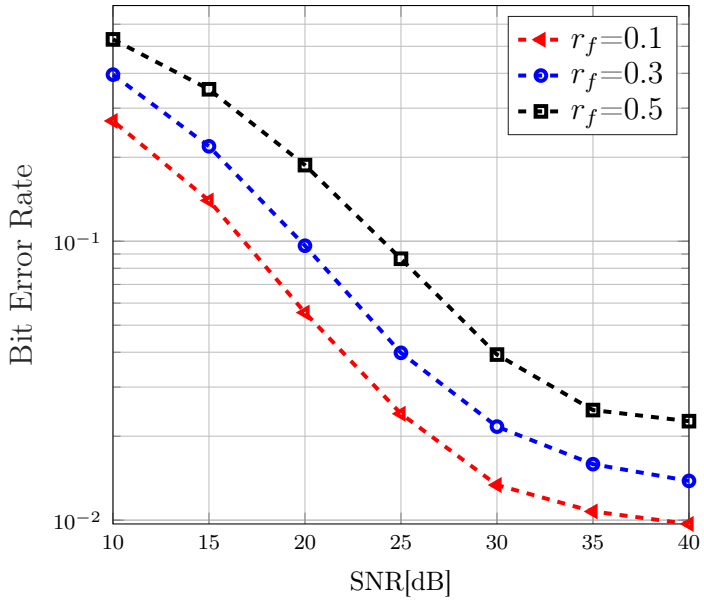

Figure 4.9: BER versus SNR for Algorithm 5 with three roll-off factors.

- Promisingly, Algorithm 4 and Algorithm 5 compensate the PN effects and decrease the BER. In comparison with Case 1 and Case 2, they significantly improve the BER; e.g., for extreme PN (1 kHz) and additive noise (SNR of 30 dB), Algorithm 4 reduces the BER by 400% (compared to the no compensation case).

- Furthermore, Algorithm 5 outperforms Algorithm 4 and significantly decreases the BER, e.g. for 1 kHz PN and additive noise (SNR of 30 dB), Algorithm 5 reduces the BER by 300% in comparison with Algorithm 4. Besides, Algorithm 5 is closed-form; thus, its computational complexity is less than Algorithm 4, which requires more iterations for convergence.

- In Algorithm 5, the GFDM demodulation matrix $\mathbf{B}$ is a part of the data detector in (4.37). For the considered ZF receiver, the GFDM demodulator contains filter parameters. In contrast, Algorithm 4 is independent of the GFDM demodulator, since first GFDM symbols are detected and then are passed through the demodulator. Therefore, the performance gap between two algorithms is because of including GFDM demodulation in data detection in Algorithm 5 and

handling the GFDM interference together with PN.

Finally, to show the impacts of non-orthogonality of GFDM on the system performance, in Figure 4.9, the BER versus SNR is plotted with three values of roll-off factor r_f for GFDM prototype filter $g[n]$. Algorithm 5, PN bandwidth $\beta = 1$ kHz and other parameters as in Figure 4.8 are considered. Clearly, the increasing roll-off factor degrades the BER. According to (4.37) in Algorithm 5, data detection depends on the GFDM modulator and demodulator matrices, which in turn are constructed based on the prototype filter. Thus, when the filter roll-off factor increases, the degree of non-orthogonality increases, which results in more interference terms and degrades the performance of data detection.

4.5.4 DL-based PN Compensation

In Figure 4.10, the accuracy of channel estimation for the proposed DL-based channel estimator (ChDNN in Section 4.3.1) is compared with that of conventional estimators, iterative linear LS [89], iterative NLS in Algorithm 3, iterative LMMSE in (4.63), and perfect LS and perfect LMMSE with perfect knowledge of PN. The interpolation factor is equal to $Q_2 = 32$, and the maximum number of iterations for conventional iterative estimators is set to ten. Furthermore, PN bandwidth is set to $\beta_2 = 1$ kHz which indicates a very strong PN [91]. In fig. 4.10, the proposed DL Algorithm 1 significantly reduces the MSE and outperforms the conventional estimators. Furthermore, it outperforms the perfect LS estimator in low SNRs ($<$30 dB). Besides, it replaces the iterative procedure of the conventional estimators. Although it does not require second-order statistics of channel and PN, it achieves lower MSE than the iterative LMMSE estimator, since the neural network has learning channel statistics implicitly.

In Figure 4.12, the data detection performance of proposed DL Algorithm 6 is compared in terms of BER with that of the conventional estimators, iterative LS in Algorithm 4, linear LS in Algorithm 5, and perfect LS and perfect LMMSE. Perfect

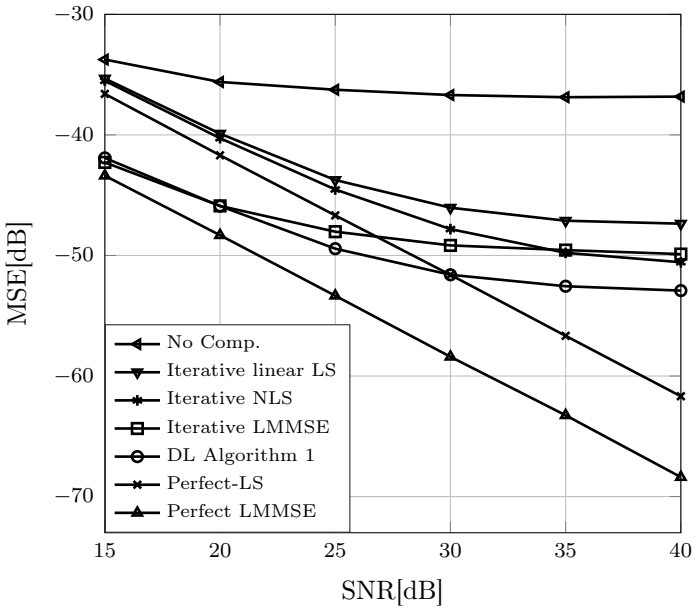

Figure 4.10: MSE of channel estimations versus SNR for DL Algorithm 6.

refers to genie-aided ideal compensation of PN and ideal knowledge of channel. In this figure, comb-type symbols mean one pilot subcarrier out of eight subcarriers. Thus, four subcarriers out of a total of 32 (12.5%) are pilots. The interpolation factor is equal to $Q_1 = 5$, the maximum number of iterations for the conventional iterative estimators is set to ten, and PN bandwidth is $\beta_1 = 100$ Hz and $\beta_2 = 1$ kHz. From fig. 4.12, proposed DL algorithm 6 reduces the BER and outperforms the conventional estimators. Moreover, for lower PN bandwidth β_1, it nearly eliminates PN impact and outperforms estimators that use perfect additional information. For higher PN bandwidth β_2 (indicating extreme levels of PN), the BER of all estimators increases because of the strong impact of PN. However, the proposed DL Algorithm 6 significantly reduces the BER, specifically in low SNRs.

Finally, to demonstrate the learning convergence, the training loss function of DnCNN (4.47) is plotted versus the number of iterations in Figure 4.13 for OFDM with PN bandwidth values β_1 and β_2, respectively.

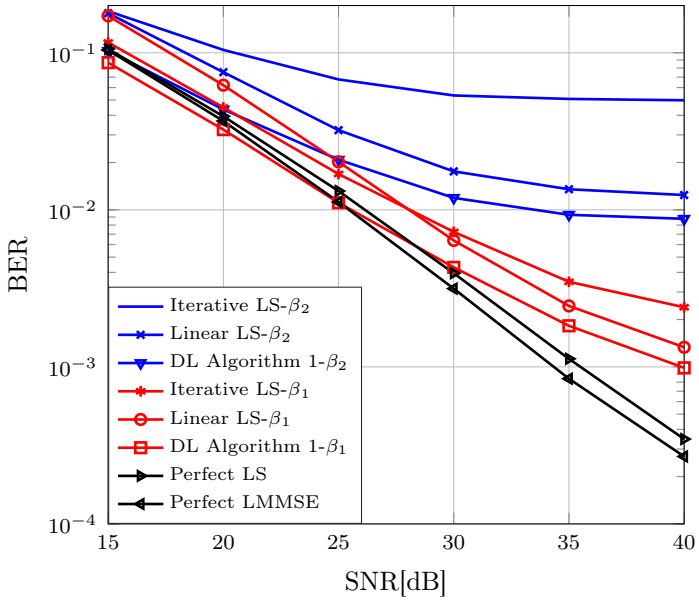

Figure 4.11: GFDM

Figure 4.12: BER versus SNR for for DL Algorithm 6.

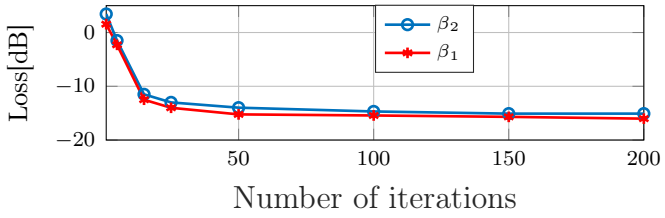

Figure 4.13: Training loss function (4.47) versus number of iterations.

4.6 Conclusion

This chapter investigated PN compensation for GFDM systems. First, it proposed an estimator for joint channel and PN estimation, which utilizes the NLS approach and a block pilot GFDM symbol. Second, it also offered an iterative LS algorithm for data detection and PN compensation. Furthermore, to reduce computational complexity, a closed-form LS algorithm for data detection was developed. The complexity of all algorithms is reduced by deploying interpolation techniques and relating channel frequency and time responses.

Moreover, the impacts of PN on GFDM are quantified via the analysis of the SINR. The proposed algorithms improve the effective SINR. Additionally, the CRLBs

for the channel and PN estimates were derived; and, this chapter found that their MSE reaches the CRLB. Finally, the BER with the joint data detection and PN compensation algorithms was evaluated. Overall, it is possible to fully compensate for the impacts of PN and thus reduce GFDM receivers' sensitivity to RF impairments.

Moreover, this chapter proposed a DL-based algorithm for PN compensation. The major advantages of it are eliminating the need for extraneous statistical information and avoiding the iterations of conventional estimators. For channel estimation part of the algorithm, his chapter developed a fully connected DNN, named ChDNN. ChDNN jointly performs channel estimation and PN compensation, significantly reduces the MSE of channel estimates, and outperforms conventional estimators. For data detection part of the algorithm, his chapter developed a fully connected DNN, named PnDNN, for PN estimation and deploy DnCNN for data detection by treating the noisy data as a 2D image. The simulation results show that the proposed DL algorithm outperforms the conventional estimators and achieves a 6 dB reduction in the MSE of channel estimates and 45% improvement in BER.

This work has the following limitations. First, the pilot design problem has not been addressed in this work, and thus optimal pilot designs that use the MSE or a similar measure can be developed. Second, this work only considered PN impairment while other RF impairments such as CFO and IQ imbalance can be incorporated with the proposed algorithms, and further afield, they may also be compensated for full-duplex transceivers.

Chapter 5

RF impairment compensation for MIMO-GFDM full-duplex systems

As shown before, RF impairments introduce interference terms and are able to degrade the performance of the non-orthogonal systems. In full-duplex wireless, they can degrade the performance of the SI cancellation techniques and in GFDM systems, they result in higher ICI and ISI terms. Chapter 4 investigates PN compensation for GFDM systems in both channel estimation and data detection. However, impacts of RF impairments on the GFDM full-duplex systems are more critical. Moreover, the considered GFDM system in Chapter 4 has single antenna, while this chapter aims to integrate MIMO with the GFDM full-duplex system. Since full-duplex wireless enables simultaneous transmission, and reception and MIMO transmits multiple streams over the same frequency band [9], integration of full-duplex and MIMO achieves SE.

Therefore, this chapter investigates joint channel, PN, and IQ imbalance estimation in MIMO-GFDM full-duplex systems. A pilot-aided LMMSE-based algorithm for joint estimation of the SI channels, intended channels, PN, and IQ imbalance is proposed. Equivalent SI and intended channels is derived by combining the channels and the impairments' parameters, which are time varying since PN rapidly varies from one symbol to another. A BEM for approximating the time-varying equivalent channels is developed by using a set of elementary functions and time-invariant coefficients. To estimate these BEM coefficients, an LMMSE estimator is proposed.

Moreover, researchers are massively interested in DL networks to improve the performance of channel estimation [103, 106, 130, 140]. Inspired by this trend, we will develop a DL network to enhance the performance of the proposed LMMSE estimator in this article. The input of the trained DL network is the estimated BEM coefficients (the output of the LMMSE estimator) and the output is the final estimated BEM coefficients. We train the DL network offline with simulation data, including LMMSE BEM estimated coefficients as the input and identical BEM coefficients as the output. Through extensive simulation, we demonstrate that the proposed DL-LMMSE algorithm (combination of the LMMSE estimator and the DL network) improves the mean-squared error (MSE) performance and outperforms the conventional estimators.

5.1 System Model

fig. 4.3 shows the considered multicarrier MIMO full-duplex system. Each full-duplex node has $N_t \geq 1$ transmit antennas and $N_r \geq 1$ receive antennas. One of the practical applications of this system is in the wireless back-haul links for connecting multiple macro-cell MIMO BCs [141]. Each full-duplex node partially suppresses SI in the RF stage by well-known techniques [9]. Therefore, the baseband signal contains residual SI. Thus, residual SI compensation requires accurate SI channel estimation.

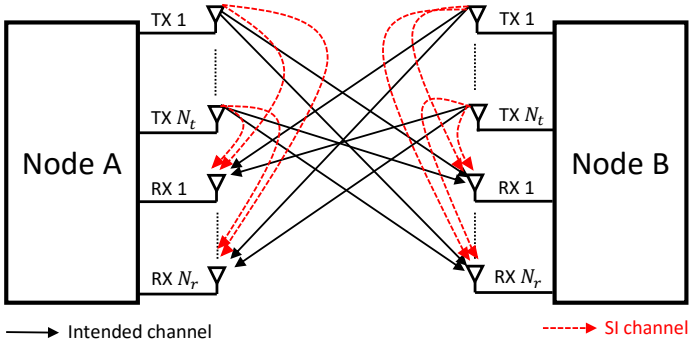

Figure 5.1: Two-way MIMO full-duplex system.

5.1.1 Signal Model

Without loss of generality, this chapter takes Node A as an example to analyze the signal model. With frequency-selective multipath channels, PNs, and IQ imbalances, the received samples of the m-th multicarrier symbol at the r-th receive antenna of Node A can be formulated as

$$\begin{aligned} y_{r,m}[n] = &\left(\sum_{t=1}^{N_t} \sum_{l=0}^{L-1} h_{t,r,m}^{d,I}[n,l] x_{t,m}^{d}[n-l] + h_{t,r,m}^{d,Q}[n,l] \right. \\ &\left. x_{t,m}^{d^*}[n-l] \right) + \left(\sum_{t=1}^{N_t} \sum_{l=0}^{L-1} h_{t,r,m}^{SI,I}[n,l] x_{t,m}^{SI}[n-l] + h_{t,r,m}^{SI,Q}[n,l] \right. \\ &\left. x_{t,m}^{SI^*}[n-l] \right) + w_{r,m}[n], \ n = 0, 1, ..., N-1, \end{aligned} \tag{5.1}$$

where $x_{t,m}^{d}[n]$ indicates the m-th intended multicarrier signal transmitted from t-th transmit antenna of Node B to Node A, and $x_{t,m}^{SI}[n]$ indicates the m-th SI multicarrier signal leaked from the t-th transmit antenna of Node A to its receiver. In addition, $w_{r,m}[n]$ is the AWGN term with a variance of σ_n^2. Moreover, the equivalent intended channels and residual SI channels are given by

$$\begin{aligned} h_{t,r,m}^{d,I}[n,l] &= h_{t,r,m}^{l} g_1^T g_1^R e^{j\phi_{t,r,m}[n,l]} + h_{t,r,m}^{l^*} g_2^{T^*} g_2^R e^{-j\phi_{t,r,m}[n,l]} \\ h_{t,r,m}^{d,Q}[n,l] &= h_{t,r,m}^{l} g_2^T g_1^R e^{j\phi_{t,r,m}[n,l]} + h_{t,r,m}^{l^*} g_1^{T^*} g_2^R e^{-j\phi_{t,r,m}[n,l]} \\ h_{t,r,m}^{SI,I}[n,l] &= \mathring{h}_{t,r,m}^{l} g_1^T g_1^R e^{j\mathring{\phi}_{t,r,m}[n,l]} + \mathring{h}_{t,r,m}^{l^*} g_2^{T^*} g_2^R e^{-j\mathring{\phi}_{t,r,m}[n,l]} \\ h_{t,r,m}^{SI,Q}[n,l] &= \mathring{h}_{t,r,m}^{l} g_2^T g_1^R e^{j\mathring{\phi}_{t,r,m}[n,l]} + \mathring{h}_{t,r,m}^{l^*} g_1^{T^*} g_2^R e^{-j\mathring{\phi}_{t,r,m}[n,l]}, \end{aligned} \tag{5.2}$$

where $h_{t,r,m}^{l}$ indicates the l-th tap gain of the intended channel between the t-th transmit antenna of Node B and the r-th receive antenna of Node A, and $\mathring{h}_{t,r,m}^{l}$ indicates the l-th tap gain of the residual SI channel between the t-th transmit antenna of Node A and its r-th receive antenna. Note that all the channels are modeled as wide-sense stationary uncorrelated scattering processes, $\mathbb{E}\{h_{t,r,m}^{l} h_{t,r,m}^{l^*}\} = \sigma_{d,l}^2$ and $\mathbb{E}\{\mathring{h}_{t,r,m}^{l} \mathring{h}_{t,r,m}^{l^*}\} = \sigma_{SI,l}^2$. Moreover, g_1^i and g_2^i, $i = \{T, R\}$, indicate IQ mixer responses for the direct and image signals, respectively. Furthermore, $\phi_{t,r,m}[n,l] = \phi_{t,m}[n-l] - \mathring{\phi}_{r,m}[n]$ and $\mathring{\phi}_{t,r,m}[n,l] = \mathring{\phi}_{t,m}[n-l] - \mathring{\phi}_{r,m}[n]$ are equivalent PNs of the m-th

symbol, where $\phi_{t,m}[n]$ indicates random PN of the t-th transmitter of Node B, and $\mathring{\phi}_{i,m}[n]$, $i = \{t, r\}$, shows random PN of the i-th transmitter or receiver of Node A. The standard free-running oscillator with a Brownian motion process has been used for modeling the PNs.

5.1.2 BEM

BEM is commonly deployed to approximate a function with a decomposition over a set of elementary functions [142]. The equivalent channels in (5.1) by using BEMs can be approximated by

$$\begin{aligned} h_{t,r,m}^{d,I}[n,l] &= \sum_{q=1}^{Q} c_{q,t,r}^{d,I}[l] b_{q,m}[n] \\ h_{t,r,m}^{d,Q}[n,l] &= \sum_{q=1}^{Q} c_{q,t,r}^{d,Q}[l] b_{q,m}[n] \\ h_{t,r,m}^{SI,I}[n,l] &= \sum_{q=1}^{Q} c_{q,t,r}^{SI,I}[l] b_{q,m}[n] \\ h_{t,r,m}^{SI,Q}[n,l] &= \sum_{q=1}^{Q} c_{q,t,r}^{SI,Q}[l] b_{q,m}[n], \end{aligned} \tag{5.3}$$

where $c_{q,t,r}^{d,I}[l]$, $c_{q,t,r}^{Q,I}[l]$, $c_{q,t,r}^{SI,I}[l]$ and $c_{q,t,r}^{SI,Q}[l]$ are the corresponding unknown coefficients related to the channels. And $b_{q,m}[n]$ is the q-th known basis function of the deployed BEM with an order of Q. In the following section, an estimator for the unknown BEM coefficients is proposed.

5.2 Channel Estimation

Without loss of generality, consider a packet of N_b symbols (data and pilots). The index set for pilots in the packet is shown by $M_p = \{m_1, ..., m_P\}$. Furthermore, quasi-static, frequency selective channels are assumed, that is, they are constant during the packet [91]. However, the equivalent channels in (5.1) are time-varying since the PNs vary from one symbol to another. a widely used complex exponential BEM

[111, 142] is deployed to generate the basis function in (5.3), in which $b_{q,m}[n] = e^{j2\pi(q-Q/2)\frac{(n+(m-1)N)}{PN}}$ for the considered packet with $m \in M_p$ and P being the number of pilot symbols.

For the set of M_p pilot symbols, the matrix presentation of all equivalent channels based on BEM functions, including intended and residual SI in (5.3), can be presented as

$$\mathbf{h} = \mathbf{B}\mathbf{c} \tag{5.4}$$

where $\mathbf{h} = \left[\mathbf{h}_{d,I}^T \mathbf{h}_{d,Q}^T \mathbf{h}_{SI,I}^T \mathbf{h}_{SI,Q}^T\right]^T$. For $a \in \{d, SI\}$ and $b \in \{I, Q\}$, we have $\mathbf{h}_{a,b} = \left[\left[\mathbf{h}_{a,b}^1\right]^T, ..., \left[\mathbf{h}_{a,b}^{N_r}\right]^T\right]^T$, $\mathbf{h}_{a,b}^r = \left[\left[\mathbf{h}_{a,b}^{1,r}\right]^T, ..., \left[\mathbf{h}_{a,b}^{N_t,r}\right]^T\right]^T$, $\mathbf{h}_{a,b}^{t,r} = \left[\left[\mathbf{h}_{a,b}^{t,r,0}\right]^T, ..., \left[\mathbf{h}_{a,b}^{t,r,L-1}\right]^T\right]^T$, $\mathbf{h}_{a,b}^{t,r,l} = \left[\left[\mathbf{h}_{a,b}^{t,r,l,m_1}\right]^T, ..., \left[\mathbf{h}_{a,b}^{t,r,l,m_P}\right]^T\right]^T$, $\mathbf{h}_{a,b}^{t,r,l,m} = \left[h_{t,r,m}^{a,b}[0,l], ..., h_{t,r,m}^{a,b}[N-1,l]\right]^T$. Moreover, $\mathbf{B} = \mathbf{I}_{4LN_tN_r} \otimes \mathbf{B}'$, $\mathbf{B}' = \left[[\mathbf{B}'_{m_1}]^T, ..., [\mathbf{B}'_{m_P}]^T\right]^T$, $\mathbf{B}'_m = [\mathbf{B}'_{m,1}, ..., \mathbf{B}'_{m,Q}]$, $\mathbf{B}'_{m,q} = [b_{q,m}[0], ..., b_{q,m}[N-1]]$. Furthermore, $\mathbf{c} = \left[\mathbf{c}_{d,I}^T \mathbf{c}_{d,Q}^T \mathbf{c}_{SI,I}^T \mathbf{c}_{SI,Q}^T\right]^T$, $\mathbf{c}_{a,b} = \left[\left[\mathbf{c}_{a,b}^1\right]^T, ..., \left[\mathbf{c}_{a,b}^{N_r}\right]^T\right]^T$, $\mathbf{c}_{a,b}^r = \left[\left[\mathbf{c}_{a,b}^{1,r}\right]^T, ..., \left[\mathbf{c}_{a,b}^{N_t,r}\right]^T\right]^T$, $\mathbf{c}_{a,b}^{t,r} = \left[\left[\mathbf{c}_{a,b}^{t,r,0}\right]^T, ..., \left[\mathbf{c}_{a,b}^{t,r,L-1}\right]^T\right]^T$, $\mathbf{c}_{a,b}^{t,r,l} = \left[c_{1,t,r}^{a,b}[l], ..., c_{Q,t,r}^{a,b}[l]\right]^T$, $a \in \{d, SI\}$ and $b \in \{I, Q\}$. Note that $\mathbf{I}_N$ is the $N \times N$ identity matrix and $\otimes$ is the Kronecker product.

For the set of M_p pilot symbols, the received signals corresponding to the N_r receive antennas in (5.1), with the BEM expressions in (5.3), can be presented in the matrix form as

$$\mathbf{y}_{M_p} = \mathbf{\Gamma}_{M_p}\mathbf{c} + \mathbf{w}_{M_p}, \tag{5.5}$$

where $\mathbf{y}_{M_p} = \left[\mathbf{y}_{m_1}^T, ..., \mathbf{y}_{m_P}^T\right]^T$, $\mathbf{y}_m = \left[\mathbf{y}_{1,m}^T, ..., \mathbf{y}_{N_r,m}^T\right]^T$, $\mathbf{y}_{r,m} = [y_{r,m}[0], ..., y_{r,m}[N-1]]^T$. Moreover, $\mathbf{\Gamma}_{M_p} = [\mathbf{\Gamma}_{d,I}, \mathbf{\Gamma}_{d,Q}, \mathbf{\Gamma}_{SI,I}, \mathbf{\Gamma}_{SI,Q}]$, $\mathbf{\Gamma}_{a,b} = \left[\left[\mathbf{\Gamma}_{a,b}^{m_1}\right]^T, ..., \left[\mathbf{\Gamma}_{a,b}^{m_P}\right]^T\right]^T$, $\mathbf{\Gamma}_{a,b}^m = \mathbf{I}_{N_r} \otimes \left[\mathbf{\Gamma}_{a,b}^{1,m}, ..., \mathbf{\Gamma}_{a,b}^{N_t,m}\right]$,
$\mathbf{\Gamma}_{a,b}^{t,m} = \left[\mathbf{\Gamma}_{a,b}^{t,m,0}\mathbf{B}'_m, ..., \mathbf{\Gamma}_{a,b}^{t,m,L-1}\mathbf{B}'_m\right]$, $\mathbf{\Gamma}_{a,b}^{t,m,0} = \text{diag}\left(\left[x_{t,m}^a[0-l], ..., x_{t,m}^a[N-1-l]\right]\right)$, $a \in \{d, SI\}$ and $b \in \{I, Q\}$. Furthermore, $\mathbf{w}_{M_p} = \left[\mathbf{w}_{m_1}^T, ..., \mathbf{w}_{m_P}^T\right]^T$, $\mathbf{w}_m = \left[\mathbf{w}_{1,m}^T, ..., \mathbf{w}_{N_r,m}^T\right]^T$, $\mathbf{w}_{r,m} = [w_{r,m}[0], ..., w_{r,m}[N-1]]^T$.

5.2.1 LMMSE Algorithm

To estimate the unknown BEM coefficients in (5.5), an LMMSE algorithm is developed, which finds the matrix $\mathbf{W}$ to minimize the MSE between $\mathbf{c}$ and the linear estimate $\hat{\mathbf{c}}_{\text{LMMSE}} = \mathbf{W}^H \mathbf{y}_{\mathbf{M_p}}$, where $\mathbf{W}$ is given by

$$\mathbf{W} = \left(\sigma_n^2 \mathbf{I}_{PNN_r} + \mathbf{\Gamma}_{\mathbf{M_p}} \mathbf{R}_c \mathbf{\Gamma}_{\mathbf{M_p}}{}^H\right)^{-1} \mathbf{\Gamma}_{\mathbf{M_p}} \mathbf{R}_c, \tag{5.6}$$

where $\mathbf{R}_c = \mathbb{E}\{\mathbf{c}\mathbf{c}^H\}$ and $\mathbb{E}\{\mathbf{w}_{M_p}\mathbf{w}_{M_p}^H\} = \sigma_n^2 \mathbf{I}_{PNN_r}$. From (5.4), we have

$$\mathbf{R}_c = \mathbf{\Lambda} \mathbf{R}_h \mathbf{\Lambda}^H, \tag{5.7}$$

where $\mathbf{\Lambda} = \left(\mathbf{B}^H \mathbf{B}\right)^{-1} \mathbf{B}^H$ and $\mathbf{R}_h = \mathbb{E}\{\mathbf{h}\mathbf{h}^H\}$. Furthermore, after straightforward manipulations, closed-form $\mathbf{R}_h$ can be expressed as

$$\begin{aligned}
&\mathbf{R}_h = \text{blkdiag}\left(\mathbf{Q} \otimes \mathbf{M}_d, \mathbf{Q} \otimes \mathbf{M}_{SI}\right) \\
&\mathbf{Q} = \begin{bmatrix} |g_1^T|^2|g_1^R|^2 + |g_2^T|^2|g_2^R|^2 & g_1^{T^*} g_2^T \left(|g_1^R|^2 + |g_2^R|^2\right) \\ g_1^T g_2^{T^*} \left(|g_1^R|^2 + |g_2^R|^2\right) & |g_2^T|^2|g_1^R|^2 + |g_1^T|^2|g_2^R|^2 \end{bmatrix} \\
&\mathbf{M}_i = \mathbf{I}_{N_t N_r} \otimes \text{blkdiag}\left(\sigma_{i,0}^2 \mathbf{N}_0, ..., \sigma_{i,L-1}^2 \mathbf{N}_{L-1}\right), \quad i \in \{d, SI\} \\
&\mathbf{N}_l = \begin{bmatrix} \mathbf{U} & \mathbf{S}_l & \dots & \mathbf{S}_l \\ \mathbf{S}_l & \mathbf{U} & \dots & \mathbf{S}_l \\ \vdots & \vdots & \ddots & \vdots \\ \mathbf{S}_l & \mathbf{S}_l & \dots & \mathbf{U} \end{bmatrix}, \mathbf{U}\left[n_1, n_2\right] = e^{-|n_1 - n_2|\sigma_\phi^2}, \\
&\mathbf{S}_l\left[n_1, n_2\right] = e^{-(n_1 + [n_2 - l])\sigma_\phi^2} \quad l = 0, ..., L-1.
\end{aligned} \tag{5.8}$$

From the LMMSE estimated matrix, $\mathbf{W}$, and $\hat{\mathbf{c}}_{\text{LMMSE}}$, the estimated channel is given by $\hat{\mathbf{h}}_{\text{LMMSE}} = \mathbf{B}\hat{\mathbf{c}}_{\text{LMMSE}}$ as in (5.4).

5.2.2 DL Network

We next develop a DL network to enhance the performance of the proposed LMMSE BEM coefficients estimator in Section 5.2.1. Indeed, we aim to improve the MSE of estimated LMMSE BEM coefficients $\hat{\mathbf{c}}_{\text{LMMSE}}$, which leads to enhancement in equivalent channel estimation. To this end, we consider a fully connected feedforward

DNN, which has L_D layers including one input, L_D-2 hidden layers, and an output. The l-th layer, $1 \leq l \leq L_D$, includes n_l neurons and one bias unit. The input of the designed DNN is the output of the LMMSE algorithm, which is the estimated unknown BEM coefficients $\hat{\mathbf{c}}_{\text{LMMSE}}$, and the output is the final estimated BEM coefficients $\hat{\mathbf{c}}_{\text{DL-LMMSE}}$. This integrated estimator reduces the MSE. The input and output size of the DL network is equal to length of the BEM coefficients vector $\mathbf{c}$ (5.4). The relation between input and output of the developed DNN can be formulated as

$$\hat{\mathbf{c}}_{\text{DL-LMMSE}} = f^{(L_D-1)}\left(...f^{(1)}\left(\hat{\mathbf{c}}_{\text{LMMSE}};\Theta_1\right);\Theta_{L_D-1}\right), \tag{5.9}$$

where $\Theta \triangleq \{\Theta_l\}_{l=1}^{L_D-1}$ indicates the set of parameter values for the DNN and $f^{(l)}$ is a nonlinear function of the l-th layer. Moreover, the parameters of the l-th layer are indicated by Θ_l, which contains weight matrix $\mathbf{W}_l$ and bias vector $\mathbf{b}_l$, respectively. The developed DNN parameters, Θ, are optimized through offline training by using actual outputs and training sets. To do this, the MSE loss function is considered as

$$L(\Theta) = \frac{1}{|\mathcal{C}|}\sum_{\mathbf{c}\in\mathcal{C}} ||\hat{\mathbf{c}}_{\text{-LMMSE}} - \mathbf{c}||^2, \tag{5.10}$$

where $\mathcal{C}$ is the set of training BEM coefficient samples, $|\mathcal{C}|$ is the size of the training set, and $\mathbf{c}$ is the actual BEM coefficients. Note that the actual BEM coefficients for the training the DNN is derived by using (5.3) as $\mathbf{c} = \mathbf{\Lambda h}$. By using the estimated BEM coefficients through the DNN $\hat{\mathbf{c}}_{\text{DL-LMMSE}}$, the estimated channel can be calculated as $\hat{\mathbf{h}}_{\text{DL-LMMSE}} = \mathbf{B}\hat{\mathbf{c}}_{\text{DL-LMMSE}}$. We summarize the proposed DL-LMMSE algorithm in Algorithm 7.

Algorithm 7 DL-LMMSE Equivalent Channel Estimator

Offline: Train the DL network by using training sets (estimated LMMSE BEM coefficients $\hat{\mathbf{c}}_{\text{LMMSE}}$) and actual outputs (actual BEM coefficients $\hat{\mathbf{c}}$ in (5.4)) .
Online: Consider packet of data and pilot symbols
1) Estimate BEM coefficients $\hat{\mathbf{c}}_{\text{LMMSE}}$ in (5.6) using the pilot symbols,
2) Input the estimated LMMSE BEM coefficients from stage 1 into the DL network and derive the final estimated BEM coefficients $\hat{\mathbf{c}}_{\text{DL-LMMSE}}$ in (5.9),
3) Calculate the estimated equivalent channels as $\hat{\mathbf{h}}_{\text{DL-LMMSE}} = \mathbf{B}\hat{\mathbf{c}}_{\text{DL-LMMSE}}$.

5.3 Numerical Results

Herein, the performance of the proposed estimator is evaluated. Each full-duplex node in Figure 5.1 contains $N_t = 2$ transmit antennas and $N_r = 2$ receive antennas. 16-QAM (quadrature amplitude modulation) is considered. For the simulation, an orthogonal GFDM waveform is considered with $N = 256$. Furthermore, frequency-selective multipath Rayleigh fading channels with $L = 4$ paths are considered. The SI channels have power profile of 0 dB, -35 dB, -40 dB and -45 dB for delays of 0, 1, 2 and 4 samples, and the intended channels have profile of 0 dB and -1 dB for delays of 0 and 3 samples [8, 60]. In addition, $g_1^T = g_1^R = 1$ and $g_2^T = g_2^R = 0.0029 - 0.013i$ [111], order of BEM is equal to $Q = 4$, length of packet is $N_b = 7$, and the length of pilots is $P = 2$ (one at the beginning of the packet and one at the end) [112]. Moreover, the variance of PN is equal to $\sigma_\phi^2 = 0.00001$ (labeled as β_1) and $\sigma_\phi^2 = 0.0001$ (labeled as β_2) [143].

The DNN is implemented with Keras and Tensorflow using a GPU and contains one hidden layer with 126 neurons. Moreover, to minimize the loss function (5.10), an ADAM optimizer is deployed. Moreover, the training rate is set to 0.001, the number of iterations is at most 300, and the batch size is 128. Furthermore, a group of SNR values (20 dB, 30 dB) is used for training and 30,000 samples for each training SNR [109, 130]. Moreover, the testing set comprises 4,000 samples for each testing SNR[109, 130].

In Figure 5.2, thsi chapter compares the MSE of the BEM coefficient estimates, $\mathbf{c}$, for the proposed DL-LMMSE estimator (5.9), the proposed LMMSE estimator (5.6), the adopted MAP estimator [112], and the LMMSE estimator without PN and IQ imbalance impairments. From the figure, the proposed LMMSE estimator outperforms the adopted MAP estimator, and specially, in low SNRs. The MSE of the former is lower than that of the latter, which is because of the superiority of the LMMSE algorithm in eliminating the power of noise [105]. Moreover, the integrated DL and

LMMSE estimator (DL-LMMSE) reduces the MSE further. Indeed, the trained DL network improves the MSE of the LMMSE estimated BEM coefficients. Moreover, when the PN level is at β_1, DL-LMMSE nearly compensates for the compound impacts of PN and IQ imbalance and achieves an MSE near the LMMSE estimator without impairments. However, as the variance of PN increases, all the estimators perform poorly because of PN's powerful effects.

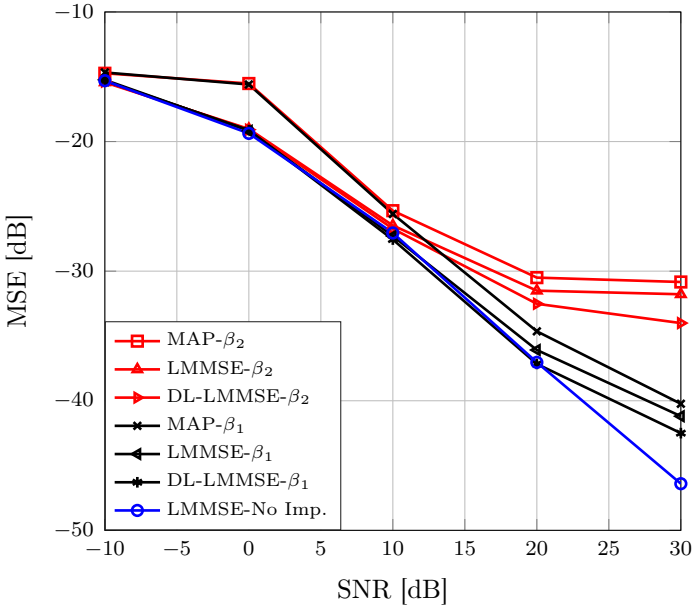

Figure 5.2: MSE of estimated BEM coefficients.

In Figure 5.3, this chapter compares the MSE of the estimated time-varying equivalent channels, $\mathbf{h}$, for the similar estimators in Figure 5.2. According to Figure 5.2, the LMMSE estimator outperforms the MAP estimator by yielding higher quality channel estimates since the MSE of LMMSE BEM estimates is lower than the MAP ones. As expected, it achieves a lower MSE for channel estimation and outperforms other estimators since DL-LMMSE decreases the MSE of BEM estimates. For PN variance at β_1, it nearly eliminates the impacts of the RF impairments, and its MSE approaches that of the ideal case (i.e., the LMMSE estimator without impairments). Therefore, the proposed DL-LMMSE accurately estimates the channels even with the RF impairments. Thus, it can be an integral part of a receiver structure for SI

cancellation and data detection.

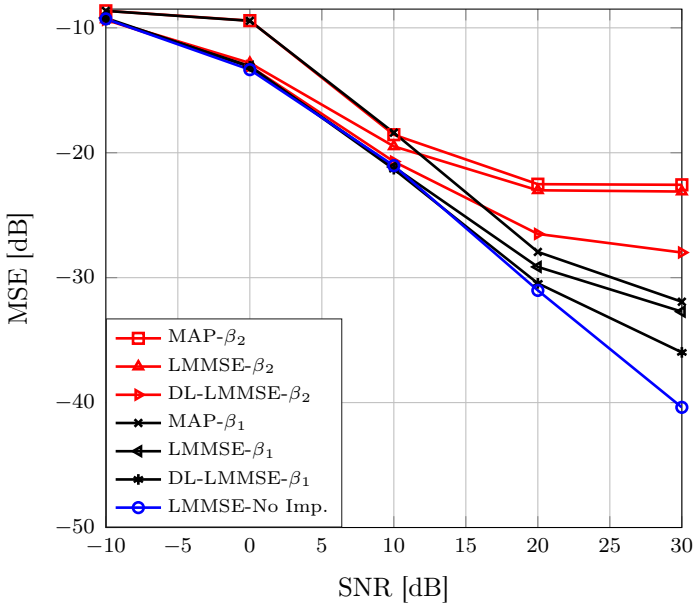

Figure 5.3: MSE of estimated time-varying equivalent channels.

Finally,this chapter analyzes and compares the computational complexities of DL-LMMSE, LMMSE, and MAP estimators. Complexity is measured by the number of floating point operations (FLOPs). For the LMMSE estimator, the total number of FLOPs is equal to $\Psi_1^3 + 2\Psi_1\Psi_2(\Psi_1 + \Psi_2) + \Psi_1\Psi_2$, where $\Psi_1 = PNN_r$ and $\Psi_2 = 4LQN_tN_r$. Moreover, the total number of FLOPs for the MAP estimator [112] is equal to $\Psi_1^3 + \Psi_2^3 + \Psi_1^2(\Psi_2 + 1)$. It is clear that the complexity of the MAP estimator is higher than that of the LMMSE estimator. Moreover, the FLOPs of the DL-LMMSE estimator arise from the LMMSE estimator and the DL network (5.9). Therefore, the complexity of the DL-LMMSE estimator can be written as [105]

$$\mathcal{C}_{\text{DL-LMMSE}} \sim \mathcal{O}\left(\Psi_1^3 + \sum_{l=1}^{L_D-1} n_l n_{l+1}\right). \tag{5.11}$$

As expected, the complexity of the DL-LMMSE estimator is higher than the conventional LMMSE estimator. However, the former outperforms the latter and provides accurate channel estimation and nearly eliminates impacts of the RF impairments. This fact is really important for the SI cancellation stage in full-duplex nodes

and data detection.

5.4 Conclusion

This chapter investigated the problem of the joint channel, PN, and IQ imbalance estimation in multicarrier full-duplex MIMO wireless systems. The equivalent time-varying channels were decomposed over a set of the elementary functions and time-invariant BEM coefficients. For this system, this chapter first proposed a pilot-aided LMMSE estimator and then enhanced it with a DNN network. The simulation results illustrate that the resulting DL-LMMSE estimator achieves lower MSE for channel estimations than the LMMSE and MAP estimators. Furthermore, it nearly eliminates the impacts of the impairments. It thus provides desirable channel estimations for SI cancellation and data detection.

This work has following limitations. First, optimal pilot designs that use the MSE or a similar measure can be developed which has not been investigated in this work. Second, this work is limited to PN and IQ imbalance impairments. However, other RF impairments such as CFO and timing offset can be incorporated with the proposed algorithm. Third, the number of antenna in the full-duplex transceivers can be enhanced and channel estimation in the presence of RF impairments in massive MIMO full-duplex systems is investigated.

Chapter 6

Conclusion and Future Research Directions

6.1 Summary of Contributions and Conclusions

Full-duplex radios, GFDM, cognitive radio and MIMO are promising technologies for enhancing SE and thereby addressing the spectrum crunch. They enable 5G-and-beyond wireless standards. However, their limitations include SI, ICI and ISI and higher sensitivity to RF impairments. Therefore, this research aims to design and analyze high SE non-orthogonal designs based on mentioned technologies in the presence of RF impairments.

Chapter 2 investigates a GFDM full-duplex BS in the presence of three common RF impairments – PN, CFO and IQ imbalance. This work considers a network of a full-duplex BS and half-duplex uplink and downlink users. For both uplink and downlink, the SIR, receiver filters for maximizing the SIR, the rates, and the closed-form optimized rate region are derived. It is shown the optimal-filter based GFDM outperforms full-duplex OFDM by 25 dB higher SIR and an uplink rate increase of 500%.

Chapter 3 investigates the performance of full-duplex GFDM transceivers operating over a spectrum hole (whose lower and upper adjacent bands are PU active) with PN, CFO, IQ imbalance, and a nonlinear PA. Both analog and digital SI cancellation techniques are considered, and the residual SI power is derived for two cases - (1) two

independent oscillators per transceiver and (2) single shared oscillator per transceiver. Moreover, the power allocation is determined to maximize the sum rate of the secondary link. For this, a series of successive convex approximations is deployed to reach a common geometric programming problem. It is shown that the full-duplex GFDM link achieves significantly higher rates than the full-duplex OFDM link. For instance, the sum rate gains as high as 100% are sometimes achieved. Therefore, given RF impairments, GFDM is a potential candidate for realizing full-duplex links in secondary networks.

Chapter 4 investigates PN compensation for GFDM systems in both stages of channel estimation and data detection. A NLS estimator is proposed for joint channel and PN estimation by using a block pilot GFDM symbol. Then, an iterative LS and closed-form LS algorithms are developed for joint data detection and PN compensation. The complexity of all algorithms is reduced by deploying interpolation techniques and relating channel frequency and time responses. Moreover, a DL-based algorithm is proposed for PN compensation which eliminates the need for extraneous statistical information and avoids the iterations of conventional estimators. It is shown that the proposed algorithms nearly compensate impact of PN and thus reduce GFDM receivers' sensitivity to RF impairments.

Chapter 5 investigates joint channel, PN, and IQ imbalance estimation in multi-carrier full-duplex MIMO wireless systems. This chapter decomposes the equivalent time-varying channels over a set of the elementary functions and time-invariant BEM coefficients. A pilot-aided LMMSE estimator is developed and then enhance it with a DNN network. The simulation results illustrate that the resulting DL-LMMSE estimator achieves lower MSE for channel estimations than the LMMSE and MAP estimators. Furthermore, it nearly eliminates the impacts of the impairments.

6.2 Future Research Directions

In the following, some future research problems are provided which can be considered as the extension of this thesis.

- In Chapter 2, the considered cellular BS communicates with two users, one uplink and one downlink. It will be an interesting topic to extend this problem to multi-cell multi-user scenario and investigate SE improvement of this system.

- In Chapter 5, channel estimation for full-duplex MIMO multicarrier systems in the presence of RF impairments. It will be an interesting topic to investigate channel estimation and data detection in massive MIMO multicarrier systems given RF impairments.

- In Chapter 4 and Chapter 5, It is shown that DL networks can enhance the performance of RF impairment compensation algorithms in both stages of channel estimation and data detection. It will be an interesting to study DL algorithms for RF impairment compensation in more practical scenarios like the multi-cell multi-user networks.

Bibliography

[1] G. Ancans *et al.*, "Spectrum considerations for 5G mobile communication systems," *Procedia Computer Science*, vol. 104, pp. 509–516, 2017.

[2] T. Wang *et al.*, "5G spectrum: Is china ready?" *IEEE Commun. Mag.*, vol. 53, no. 7, pp. 58–65, 2015.

[3] J. Tang, D. K. C. So, E. Alsusa, and K. A. Hamdi, "Resource efficiency: A new paradigm on energy efficiency and spectral efficiency tradeoff," *IEEE Trans. Wireless Commun.*, vol. 13, no. 8, pp. 4656–4669, 2014. DOI: 10.1109/TWC.2014.2316791.

[4] E. Björnson, J. Hoydis, and L. Sanguinetti, "Massive MIMO networks: Spectral, energy, and hardware efficiency," *Foundations and Trends in Signal Processing*, vol. 11, no. 3-4, pp. 154–655, 2017.

[5] L. Dai, B. Wang, Y. Yuan, S. Han, I. Chih-lin, and Z. Wang, "Non-orthogonal multiple access for 5G: Solutions, challenges, opportunities, and future research trends," *IEEE Commun. Mag.*, vol. 53, no. 9, pp. 74–81, 2015. DOI: 10.1109/MCOM.2015.7263349.

[6] E. Yaacoub and Z. Dawy, "A survey on uplink resource allocation in OFDMA wireless networks," *IEEE Commun. Surveys Tut.*, vol. 14, no. 2, pp. 322–337, 2012. DOI: 10.1109/SURV.2011.051111.00121.

[7] D. Kim, H. Lee, and D. Hong, "A survey of in-band full-duplex transmission: From the perspective of PHY and MAC layers," *IEEE Commun. Surveys Tut.*, vol. 17, no. 4, pp. 2017–2046, 2015. DOI: 10.1109/COMST.2015.2403614.

[8] V. Syrjälä, M. Valkama, L. Anttila, T. Riihonen, and D. Korpi, "Analysis of oscillator phase-noise effects on self-interference cancellation in full-duplex OFDM radio transceivers," *IEEE Trans. Wireless Commun.*, vol. 13, no. 6, pp. 2977–2990, 2014.

[9] C. D. Nwankwo, L. Zhang, A. Quddus, M. A. Imran, and R. Tafazolli, "A survey of self-interference management techniques for single frequency full duplex systems," *IEEE Access*, vol. 6, pp. 30 242–30 268, 2018.

[10] Y. Liu *et al.*, "A full-duplex transceiver with two-stage analog cancellations for multipath self-interference," *IEEE Trans. Microw. Theory Techn.*, vol. 65, no. 12, pp. 5263–5273, 2017.

[11] A. Sabharwal *et al.*, "In-band full-duplex wireless: Challenges and opportunities," *IEEE J. Selected Areas Commun.*, vol. 32, no. 9, pp. 1637–1652, 2014. DOI: 10.1109/JSAC.2014.2330193.

[12] D. Bharadia, E. McMilin, and S. Katti, "Full duplex radios," in *Proc. SIGCOMM*, 2013, pp. 375–386.

[13] M. Jain *et al.*, "Practical, real-time, full duplex wireless," in *Proc. 17th Annu. Int. Conf. Mobile Comput. Netw.*, 2011, pp. 301–312.

[14] J. I. Choi, M. Jain, K. Srinivasan, P. Levis, and S. Katti, "Achieving single channel, full duplex wireless communication," in *Proc. ACM MobiCom*, 2010, pp. 1–12.

[15] E. Everett, M. Duarte, C. Dick, and A. Sabharwal, "Empowering full-duplex wireless communication by exploiting directional diversity," in *Proc. Conf. Rec. 45th Asilomar Signals Syst. Comput. (ASILOMAR)*, IEEE, 2011, pp. 2002–2006.

[16] M. Chung, M. S. Sim, J. Kim, D. K. Kim, and C. B. Chae, "Prototyping real-time full duplex radios," *IEEE Commun. Mag.*, vol. 53, no. 9, pp. 56–63, 2015.

[17] K. E. Kolodziej, J. G. McMichael, and B. T. Perry, "Multitap RF canceller for in-band full-duplex wireless communications," *IEEE Trans. Wireless Commun.*, vol. 15, no. 6, pp. 4321–4334, 2016. DOI: 10.1109/TWC.2016.2539169.

[18] D. Korpi, M. Heino, C. Icheln, K. Haneda, and M. Valkama, "Compact inband full-duplex relays with beyond 100 db self-interference suppression: Enabling techniques and field measurements," *IEEE Trans. Antennas Propag.*, vol. 65, no. 2, pp. 960–965, 2017. DOI: 10.1109/TAP.2016.2632740.

[19] M. A. Khojastepour, K. Sundaresan, S. Rangarajan, X. Zhang, and S. Barghi, "The case for antenna cancellation for scalable full-duplex wireless communications," in *Proc. 10th ACM Workshop on Hot Topics in Networks*, 2011, pp. 1–6.

[20] C. R. Anderson *et al.*, "Antenna isolation, wideband multipath propagation measurements, and interference mitigation for on-frequency repeaters," in *Proc. IEEE SoutheastCon, 2004. Proceedings.*, 2004, pp. 110–114. DOI: 10.1109/SECON.2004.1287906.

[21] S. Li and R. D. Murch, "An investigation into baseband techniques for single-channel full-duplex wireless communication systems," *IEEE Trans. Wireless Commun.*, vol. 13, no. 9, pp. 4794–4806, 2014. DOI: 10.1109/TWC.2014.2341569.

[22] J. Zhou *et al.*, "Integrated full duplex radios," *IEEE Commun. Mag.*, vol. 55, no. 4, pp. 142–151, 2017. DOI: 10.1109/MCOM.2017.1600583.

[23] T. Dinc *et al.*, "A 60 GHz CMOS full-duplex transceiver and link with polarization-based antenna and RF cancellation," *IEEE J. Solid-State Circuits*, vol. 51, no. 5, pp. 1125–1140, 2016. DOI: 10.1109/JSSC.2015.2507367.

[24] E. Everett, A. Sahai, and A. Sabharwal, "Passive self-interference suppression for full-duplex infrastructure nodes," *IEEE Trans. Wireless Commun.*, vol. 13, no. 2, pp. 680–694, 2014. DOI: 10.1109/TWC.2013.010214.130226.

[25] E. A. others, "MIDU: Enabling MIMO full duplex," in *Proceedings of the 18th annual international conference on Mobile computing and networking*, 2012, pp. 257–268.

[26] J. Ma, G. Y. Li, J. Zhang, T. Kuze, and H. Iura, "A new coupling channel estimator for cross-talk cancellation at wireless relay stations," in *Proc. IEEE Global Telecommunications Conference*, 2009, pp. 1–6. DOI: 10.1109/GLOCOM.2009.5425817.

[27] A. Sahai, G. Patel, C. Dick, and A. Sabharwal, "On the impact of phase noise on active cancelation in wireless full-duplex," *IEEE Trans. Veh. Technol.*, vol. 62, no. 9, pp. 4494–4510, 2013.

[28] A. K. Khandani, "Two-way (true full-duplex) wireless," in *2013 13th Canadian Workshop on Information Theory*, IEEE, 2013, pp. 33–38.

[29] D. Bliss, P. Parker, and A. Margetts, "Simultaneous transmission and reception for improved wireless network performance," in *Proc. 14th Workshop on Statistical Signal Processing*, IEEE, 2007, pp. 478–482.

[30] N. Michailow *et al.*, "Generalized frequency division multiplexing for 5th generation cellular networks," *IEEE Trans. Commun.*, vol. 62, no. 9, pp. 3045–3061, 2014, ISSN: 0090-6778. DOI: 10.1109/TCOMM.2014.2345566.

[31] B. Lim and Y. Ko, "SIR analysis of OFDM and GFDM waveforms with timing offset, CFO, and phase noise," *IEEE Trans. Wireless Commun.*, vol. 16, no. 10, pp. 6979–6990, 2017.

[32] B. Lim and Y. Ko, "Multiuser interference cancellation for GFDM with timing and frequency offsets," *IEEE Trans. Commun.*, vol. 67, no. 6, pp. 4337–4349, 2019.

[33] H. Cheng *et al.*, "Joint channel estimation and Tx/Rx I/Q imbalance compensation for GFDM systems," *IEEE Trans. Wireless Commun.*, vol. 18, no. 2, pp. 1304–1317, 2019.

[34] P. Chen, B. Su, and Y. Huang, "Matrix characterization for GFDM: Low complexity MMSE receivers and optimal filters," *IEEE Trans. Signal Process.*, vol. 65, no. 18, pp. 4940–4955, 2017.

[35] Z. Na *et al.*, "Turbo receiver channel estimation for GFDM-based cognitive radio networks," *IEEE Access*, vol. 6, 2018.

[36] Z. Wang, L. Mei, X. Sha, and V. C. M. Leung, "Minimum BER power allocation for space-time coded generalized frequency division multiplexing systems," *IEEE Wireless Commun. Lett.*, pp. 1–1, 2018.

[37] F. Li, K. Zheng, L. Zhao, H. Zhao, and Y. Li, "Design and performance of a novel interference-free GFDM transceiver with dual-filter," *IEEE Trans. Veh. Technol.*, pp. 1–1, 2019.

[38] K. Liu, W. Deng, and Y. Liu, "Theoretical analysis of the peak-to-average power ratio and optimal pulse shaping filter design for GFDM systems," *IEEE Trans. Signal Process.*, vol. 67, no. 13, pp. 3455–3470, 2019.

[39] S. Ehsanfar, M. Matthé, M. Chafii, and G. P. Fettweis, "Pilot- and CP-aided channel estimation in MIMO non-orthogonal multi-carriers," *IEEE Trans. Wireless Commun.*, vol. 18, no. 1, pp. 650–664, 2019.

[40] Z. Na *et al.*, "Joint subcarrier and subsymbol allocation based simultaneous wireless information and power transfer for multiuser GFDM in IoT," *IEEE Internet Things J.*, pp. 1–1, 2019.

[41] F. Tian *et al.*, "A novel concatenated coded modulation based on GFDM for access optical networks," *IEEE Photon. J.*, vol. 10, no. 2, pp. 1–8, 2018.

[42] M. H. Islam *et al.*, "Spectrum survey in singapore: Occupancy measurements and analyses," in *2008 3rd International Conference on Cognitive Radio Oriented Wireless Networks and Communications (CrownCom 2008)*, 2008, pp. 1–7. DOI: 10.1109/CROWNCOM.2008.4562457.

[43] S. Haykin, "Cognitive radio: Brain-empowered wireless communications," *IEEE J. Sel. Areas Commun.*, vol. 23, no. 2, pp. 201–220, 2005. DOI: 10.1109/JSAC.2004.839380.

[44] "IEEE standard for information technology - telecommunications and information exchange between systems - local and metropolitan area networks - specific requirements - part 11: Wireless LAN medium access control (MAC) and physical layer (PHY) specifications amendment 5: Television white spaces (TVWS) operations," *IEEE Std 802.11af-2013 (Amendment to IEEE Std 802.11-2012, as amended by IEEE Std 802.11ae-2012, IEEE Std 802.11aa2012, IEEE Std 802.11ad-2012, and IEEE Std 802.11ac-2013)*, 1–198, 2014.

[45] S. Kusaladharma and C. Tellambura, "Aggregate interference analysis for underlay cognitive radio networks," *IEEE Wireless Commun. Lett.*, vol. 1, no. 6, pp. 641–644, 2012.

[46] B. Razavi, *RF Microelectronics Second Edition*. Prentice Hall New Jersey, 2012.

[47] T.-D. Chiueh and P.-Y. Tsai, *OFDM baseband receiver design for wireless communications*. John Wiley & Sons, 2008.

[48] C. Y. Soo and et al., MIMO-OFDM *wireless communications with* MATLAB. Wiley, 2010.

[49] A. Tarighat, R. Bagheri, and A. H. Sayed, "Compensation schemes and performance analysis of IQ imbalances in OFDM receivers," *IEEE Trans. Signal Process.*, vol. 53, no. 8, pp. 3257–3268, 2005.

[50] D. Korpi, L. Anttila, V. Syrjälä, and M. Valkama, "Widely linear digital self-interference cancellation in direct-conversion full-duplex transceiver," *IEEE J. Sel. Areas Commun.*, vol. 32, no. 9, pp. 1674–1687, 2014.

[51] R. Li, A. Masmoudi, and T. Le-Ngoc, "Self-interference cancellation with nonlinearity and phase-noise suppression in full-duplex systems," *IEEE Trans. Veh. Technol.*, vol. 67, no. 3, pp. 2118–2129, 2018.

[52] M. Baghani, A. Mohammadi, M. Majidi, and M. Valkama, "Analysis and rate optimization of OFDM-based cognitive radio networks under power amplifier nonlinearity," *IEEE Trans. Commun.*, vol. 62, no. 10, pp. 3410–3419, 2014, ISSN: 0090-6778. DOI: 10.1109/TCOMM.2014.2360384.

[53] A. Mohammadian and C. Tellambura, "RF impairments in wireless transceivers: Phase noise, CFO, and IQ imbalance – a survey," *IEEE Access*, vol. 9, pp. 111 718–111 791, 2021. DOI: 10.1109/ACCESS.2021.3101845.

[54] E. Park, J. Bae, H. Ju, and Y. Han, "Resource allocation for full-duplex systems with imperfect co-channel interference estimation," *IEEE Trans. Wireless Commun.*, vol. 18, no. 4, pp. 2388–2400, 2019.

[55] M. Zhou, H. Li, N. Zhao, S. Zhang, and F. R. Yu, "Feasibility analysis and clustering for interference alignment in full-duplex-based small cell networks," *IEEE Trans. Commun.*, vol. 67, no. 1, pp. 807–819, 2019.

[56] X. Xia, K. Xu, D. Zhang, Y. Xu, and Y. Wang, "Beam-domain full-duplex massive MIMO: Realizing co-time co-frequency uplink and downlink transmission in the cellular system," *IEEE Trans. Veh. Technol.*, vol. 66, no. 10, pp. 8845–8862, 2017.

[57] K. Xu, Z. Shen, Y. Wang, X. Xia, and D. Zhang, "Hybrid time-switching and power splitting SWIPT for full-duplex massive MIMO systems: A beam-domain approach," *IEEE Trans. Veh. Technol.*, vol. 67, no. 8, pp. 7257–7274, 2018.

[58] F. Shu, J. Wang, J. Li, R. Chen, and W. Chen, "Pilot optimization, channel estimation, and optimal detection for full-duplex OFDM systems with IQ imbalances," *IEEE Trans. Veh. Technol.*, vol. 66, no. 8, pp. 6993–7009, 2017.

[59] S. Li and R. D. Murch, "An investigation into baseband techniques for single-channel full-duplex wireless communication systems," *IEEE Trans. Wireless Commun.*, vol. 13, no. 9, pp. 4794–4806, 2014.

[60] L. Samara, M. Mokhtar, O. Özdemir, R. Hamila, and T. Khattab, "Residual self-interference analysis for full-duplex OFDM transceivers under phase noise and I/Q imbalance," *IEEE Commun. Lett.*, vol. 21, no. 2, pp. 314–317, 2017.

[61] S. Han, Y. Sung, and Y. H. Lee, "Filter design for generalized frequency-division multiplexing," *IEEE Trans. Signal Process.*, vol. 65, no. 7, pp. 1644–1659, 2017.

[62] D. Gaspar, L. Mendes, and T. Pimenta, "GFDM BER under synchronization errors," *IEEE Commun. Lett.*, vol. 21, no. 8, pp. 1743–1746, 2017.

[63] W. Chung *et al.*, "Interference cancellation architecture for full-duplex system with GFDM signaling," in *Signal Processing Conference (EUSIPCO)*, 2016, pp. 788–792.

[64] M. Amjad, F. Akhtar, M. H. Rehmani, M. Reisslein, and T. Umer, "Full-duplex communication in cognitive radio networks: A survey," *IEEE Commun. Surveys Tut.*, vol. 19, no. 4, pp. 2158–2191, 2017. DOI: 10.1109/COMST.2017.2718618.

[65] F. Akhtar, M. H. Rehmani, and M. Reisslein, "White space: Definitional perspectives and their role in exploiting spectrum opportunities," *Telecommunications Policy*, vol. 40, no. 4, pp. 319–331, 2016.

[66] S. Herath, N. Rajatheva, and C. Tellambura, "Unified approach for energy detection of unknown deterministic signal in cognitive radio over fading channels," ser. IEEE International Conference on Communications Workshop, 2009, pp. 1–5.

[67] S. Atapattu, C. Tellambura, and H. Jiang, *Energy detection for spectrum sensing in cognitive radio*. Springer New York, NY, USA, 2014.

[68] R. Datta *et al.*, "Generalized frequency division multiplexing in cognitive radio," ser. European Signal Process Conference (EUSIPCO), 2012, pp. 2679–2683.

[69] D. Panaitopol, R. Datta, and G. Fettweis, "Cyclostationary detection of cognitive radio systems using GFDM modulation," ser. IEEE Wireless Communications and Networking Conference (WCNC), 2012, pp. 930–934.

[70] G. Bansal, M. Hossain, and V. Bhargava, "Optimal and suboptimal power allocation schemes for OFDM-based cognitive radio systems," *IEEE Trans. Wireless commun.*, vol. 7, no. 11, pp. 4710–4718, 2008.

[71] Y. Zhang and C. Leung, "Resource allocation in an OFDM-based cognitive radio system," *IEEE Trans. Commun.*, vol. 57, no. 7, pp. 1928–1931, 2009.

[72] S. Wang, F. Huang, and Z. Zhou, "Fast power allocation algorithm for cognitive radio networks," *IEEE Commun. Lett.*, vol. 15, no. 8, pp. 845–847, 2011.

[73] A. A. Rosas *et al.*, "Proposed optimization technique for maximization of throughput under using different multicarrier systems in cognitive radio networks," ser. The Proceedings of Second International Conference on Electronics Engineering, Clean Energy and Green Computing (EEECEGC), 2015, pp. 25–33.

[74] A. Dawoud *et al.*, "PSO-adaptive power allocation for multiuser GFDM-based cognitive radio networks," ser. International Conference on Selected Topics in Mobile Wireless Networking (MoWNeT), 2016, pp. 1–8.

[75] E. Costa and S. Pupolin, "M-QAM-OFDM system performance in the presence of a nonlinear amplifier and phase noise," *IEEE Trans. Commun.*, vol. 50, no. 3, pp. 462–472, 2002. DOI: 10.1109/26.990908.

[76] P. Mathecken, T. Riihonen, S. Werner, and R. Wichman, "Performance analysis of OFDM with wiener phase noise and frequency selective fading channel," *IEEE Trans. Commun.*, vol. 59, no. 5, pp. 1321–1331, 2011. DOI: 10.1109/TCOMM.2011.030411.100401.

[77] P. Mathecken, T. Riihonen, N. N. Tchamov, S. Werner, M. Valkama, and R. Wichman, "Characterization of OFDM radio link under PLL-based oscillator phase noise and multipath fading channel," *IEEE Trans. Commun.*, vol. 60, no. 6, pp. 1479–1485, 2012. DOI: 10.1109/TCOMM.2012.041212.110091.

[78] M. R. Gholami, S. Nader-Esfahani, and A. A. Eftekhar, "A new method of phase noise compensation in OFDM," in *IEEE International Conference on Communications (ICC)*, vol. 5, 2003, 3443–3446 vol.5. DOI: 10.1109/ICC.2003.1204094.

[79] R. A. Casas, S. L. Biracree, and A. E. Youtz, "Time domain phase noise correction for OFDM signals," *IEEE Trans. Broadcast.*, vol. 48, no. 3, pp. 230–236, 2002. DOI: 10.1109/TBC.2002.803711.

[80] G. Liu and W. Zhu, "Compensation of phase noise in OFDM systems using an ICI reduction scheme," *IEEE Trans. Broadcast.*, vol. 50, no. 4, pp. 399–407, 2004. DOI: 10.1109/TBC.2004.837884.

[81] V. Syrjälä, M. Valkama, N. N. Tchamov, and J. Rinne, "Phase noise modelling and mitigation techniques in OFDM communications systems," in *Wireless Telecommunications Symposium*, 2009, pp. 1–7. DOI: 10.1109/WTS.2009.5068965.

[82] N. N. Tchamov, J. Rinne, A. Hazmi, M. Valkama, V. Syrjälä, and M. Renfors, "Enhanced algorithm for digital mitigation of ICI due to phase noise in OFDM receivers," *IEEE Wireless Commun. Lett.*, vol. 2, no. 1, pp. 6–9, 2013. DOI: 10.1109/WCL.2012.091912.120412.

[83] S. Negusse, P. Zetterberg, and P. Händel, "Phase-noise mitigation in OFDM by best match trajectories," *IEEE Trans. Commun.*, vol. 63, no. 5, pp. 1712–1725, 2015, ISSN: 1558-0857. DOI: 10.1109/TCOMM.2015.2422829.

[84] P. Mathecken, T. Riihonen, S. Werner, and R. Wichman, "Phase noise estimation in OFDM: Utilizing its associated spectral geometry," *IEEE Trans. Signal Process.*, vol. 64, no. 8, pp. 1999–2012, 2016, ISSN: 1941-0476. DOI: 10.1109/TSP.2015.2512532.

[85] P. Mathecken, T. Riihonen, S. Werner, and R. Wichman, "Constrained phase noise estimation in OFDM using scattered pilots without decision feedback," *IEEE Trans. Signal Process.*, vol. 65, no. 9, pp. 2348–2362, 2017.

[86] J-H. Lee, J-S. Yang, S-C. Kim, and Y-W. Park, "Joint channel estimation and phase noise suppression for OFDM systems," in *2005 IEEE 61st Vehicular Technology Conference*, vol. 1, 2005, 467–470 Vol. 1. DOI: 10.1109/VETECS.2005.1543334.

[87] F. Munier, T. Eriksson, and A. Svensson, "An ICI reduction scheme for OFDM system with phase noise over fading channels," *IEEE Trans. Commun.*, vol. 56, no. 7, pp. 1119–1126, 2008. DOI: 10.1109/TCOMM.2008.050063.

[88] R. Carvajal, J. C. Aguero, B. I. Godoy, and G. C. Goodwin, "EM-based maximum-likelihood channel estimation in multicarrier systems with phase distortion," *IEEE Trans. Veh. Technol.*, vol. 62, no. 1, pp. 152–160, 2013, ISSN: 1939-9359. DOI: 10.1109/TVT.2012.2217361.

[89] Q. Zou, A. Tarighat, and A. H. Sayed, "Compensation of phase noise in OFDM wireless systems," *IEEE Trans. Signal Process.*, vol. 55, no. 11, pp. 5407–5424, 2007.

[90] Q. Zou, A. Tarighat, and A. H. Sayed, "Joint compensation of IQ imbalance and phase noise in OFDM wireless systems," *IEEE Trans. Commun.*, vol. 57, no. 2, pp. 404–414, 2009.

[91] O. H. Salim, A. A. Nasir, H. Mehrpouyan, W. Xiang, S. Durrani, and R. A. Kennedy, "Channel, phase noise, and frequency offset in OFDM systems: Joint estimation, data detection, and hybrid Cramér-Rao lower bound," *IEEE Trans. Commun.*, vol. 62, no. 9, pp. 3311–3325, 2014, ISSN: 1558-0857. DOI: 10.1109/TCOMM.2014.2345056.

[92] W. Liu, S. Schwarz, M. Rupp, D. Chen, and T. Jiang, "Preamble-based channel estimation for OQAM/FBMC systems with delay diversity," *IEEE Trans. Wireless Commun.*, vol. 19, no. 11, pp. 7169–7180, 2020. DOI: 10.1109/TWC.2020.3008736.

[93] D. Ren, J. Li, G. Zhang, G. Lu, and J. Ge, "Multi-tap channel estimation for preamble-based FBMC/OQAM systems," *IEEE Access*, vol. 8, pp. 176 232–176 240, 2020. DOI: 10.1109/ACCESS.2020.3026341.

[94] J. C. Estrada-Jimenez, K. Chen-Hu, M. J. F. Garcia, and A. Garcia Armada, "Power allocation and capacity analysis for FBMC-OQAM with superimposed training," *IEEE Access*, vol. 7, pp. 46 968–46 976, 2019. DOI: 10.1109/ACCESS.2019.2909405.

[95] L. D. Le and H. H. Nguyen, "Phase noise compensation for CFBMC–OQAM systems under imperfect channel estimation," *IEEE Access*, vol. 8, pp. 47 247–47 263, 2020. DOI: 10.1109/ACCESS.2020.2979376.

[96] J. Jeong, Y. Park, S. Weon, J. Kim, S. Choi, and D. Hong, "Eigendecomposition-based GFDM for interference-free data transmission and pilot insertion for channel estimation," *IEEE Trans. Wireless Commun.*, vol. 17, no. 10, pp. 6931–6943, 2018.

[97] H. Shayanfar, H. Saeedi-Sourck, and A. Farhang, "CFO and channel estimation techniques for GFDM," in *IEEE International Microwave Workshop Series on 5G Hardware and System Technologies (IMWS-5G)*, 2018, pp. 1–3.

[98] H. Shayanfar, H. Saeedi-Sourck, and A. Farhang, "Low-complexity search method for CFO estimation in GFDM," *Electronics Letters*, vol. 55, no. 6, pp. 355–357, 2019.

[99] Y. Liu, X. Zhu, E. G. Lim, Y. Jiang, and Y. Huang, "Robust semi-blind estimation of channel and CFO for GFDM systems," in *2019 IEEE International Conference on Communications (ICC)*, 2019, pp. 1–7.

[100] N. Tang, S. He, H. Wang, Y. Huang, and L. Yang, "Training sequence design for channel estimation and IQ imbalance compensation in GFDM systems," in *9th International Conference on Wireless Communications and Signal Processing (WCSP)*, 2017, pp. 1–6.

[101] H. Cheng, Y. Xia, Y. Huang, L. Yang, and D. P. Mandic, "A normalized complex LMS based blind I/Q imbalance compensator for GFDM receivers and its full second-order performance analysis," *IEEE Trans. Signal Process.*, vol. 66, no. 17, pp. 4701–4712, 2018.

[102] L. D. Le and H. H. Nguyen, "Compensation of phase noise and IQ imbalance in multi-carrier systems," *IEEE Access*, vol. 8, pp. 191 263–191 277, 2020. DOI: 10.1109/ACCESS.2020.3032555.

[103] M. Soltani, V. Pourahmadi, A. Mirzaei, and H. Sheikhzadeh, "Deep learning-based channel estimation," *IEEE Commun. Lett.*, vol. 23, no. 4, pp. 652–655, 2019. DOI: 10.1109/LCOMM.2019.2898944.

[104] M. Soltani, V. Pourahmadi, and H. Sheikhzadeh, "Pilot pattern design for deep learning-based channel estimation in OFDM systems," *IEEE Wireless Commun. Lett.*, vol. 9, no. 12, pp. 2173–2176, 2020. DOI: 10.1109/LWC.2020.3016603.

[105] Y. Yang, F. Gao, X. Ma, and S. Zhang, "Deep learning-based channel estimation for Doubly selective fading channels," *IEEE Access*, vol. 7, pp. 36 579–36 589, 2019. DOI: 10.1109/ACCESS.2019.2901066.

[106] C. Chun, J. Kang, and I. Kim, "Deep learning-based channel estimation for massive MIMO systems," *IEEE Wireless Commun. Lett.*, vol. 8, no. 4, pp. 1228–1231, 2019. DOI: 10.1109/LWC.2019.2912378.

[107] H. Huang, J. Yang, H. Huang, Y. Song, and G. Gui, "Deep learning for super-resolution channel estimation and DOA estimation based massive MIMO system," *IEEE Trans. Veh. Technol.*, vol. 67, no. 9, pp. 8549–8560, 2018. DOI: 10.1109/TVT.2018.2851783.

[108] H. Ye, G. Y. Li, and B. Juang, "Power of deep learning for channel estimation and signal detection in OFDM systems," *IEEE Wireless Commun. Lett.*, vol. 7, no. 1, pp. 114–117, 2018. DOI: 10.1109/LWC.2017.2757490.

[109] X. Yi and C. Zhong, "Deep learning for joint channel estimation and signal detection in OFDM systems," *IEEE Commun. Lett.*, vol. 24, no. 12, pp. 2780–2784, 2020. DOI: 10.1109/LCOMM.2020.3014382.

[110] E. Ahmed and A. M. Eltawil, "On phase noise suppression in full-duplex systems," *IEEE Trans. Wireless Commun.*, vol. 14, no. 3, pp. 1237–1251, 2015, ISSN: 1558-2248. DOI: 10.1109/TWC.2014.2365536.

[111] R. Li, A. Masmoudi, and T. Le-Ngoc, "Self-interference cancellation with nonlinearity and phase-noise suppression in full-duplex systems," *IEEE Trans. Veh. Technol.*, vol. 67, no. 3, pp. 2118–2129, 2018, ISSN: 1939-9359. DOI: 10.1109/TVT.2017.2754489.

[112] V. Nguyen-Duy-Nhat *et al.*, "Joint phase noise and doubly selective channel estimation in full-duplex MIMO-OFDM systems," in *2016 International Conference on Advanced Technologies for Communications (ATC)*, 2016, pp. 413–418. DOI: 10.1109/ATC.2016.7764817.

[113] A. Mohammadian and C. Tellambura, "Full-duplex GFDM radio transceivers in the presence of phase noise, CFO and IQ imbalance," in *IEEE International Conference on Communications (ICC)*, 2019, pp. 1–6. DOI: 10.1109/ICC.2019.8761894.

[114] A. Mohammadian, C. Tellambura, and M. Valkama, "Analysis of self-interference cancellation under phase noise, CFO and IQ imbalance in GFDM full-duplex transceivers," *IEEE Trans. Veh. Technol.*, vol. 69, no. 1, pp. 700–713, 2020.

[115] G. H. Golub and C. F. V. Loan, *Matrix computations*, vol. 3. Baltimore, MD, USA: JHU Press, 2012.

[116] M. Sadek, A. Tarighat, and A. H. Sayed, "A leakage-based precoding scheme for downlink multi-user MIMO channels," *IEEE Trans. Wireless Commun.*, vol. 6, no. 5, pp. 1711–1721, 2007.

[117] S. M. R. Tandra and A Sahai, "What is a spectrum hole and what does it take to recognize one?" *Proceedings of IEEE*, vol. 97, no. 5, pp. 824–848, 2009.

[118] S. Parsaeefard *et al.*, "Dynamic resource allocation for virtualized wireless networks in massive-MIMO-aided and fronthaul-limited C-RAN," *IEEE Trans. Veh. Technol.*, vol. 66, no. 10, pp. 9512–9520, 2017.

[119] A. Mohammadian and C. Tellambura, "GFDM-modulated full-duplex cognitive radio networks in the presence of RF impairments," in *Annual International Symposium on Personal, Indoor and Mobile Radio Communications (PIMRC)*, 2019, pp. 1–6. DOI: 10.1109/PIMRC.2019.8904423.

[120] A. Mohammadian, M. Baghani, and C. Tellambura, "Optimal power allocation of GFDM secondary links with power amplifier nonlinearity and ACI," *IEEE Wireless Commun. Lett.*, vol. 8, no. 1, pp. 93–96, 2019.

[121] A. Mohammadian and C. Tellambura, "Cognitive GFDM full-duplex radios with RF impairments and ACI constraints," *IEEE Open J. Commun. Soc.*, vol. 1, pp. 732–749, 2020. DOI: 10.1109/OJCOMS.2020.2993611.

[122] H. Moazzen, A. Mohammadi, and M. Majidi, "Performance analysis of linear precoded MU-MIMO-OFDM systems with nonlinear power amplifiers and correlated channel," *IEEE Trans. Commun.*, vol. 67, no. 10, pp. 6753–6765, 2019.

[123] M. Baghani, S. Parsaeefard, M. Derakhshani, and W. Saad, "Dynamic non-orthogonal multiple access (NOMA) and orthogonal multiple access (OMA) in 5g wireless networks," *IEEE Trans. Commun.*, pp. 1–1, 2019.

[124] H. Qian, S. Yao, H. Huang, and W. Feng, "A low-complexity digital predistortion algorithm for power amplifier linearization," *IEEE Trans. Broadcast.*, vol. 60, no. 4, pp. 670–678, 2014.

[125] R. J. Baxley, C. Zhao, and G. T. Zhou, "Constrained clipping for crest factor reduction in OFDM," *IEEE Trans. Broadcast.*, vol. 52, no. 4, pp. 570–575, 2006.

[126] S. Atapattu, C. Tellambura, and H. Jiang, "Energy detection of primary signals over fading channels," in *International Conference on Industrial and Information Systems (ICIIS)*, 2009, pp. 118–122. DOI: 10.1109/ICIINFS.2009.5429879.

[127] S. P. Herath., N. Rajatheva, and C. Tellambura, "Unified approach for energy detection of unknown deterministic signal in cognitive radio over fading channels," in *IEEE International Conference on Communications Workshops*, 2009, pp. 1–5. DOI: 10.1109/ICCW.2009.5208031.

[128] S. M. Kay, *Fundamentals of statistical signal processing*. Upper Saddle River, NJ, USA: Prentice-Hall, 1993.

[129] A. Mohammadian and C. Tellambura, "Joint channel and phase noise estimation and data detection for GFDM," *IEEE Open J. Commun. Soc.*, vol. 2, pp. 915–933, 2021. DOI: 10.1109/OJCOMS.2021.3073348.

[130] A. Mohammadian, C. Tellambura, and G. Y. Li, "Deep learning-based phase noise compensation in multicarrier systems," *IEEE Wireless Commun. Lett.*, pp. 1–1, 2021, doi:10.1109/LWC.2021.3093574.

[131] T. Cui, C. Tellambura, and Y. Wu, "Low-complexity pilot-aided channel estimation for OFDM systems over doubly-selective channels," in *IEEE International Conference on Communications (ICC)*, vol. 3, 2005, 1980–1984 Vol. 3. DOI: 10.1109/ICC.2005.1494685.

[132] G. Wang, F. Gao, Y. Wu, and C. Tellambura, "Joint CFO and channel estimation for OFDM-based two-way relay networks," *IEEE Trans. Wireless Commun.*, vol. 10, no. 2, pp. 456–465, 2011. DOI: 10.1109/TWC.2010.120310.091615.

[133] T. Cui and C. Tellambura, "Semiblind channel estimation and data detection for OFDM systems with optimal pilot design," *IEEE Trans. Commun.*, vol. 55, no. 5, pp. 1053–1062, 2007. DOI: 10.1109/TCOMM.2007.895985.

[134] B. C. Levy, *Principles of signal detection and parameter estimation*. Springer Science & Business Media, 2008.

[135] T. Strutz, *Data Fitting and Uncertainty: A Practical Introduction to Weighted Least Squares and beyond*. Springer Vieweg, 2016.

[136] D. Ham and A. Hajimiri, "Virtual damping and Einstein relation in oscillators," *IEEE J. Solid-State Circuits*, vol. 38, no. 3, pp. 407–418, 2003.

[137] A. Demir, "Phase noise and timing jitter in oscillators with colored-noise sources," *IEEE Trans. Circuits Syst. I, Fundam. Theory Appl.*, vol. 49, no. 12, pp. 1782–1791, 2002.

[138] K. Zhang, W. Zuo, Y. Chen, D. Meng, and L. Zhang, "Beyond a Gaussian denoiser: Residual learning of deep CNN for image denoising," *IEEE Trans. Image Process.*, vol. 26, no. 7, pp. 3142–3155, 2017. DOI: 10.1109/TIP.2017.2662206.

[139] Z. Xiao *et al.*, "Achievable sum rates of half- and full-duplex bidirectional OFDM communication links," *IEEE Trans. Veh. Technol.*, vol. 66, no. 2, pp. 1351–1364, 2017.

[140] Z.-J. Qin, H. Ye, G. Y. Li, and B.-H. F. Juang, "Deep learning in physical layer communications," *IEEE Wireless Commun.*, vol. 26, no. 2, pp. 93–99, 2019. DOI: 10.1109/MWC.2019.1800601.

[141] A. Koc and T. Le-Ngoc, "Full-duplex mmwave massive MIMO systems: A joint hybrid precoding/combining and self-interference cancellation design," *IEEE Open J. Commun. Soc.*, vol. 2, pp. 754–774, 2021. DOI: 10.1109/OJCOMS.2021.3069672.

[142] Z. Tang *et al.*, "Pilot-assisted time-varying channel estimation for OFDM systems," *IEEE Trans. Signal Process.*, vol. 55, no. 5, pp. 2226–2238, 2007. DOI: 10.1109/TSP.2007.893198.

[143] H. Mehrpouyan, A. A. Nasir, S. D. Blostein, T. Eriksson, G. K. Karagiannidis, and T. Svensson, "Joint estimation of channel and oscillator phase noise in MIMO systems," *IEEE Trans. Signal Process.*, vol. 60, no. 9, pp. 4790–4807, 2012. DOI: 10.1109/TSP.2012.2202652.

Appendix A:

A.1 Proof of *Proposition 1*

Let us define implicit function $F(\alpha, \alpha_s) = R^{down}(\alpha, \alpha_s) - R_c = 0$ which maps α onto α_s implicitly. The derivation of $R^{up}(\alpha, \alpha_s)$ with respect to α_s can be written as

$$\frac{dR^{up}(\alpha, \alpha_s)}{d\alpha_s} = \frac{\partial R^{up}(\alpha, \alpha_s)}{\partial \alpha_s} + \frac{\partial R^{up}(\alpha, \alpha_s)}{\partial \alpha} \frac{d\alpha}{dF(\alpha, \alpha_s)} \frac{dF(\alpha, \alpha_s)}{d\alpha_s}. \tag{A.1}$$

From algebraic fractions in (2.49), it can be readily proved that $R^{up}(\alpha, \alpha_s)$ is monotonically increasing over α_s and monotonically decreasing over α, while $R^{down}(\alpha, \alpha_s)$ is monotonically increasing over α and monotonically decreasing over α_s. By exploiting these properties, it can be shown that $\frac{\partial R^{up}(\alpha,\alpha_s)}{\partial \alpha_s}$ and $\frac{dF(\alpha,\alpha_s)}{d\alpha}$ are positive, while $\frac{\partial R^{up}(\alpha,\alpha)}{\partial \alpha}$ and $\frac{dF(\alpha,\alpha_s)}{d\alpha_s}$ are negative. Thus, $\frac{dR^{up}(\alpha,\alpha_s)}{d\alpha_s}$ is positive and $R^{up}(\alpha, \alpha_s)$ is monotonically increasing over α_s, which transforms the objective function of optimization problem (2.50) $R^{up}(\alpha, \alpha_s)$ to α_s.

According to behavior of $R^{down}(\alpha, \alpha_s)$ over α and α_s, if $R^{down}(\alpha, \alpha_s) = R_c \leq R_{th} = R^{down}(P_{max}, P_{max})$, it is required to $\alpha \leq P_{max}$ or $\alpha_s \geq P_{max}$. Thus, in this case, the solution is $\alpha_s^{opt} = P_{max}$ and $\alpha^{opt} < P_{max}$. Otherwise, when $R^{down}(\alpha, \alpha_s) = R_c \geq R_{th}$, α_s^{opt} is derived by considering $\alpha^{opt} = P_{max}$. The proof of *Proposition 1* is completed.

Appendix B:

B.1 Desired symbol

Based on the detected symbol model (3.10), the received signal from SU_2 can be written as a summation of desired symbol $d^{2,s}_{k',m'}$ and interference $d^{21}_{k',m'}$. Thus, we have

$$R^{21}_{k',m'} = \mu^{s}_{k',m'} d^{2}_{k',m'} + d^{21}_{k',m'} \tag{B.1}$$

where $d^{2,s}_{k',m'} = \mu^{s}_{k',m'} d^{2}_{k',m'}$. Since desired symbol and interference should be independent, we can derive $\mu^{s}_{k',m'}$ by $\mu^{s}_{k',m'} = \mathbb{E}[R^{21}_{k',m'} d^{*2}_{k',m'}]$. It is defined that $R^{21}_{k',m'} = R^{21,I}_{k',m'} + R^{21,Q}_{k',m'} + R^{21,PA,I}_{k',m'} + R^{21,PA,Q}_{k',m'}$. Since complex data symbols are uncorrelated ($\mathbb{E}_d[d_{k_1,m_1} d^{*}_{k_2,m_2}] = \delta[k_1 - k_2]\delta[m_1 - m_2]$), $R^{21,Q}$ and $R^{21,PA,Q}$ are independent from $d^{*2}_{k',m'}$, $\mathbb{E}[R^{21,Q}_{k',m'} d^{*2}_{k',m'}] = \mathbb{E}[R^{21,PA,Q}_{k',m'} d^{*2}_{k',m'}] = 0$. Therefore, by using discrete GFDM signal in (1.2) and expressions in (3.8)-(3.10), we have that

$$\begin{aligned} \mu^{s}_{k',m'} = \mathbb{E}[(R^{21,I}_{k',m'} + R^{21,PA,I}_{k',m'}) d^{*2}_{k',m'}] = \sum_{l_1=0}^{L_1-1} \sum_{n=0}^{MK-1} h^{I}_{21}[n, l_1] \\ \left(a_1 \mathbb{E}[x_2[n - l_1] d^{*2}_{k',m'}] + a_3 \mathbb{E}[x_{PA,2}[n - l_1] d^{*2}_{k',m'}] \right) \\ f_{m'}[n] e^{\frac{-j2\pi k' n}{K}} \end{aligned} \tag{B.2}$$

where $\mathbb{E}[x_2[n - l_1] d^{*2}_{k',m'}]$ is derived as

$$\mathbb{E}[x_2[n - l_1] d^{*2}_{k',m'}] = \sqrt{p_2} g_{m'}[n - l_1] e^{\frac{j2\pi k' (n - l_1)}{K}}. \tag{B.3}$$

Moreover, according to that $x_{PA,2}[n - l_1] = x_2[n - l_1]|x_2[n - l_1]|^2$, $\mathbb{E}[x_{PA,2}[n - l_1] d^{*2}_{k',m'}]$ is derived as

$$\mathbb{E}[x_{2,PA}[n-l_1]d^{*2}_{k',m'}] = \sum_{k_1,k_2,k_3=0}^{K-1} \sum_{m_1,m_2,m_3=0}^{M-1} \mathbb{E}\left[d^1_{k_1,m_1} d^1_{k_2,m_2} d^{*1}_{k_3,m_3} d^{*1}_{k',m'}\right] g_{m_1}[n-l_1] g_{m_2}[n-l_1] g^*_{m_3}[n-l_1] \; e^{j2\pi \frac{k1+k2-k3}{K}(n-l_1)}. \tag{B.4}$$

Since complex data symbols are uncorrelated ($\mathbb{E}_d[d_{k_1,m_1} d^*_{k_2,m_2}] = \delta[k_1-k_2]\delta[m_1-m_2]$), for solving (B.4), we should consider two cases; 1) $k_1 = k_3$, $m_1 = m_3$, $k_2 = k'$, $m_2 = m'$, and 2) $k_1 = k'$, $m_1 = m'$, $k_2 = k_3$, $m_2 = m_2$. Thus, by calculating these two cases and after straightforward manipulation, (B.4) is simplified as

$$\mathbb{E}[x_{2,PA}[n-l_1]d^{*2}_{k',m'}] = 2p_2\sqrt{p_2}K e^{\frac{j2\pi k'(n-l_1)}{K}} g_{m'}[n-l_1] \sum_{m=0}^{M-1} |g_m[n-l_1]|^2. \tag{B.5}$$

Therefore, by substituting (B.3) and (B.5) in (B.2), $\mu^s_{k',m'}$ is derived. In result, $d^{2,s}_{k',m'} = \mu^s_{k',m'} d^2_{k',m'}$ is derived in (3.12).

B.2 digital cancellation symbols

By using detected symbol in (3.10), residual SI signal after active digital cancellation can be derived as

$$d^{RSI,1}_{k',m'} = R^1_{k',m'} - \mu^I_{k',m'} d^1_{k',m'} - \mu^Q_{k',m'} d^{*1}_{k',m'} \tag{B.6}$$

where $R^{DLC,I}_{k',m'} = \mu^I_{k',m'} d^1_{k',m'}$ and $R^{DLC,Q}_{k',m'} = \mu^Q_{k',m'} d^{*1}_{k',m'}$. Since linear and conjugate active digital cancellation symbols should be independent from each other and also $d^{RSI,1}_{k',m'}$, we can derive $\mu^I_{k',m'}$ and $\mu^Q_{k',m'}$ by $\mu^I_{k',m'} = \mathbb{E}[R^1_{k',m'} d^{*1}_{k',m'}]$ and $\mu^Q_{k',m'} = \mathbb{E}[R^1_{k',m'} d^1_{k',m'}]$, respectively. Similar to Appendix A and using discrete GFDM signal in (1.2) and expressions in (3.8)-(3.10), $\mu^I_{k',m'}$ and $\mu^Q_{k',m'}$ and in result $R^{DLC,I}_{k',m'} = \mu^I_{k',m'} d^1_{k',m'}$ and $R^{DLC,Q}_{k',m'} = \mu^Q_{k',m'} d^{*1}_{k',m'}$ can be derived.

B.3 Power of the desired symbol

By using desired symbol in (3.12), $p^{2,s}_{k',m'} = \mathbb{E}\left[|d^{2,s}_{k',m'}|^2\right]$ can be written as

$$\begin{aligned} p^{2,s}_{k',m'} &= \mathbb{E}\left[|d^{2,s}_{k',m'}|^2\right] = p_2\mathbb{E}[d^2_{k',m'}d^{*2}_{k',m'}] \sum_{l_1,l_3=0}^{L_1-1}\sum_{n_1,n_2=0}^{MK-1} \\ &\mathbb{E}[h^I_{21}[n_1,l_1]h^{*I}_{21}[n_2,l_3]](a_1+2Ka_3p_2\gamma[n_1-l_1]) \\ &(a^*_1+2Ka^*_3p_2\gamma[n_2-l_3])f_{m'}[n_1]f^*_{m'}[n_2]g_{m'}[n_1-l_1]g^*_{m'}[n_2-l_3]. \end{aligned} \tag{B.7}$$

We know that $\mathbb{E}[d^2_{k',m'}d^{*2}_{k',m'}] = 1$. Moreover, by considering the autocorrelation of phase noise in (3.14) and also $\mathbb{E}\left[|h_{21,l_1}|^2\right] = \sigma^2_{21,l_1}$, $l_1 = 0,1,...,L_1-1$, $\mathbb{E}[h^I_{21}[n_1,l_1]h^{*I}_{21}[n_2,l_3]]$ can be derived as

$$\begin{aligned} \mathbb{E}[h^I_{21}[n_1,l_1]h^{*I}_{21}[n_2,l_3]] &= \sigma^2_{21,l_1}e^{-4|n_1-n_2|\pi\beta T_s}\Big(|g_{TX,d}g_{RX,d}|^2 \\ e^{\frac{j2\pi(n_1-n_2)\epsilon}{K}} &+ |g_{TX,I}g_{RX,I}|^2e^{\frac{-j2\pi(n_1-n_2)\epsilon}{K}}\Big)\delta[l_1-l_3]. \end{aligned} \tag{B.8}$$

Therefore, by substituting (B.8) in (B.7), $p^{2,s}_{k',m'}$ can be derived. Furthermore, $p^{2,s}_{k',m'}$ can be written as a summation of three terms as $p^{2,s}_{k',m'} = p_2T^{2,s,1}_{k',m'} + p_2^2T^{2,s,2}_{k',m'} + p_2^3T^{2,s,3}_{k',m'}$ in (3.15)-(3.17).

B.4 Power of interference terms

By using detected symbol in (3.10), we rewrite $R^{21}_{k',m'}$ as $R^{21}_{k',m'} = \chi^1_{k',m'} + \chi^2_{k',m'}$, where

$$\begin{aligned} \chi^1_{k',m'} &= \sum_{l_1=0}^{L_1-1}\sum_{n=0}^{M-1} a_1\big(h^I_{21}[n,l_1]x_2[n-l_1] + h^Q_{21}[n,l_1] \\ &x^*_2[n-l_1]\big)f_{m'}[n]e^{-j2\pi\frac{k'}{K}n} \\ \chi^2_{k',m'} &= \sum_{l_1=0}^{L_1-1}\sum_{n=0}^{M-1} a_3\Big(h^I_{21}[n,l_1]x_{PA,2}[n-l_1] + h^Q_{21}[n,l_1] \\ &x^*_{PA,2}[n-l_1]\Big)f_{m'}[n]e^{-j2\pi\frac{k'}{K}n}. \end{aligned} \tag{B.9}$$

Now, $p^{21,t}_{k',m'} = \left[|R^{21}_{k',m'}|^2\right]$ is equal to

$$p_{k',m'}^{21,t} = \mathbb{E}\left[|\chi_{k',m'}^{1}|^2\right] + 2\Re\left[\mathbb{E}\left[\chi_{k',m'}^{1}\chi_{k',m'}^{*2}\right]\right] + \mathbb{E}\left[|\chi_{k',m'}^{2}|^2\right]. \tag{B.10}$$

Now each component is derived.

B.4.1 $\mathbb{E}\left[|\chi_{k',m'}^{1}|^2\right]$ derivation

According to (B.9) and this fact that $\mathbb{E}[x_2[n_1-l_1]x_2^*[n_2-l_3]] = \mathbb{E}[x_2^*[n_1-l_1]x_2[n_2-l_3]]$, $\mathbb{E}\left[|\chi_{k',m'}^{1}|^2\right]$ can be formulated as

$$\begin{aligned}\mathbb{E}\left[|\chi_{k',m'}^{1}|^2\right] = |a_1|^2 \sum_{l_1,l_3=0}^{L_1-1}\sum_{n_1,n_2=0}^{M-1}\Big(&\mathbb{E}\big[h_{21}^{I}[n_1,l_1]h_{21}^{*I}[n_2,l_3]\big] \\ &+ \mathbb{E}\big[h_{21}^{Q}[n_1,l_1]h_{21}^{*Q}[n_2,l_3]\big]\Big)\mathbb{E}[x_2[n_1-l_1]x_2^*[n_2-l_3]] \\ &f_{m'}[n_1]f_{m'}^*[n_1]e^{-j2\pi\frac{k'}{K}[n_1-n_2]}.\end{aligned} \tag{B.11}$$

Like as $\mathbb{E}\big[h_{21}^{I}[n_1,l_1]h_{21}^{*I}[n_2,l_3]\big]$ derivation in (B.8), $\mathbb{E}\big[h_{21}^{Q}[n_1,l_1]h_{21}^{*Q}[n_2,l_3]\big]$ is derived. The summation of these two terms can be summarized as

$$\begin{aligned}&\mathbb{E}\big[h_{21}^{I}[n_1,l_1]h_{21}^{*I}[n_2,l_3]\big] + \mathbb{E}\big[h_{21}^{Q}[n_1,l_1]h_{21}^{*Q}[n_2,l_3]\big] = \\ &\sigma_{21,l_1}^2 e^{-4|n_1-n_2|\pi\beta T_s}(|g_{TX,d}|^2 + |g_{TX,I}|^2) \\ &\left(|g_{RX,d}|^2 e^{\frac{j2\pi(n_1-n_2)\epsilon}{K}} + |g_{RX,I}|^2 e^{\frac{-j2\pi(n_1-n_2)\epsilon}{K}}\right)\delta[l_1-l_3].\end{aligned} \tag{B.12}$$

On the other hand, $\mathbb{E}[x_2[n_1-l_1]x_2^*[n_2-l_3]]$ can be derived as

$$\begin{aligned}\mathbb{E}[x_2[n_1-l_1]x_2^*[n_2-l_3]] =& p_1\sum_{k=0}^{K-1}\sum_{m=0}^{M-1} g_m[n_1-l_1]g_m^*[n_2-l_3] \\ &e^{j2\pi\frac{n_1-n_2}{K}k}.\end{aligned} \tag{B.13}$$

Now by substituting (B.12) and (B.13) into (B.11), $\mathbb{E}\left[|\chi_{k',m'}^{1}|^2\right]$ can be derived. To reduce complexity, it is considered that $\sum_{k=0}^{K-1} e^{-j2\pi\frac{k(n_1-n_2)}{K}} = K\sum_{t=0}^{M-1}\delta(n_1-n_2-tK)$. Final derivation can be presented by $\mathbb{E}\left[|\chi_{k',m'}^{1}|^2\right] = p_2 T_{k',m'}^{21,t,1}$, where $T_{k',m'}^{21,t,1}$ is given in (3.18).

B.4.2 $\mathbb{E}\left[\chi^1_{k',m'}\chi^{*2}_{k',m'}\right]$ derivation

According to that $\mathbb{E}[h_{21,l_1}h_{21,l_3}]=0$, It can be easily shown that $\mathbb{E}[h^I_{21}[n_1,l_1]h^{*Q}_{21}[n_2,l_3]]=0$. Therefore, according to (B.9), $\mathbb{E}\left[\chi^1_{k',m'}\chi^{*2}_{k',m'}\right]$ can be derived as

$$\begin{aligned}\mathbb{E}\left[\chi^1_{k',m'}\chi^{*2}_{k',m'}\right] &= a_1a_3^*\sum_{l_1,l_3=0}^{L_1-1}\sum_{n_1,n_2=0}^{M-1}\Big(\mathbb{E}\big[h^I_{21}[n_1,l_1]h^{*I}_{21}[n_2,l_3]\big]\\ &+\mathbb{E}\big[h^Q_{21}[n_1,l_1]h^{*Q}_{21}[n_2,l_3]\big]\Big)\mathbb{E}[x_2[n_1-l_1]x^*_{PA,2}[n_2-l_3]]\\ &f_{m'}[n_1]f^*_{m'}[n_1]e^{-j2\pi\frac{k'}{K}[n_1-n_2]}.\end{aligned}\tag{B.14}$$

By considering different cases like as what it has been done in (B.5) and utilizing the mentioned equality for deriving $\mathbb{E}\left[|\chi^1_{k',m'}|^2\right]$, $\mathbb{E}[x_2[n_1-l_1]x^*_{PA,2}[n_2-l_3]]$ can be derived. Therefore, by using derivations in (B.12) and (B.14), the final derivation is expressed as $2\Re\left[E\left[\chi^1_{k',m'}\chi^{*2}_{k',m'}\right]\right]=p_2^2T^{21,t,2}_{k',m'}$, where $T^{21,t,2}_{k',m'}$ is presented in (3.19).

B.4.3 $\mathbb{E}\left[|\chi^2_{k',m'}|^2\right]$ derivation

Like as two previous subsections, $\mathbb{E}\left[\chi^1_{k',m'}\chi^{*2}_{k',m'}\right]$ can be written as

$$\begin{aligned}\mathbb{E}\left[|\chi^1_{k',m'}|^2\right] &= |a_3|^2\sum_{l_1,l_3=0}^{L_1-1}\sum_{n_1,n_2=0}^{M-1}\Big(\mathbb{E}\big[h^I_{21}[n_1,l_1]h^{*I}_{21}[n_2,l_3]\big]+\\ &\mathbb{E}\big[h^Q_{21}[n_1,l_1]h^{*Q}_{21}[n_2,l_3]\big]\Big)\mathbb{E}[x_{PA,2}[n_1-l_1]x^*_{PA,2}[n_2-l_3]]\\ &f_{m'}[n_1]f^*_{m'}[n_1]e^{-j2\pi\frac{k'}{K}[n_1-n_2]}.\end{aligned}\tag{B.15}$$

$\mathbb{E}[x_{PA,2}[n_1-l_1]x^*_{PA,2}[n_2-l_3]]$ is derived in [120]. By using derivations in (B.12) and (B.15), $\mathbb{E}\left[|\chi^2_{k',m'}|^2\right]=p_1^3T^{1,t,3}_{k',m'}$, where $T^{1,t,3}_{k',m'}$ is presented in (3.20)

B.5 Proof of (3.41)

The SINR of desired signal transmitted from SU_2 to SU_1 (3.32) at t iteration is written as $\Gamma^{21}_{k',m'}(t)=F(p_2(t))/G(p_2(t),p_1(t))$, where $F(p_2(t))=\sum_{a=1}^{3}p_2^a(t)T^{2,s,a}_{k',m'}$ and $G(p_2(t),p_1(t))=\left(\sum_{a=1}^{3}p_2^a(t)T^{21,s,a}_{k',m'}+p_1^a(t)T^{11,s,a}_{k',m'}\right)+\sigma^n_{k',m'}$. Now, the approximation of

$F(p_2(t))$ and $G(p_2(t), p_1(t))$ with affine functions at points $p_2(t-1)$ and $p_1(t-1)$ is calculated as $\tilde{F}(p_2(t)) = F(p_2(t-1)) + \frac{\partial F}{\partial p_2}(p_2(t-1))(p_2(t) - p_2(t-1))$ and $\tilde{G}(p_2(t), p_1(t)) = G(p_2(t-1), p_1(t-1)) + \frac{\partial G}{\partial p_2}(p_2(t-1))(p_2(t) - p_2(t-1)) + \frac{\partial G}{\partial p_1}(p_1(t-1))(p_1(t) - p_1(t-1))$. Therfeore, $\tilde{\Gamma}^{21}_{k',m'}(t) = \tilde{F}(p_2(t))/\tilde{G}(p_2(t), p_1(t))$. The final approximated $\tilde{\Gamma}^{21}_{k',m'}(t)$ is presented in (3.41), where

$$
\begin{aligned}
A^2_{k',m'}(t-1) &= \sum_{a=1}^{3} a p_2^{a-1}(t-1) T^{2,s,a}_{k',m'} \\
B^2_{k',m'}(t-1) &= \sum_{a=1}^{3} a p_2^{a-1}(t-1) T^{21,s,a}_{k',m'} \\
C^1_{k',m'}(t-1) &= \sum_{a=1}^{3} a p_1^{a-1}(t-1) T^{11,s,a}_{k',m'} \\
E^2_{k',m'}(t-1) &= -\sum_{a=2}^{3} (a-1) p_2^{a}(t-1) T^{2,s,a}_{k',m'} \\
F^2_{k',m'}(t-1) &= -\Bigg(\sum_{a=2}^{3} (a-1)(p_2^a(t-1) T^{21,s,a}_{k',m'} + p_1^a(t-1) \\
& T^{11,s,a}_{k',m'}) \Bigg) + \sigma^n_{k',m'}.
\end{aligned}
\tag{B.16}
$$

Similarly, $\tilde{\Gamma}^{12}_{k',m'}(t)$ in (3.41) can be calculated. Similar to (B.16), $A^1_{k',m'}(t-1)$, $B^1_{k',m'}(t-1)$, $C^2_{k',m'}(t-1)$, $E^1_{k',m'}(t-1)$, and $F^1_{k',m'}(t-1)$ are derived.

Appendix C:

C.1 derivation of $\mathbf{\Gamma}$ in (4.29)

To obtain the matrix $\mathbf{\Gamma}$ derivation in (4.29), the cost function is written in (4.27) as

$$||\mathbf{z} - \mathbf{T}'_{i-1}\mathbf{F}'_c\Delta\bar{\mathbf{c}}' - \hat{\mathbf{J}}'_{i-1}\mathbf{X}\mathbf{F}_h\Delta\bar{\mathbf{h}}||^2 = ||\Re\{\mathbf{z}\} - \Re\{\mathbf{T}'_{i-1}\mathbf{F}'_c\Delta\bar{\mathbf{c}}'\} - \Re\{\hat{\mathbf{J}}'_{i-1}\mathbf{X}\mathbf{F}_h\Delta\bar{\mathbf{h}}\}||^2 + ||\Im\{\mathbf{z}\} - \Im\{\mathbf{T}'_{i-1}\mathbf{F}'_c\Delta\bar{\mathbf{c}}'\} - \Im\{\hat{\mathbf{J}}'_{i-1}\mathbf{X}\mathbf{F}_h\Delta\bar{\mathbf{h}}\}||^2. \tag{C.1}$$

By using (4.28),

$$\begin{bmatrix} \Re\{\mathbf{F}_h\Delta\bar{\mathbf{h}}\} \\ \Im\{\mathbf{F}_h\Delta\bar{\mathbf{h}}\} \\ \Re\{\mathbf{F}'_c\Delta\bar{\mathbf{c}}'\} \\ \Im\{\mathbf{F}'_c\Delta\bar{\mathbf{c}}'\} \end{bmatrix} = \mathbf{\Gamma}_1\mathbf{\Theta}, \tag{C.2}$$

where

$$\mathbf{\Gamma}_1 = \begin{bmatrix} \Re\{\mathbf{F}_h\} & -\Im\{\mathbf{F}_h\} & \mathbf{0} & \mathbf{0} \\ \Im\{\mathbf{F}_h\} & \Re\{\mathbf{F}_h\} & \mathbf{0} & \mathbf{0} \\ \mathbf{0} & \mathbf{0} & \Re\{\mathbf{F}'_c\} & -\Im\{\mathbf{F}'_c\} \\ \mathbf{0} & \mathbf{0} & \Im\{\mathbf{F}'_c\} & \Re\{\mathbf{F}'_c\} \end{bmatrix}. \tag{C.3}$$

Now, according to (C.1) and (C.2), $\mathbf{\Gamma}$ can be derived as

$$\mathbf{\Gamma} = \mathbf{\Gamma}_2\mathbf{\Gamma}_1, \tag{C.4}$$

where

$$\mathbf{\Gamma}_2 = \begin{bmatrix} \Re\{\hat{\mathbf{J}}'_{i-1}\mathbf{X}\} & -\Im\{\hat{\mathbf{J}}'_{i-1}\mathbf{X}\} & \Re\{\mathbf{T}'_{i-1}\} & -\Im\{\mathbf{T}'_{i-1}\} \\ \Im\{\hat{\mathbf{J}}'_{i-1}\mathbf{X}\} & \Re\{\hat{\mathbf{J}}'_{i-1}\mathbf{X}\} & \Im\{\mathbf{T}'_{i-1}\} & \Re\{\mathbf{T}'_{i-1}\}. \end{bmatrix} \tag{C.5}$$

C.2 SINR (4.48) with ideal compensation

First, based on (4.4) and $\mathbb{E}\{\mathbf{d}\mathbf{d}^H\} = \sigma_d^2\mathbf{I}_N$. Second, $\sigma_{J,l}^2 = \mathbb{E}\{J[l]J^*[l]\}$ is derived as

$$\sigma_{J,l}^2 = \frac{1}{N^2}\sum_{n_1=0}^{N-1}\sum_{n_2=0}^{N-1} e^{-2|n_1-n_2|\pi\beta T_s} e^{-j\frac{2\pi(n_1-n_2)l}{N}}. \tag{C.6}$$

It can be easily shown that $\sum_{l=0}^{N-1}\sigma_{J,l}^2 = \frac{1}{N}$. Now,

$$\mathbb{E}\{\mathbf{x}^H\mathbf{H}^H\mathbf{J}^H\mathbf{J}\mathbf{H}\mathbf{x}\} = \mathbb{T}\{\mathbb{E}\{\mathbf{J}\mathbf{H}\mathbf{x}\mathbf{x}^H\mathbf{H}^H\mathbf{J}^H\}\} = \mathbb{T}\{\mathbf{J}\left(\mathbf{R}_x \circ \mathbb{E}\{\mathbf{h}\mathbf{h}^H\}\right)\mathbf{J}^H\}, \tag{C.7}$$

where $\mathbf{R}_x = \mathbb{E}\{\mathbf{x}\mathbf{x}^H\}$, $\mathbf{h} = [H[0], ..., H[N-1]] \in \mathbb{C}^{N\times 1}$. Since the channel coefficients $H[l]$ are circularly symetric Gaussian distributed with mean zero and variance σ_h^2, $\mathbb{E}\{\mathbf{h}\mathbf{h}^H\} = \sigma_h^2\mathbf{I}_N$. Thus,

$$\mathbb{T}\{\mathbf{J}\left(\mathbf{R}_x \circ \mathbb{E}\{\mathbf{h}\mathbf{h}^H\}\right)\mathbf{J}^H\} = \frac{\sigma_h^2\sigma_d^2}{N}\sum_{l_1=0}^{N-1}\left(|\gamma_{l_1'}|^2 + |\gamma_{M+l_1'}|^2\right) \quad , \tag{C.8}$$

where $\{\gamma_0, \gamma_1, ..., \gamma_{2M-1}\}$ indicates the frequency response of the prototype filter and $l_1' = (l_1)_M$.

C.3 Derivation of constant μ

We have

$$\mu = \Re\{\mathbb{E}\{J[0]\}\} = \frac{1}{N}\Re\{\mathbb{E}\{\sum_{n=0}^{N-1} e^{j\phi[n]}\}\} = \frac{1}{N}\left(\sum_{n=0}^{N-1} e^{-\frac{1}{2}\mathbb{E}\{|\phi[n]|^2\}}\right) \quad . \tag{C.9}$$

Since $[\phi[n+1]-\phi[n]] \sim \mathcal{N}(0, 4\pi\beta T_s)$, $\mathbb{E}\{|\phi[n]|^2\} = (n+1)4\pi\beta T_s$, $n = 0, 1, ..., N-1$. Thus, μ is derived as

$$\mu = \frac{1}{N}\left(\sum_{n=0}^{N-1} e^{-2\pi\beta T_s(n+1)}\right) = \begin{cases} 1 & \beta = 0 \\ \frac{1}{N}\frac{e^{-2\pi\beta T_s} - e^{-2\pi\beta T_s(N+1)}}{1-e^{-2\pi\beta T_s}} & \beta > 0. \end{cases} \tag{C.10}$$

C.4 SINR with the proposed algorithm

Similar to Appendix B and based on the SINR formulation (4.53) and using the SINR for ideal compensation in (4.48),

$$\begin{aligned}\mathrm{SINR}_{\mathrm{prop}} &= \frac{\mathbb{T}\{\mathbb{E}\{\hat{\mathbf{J}}\hat{\mathbf{J}}^H\}\}\mathrm{SINR}_{\mathrm{ideal}}}{\mathbb{T}\{\mathbb{E}\{\left(\mathbf{J}-\hat{\mathbf{J}}\right)\left(\mathbf{J}-\hat{\mathbf{J}}\right)^H\}\}\mathrm{SINR}_{\mathrm{ideal}}+\frac{1}{N}} \\ &= \frac{\mathbb{E}\{||\tilde{\mathbf{j}}_{\mathbf{app}}||^2\}\mathrm{SINR}_{\mathrm{ideal}}}{\mathbb{E}\{||\tilde{\mathbf{j}}-\tilde{\mathbf{j}}_{\mathbf{app}}||^2\}\mathrm{SINR}_{\mathrm{ideal}}+\frac{1}{N}}.\end{aligned} \tag{C.11}$$

Based on $\tilde{\mathbf{j}}_{\mathbf{app}} = \mathbf{F}_c\bar{\mathbf{p}}$ and $\mathbf{F}_c = \frac{1}{N}\mathbf{F}_N\boldsymbol{\Upsilon}$, we have

$$\mathbb{E}\{||\tilde{\mathbf{j}}_{\mathbf{app}}||^2\} = \frac{1}{N^2}\mathbb{T}\{\mathbb{E}\{\boldsymbol{\Upsilon}\bar{\mathbf{p}}\bar{\mathbf{p}}^H\boldsymbol{\Upsilon}^H\}\} = \frac{1}{N^2}\mathbb{T}\{\boldsymbol{\Upsilon}\mathbf{R}_{\bar{\mathbf{p}}}\boldsymbol{\Upsilon}^H\}. \tag{C.12}$$

Moreover, based on $\tilde{\mathbf{j}} = \frac{1}{N}\mathbf{F}_N\tilde{\mathbf{p}}$, we have

$$\begin{aligned}&\mathbb{E}\{||\tilde{\mathbf{j}}-\tilde{\mathbf{j}}_{\mathbf{app}}||^2\} = \frac{1}{N^2}\mathbb{E}\{||\tilde{\mathbf{p}}-\boldsymbol{\Upsilon}\bar{\mathbf{p}}||^2\} \\ &= \frac{1}{N^2}\Bigg(\mathbb{T}\{\mathbb{E}\{\tilde{\mathbf{p}}\tilde{\mathbf{p}}^H\}\}+\mathbb{T}\{\mathbb{E}\{\boldsymbol{\Upsilon}\bar{\mathbf{p}}\bar{\mathbf{p}}^H\boldsymbol{\Upsilon}^H\}\} \\ &- 2\Re\Big\{\mathbb{T}\{\mathbb{E}\{\tilde{\mathbf{p}}\bar{\mathbf{p}}^H\boldsymbol{\Upsilon}^H\}\}\Big\}\Bigg) = \frac{1}{N}+\frac{1}{N^2}\mathbb{T}\{\boldsymbol{\Upsilon}\mathbf{R}_{\bar{\mathbf{p}}}\boldsymbol{\Upsilon}^H\} \\ &- 2\Re\Big\{\frac{1}{N^2}\mathbb{T}\{\mathbf{R}_{\tilde{\mathbf{p}},\bar{\mathbf{p}}}\boldsymbol{\Upsilon}^{\mathbf{H}}\}\Big\}.\end{aligned} \tag{C.13}$$

By substituting (C.12) and (C.13) in (C.11), effective SINR for proposed method in (4.53) is derived.

C.5 $\partial\mathbf{S}_{\boldsymbol{\Theta}}/\partial\boldsymbol{\Theta}$ derivation

Based on (4.8), we have $\mathbf{S}_{\boldsymbol{\Theta}} = \mathbf{J}'_{\mathbf{app}}\mathbf{X}\mathbf{F}_h\bar{\mathbf{h}}$. Moreover, based on (4.12) and (4.25), we have $\mathbf{S}_{\boldsymbol{\Theta}} = \mathbf{T}'\mathbf{F}'_c\bar{\mathbf{c}}'$, where $\mathbf{T}'$ is a circulant matrix formed by elements of $\mathbf{H}'\mathbf{x}$. According to aforementioned expressions for $\mathbf{S}_{\boldsymbol{\Theta}}$ and (4.28), $\partial\mathbf{S}_{\boldsymbol{\Theta}}/\partial\boldsymbol{\Theta}$ can be derived in an element by element as

$$
\begin{aligned}
\frac{\partial \mathbf{S}_{\boldsymbol{\Theta}}}{\partial \Re\{h'[n]\}} &= \left(\mathbf{J}'_{\mathbf{app}}\mathbf{X}\mathbf{F}_h\right) a_{n+1},\ n = 0, ..., L_{ch} - 1 \\
\frac{\partial \mathbf{S}_{\boldsymbol{\Theta}}}{\partial \Im\{h'[n]\}} &= j\left(\mathbf{J}'_{\mathbf{app}}\mathbf{X}\mathbf{F}_h\right) a_{n+1},\ n = 0, ..., L_{ch} - 1 \\
\frac{\partial \mathbf{S}_{\boldsymbol{\Theta}}}{\partial \Re\{c'[n]\}} &= \left(\mathbf{T}'\mathbf{F}'_c\right) e_n,\ n = 1, ..., Q - 1 \\
\frac{\partial \mathbf{S}_{\boldsymbol{\Theta}}}{\partial \Im\{c'[n]\}} &= j\left(\mathbf{T}'\mathbf{F}'_c\right) e_n,\ n = 1, ..., Q - 1,
\end{aligned}
\tag{C.14}
$$

where a_{n+1} is $(n+1)$-th columns of $\mathbf{I}_{L_{ch}}$ and e_n is (n)-th columns of $\mathbf{I}_{Q-1}$.